EXPERIMENTAL AND COMPUTATIONAL INVESTIGATION OF INCLINED JETS IN A CROSSFLOW

By

Matthew J. Findlay

B. A. Sc. (Engineering Science) University of Toronto

A THESIS SUBMITTED IN PARTIAL FULFILLMENT OF

THE REQUIREMENTS FOR THE DEGREE OF

DOCTOR OF PHILOSOPHY

in

THE FACULTY OF GRADUATE STUDIES

MECHANICAL ENGINEERING

THE UNIVERSITY OF BRITISH COLUMBIA

April 1998

Abstract

The flow field characteristics of four different geometries of a row of square jets in a crossflow at velocity ratios relevant to gas turbine film cooling applications have been examined using experimental and computational methods. The geometries considered were: long and short entry length streamwise-inclined jets, spanwise-inclined jets, and compound-angle jets. Mean velocity and turbulence measurements were made using a three-component LDV system. Jet penetration, spreading, and film cooling effectiveness were measured using a flame ionization detector. Numerical simulations were performed using three different turbulence models: the standard $k-\epsilon$ model, Menter's baseline blended $k-\epsilon/k-\omega$ model, and Menter's shear stress transport model.

The flow field at the jet exit is strongly influenced by the crossflow, as well as by the inlet conditions at the entrance to the jet orifice. At low velocity ratios the jets do not penetrate beyond the upstream boundary layer thickness. As the velocity ratio increases, the jet penetrates beyond the boundary layer resulting in stronger interaction with the crossflow. Considerable anisotropy of the turbulent flow field is observed. The film cooling effectiveness is best at the lowest velocity ratio as the jet is deflected strongly towards the floor of the wind tunnel, although the improvement is more significant for the streamwise injection case. At the highest velocity ratio the spanwise jets provide the best film cooling effectiveness but provide increased blockage to the crossflow.

The results of the preliminary computational analysis indicate that the flow field produced by each of the geometries provides a serious challenge for numerical modelling. Mean velocity gradients and turbulence kinetic energy levels are typically underpredicted by the computations due to the assumption of equilibrium turbulence inherent in the

models. The use of an isotropic eddy viscosity model must be reconsidered in light of the measured turbulence anisotropy and generation of turbulent shear stresses from velocity gradients not included in the standard eddy viscosity formulation.

Table of Contents

List of Tables

List of Figures

List of Symbols

D	Diameter of jet
I	Jet-to-crossflow momentum flux ratio $\left(=\frac{\rho_j V_j^2}{\rho_\infty V_\infty^2}\right)$
L	Length of jet hole; turbulence macroscale
M	Jet-to-crossflow mass flux (blowing) ratio $\left(=\frac{\rho_j V_j}{\rho_\infty V_\infty}\right)$
N	Number of data points in a sample
Pr	Prandtl number
R	Jet-to-crossflow velocity ratio $\left(=\frac{V_j}{V_\infty}\right)$
Re	Reynolds number $\left(=\frac{VD}{\nu}\right)$
Re_t	Turbulence Reynolds number $\left(=\frac{k^2}{\nu\epsilon}\right)$
St	Stanton number $\left(=\frac{q_w}{\rho U c_p (T_w - T_\infty)}\right)$
T	Temperature
Tu	Turbulence intensity $\left(=\frac{u'}{U}\right)$
U, V, W	Mean velocity components in the x-, y-, and z-directions, respectively
V_j	Bulk jet velocity
c_p	Specific heat
d	Diameter (LDV)
h	Heat transfer coefficient
k	Turbulent kinetic energy $(=\frac{1}{2}(\overline{uu}+\overline{vv}+\overline{ww}))$
l	Length (LDV)
q	Heat

s	Jet-to-jet spacing; general flow statistic (LDV)
t	Time
u, v, w	Fluctuating velocity components in the x-, y-, and z-directions, respectively
u', v', w'	Turbulent (r.m.s.) normal stresses
$\overline{uv}, \overline{uw}, \overline{vw}$	Turbulent shear stresses

Greek

Φ	Scalar variable; Dissipation function
ϵ	Turbulence dissipation rate
κ	Half angle of beam pair (LDV); von Karman constant
λ	Wavelength; turbulence Taylor microscale
μ	Dynamic viscosity
ν	Kinematic viscosity
η_f	Adiabatic film cooling effectiveness $\left(= \frac{T_{aw} - T_\infty}{T_2 - T_\infty}\right)$
$\overline{\eta_f}$	Spanwise-averaged film cooling effectiveness.
ρ	Density
ω	Turbulence specific dissipation rate

Subscripts

2	Refers to coolant conditions
8	Refers to time for eight fringe crossings for LDV
aw	Adiabatic wall
bd	Between data
e^{-2}	Refers to beam width at LDV probe
f	Fringe spacing
i	Index for data point in a sample

j	Refers to jet quantities
m	Measurement volume (LDV); mass; mixing length
p	Particle (LDV)
t	Refers to turbulence quantities
∞	Refers to free stream conditions

Superscripts

i	i^{th} component of a surface vector

Acknowledgement

I would like to thank my research supervisors, Dr. Ian Gartshore and Dr. Martha Salcudean, for their continuing support and encouragement over the course of this work. The financial support of NSERC and Pratt and Whitney Canada for the experimental phase of this thesis is appreciated. The assistance of Dr. Ibrahim Hassan in gaining a better understanding of CFD codes and converged solutions is gratefully acknowledged. Discussions on matters academic and otherwise with my colleagues at UBC - namely Dragos Licu, Michael Savage, Sid Chan, and Ken Thompson - helped make graduate school an enjoyable experience. Finally, I would like to thank my wife, Kim, for her encouragement and patience, particularly during the writing phase of this work.

Chapter 1

Introduction

1.1 Background

In the competitive market of gas turbine engines, whether for aerospace or electrical power generation applications, small improvements in performance can give a sizeable advantage in the marketplace. As such, engine designers are constantly looking for innovative methods for improving the performance of their engines. One such method, known as film cooling, has been in use since the 1950's and is one of the reasons that modern gas turbine engines have been able to attain very high efficiencies.

When considering the performance of a gas turbine engine, there are essentially two limiting factors: compressibility and blade stress. The mass flow that can pass through a given turbine will be limited by compressibility considerations. The square of the rotation speed is proportional to the work done by that stage of the turbine (Hill and Peterson (1992)) and the allowable blade stress limits the rotation speed of the turbine wheel. However, as the maximum engine temperature is increased, the allowable blade stress is reduced. Why, then, would it be desireable to increase the operating temperature of such an engine? The answer lies in considering the work done by the turbine. The work per unit mass is proportional to the inlet stagnation temperature of the turbine stage for a given pressure ratio and adiabatic efficiency. The turbine work is typically two or three times the useful output of the engine so a 1% increase in the turbine inlet temperature can result in a 2% to 3% increase in engine output. As a result, engine designers are willing

to consider fairly elaborate methods to allow for this increased operating temperature.

The use of advanced materials has allowed for some increase in operating temperatures but these materials can be very expensive to use and sometimes have undesirable characteristics for long-term applications (they may have poor oxidation resistance or tend to be brittle.) One of the most effective cooling methods is through mass transfer, which involves the injection of a secondary coolant fluid into the boundary layer on the surface to be protected. Two primary methods may be used to inject this secondary fluid: transpiration cooling and film cooling. A third method, ablation cooling consists of a coating on the surface which undergoes sublimation when exposed to high temperatures. This method is only useful in applications where the high temperatures are present for a short duration as the thermal protection is not renewable during operation.

In transpiration cooling the surface to be protected is porous and the secondary fluid enters the boundary layer through the small holes in the wall. This method is very effective for cooling the area at the porous wall and tends to increase the thickness of the boundary layer, reducing heat transfer from the hot flow outside the boundary layer. However, transpiration cooling is not practical for most gas turbine applications as the fabrication of porous materials is difficult and the materials tend to lack the strength required. In addition, the small pores are prone to clogging which would result in local 'hot spots', increasing the thermal stress on the blade.

In film cooling the secondary fluid enters the boundary layer through holes or slots in the surface. Slots are not used in gas turbine applications since the strength of the blade is reduced too much. Film cooling is not as effective as transpiration cooling for reducing heat transfer in the immediate vicinity of the injection point but provides good protection downstream of injection. One critical region requiring thermal protection is the leading edge of the turbine or stator blades. In this region (often referred to as

the 'shower-head' region) a large number of holes are drilled to simulate the good local coverage provided by transpiration cooling. The internal heat transfer in this critical region is also improved due to the coolant passing through the holes. There is a trade-off between having enough cooling holes and maintaining the strength of the blade.

Film cooling has been referred to as a 'three-temperature' problem where the temperatures involved are those of the free stream, T_∞, the coolant, T_2, and the wall, T_w. In dealing with film cooling processes, designers are primarily interested in the heat transfer rate per unit area, q, and the wall temperature, T_w. In order to determine these values, two primary methods have been developed, referred to as calculation methods A and B by Eckert (1984). Both methods make use of the assumption that the fluid properties are constant and equal for the main stream and coolant fluids. While this assumption is not entirely correct it may not be as poor as it initially appears, provided that the appropriate reference temperature is used to calculate the fluid properties (Eckert (1955)), (Knuth (1963a)), (Knuth (1963b)). With these assumptions the energy equation becomes linear and the technique of superposition may be used to find solutions.

The more widely used calculation technique, method A, defines the heat transfer coefficient, h, based on the adiabatic wall temperature, T_{aw}:

$$h = \frac{q}{T_w - T_{aw}} \tag{1.1}$$

This definition of h has the useful property that $q = 0$ when $T_w = T_{aw}$, and h is well-behaved (no infinite values). In addition, for the constant fluid property assumption h is independent of the temperature difference $T_w - T_{aw}$. The adiabatic wall temperature is usually non-dimensionalized as:

$$\eta_f = \frac{T_{aw} - T_\infty}{T_2 - T_\infty} \tag{1.2}$$

where T_∞ is the temperature of the main stream and T_2 is the temperature of the coolant. Both T_∞ and T_2 are assumed to be constant. This dimensionless adiabatic wall temperature, η_f, is referred to as the film cooling effectiveness or FCE.

Two coefficients are required to solve this three-temperature problem: the heat transfer coeffient, h, and the film cooling effectiveness, η_f. The values of these coefficients can be found, for example, from two experiments: one where the coolant is ejected at a temperature, T_2 with an adiabatic wall ($q_w = 0$), and one where the coolant temperature is equal to the free stream T_∞ with a finite heat flux prescribed along the wall. The first experiment simulates the influence of the mixing of the free stream and coolant fluids without the complication of the wall heat transfer while the second deals with the influence of the wall heat transfer without the complication of the mixing of the two fluid streams at different temperatures. The actual wall temperature is then just the sum of the wall temperatures from the two experiments.

With calculation method B, proposed by Metzger *et al.* (1968), the possibility exists that the heat transfer coefficient can go to infinity if certain conditions are met. The advantage of this method is that an adiabatic wall is not required. Eckert (1984) showed that the two calculation methods are similar and that the parameters from one approach may be converted into the parameters of the other. As such, method A has been selected for this work, primarily due to the advantage of determining η_f using the heat/mass transfer analogy. This will be discussed in more detail later.

An important consideration in the use of the method of superposition to determine the heat transfer parameters is that the fluid properties have been assumed constant and equal for both the coolant and free stream fluids. This allows the momentum and energy equations to become decoupled so that once the flow field is specified the temperature field may be determined. In much of the early work on film cooling, measurements were

made of heat transfer coefficients and film cooling effectiveness but very few researchers endeavoured to measure the flow field. However, the motion of the fluid is of critical importance in determining the temperature distribution on a film cooled surface. Consequently the study of jets in a crossflow became an important aspect of film cooling research which aims at a better understanding of the mechanisms behind the heat transfer. The importance of understanding the flow field becomes apparent when considering the use of numerical simulation to predict heat transfer on a surface. If the flow field is not predicted correctly, the temperature distribution on the surface will not be correct.

Jets in a crossflow are found in many applications ranging from smokestack pollution dispersion to V/STOL aircraft control to film cooling in gas turbine engines. Although similar characteristics can be found in all these flow fields, the details for a particular geometry can be quite different depending primarily on the jet-to-crossflow momentum flux ratio (I) (Holdeman and Walker (1977)). For film cooling applications the momentum flux ratio is typically fairly low, around 1.0 or lower, reflecting a trade-off between the heat transfer and the aerodynamics of the turbine blade, as well as considerations of power output. At higher momentum flux ratios, more coolant fluid is available to provide protection to the blade but the jet is more likely to separate from the surface leaving sections exposed to the hot crossflow. The increased injection also results in aerodynamic losses due to the increased interaction with the crossflow.

1.2 Literature Review

In general, three techniques are commonly used in the study of fluid flow and heat transfer: 1) analytical solutions of the relevant equations, 2) experimental measurements and subsequent empirical correlations, and 3) numerical simulation using Computational Fluid Dynamics (CFD) to solve the modelled equations of fluid flow and heat transfer.

Previous work using these techniques as applied to the film cooling process or jets in a crossflow will be discussed in the following sections. As noted earlier, jets in a crossflow at low momentum flux ratios are of primary interest for gas turbine film cooling applications and most of the literature cited will be at low I.

1.2.1 Analytical Studies

Most of the existing models in the literature seek to predict the jet trajectory and entrainment rate. Typically, empirical coefficients are used to reach this goal. As a result, better predictions are not necessarily based on a better understanding of the underlying physics.

Needham *et al.* (1988) and Needham *et al.* (1990) used an inviscid flow analysis to determine if an inviscid mechanism exists for the deflection of a three-dimensional jet in a crossflow. In these studies the jet is considered to emerge from a pipe inclined to the main flow. A small-disturbances treatment of an inviscid three-dimensional vortex sheet model is applied and an inviscid mechanism for the deflection of the jet is found in this way. However, such a mechanism only exists when the jet has a component of velocity in the crossflow direction. In the case of a three-dimensional jet perpendicular to the crossflow there is no inviscid mechanism for the jet deflection. For two-dimensional flows this is not the case (Stropky (1993)) but the focus of this thesis is on three-dimensional jets in a crossflow.

The model of Needham is typical of those used for the analysis of a three-dimensional jet in a crossflow and is only valid for situations where the jets are much stronger than the crossflow (ie. large velocity or blowing ratios.) In the case of very weak jets it is possible to use the boundary layer equations and treat the jet as a perturbation. In the case typical of gas turbine film cooling where the jet-to-crossflow velocity ratio, R, is of

order one, neither of these simplifications is appropriate.

1.2.2 Experimental Studies

Film cooling studies for multiple rows of holes are becoming more common and extensive work has been done by Prof. Ligrani's group in this area: Ligrani *et al.* (1994a), Ligrani *et al.* (1992), and Ligrani and Ramsey (1995). These studies have concentrated on film cooling effectiveness and heat transfer. Film cooling effectiveness over curved surfaces with various hole geometries has been examined by Ou and Han (1994), Mehendale and Han (1992), and Salcudean *et al.* (1994), among others. However, as the present work deals with single rows of jets on a flat surface, the literature review will focus on similar studies.

Early studies on jets in a crossflow as applied to the film cooling process focussed primarily on measuring the adiabatic film cooling effectiveness (η_f) or heat transfer along the surface downstream of the slot or jets. Measurements of the flow field were not common, as seen in the review paper by Goldstein (1971). In addition, most of the references cited are for a two-dimensional slot flow ejecting into the crossflow. Slots are not practical for most film cooling applications since, as is common in gas turbine blade cooling applications, the slots reduce the strength of the blade which reduces the potential power output of the engine. As a result, research started to focus more on discrete-hole cooling. However, the experimental measurements were primarily for the film cooling effectiveness, η_f, along the surface with occasional measurements of scalar transport (temperature or concentration) or one velocity component (typically streamwise) in the crossflow downstream of the jet(s).

Andreopoulos and Rodi (1984) made one of the first detailed flow field studies using a three-sensor hot-wire probe. They investigated the flow produced by a single round

jet perpendicular to the crossflow at low velocity ratios of $R = 0.5, 1.0, 2.0$. Many of the features found in the single jet case are also present in a row of jets. In fact, as pointed out by Goldstein (1971), superposition of η_f data for a single jet may be used to predict η_f for a row of jets if the velocity ratio, R, is small and the jet-to-jet spacing, s, is reasonably large (depending on R) so that jet-to-jet interaction is small. At low R the momentum of the injected fluid is insufficient to penetrate beyond the boundary layer into the mainstream flow and remains close to the wall. As the velocity ratio is increased the jet eventually penetrates beyond the boundary layer and is deflected in the direction of the crossflow. In addition, two counter-rotating vortices form inside the jet due to the transport of vorticity from the edges of the injection hole, giving the classic 'kidney-shaped' vortex pair which is characteristic of this flow field.

The jet spacing-to-diameter ratio, s/D, is an important parameter in the study of a row of jets in a crossflow. For rectangular holes the limiting case of $s/D = 1$ corresponds to a two-dimensional slot which has the greatest penetration into the crossflow. As s/D increases to between 3 and 5 the jet penetration is reduced as the free-stream fluid is entrained in the jet, enhancing deflection. As the spacing is increased further the jet penetration increases again due to the presence of the free-stream fluid flowing between adjacent jets which tends to increase the pressure on the downstream side of the jets (Sterland and Hollingsworth (1975)). The vortices from adjacent jets which induce a velocity field that tends to push the jets towards the floor (Haven and Kurosaka (1996)) are also moved farther away and have less influence on the jet penetration. Ligrani *et al.* (1994b) found indications of this tendency when comparing the adiabatic film cooling effectiveness from a single row of holes with a compound (streamwise and spanwise) angle orientation at two different s/D ratios. For $s/D = 6$, the spanwise-averaged effectiveness is 20 to 39 percent higher than when a spacing of $s/D = 7.8$ is used due to the increased

penetration of the jets with wider spacing.

In many of the earlier studies on jets in a crossflow, the entry length of the jet tube was long so that the flow was fully-developed before entering the crossflow. Long entry lengths are not possible on gas turbine blades and one of the first detailed studies was performed by Pietrzyk *et al.* (1989) who used a short entry length (L/D = 3.5) to simulate more closely the conditions typical in film cooling applications. Their data, from two-dimensional LDV measurements at R = 0.25, 0.5, and 1.0 on 35° streamwise-inclined jets, suggested the presence of a separation bubble from the sharp entrance to the jet orifice.

The use of round holes for jet in crossflow studies is far more common than square or rectangular jets. Kavsaoglu *et al.* (1989) investigated the surface pressure distributions along with some velocity and turbulence data produced by two 90° and two 60° streamwise-inclined rectangular jets at R =2, 4, and 8. Some comparisons are made between the pressure distributions produced by these jets and a single circular jet (Kavsaoglu and Schetz (1989)). The main difference between the round and rectangular jets is the sharp negative peak pressure coefficient around the upstream corners of the rectangular jets. The maximum negative pressure coefficient is lower for circular jets and occurs at the sides of the jets, although the area of negative pressure is larger for round jets.

Detailed studies of a turbulent free square jet were undertaken by Quinn and Militzer (1988) and Quinn (1992). Comparisons were made with data for a circular jet with the same upstream conditions and exit area. These studies showed that a square jet spreads faster than a circular jet in the near flow field. If the spreading of a turbulent free jet is viewed as the result of entrainment of the ambient fluid, then a square jet entrains fluid faster than an equivalent circular jet in the near field. By 20 'equivalent jet diameters'

(defined as the diameter of a circular jet with the same exit plane area as the square jet) downstream, the jet is fully axisymmetric. Recent work by Haven and Kurosaka (1997) indicates that square jets do not penetrate as far into the crossflow as do round jets. However, implications of improved film cooling for square jets are not clear due to the increased mixing with the crossflow.

In most film cooling applications there is a significant difference in the temperatures of the coolant and crossflow which results in a density difference between the two streams. This effect was investigated by Goldstein *et al.* (1974) for a row of round jets with lateral spacing of $s/D = 3$ inclined at 35° in the streamwise direction. They found that the use of a relatively dense secondary fluid ($DR = \rho_j/\rho_\infty \approx 3.5$) requires a significantly higher blowing ratio to cause jet separation from the surface than when the densities are the same. This effect results in considerably better cooling for $0.2 < M = \rho_j U_j/\rho_\infty U_\infty < 1.0$ ($0.057 < R < 0.286$). The data for the cooling effectiveness appear to collapse fairly well when plotted as a function of the momentum flux ratio, I.

In gas turbine applications there is also a large favourable pressure gradient which is not present in most flat-plate film cooling studies. Schmidt and Bogard (1995) investigated this effect using a pressure distribution representative of the suction side of a gas turbine blade and compared the results with zero-gradient data obtained in the same facility. The experiments used a density ratio of 1.6 with a range of blowing ratios from $M = 0.4$ to 1.5 ($R = 0.25$ to $R = 0.94$). When the cooling jets did not detach from the surface, the application of the pressure gradient resulted in an improvement of the lateral spread of the jets immediately downstream of the film cooling holes and increased the decay rate of the spanwise-averaged effectiveness. However, overall changes in effectiveness were small. At the high blowing ratio ($M = 1.5$) when the cooling jets were completely detached, the pressure gradient had essentially no effect on the resulting

effectiveness.

The upstream conditions can have a significant effect on the flowfield. Sinha *et al.* (1991) examined the influence of upstream conditions on a row of 35° streamwise-inclined jets. In this case the modified conditions were created by a similar row of jets which were 40D upstream. The main flow features which were present for the first row were also present for the second row. However, due to the thicker boundary layer present for the second row, the strength of these features was reduced. The lower momentum of the cross stream resulted in reduced velocity gradients and consequently lower levels of turbulence were generated downstream of the second row. The penetration of the jets from the second row into the cross stream flow was greater than the penetration from the first row as the blowing ratio was effectively increased for the second row due to the lower-velocity crossflow near the wall.

Kohli and Bogard (1995) investigated the effect of injection angle on the adiabatic effectiveness, thermal field, and two components of the velocity and turbulence fields at a density ratio (ρ_j/ρ_∞) of 1.6 and at injection angles of 35 and 55 degrees. At low momentum flux ratios the 55° holes showed only a slight decrease in the centreline effectiveness as compared to the 35° holes but there was a significant reduction at high momentum ratios. The more rapid change in the thermal field and higher turbulence levels for the 55° holes indicated that the stronger interaction with the crossflow resulted in more rapid mixing of the jet and crossflow as compared with the 35° case.

Detailed mean velocity field measurements were made by Lee *et al.* (1994) for a single 35° streamwise-inclined jet in a crossflow on a flat plate. All three components of velocity were measured using a five-hole probe and the interface between the jet and the crossflow was inferred from the vorticity distribution. Some difficulties were found with this inference method as the authors noted that at low velocity ratios the jet flow was

dominated by turbulence. As a result, the interface was only indicated for the highest velocity ratio of $R = 2.0$ where there was a more distinct change in the vorticity field between the jet and the crossflow. It was also suggested that the flow is sufficiently three-dimensional so that previous two-dimensional studies which attempted to characterize the flow field were unable to adequately describe the flow structure.

Honami *et al.* (1994) investigated the thermal and velocity fields for 30° spanwise-inclined jets with $s/D = 5$ and at velocity ratios of $R = 0.5, 0.85, 1.2$. Temperature and one (streamwise) velocity component data were obtained simultaneously using a double-wire probe. Surface temperature data were obtained using an encapsulated thermotropic liquid crystal. The authors found that the jet flow was asymmetric with a large vortex on one side. The asymmetry was increased with the velocity ratio which resulted in low film cooling effectiveness.

The influence of jet orientation relative to the crossflow was investigated by Lee *et al.* (1995). Their work indicated that, for a fixed inclination angle relative to the tunnel floor, as the orientation angle relative to the crossflow increased there was an improvement in the film coverage on the test surface. The researchers also found that the aerodynamic losses grew larger as the orientation angle was increased.

1.2.3 Computational Studies

As the experimental work on jets in a crossflow has become more sophisticated, the numerical predictions have been improving as well. In a sense, the need for validation of the numerical models has been the motivation for the increased attention to the flow field details in the experimental literature.

An early paper by Patankar *et al.* (1977) showed reasonable success in predicting the jet trajectory and mean velocity field for a single, circular jet injected perpendicular

to the crossflow at velocity ratios ranging from 2 to 10. However, a uniform, vertical velocity was prescribed at the jet exit and, since a rectangular grid was used, the circular hole was approximated by using a number of cells with a total area equivalent to the circular hole area. In light of this, and the coarse grid which was used ($10 \times 15 \times 15$ nodes for a $10D \times 15D \times 18D$ domain) the results are remarkable.

Bergeles *et al.* (1978) investigated the flow from perpendicular and 30^o inclined jets using a "partially parabolic" scheme in which the pressure information was allowed to propagate upstream while all other flow variables were treated using a fully-parabolic space-marching procedure. Initially the authors believed that the near field region of the jet was insensitive to the jet exit profile. Based on this assumption a uniform jet exit profile was prescribed. An anisotropic k-ϵ turbulence model was used but the grid was fairly coarse (5415 cells). The results indicated that a fully elliptic procedure was needed to deal with the near hole region of the jet, particularly in cases where a separation region appeared downstream of the jet hole. The authors also found that their assumption of insensitivity to the jet exit velocity profile was only valid for low blowing ratios ($M < 0.2$) and suggested that the domain be extended into the cooling hole.

The influence of the jet exit plane conditions on the downstream results has been investigated recently (Garg and Gaugler (1997)). The authors performed simulations for three different blade configurations using a $1/7^{th}$ power-law and "tuned" polynomial jet exit profiles for velocity and temperature distributions. The results showed that the downstream heat transfer coefficients may differ by as much as 60%, depending on the exit profile which was used, highlighting the importance of the near-hole region.

A simulation of the experiment performed by Andreopoulos and Rodi (1984) was computed by Demuren (1993) using a second-moment closure scheme for the modelling of the Reynolds stresses. All the trends in the experimental data were correctly predicted

but there was some uncertainty with the height of jet penetration into the crossflow. The discrepancies were attributed partly to the inability of the turbulence model to capture any large-scale coherent structures which were observed in the experiments and partly to the limitations inherent in hot-wire measurements in highly turbulent regions.

Zhou (1994) investigated the two- and three-dimensional flow from a slot and a row of square jets, respectively, which were perpendicular to the crossflow. The jet holes were included in the computational domain. A multiple-time-scale turbulence model (Kim and Chen (1989)), which helps account for the non-equilibrium turbulence, along with a low-Re k model near the wall provided the best agreement with the $2D$ experimental data. For the $3D$ model, a non-isotropic $k-\epsilon$ turbulence model was used in combination with the low-Re k model as the near-wall treatment. Good agreement between experimental and computational data for the spanwise-averaged film cooling effectiveness was found at lower mass flow ratios ($M = 0.2, 0.4$) but the agreement deteriorated as M increased to 0.8. In order to facilitate computations on more realistic, curved turbine blade geometries, He (1995) developed a general, curvilinear, structured grid code.

Recently, Leylek and Zerkle (1994) investigated the flow from a row of streamwise-inclined jets with short entrance lengths ($L/D = 3.5$ and $L/D = 1.75$), a jet-to-crossflow density ratio of $DR = 2$, and blowing ratios from $0.5 < M < 2$ ($0.25 < R < 1$). Of particular interest in this study was the fact that the computational domain included the plenum before the jet orifice. Their study confirmed the presence of a separation bubble at the inlet to the jet orifice as suspected by Pietrzyk *et al.* (1989). In a subsequent study of the same problem, efforts were made to identify the sources of discrepancy between measured and computed results (Walters and Leylek (1996)). This study used an unstructured, adaptive grid along with a second-order discretization scheme. The

authors identified the near-wall treatment and turbulence models which accurately represent anisotropic turbulence as areas requiring improvement for proper prediction of the downstream flow field.

1.3 Objectives and Scope

The literature survey has reviewed the progress of research on jets in a crossflow, both experiments and computations. It has been shown that, particularly in the case of jets with short entry lengths, the flow field near the jet exit is strongly influenced by the inlet conditions and, in turn, has a significant effect on the downstream flow. However, there are only a few studies in which detailed measurements of the three-dimensional flow field have been made. Even fewer have endeavoured to measure the turbulence field, particularly in the case of inclined jets. Of the detailed three-dimensional studies, the jet penetration and spreading is typically inferred from gradients in turbulence kinetic energy or vorticity, for example, rather than from direct measurements of the transport of jet fluid.

The objectives of the experimental investigation are as follows:

1. To obtain detailed flowfield measurements for inclined jets in a crossflow at velocity ratios of interest for gas turbine film cooling applications.

2. To determine the film cooling effectiveness and scalar transport for inclined jets in a crossflow using a heat/mass transfer analogy.

3. To provide a comprehensive experimental data set for validation of numerical simulations for this class of problems.

The objectives of the numerical investigation are as follows:

1. To perform a preliminary study on the prediction of the turbulent flow and scalar transport for inclined jets in a crossflow using a curvilinear grid.

2. To determine the critical parameters for an effective simulation of the flowfield based on comparisons with the experimental data set.

3. To assess the potential of several turbulence models to deal with the complicated flowfield produced by inclined jets in a crossflow.

It should be noted that the inclusion of all the parameters relevant to gas turbine film cooling (density differences between the jet and crossflow fluid, Mach number effects, pressure gradients, etc.) is beyond the scope of the present study. The intent is to gain a better understanding of the flow field and turbulence characteristics so that the numerical modelling of these simplified conditions may be improved before being extended to more realistic (and complicated) situations.

As noted previously, the complete solution of the film cooling problem requires two coefficients: the heat transfer coefficient, h, and the adiabatic film cooling effectiveness, η_f. The work presented in this thesis involves only the film cooling effectiveness since the heat/mass transfer analogy which was used for the scalar transport experiments provides an 'adiabatic' wall condition for the solid surfaces used here. The addition of heat transfer coefficient measurements would require extensive modifications to the existing experimental apparatus in order to obtain accurate measurements of the wall temperature downstream of the jets. These modifications are beyond the scope of the present investigation. The heat transfer coefficient could be inferred from computational analysis but there are many additional difficulties associated with the computation of heat transfer in complex flow fields (Launder (1988)). As such, the focus of the current study is on the correct prediction of the velocity fields and scalar transport data for the

various geometries. Once this information may be predicted with reasonable accuracy, the computations should be extended to include heat transfer predictions.

In the subsequent chapters a detailed investigation of inclined jets in a crossflow will be presented. In Chapter 2 the experimental methods are described. This includes the description of the configurations studied as well as the experimental techniques employed. Chapter 3 presents the analysis methods and results of the experimental investigation including the mean and turbulent flowfields as well as jet penetration and spreading from scalar transport measurements. In Chapter 4 the computational methodology for the numerical simulations on a curvilinear grid is introduced. In addition, several different turbulence models and the assumptions upon which they are based are presented. In Chapter 5 comparisons between the experimental and computational results are made. Finally, Chapter 6 presents the conclusions of this work and recommendations for future investigations are made.

Chapter 2

Experimental Arrangement and Measurement Techniques

In this chapter the experimental facilities and methodology used for this study of inclined jets in a crossflow are presented. The wind tunnel where the measurements were made is described and the configurations for the various inclined jet geometries are shown. The two primary experimental measurement tools, namely the laser Doppler velocimeter (LDV) and the flame ionization detector (FID), are described, along with the parameters of operation for the measurements.

2.1 Experimental Apparatus and Equipment

2.1.1 Wind Tunnel Facility

The experiments were performed in the Aerodynamics Laboratory in the Univerisity of British Columbia Department of Mechanical Engineering. The wind tunnel used for the experiments is an open-loop, forced-draft tunnel with a test section measuring $26.7cm \times 40.6cm \times 100cm$ and is shown in the schematic of Fig. 2.1. Air speed was controlled using a Variac connected to the 3.8 kW D.C. motor which drives the fan. The test section is located just downstream of a 4:1 area contraction with the row of jets being located $40.6cm$ from the entrance to the test section. The flow before the contraction was conditioned by five screens and a section of honeycomb $5cm$ thick. To ensure that the boundary layer was turbulent for all the experimental conditions a boundary layer trip wire, $2.4mm$ in diameter, was attached to the tunnel floor at the entrance to the

test section. The coordinate system used in the experiments is indicated in Fig. 2.1 with the x-axis in the direction of the crossflow, the z-axis vertical from the tunnel floor, and the y-axis spanwise across the tunnel to form a right-handed coordinate system with the origin at the centre of one hole.

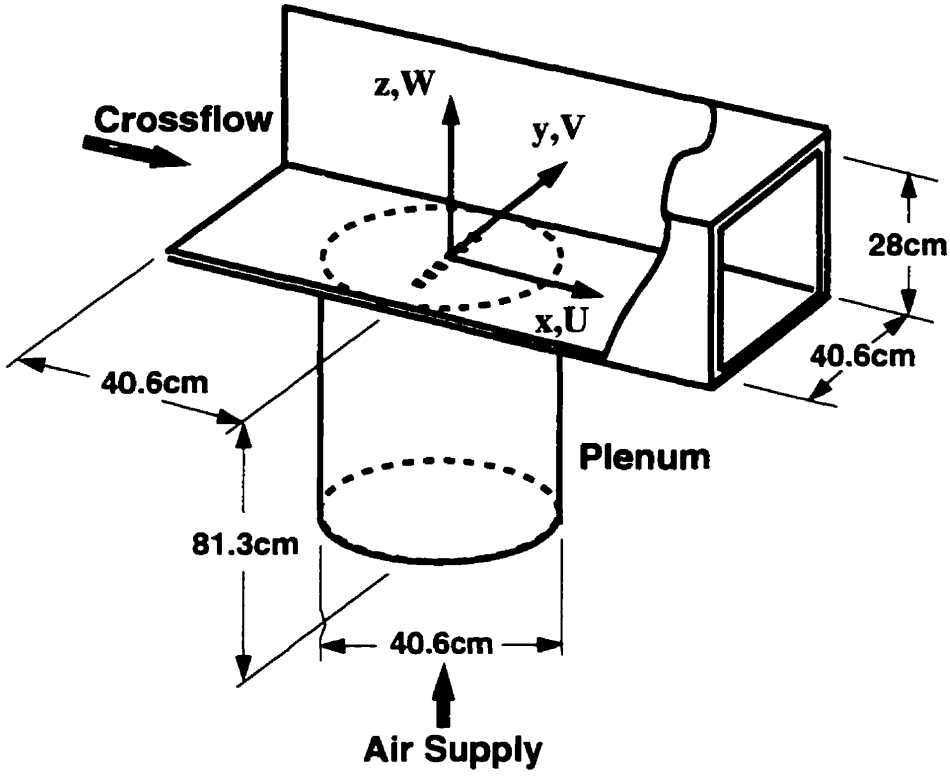

Figure 2.1: Wind tunnel schematic

The side walls of the test section were made of clear plexiglass to allow observation and flow visualization. The ceiling was made of $5mm$ plywood and the height of the downstream end of the ceiling was adjustable. The floor of the test section was plexiglass which was painted flat black to reduce reflections from the LDV beams in an effort to improve the signal-to-noise ratio (SNR). This was also beneficial with regards to optical exposure of the user to the laser beams. The ceiling and one side wall of the test section were designed with several small, removable sections to allow unobstructed optical access

to the test section. As a result, two openings were left in the test section which were just large enough to allow the beam pairs from the LDV probes to enter the wind tunnel without being refracted by the plexiglass walls. This also served to reduce the attenuation of the signal from the sampling volume back to the probes. Efforts were made to keep the size of the holes to a minimum to reduce any influence of the openings on the flow uniformity. The ceiling was adjusted so that there was no pressure gradient along the test section with the jets off and the ceiling and wall access holes open. The pressure in the test section is essentially atmospheric so that the holes in the walls do not create significant inflow/outflow disturbances.

2.1.1.1 Injection Geometries

Four different models were used for the experiments, as shown in Fig. 2.2 The jet holes were square in cross section so the inclination relative to the tunnel floor results in a rectangular jet exit hole. Throughout this work, reference is made to the 'diameter', D, of the jet. Since the jet holes are actually square, the diameter refers to the width of the jet (with cross-sectional area D^2.) The use of square, rather than round, jets is to allow for comparisons with previous work (Ajersch (1995)), (Zhou (1994)). In these studies, prependicular square jets were used since the CFD code which was used required orthogonal grids. As noted in the literature review in Chapter 1, there are some differences between square and round jets, particularly in the near-hole region. However, the experimental data presented here is primarily intended as a data set for numerical validation so that improvements in the computational modelling of these flows may be attained. Since it is the fine details which differ between the flow fields for square and round jets, it is believed that a CFD code capable of accurately simulating square jets in a crossflow will be able to simulate round jets with comparable accuracy. Further

information on the detailed structure of square jets may be found in Green (1995).

Two different entry lengths were used for the streamwise-inclined jets ($L/D = 4$ and $L/D = 8$) while the spanwise and compound-angle jets had entry lengths of $L/D = 4$. In all cases, the jets were inclined at 30° to the wind tunnel floor and the entrance to the jet ducts were sharp-edged. The square jets were assembled in pieces, rather than carving square holes in a solid block of plexiglass. The origin of the coordinate system for each case shown in Fig. 2.2 indicates the particular jet location used for the experiments. Also indicated are the directions of the jet flows for each case and the direction of the crossflow, showing that the row of jets was perpendicular to the crossflow direction for each case. The origin of the tunnel coordinate system is at the centre of the jet hole in the plane of the test section floor.

In the case of the streamwise-inclined jets two planes of symmetry were assumed: one down the centreline of the jet and one midway between adjacent jets. In the case of the spanwise and compound-angle jets, symmetry planes were not appropriate and two (spatially) periodic planes were assumed so that the row of jets was effectively infinite in extent. The justification for this treatment is discussed in Chapter 3. The planes of symmetry and periodicity are shown in Fig. 2.2.

The air supply to the jets was from a 400 kPa (static) compressed air line which was regulated by two flow regulators in series. A 0.918 m^3/min (F.S.) rotometer was used to measure the volume flow rate. The flow entered a plenum, or settling chamber, $\varnothing 40.6cm \times 81.3cm$ tall, which was placed below the tunnel floor as seen in Fig. 2.1. A radial diffuser was placed at the entrance to the plenum and an $10.2cm$ section of honeycomb helped to distribute the flow between the supply line and the jets.

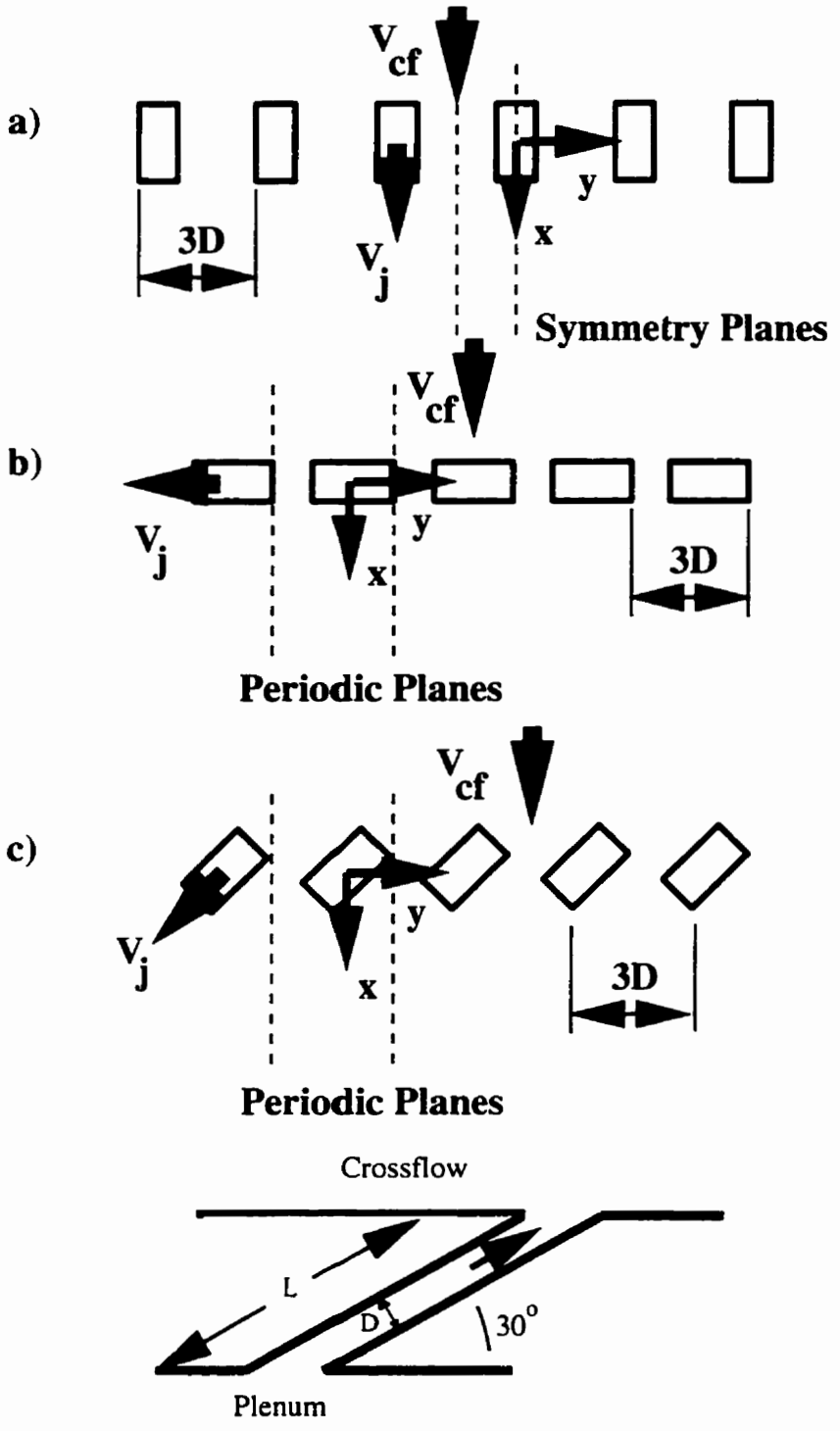

Figure 2.2: Coordinate definitions for a) streamwise-inclined jets, b) spanwise-inclined jets, and c) compound-angle inclined jets.

2.1.2 Laser Doppler Velocimetry

All of the mean velocities and turbulence quantities for these experiments were measured using laser Doppler velocimetry (LDV). In this section the principles of operation and the particular system used for the measurements are described.

2.1.2.1 Background

The principle idea behind LDV is that when two laser beams intersect at a common focal point, a fringe pattern is created. This focal location is not a true point and is actually finite in size. The focal location is referred to as the measurement or sampling volume. When a particle, travelling with the flow field, crosses through this fringe pattern, light is scattered at a frequency related to the particle velocity. It is apparent that in this configuration it is not possible to determine the direction of travel of the particle. In order to remove this ambiguity it is possible to frequency-shift one of the beams in the pair which results in a fringe pattern which moves within the measurement volume at a speed proportional to the shift frequency. If the shift frequency is high enough, a particle passing through the sample volume will always move in the same direction relative to the fringes.

The light that is scattered by a particle passing through the sample volume must be gathered by a receiver to be processed. If the receiver is incorporated into the probe which transmits the beam pair the method is referred to as 'back-scatter'. If the receiver is separate from the transmitting probe two other methods are possible: forward-scatter and side-scatter. In forward-scatter the receiver is in-line with the transmitting probe and has the strongest Doppler signal. As the name implies, side-scatter refers to configurations where the receiver is off the axis of the beam pair and is the method used in the present experiments. One pair of laser beams is required to measure one component of velocity

which is in the plane of the beams. If more than one component of velocity is required, more beam pairs are needed and all must intersect at a common point. The measurement of three velocity components usually precludes the use of forward-scatter operation due to the need for an unobstructed path between the transmitter and receiver.

2.1.2.2 Apparatus

In these experiments a Coherent Innova 5.0W argon-ion laser along with a TSI Colorburst 9201 multicolour beam separator was used to generate the three, different-coloured beam pairs: green, blue, and violet. The Colorburst 9201 contains a Bragg cell to allow for frequency shifting of one of the beams in each of the beam pairs. The beams were directed through fiber optic cables to two probes, TSI models 9831 and 9832, which were positioned to focus the beams to a single measurement volume. The configuration is shown in Fig. 2.3 and the properties of the beam pairs are indicated in Table 2.1. The fiber optic cables allowed for flexibility in positioning the probes. The probes also

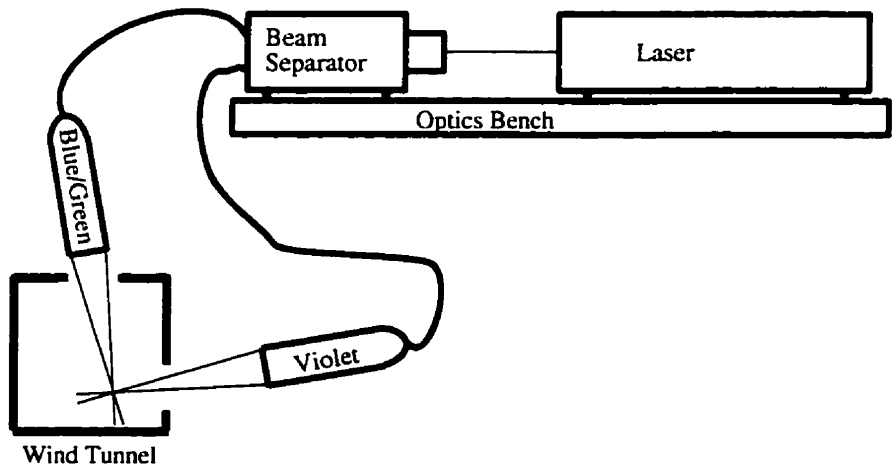

Figure 2.3: LDV system schematic

	Probe #1 Green Beam Pair	Probe #1 Blue Beam Pair	Probe #2 Violet Beam Pair
λ $[nm]$	514.5	488.0	476.5
$d_{e^{-2}}$ $[mm]$	2.82	2.82	2.82
d_f $[\mu m]$	3.73	3.54	3.46
d_m $[\mu m]$	90.5	85.8	83.8
l_m $[mm]$	1.31	1.24	1.22
κ $[^o]$	3.95	3.95	3.95

where λ = wavelength
$d_{e^{-2}}$ = diameter of beam at probe
d_f = fringe spacing
d_m = diameter of measurement volume
l_m = length of measurement volume
κ = half angle of the beam pair

Table 2.1: LDV beam properties

contained the receiving optics which coupled the received Doppler signal back through the fiber optic cables to a TSI Colorlink 9230 photomultiplier. The photomultiplier filtered the appropriate-coloured beams and passed the signal on to three TSI IFA550 signal processors, one for each component of velocity.

Seed particles for the flow were obtained from two separate devices. A Rosco 1500 smoke generator was used to seed the crossflow and a Genie smoke machine was used to seed the jet air. Both machines used Rosco smoke fluid which is a proprietary, CSA-approved, water-based solution usually used for theatre productions. Crossflow seeding was attained by simply blowing the smoke from the Rosco 1500 toward the tunnel intake end. The Genie smoke machine was placed in a sealed container which was in-line with the jet air supply and plenum.

2.1.2.3 Data Acquisition

The acquisition and storage of the raw data was controlled by software from TSI – FIND v. 4.03. The program allows the user to select the frequency shifts, signal filters (high and low cut-off), coincidence windows (which will be discussed in section 2.2.2.2), and provides a histogram of the most recent data points. A signal was accepted as valid if the IFA550 processors counted eight consecutive fringe crossings from a particle passing through the measurement volume, subject to some constraints on the timing of the fringe crossings. The time for the eight fringe crossings, denoted t_8, as well as the time between consecutive valid data points, t_{bd}, were stored on disk.

The velocity of the particle could then be determined from:

$$V = d_f\left(\frac{8}{t_8} \times 1000 - f_s\right) \tag{2.1}$$

where V = velocity, in m/s

f_s = frequency shift, in MHz

d_f = fringe spacing, in μm

t_8 = time for eight fringe crossings, in ns

and the fringe spacing is known for each beam pair (see Table 2.1).

2.1.2.4 Alignment

Two different types of alignment were required for these experiments: alignment of the beam pairs with respect to each other, and alignment of the beams with respect to the coordinate axis of the wind tunnel. Both of these issues are discussed in this section.

As mentioned previously, the measurement of three velocity components requires three beam pairs which intersect at a common point. With the system used in these

experiments the green and blue beams were transmitted through a common lens in one probe and were designed to intersect at one point with the plane of the beam pairs perpendicular to each other. The third component of velocity was measured from a violet beam pair transmitted from a second, separate probe which was perpendicular to the other two beam pairs. Alignment of the measurement volume from the violet component with the green and blue components was not a simple matter. The probes were mounted on a traverse mechanism which was designed so that the beams would intersect, but due to finite tolerances in the machining and flexibility in the mounting arms as well as the small diameter of the beams at the focal point, it was impossible to have the beams aligned without further adjustment. Small adjustments were made possible by set screws on the mounting arms.

Two methods were used for this alignment, each with certain advantages. The first method, referred to as the pinhole method, uses the principle that the beam intensity of a laser has a Gaussian profile (Rickards *et al.* 1993). As a result, when a laser beam is transmitted through a hole with a diameter smaller than the beam diameter the maximum power transmitted will occur when the beam and the hole are perfectly aligned. A pinhole unit was used for the alignment of the beams for the two streamwise-inclined jet geometries. The device was a 2.54 cm tall aluminum block with a top surface inclined at 45° which contained a photo-resistor covered by a 30 μm metal film with a 20 μm pinhole in the centre. A multimeter was used to measure the resistance of the sensor, which is inversely related to the light power incident on its surface. The pinhole unit was mounted on a rod that fit snugly in a jet hole so that a fixed point of reference was obtained for the alignment. The probes were adjusted until the maximum light power through the pinhole was obtained. The advantage of this technique is that the alignment is based on a quantitative rather than a qualitative assessment of beam position.

While the pinhole technique is a good method, it is not without certain limitations which were discovered during the alignment of the probes for the spanwise-inclined jet measurements. One of the blue beams had become misaligned with the others in the blue/green probe during movement to and from another set of experiments. With the pinhole method it was possible to iteratively adjust the position of the probes so that the maximum amount of light was passed through the pinhole for the particular beam configuration. However, it was found that the data rate was much lower than expected. The misalignment of the blue beam was discovered using a pin which was attached to a block. The end of the pin provided a fixed reference point. The beams were focussed on the pin head and projected through a microsope lens onto a wall. When the head of the pin was approximately at the centre of each of the beams the probes were considered aligned. The alignment procedure which evolved consisted of using the pinhole method to adjust the longitudinal position of each probe so that the beams would intersect midway along the length of their measurement volumes, l_m. The pin was then mounted on the block and the lateral adjustment of the beams was performed using this technique. Finally, the light power through the pinhole was checked to ensure that a maximum was attained. This method proved to be considerably faster than just using the pinhole method as the qualitative adjustment of the lateral position was more direct than the pinhole method. The method also resulted in better data rates as the probes were more precisely aligned.

In theory, the pinhole method should be superior to the more qualitative approach used here. However, for this to be the case, the plane of the pinhole sheet should be perpendicular to the beam to avoid any errors in assessing the location of maximum beam power. This would require a mounting device which allowed the pinhole sheet and photo-resistor to be rotated to face each beam while maintaining the pinhole at a

constant position in space. While it is not impossible to construct such a device, the simplicity of the combined approach is appealing.

The second alignment concern is that of the probes relative to the coordinate system of the jets in the wind tunnel. In the present experiments the probes were rotated approximately 6° about the tunnel x-axis to allow measurements near the floor without the bottom beam of the violet probe becoming obstructed (see Fig. 2.3). The importance of alignment relative to the reference coordinate system may be seen by considering the measurement of a small velocity component in the presence of a large one. If the beams are not aligned accurately, part of the large velocity will be picked up by the beams which should be measuring the small component. The effect may be corrected if the other two velocity components are known (or may be estimated) or if the precise angle of relative alignment is known. For the complex, three-dimensional flow present in the current investigation, *a priori* knowledge of the flow field is not available. In addition to the velocity components, if the turbulent shear stresses are to be measured the deviation of the beam pairs from orthogonality with respect to one another must be known for the correlation of orthogonal components. The angles about the x-, y-, and z-axes are referred to as α, β, and γ respectively, as shown in Fig. 2.4.

A detailed description of the alignment procedure, along with the measured angles of alignment, is given in Appendix A.

Once the angles of alignment have been determined, the measured velocities can be transformed to velocity components parallel to the tunnel axes through a coordinate rotation. The measured velocities are related to the tunnel coordinate velocities as follows:

$$\mathbf{U_m} = \mathbf{CU} \tag{2.2}$$

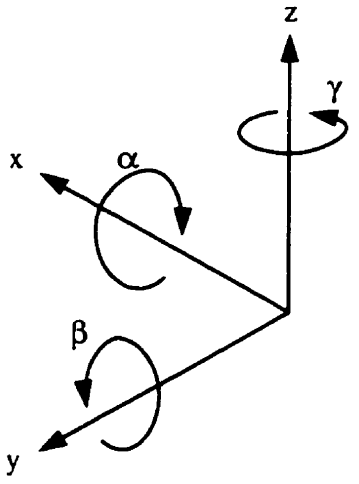

Figure 2.4: Alignment angles

where the subscript 'm' denotes the measured velocities and

$$\mathbf{U_m} = \begin{pmatrix} U_m \\ V_m \\ W_m \end{pmatrix} \quad \mathbf{U} = \begin{pmatrix} U \\ V \\ W \end{pmatrix} \tag{2.3}$$

$$\mathbf{C} = \begin{bmatrix} \cos\beta_1 \cos\gamma_1 & \cos\beta_1 \sin\gamma_1 & -\sin\beta_1 \cos\gamma_1 \\ -\cos\alpha_1 \sin\gamma_1 & \cos\alpha_1 \cos\gamma_1 & \sin\alpha_1 \cos\gamma_1 \\ \cos\alpha_2 \sin\beta_2 & -\sin\alpha_2 \cos\beta_2 & \cos\alpha_2 \cos\beta_2 \end{bmatrix}$$

However, the values which are known are those measured by the LDV system, $\mathbf{U_m}$, so if the velocities in the tunnel coordinate system are required, Equation (2.2) is rewritten as:

$$\mathbf{U} = \mathbf{C^{-1}U_m} \tag{2.4}$$

where C can be inverted numerically. The values obtained for C^{-1} are shown in Appendix A. These transformations were used to calculate the velocity in the tunnel coordinate system for each data point accepted by the LDV processor.

Finally, the position of the measurement volume with respect to the tunnel coordinate system was determined. This alignment was performed by moving the measurement volume to several reference locations within the test section. The reference locations used were the test section floor and the edges of the jet holes which had known locations in the tunnel coordinate system (see section 2.1.1). The measurement volume was positioned at the reference locations and the position of the probe traverse mechanism was recorded. The procedure was repeated several times.

2.1.3 Flame Ionization Detector

Measurements of the mass concentration distribution downstream of the jet holes are made using a flame ionization detector (FID). A flame ionization detector is an instrument which can be used to measure the concentration of a hydrocarbon contaminant, such as propane. A detailed description of a FID system for turbulent concentration measurements may be found in Fackrell (1978) and Fackrell (1980). Essentially, a FID consists of a hydrogen-in-air flame burning in an insulated chamber across which a voltage is applied. Upon introducing a hydrocarbon fuel to the chamber, ions are produced which results in a current. This current is converted to a voltage output and amplified to provide a precise measurement of the mass concentration of the contaminant.

In the present experiments, a 'rake' of eleven fine tubes ($0.5mm$ OD) was used for sampling the air/contaminant mixture. The contaminant used in the experiments was propane. The tubes may be placed along any line in the flow field. The height of the rake above the wind tunnel floor was set using a dial gauge attached to a vertical mounting

rod which was attached to the rake. The accuracy of positioning with this method was $\pm 1mm$. The contaminated air was sampled through each tube in turn, controlled by a Scanivalve, and sent to the FID.

In theory, the FID responds to the rate of mass of hydrocarbons entering the flame chamber. For a constant mass concentration, C, entering the chamber the output voltage should be $E = A\rho CQ$ where E is the output voltage, A is a constant, ρ is the density of the trace gas, and Q is the volume flow rate to the chamber. However, the ionization efficiency varies with the flow rate so the output voltage may be expressed as:

$$E = A\rho C f(Q) \tag{2.5}$$

As can be seen from Equation (2.5), the output voltage is a linear function of the concentration. Tests performed by Fackrell (1978) indicate that the response is indeed linear with contaminant concentrations between 0 and 2000 ppm. As such, only two calibration points are required for the system, namely the 0% and 100% points which correspond to FID measurements taken with no hydrocarbon contaminant and those taken from the contaminated supply air, respectively.

2.2 Experimental Procedures

This section details the operating parameters which were varied during the experiments. These include both the flow conditions and the methods used for data acquisition with the LDV and FID systems. As this study of inclined jets in a crossflow was motivated by the need for better flowfield information in the near hole region of a gas turbine film cooling situation, some of the parameters used are based on recommendations by Pratt & Whitney Canada (Pratt & Whitney Canada (1993)).

2.2.1 Flow Conditions

As mentioned previously, the jet-to-crossflow momentum flux ratio (I) is an important parameter in determining the hydrodynamic flow field characteristics for jets in a crossflow and is defined as:

$$I = \frac{\rho_j V_j^2}{\rho_\infty V_\infty^2} \tag{2.6}$$

where ρ is the density, V is the velocity, and the subscripts 'j' and '∞' refer to the jet and crossflow respectively. Another parameter frequently used in film cooling studies is the jet-to-crossflow mass flow or blowing ratio:

$$M = \frac{\rho_j V_j}{\rho_\infty V_\infty} \tag{2.7}$$

In this study, no temperature difference was introduced between the jets and the crossflow and since the velocities involved in these experiments were low the densities in Equation (2.7) cancel and the relevant parameter becomes the jet-to-crossflow velocity ratio R:

$$R = \frac{V_j}{V_\infty} \tag{2.8}$$

It has been found that the momentum flux ratio, I, is a more suitable parameter for scaling film cooling effectiveness (η_f) data than the mass flow or velocity ratios for weak injection cases where the jet does not separate from the surface. For strong injection cases, η_f appears to scale with R (Forth and Jones (1986)). Since the present experiments are in a range where both the strong and weak injection cases may occur, and for consistency with previously-published work ((Ajersch *et al.* 1997), (Findlay *et al.* 1996), (Findlay *et al.* 1997), among others) the velocity ratio, R, will be used here.

Geometry	$V_j[m/s]$	$D[mm]$	Re
Streamwise $(L/D = 8)$	6.05	12.0	4972
Streamwise $(L/D = 4)$	6.05	12.0	4972
Spanwise	5.71	12.9	5038
Compound-Angle	5.75	12.7	5000

Table 2.2: Jet flow conditions

The flow through the jets was at a fixed Reynolds number for all the experiments ($Re \approx 5000$) so that the jet flow was turbulent for all cases. The jet bulk velocity (V_j) was initially determined using the jet diameter, D, the kinematic viscosity of air, ν, at STP, and $Re = 5000$. Once V_j was known, the volume flow rate for the entire row of jets was calculated then adjusted so that the flow rate matched one of the marks on the rotometer in order to reduce the error in setting the flow rate. The new V_j was then calculated from the volume flow rate and Re was recalculated. The resulting jet conditions for each geometry are shown in Table 2.2.

Three different velocity ratios were used for each geometry: $R = 0.5$, 1.0, and 1.5. Since the jet velocity was fixed, the different velocity ratios were obtained by varying the crossflow velocity. This resulted in crossflow velocities of approximately (the actual values vary for each geometry): $V_\infty = 11.5m/s, 5.75m/s$, and $3.83m/s$ for $R = 0.5$, 1.0, and 1.5, respectively.

2.2.2 LDV Operation Parameters

The particular methods required in these experiments to obtain measurements of the mean and turbulent flow fields are discussed in the following sections.

2.2.2.1 Cross-coupled Operation

As mentioned previously, LDV systems can operate in several different modes: forward-, backward-, and side-scatter. The TSI system described in section 2.1.2.1 was initially configured to operate in back-scatter mode, which was satisfactory for measurements away from the wall. However, in the case of near-wall measurements (typically within $12.7mm$ or 1 jet diameter) the data rate was reduced, particularly for the velocity components measured by the blue/green probe above the wind tunnel. Since the data rate from the violet probe implied that the flow was seeded with particles as well as other regions in the flow field, and since it was possible to achieve good data rates in the plane of the floor at the jet exit hole, it was concluded that the proximity of the floor, possibly due to reflections, was responsible for the reduction in the data rate. To rectify the situation, the LDV system was operated in side-scatter, or cross-coupled mode (Rickards *et al.* 1993). By switching the optical fiber-to-photomultiplier connections, the signal generated from the green and blue beams was directed to the photomultiplier via the violet probe and *vice versa*. The data rates for the near-wall measurements were improved in this mode of operation.

This technique had the additional benefit that the effective size of the measurement volume was reduced, improving the resolution of the measurements. This is due to the receiving optics which are focussed on the measurement volume. In side-scatter operation, the receiving optics only 'see' a section of the measurement volume, rather than the entire length ($l_m \approx 1.25mm$) since the diameter of the receiving region is only $d_m \approx 85\mu m$ at the focus. Note that approximate values are given since l_m and d_m vary depending on the colour of the beam pair (see Table 2.1). This reduced measurement volume helps to minimize 'false turbulence' measurements due to velocity gradients. To understand the concept of 'false turbulence', consider the flow in a laminar boundary layer. Due

to the finite size of the measurement volume, if LDV measurements are made, particles passing through the volume at one side will have a different velocity than particles passing through the other side. These different velocities will appear as velocity fluctuations even though the flow might be perfectly steady.

2.2.2.2 Coincidence Mode

In order to measure the turbulent shear stresses it was necessary to operate the LDV system in coincidence mode. In this mode a measurement was accepted only if all three IFA550 processors received a valid signal within a user-selected time span, or coincidence window. The appropriate size of the coincidence window was estimated by dividing the diameter of the measurement volume by the approximate fluid velocity which calculates the estimated residence time of a particle passing through the measurement volume. If the coincidence window selected is too large it is possible that a given velocity measurement would be obtained from different particles passing through the measurement volume. If the selected coincidence window is too small the data rate decreases since the probability of obtaining a valid signal from all three processors within the allowed time would be reduced. A coincidence window smaller than the estimated residence time was always selected, even if it resulted in lower data rates.

2.2.2.3 LDV Measurement Locations

The measurement locations were selected so that the near-hole development of the jet could be resolved. For each velocity ratio, the boundary layer five jet diameters upstream of the jet exit ($x/D = -5$) was measured. With the exception of the streamwise-inclined ($L/D = 8$) case which used a lateral measurement spacing of $y/D = 0.5$, the measurements were made at $y/D = 0.25$ intervals at streamwise locations $x/D = -1, 0, 1, 2, 3, 5,$

and 8 and at vertical locations $z/D = 0.2, 0.4, 0.6, \ldots, 2.0, 2.5, 3.0, 3.5$, and 4.0. For the streamwise-inclined jets only half of the flowfield for a particular jet was measured due to the symmetry of the row. The coordinate axes with the measurement locations are shown in Figure 2.5 In addition, measurements were taken at the jet exit in the plane of the tunnel floor ($z/D = 0$). Except for the compound-angle jets, a 6×12 grid was used for the measurement locations, for a total of 72 data points. In the compound-angle case, a total of 85 locations were measured.

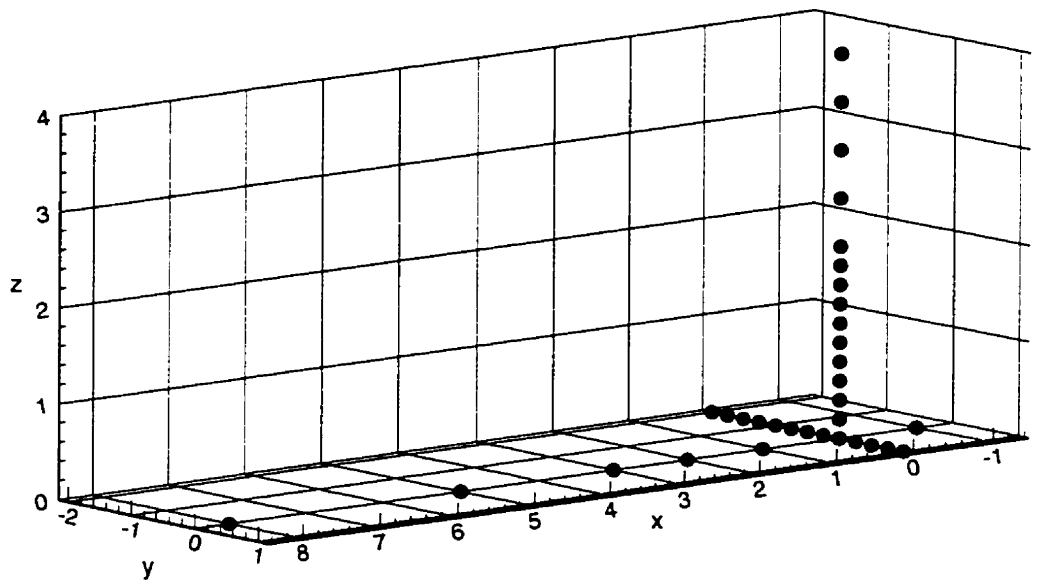

Figure 2.5: LDV measurement locations.

2.2.2.4 Additional Considerations

Two additional factors must be taken into account for the LDV measurements performed in these experiments. The first involves possible errors from non-uniform seeding of the flow. One type of non-uniform seeding occurs when the seeding density is dependent on the local flow velocity. There may be regions of densely-seeded, low velocity flow which would result in more low velocity readings being made by the processors, thus biasing the ensemble averages used to calculate the velocities. This form of non-uniform seeding was eliminated by thoroughly mixing the seed particles with the flow before entering the test section.

Another form of non-uniform seeding may occur if the particles are injected into the flow domain from more than one location, as was the case in these experiments. Although the flow from the jets and the crossflow were each uniformly seeded, differences in seeding density may have occurred as each flow was seeded independently. This difference in seeding density can lead to a bias in the flow measurements towards one fluid stream or the other. While it was difficult to accurately assess whether the two flows were uniformly seeded, it was noted that the intensity of the reflected laser light from the beam pairs varied with the seed density. By adjusting the seeding rates to minimize the differences in light intensity, the seeding densities of the two streams were roughly equalized.

The second factor which must be taken into account is the effect of multiple realizations. The IFA550 processors continuously check the incoming signal to determine whether or not a valid Doppler signal is present. After each measurement of t_8 is accepted, the processor resets to accept another signal, but if a seed particle remains inside the measurement volume during this time the particle velocity may be measured again. This situation can be seen if a typical flow situation is considered:

$$V = 5.0 \text{ m/s}$$
$$f_s = 500 \text{ kHz}$$
$$d_f = 3.54\ \mu m$$
$$d_m = 85.8\ \mu m$$

where V is the component of velocity in the direction measured by the blue beam pair. Using Equation (2.1) it is found that $t_8 = 4183ns$. If the particle travels the full diameter of the measurement volume it will have a residence time of $17080ns (= d_m/V)$ which could possibly result in 4 readings (= 17080/4183) from the same particle. Slower-moving particles reside in the measurement volume for a longer time and will produce a greater number of realizations (in the limit of a zero velocity particle where frequency shifting is used the number of realizations is infinite) which will bias the flow statistics. The selection of a coincidence window which was close to the expected residence time forced the processors to reset after the coincidence time, rather than immediately after t_8 was measured, which helped to ensure that a given particle was no longer in the measurement volume. The bias in the mean flow data due to fluctuations in the velocity, which is often discussed in the LDV literature, will be discussed in section 3.1.1.3.

2.2.3 FID Operation Parameters

In this section the methodology for the jet concentration measurements is described. The description includes the calibration and data acquisition techniques as well as the measurement locations. Measurements were made for all the velocity ratios ($R = 0.5, 1.0, 1.5$) and for all the geometries except the streamwise-inclined $L/D = 8$ case.

2.2.3.1 Calibration

The calibration method described here is based on the assumption that the relationship between the FID output voltage and propane concentration is linear, as found by Fackrell (1978). Several tests have been carried out for the FID system used in these experiments (Salcudean *et al.* (1994), Sun (1995)) which have shown the system response to be linear.

In the present experiments, each tube in the rake is calibrated individually. The flow rate through each tube is kept constant by a suction pump associated with the FID. The calibration at the 0% and 100% reference points is recorded in the computer for each tube. During the experiments the concentration inside the plenum (the 100% reference) is checked before each measurement to ensure that the reference concentration is unchanged within $\pm 2\%$. All the measurements are made with a data acquisition system which controls the switching between tubes, processes the FID voltage signals and outputs the concentration measurements to disk. A time-delay is used after switching sampling tubes to clear the line of any air which was sampled from another location.

2.2.3.2 FID Measurement Locations

The FID measurement locations were selected to coincide with the LDV measurement locations. In the streamwise direction, measurements were made at $x/D = 1, 2, 3, 5$, and 8 at vertical spacings of $z/D = 0.4$ from the floor ($z/D = 0$) to a height where all the probes in the rake measured a zero for the concentration of propane in the flow. The spanwise locations were determined by the spacing of the tubes in the rake. The first 9 tubes were spaced $0.25D$ apart and the remainder of the eleven tubes were $0.375D$ apart which resulted in a total span of $2.75D$. For the streamwise-inclined jets ($L/D = 4$) the rake was positioned with the first tube at the mid-jet plane $y/D = -1.5$ and the remainder in the direction of increasing y. For the spanwise-inclined and compound-angle

jets the first tube was positioned at $y/D = -2$. Additional measurement planes were introduced at $x/D = 1.5$ for the streamwise $L/D = 4$ case, at $x/D = 0.5$ for the spanwise case, and at $z/D = 0.2$ intervals for the compound-angle case in order to better resolve regions of interest in the flow.

2.2.3.3 Additional Considerations

Measurements of concentration for η_f are not taken exactly at the wall, but rather at a slight distance from the surface. A correction for this difference has been suggested by Sun (1995) using wall functions to correct the mass transfer Stanton numbers (St_m) for two-dimensional transpiration cooling. However, in this case the wall is simulated as adiabatic which would have a temperature gradient of zero at the wall. In addition, the use of wall functions for the three-dimensional, complicated flow field produced by discrete jets in a crossflow is not entirely appropriate.

Chapter 3

Experimental Results

In this chapter, the experimental results from the LDV and FID measurements are presented and discussed. The techniques applied for the processing of the data are described. Results are presented for all four geometries at various velocity ratios. The data presented includes the mean velocities, the turbulent normal and shear stresses, and scalar transport measurements. Most of the results presented are at the velocity ratios $R = 0.5$ and $R = 1.5$ since the behaviour of the flow field at the velocity ratio of $R = 1.0$ is typically intermediate between the observed behaviours at the other two R values. A disk containing all the experimental data is included with the thesis.

3.1 Data Analysis

3.1.1 LDV Data

As discussed in section 2.1.2.3, the data from each measurement position in the flow field was stored on disk in the form of t_8 values for each data point. One thousand data points were taken at each measurement location. These values must be converted into velocities (using Equation (2.1)) and transformed from the LDV coordinate system into the tunnel coordinate system using the transformation matrices of Equation (A.5). It was found that the TSI software was not suitable for this task since it did not allow for any corrections to the velocity statistics and was only able to analyse fixed numbers of the t_8 data points (ie. only blocks of 1000 data points were used so that of, say, 1800

data points, 800 would not be used in the analysis). In order to resolve these difficulties an analysis software program was written: XFORMV20 (Ajersch (1993)). The features of this program, as they apply to the analysis of the data for these experiments, will be described in the following sections. Figures showing the effects of the various corrections applied to the data are shown at arbitrary locations in the flowfield which should represent typical profiles.

It should be noted that the raw data files containing the t_s values were not altered as a result of the analysis or coordinate transformation so that other analysis techniques could be used on the raw data in the future.

3.1.1.1 Removal of Bad Data Points

The XFORMV20 software allows the user to remove velocities which are outside three standard deviations from the mean. This allowed the analysis to exclude data points which were considered strange or unlikely and was used for all the results presented here. The removal of data outside three standard deviations has been used previously (Nakao *et al.* 1987) to remove the apparent turbulence produced by the ambiguity noise in the signal (George and Lumley (1973)). Tests for the experiments performed here indicated that there was no noticeable difference between the mean velocity results obtained using this approach and those with no data point removal.

3.1.1.2 Velocity Transformation

In order to perform the velocity transformation from the angles of alignment of the LDV system with respect to the tunnel coordinates, a data file with the angles was read into XFORMV20. The transformation matrix, $\mathbf{C^{-1}}$, was then calculated for use in Equation 2.4. The individual velocity measurements were transformed into the tunnel coordinate

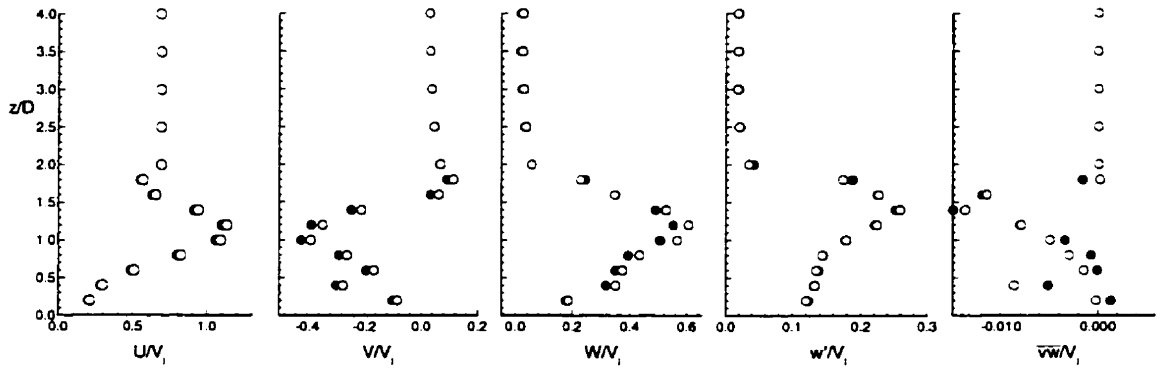

Figure 3.1: Comparison of data with (•) and without (○) angular corrections. Compound-angle jet, $R = 1.5$, $x/D = 2$, $y/D = -1$.

system before the calculation of the flow statistics. The angles and transformation matrices are presented in Appendix A. The graphs in Fig. 3.1 show the effect the angular transformation has on the data. Again, the three mean velocities, one turbulent normal stress, and one turbulent shear stress are shown. The solid and hollow symbols represent the transformed and untransformed data respectively. The streamwise component of velocity, U/V_j, appears to be affected the least by the transformation ($\approx 5\%$) with the largest corrections occuring in the jet-affected region of the flow where there are significant spanwise (V/V_j) and vertical (W/V_j) components of velocity. At velocity ratios lower than the $R = 1.5$ shown, where the crossflow velocity becomes dominant, the corrections to U/V_j become almost negligible. The V/V_j and W/V_j values change by approximately 10% in the jet-affected region. Typically the turbulence quantities do not change significantly as a result of the angular transformation since they are calculated from the fluctuations of the velocity. However, in regions of high turbulence where $\sqrt{k}/V_j$ reaches 25%, the corrections are more significant (Fig. 3.1). The effect of the angular transformation in the freestream is small for all the variables shown in Fig. 3.1 as the velocities are moderate and the turbulent fluctuations are small. The source of the

deviation in the V/V_j and $\overline{vw}$ data near the wall is not clear as the data were obtained from the same particles that produced the smooth curves for the other variables.

3.1.1.3 Calculation of Expected Values – Velocity Bias Correction

When mean flow statistics are calculated from LDV data using arithmetic averages, a bias in the statistics will exist (Edwards (1987)). The velocity bias described here differs from the bias described in section 2.2.2.4 in that it is assumed the flow is uniformly seeded. The bias described here occurs because, in a uniformly seeded flow, more particles will pass through the measurement volume in a given time when the flow velocity is high than when the velocity is low. If a simple arithmetic average is taken, the statistics will be biased towards the high velocities. A number of different correction schemes, typically weighted averages, are available to reduce this bias (Edwards (1987)). Inverse velocity weighting, first proposed by McLaughlin and Tiederman (1973), is used here. With this technique, the expected value of some general flow variable, s, is given by:

$$\langle s \rangle = \frac{\sum_{i=1}^{N} \frac{s_i}{|\vec{\mathbf{V}}_i|}}{\sum_{i=1}^{N} \frac{1}{|\vec{\mathbf{V}}_i|}} \tag{3.1}$$

where s_i is the contribution from the i^{th} data point, $\vec{\mathbf{V}}_i$ is the velocity for that data point (all three components), and N is the number of data points in a particular sample.

With this approach in mind, the flow statistics for these experiments are defined in the following way: once the velocity transformations for the angular alignment have been made a general velocity component is considered:

$$U_i = U + u_i \tag{3.2}$$

where U_i is the instantaneous velocity for the i^{th} data point, U is the mean velocity averaged over N data points, and u_i is the fluctuating component of the velocity for the i^{th} data point. The expected values are then calculated from the following equations.

Mean velocities:

$$\langle U \rangle = \frac{\sum_{i=1}^{N} \frac{U_i}{|\vec{V}_i|}}{\sum_{i=1}^{N} \frac{1}{|\vec{V}_i|}} \qquad \langle V \rangle = \frac{\sum_{i=1}^{N} \frac{V_i}{|\vec{V}_i|}}{\sum_{i=1}^{N} \frac{1}{|\vec{V}_i|}} \qquad \langle W \rangle = \frac{\sum_{i=1}^{N} \frac{W_i}{|\vec{V}_i|}}{\sum_{i=1}^{N} \frac{1}{|\vec{V}_i|}} \tag{3.3}$$

Turbulent normal stresses:

$$\langle u' \rangle = \langle \sqrt{\overline{uu}} \rangle = \sqrt{\frac{\sum_{i=1}^{N} \frac{u_i^2}{|\vec{V}_i|}}{\sum_{i=1}^{N} \frac{1}{|\vec{V}_i|}}} \quad \langle v' \rangle = \langle \sqrt{\overline{vv}} \rangle = \sqrt{\frac{\sum_{i=1}^{N} \frac{v_i^2}{|\vec{V}_i|}}{\sum_{i=1}^{N} \frac{1}{|\vec{V}_i|}}} \quad \langle w' \rangle = \langle \sqrt{\overline{ww}} \rangle = \sqrt{\frac{\sum_{i=1}^{N} \frac{w_i^2}{|\vec{V}_i|}}{\sum_{i=1}^{N} \frac{1}{|\vec{V}_i|}}} \tag{3.4}$$

Turbulent shear stresses:

$$\langle \overline{uv} \rangle = \frac{\sum_{i=1}^{N} \frac{u_i v_i}{|\vec{V}_i|}}{\sum_{i=1}^{N} \frac{1}{|\vec{V}_i|}} \qquad \langle \overline{uw} \rangle = \frac{\sum_{i=1}^{N} \frac{u_i w_i}{|\vec{V}_i|}}{\sum_{i=1}^{N} \frac{1}{|\vec{V}_i|}} \qquad \langle \overline{vw} \rangle = \frac{\sum_{i=1}^{N} \frac{v_i w_i}{|\vec{V}_i|}}{\sum_{i=1}^{N} \frac{1}{|\vec{V}_i|}} \tag{3.5}$$

The analysis software, XFORMV20, then outputs these values for each data location to a file formatted for use by TECPLOT, a graphing package.

The effect of inverse velocity weighting is shown in Fig. 3.2. As in the previous sections the three mean velocities, one turbulent normal stress, and one turbulent shear stress are shown. The solid and hollow symbols represent the corrected and uncorrected data respectively. The inverse velocity weighting tends to reduce the magnitude of the mean velocities, as expected. Corrections in the freestream are small since the turbulence levels are low with little spread in the measured velocities.

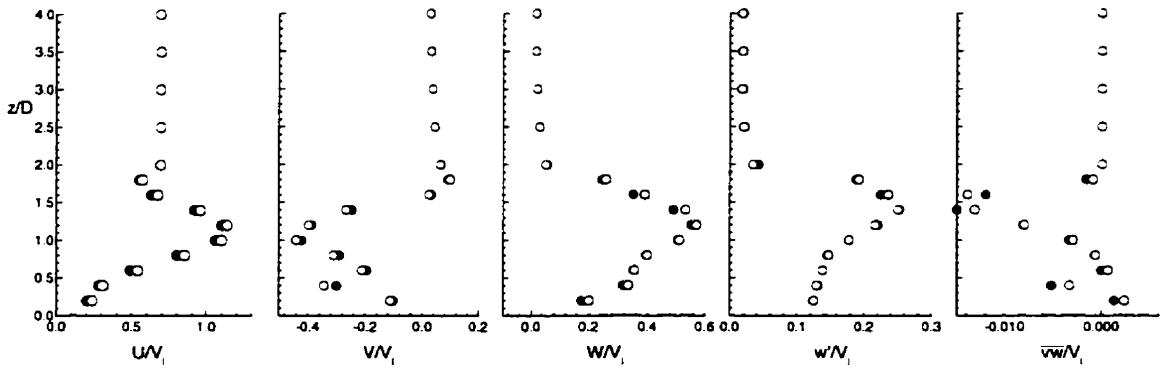

Figure 3.2: Comparison of data with (•) and without (o) inverse velocity weighting. Compound-angle jet, $R = 1.5$, $x/D = 2$, $y/D = -1$.

3.1.2 FID Data

The signal from the FID was converted to a digital output and the results for each probe were stored on disk. The A/D board was set for a sampling frequency of $130Hz$ and 2000 data points were taken, resulting in a sampling time of $15.4s$.

3.2 Error Analysis

3.2.1 Angular Alignment of the LDV System

As was discussed in section 2.1.2.4, the two probes were aligned at an angle relative to the tunnel coordinate system. The angles of alignment were determined using the techniqes described in Appendix A. The variance of each measured angle is used to estimate the error in the velocities which is produced due to the transformation of coordinate systems.

The variance of a function, T, of k random variables, $\theta_1 \ldots \theta_k$, is given by:

$$var(T) \approx \sum_{i=1}^{k}\sum_{j=1}^{k}\left(\frac{\partial T}{\partial E\theta_i}\right)\left(\frac{\partial T}{\partial E\theta_j}\right)cov(\theta_i, \theta_j) \tag{3.6}$$

where E is the expectation operator (Bury (1995)). For the error due to the alignment

angles the function of interest is the velocity component measured by one of the beam pairs, say U_i, which is a function of the angles $\alpha_1, \beta_1, \gamma_1, \alpha_2, \text{and} \beta_2$. The variance in U_i due to the uncertainty in the measured angles is then:

$$var(U_i) \approx \left(\frac{\partial U_i}{\partial E\alpha_1}\right)^2 var(\alpha_1) + \left(\frac{\partial U_i}{\partial E\beta_1}\right)^2 var(\beta_1) + \cdots + \left(\frac{\partial U_i}{\partial E\beta_2}\right)^2 var(\beta_2) \tag{3.7}$$

The terms involving the covariance of two different angles are assumed to be zero since there is no reason why the uncertainty in the measurement of one angle should be correlated with that of another.

Regardless of the angles of alignment, the use of the three-component LDV system with orthogonal measurement directions are less susceptible to calibration and sampling errors (Orloff and Snyder (1982)).

In the analysis of the error it was assumed that the error in the measured velocity from the LDV system was negligible relative to the error in the angular alignment values. In other words, the measured velocity vector $\mathbf{U_m}$ in Equation (2.4) was assumed to be accurate so that the variance in $\mathbf{U}$ was determined by obtaining the partial derivatives of the transformation matrix $\mathbf{C^{-1}}$ for use in Equation (3.7). However, as can be seen in Appendix A, the transformation matrix $\mathbf{C^{-1}}$ (Equation (A.9)) consists of many terms with 45 possible partial derivatives. Consequently, numerical differentiation was used for this task and a modified Ridder's method (MathSoft (1994)) was implemented in XFORMV20.

To calculate the variance of the expected values of the measured velocities and turbulent stresses indicated in section 3.1.1.3, inverse velocity weighting was not used as it was assumed to have only a second-order effect on the results. If inverse velocity weighting is ignored, the variances in the expected values are as follows:

Mean velocities:

$$var(\langle U \rangle) = \frac{1}{N}\sum_{i=1}^{N} var(U_i) \quad var(\langle V \rangle) = \frac{1}{N}\sum_{i=1}^{N} var(V_i) \quad var(\langle W \rangle) = \frac{1}{N}\sum_{i=1}^{N} var(W_i) \tag{3.8}$$

Turbulent normal stresses:

$$\begin{aligned} var(\langle u' \rangle) &= \frac{1}{(\langle u' \rangle N)^2}\sum_{i=1}^{N} u_i^2 var(U_i) \\ var(\langle v' \rangle) &= \frac{1}{(\langle v' \rangle N)^2}\sum_{i=1}^{N} v_i^2 var(V_i) \\ var(\langle w' \rangle) &= \frac{1}{(\langle w' \rangle N)^2}\sum_{i=1}^{N} w_i^2 var(W_i) \end{aligned} \tag{3.9}$$

Turbulent shear stresses:

$$\begin{aligned} var(\langle \overline{uv} \rangle) &= \frac{1}{N^2}\sum_{i=1}^{N} [u_i^2 var(V_i) + v_i^2 var(U_i)] \\ var(\langle \overline{uw} \rangle) &= \frac{1}{N^2}\sum_{i=1}^{N} [u_i^2 var(W_i) + w_i^2 var(U_i)] \\ var(\langle \overline{vw} \rangle) &= \frac{1}{N^2}\sum_{i=1}^{N} [v_i^2 var(W_i) + w_i^2 var(V_i)] \end{aligned} \tag{3.10}$$

Error bars representing ± 3 standard deviations are shown on the graphs of Fig. 3.3. The graphs show the three mean velocities, a turbulent normal stress, and a turbulent shear stress for a case where inverse velocity weighting has been applied and the angular corrections have been made. Note that the inverse velocity weighting only affects the value of the variable shown in Fig. 3.3, not the error bounds. No symbols are shown at the data locations so that the error bars may be seen clearly. Comparison with Fig. 3.1 indicates that the largest errors occur for the locations with the largest angular

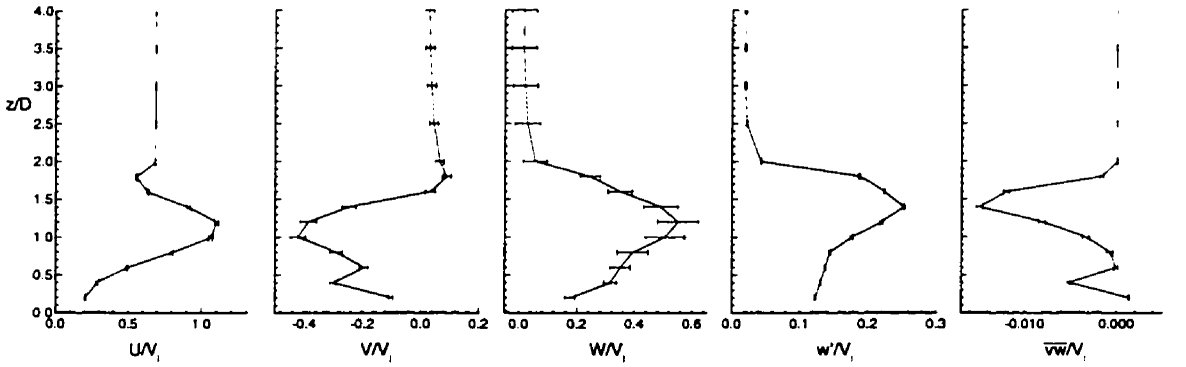

Figure 3.3: Measurement uncertainty due to angular uncertainty in coordinate transformation for compound-Angle jets $R = 1.5$, $x/D = 2$, $y/D = -1$.

corrections. As an overall estimate of the error, the velocities are typically $\pm 0.01 V_j$ and the uncertainties in the turbulent normal and shear stresses are $\pm 0.001 V_j^2$ and $\pm 0.0002 V_j^2$ respectively. These values may be higher in regions of high turbulence, as discussed in section 3.2.3.

3.2.2 Seed Particles

The use of LDV to measure flow velocities depends on the existence of small scattering particles in the flow which have a negligible slip velocity relative to the surrounding fluid. In effect, LDV indicates the velocity of the seed particles in the flow rather than the velocity of the fluid itself. The equation of motion for a sphere relative to a surrounding, viscous fluid is (Durst *et al.* (1981)):

$$\frac{\pi d_p^3 \rho_p}{6}\frac{dU_p}{dt} = 3\pi\mu d_p V + \frac{\pi d_p^3 \rho_f}{6}\frac{dU_f}{dt} + \frac{1}{2}\frac{\pi d_p^3 \rho_f}{6}\frac{dV}{dt} + \frac{3}{2}d_p^2\sqrt{\pi\mu\rho_f}\int_{t_0}^{t}\frac{dV}{d\xi}\frac{d\xi}{\sqrt{t-\xi}} \tag{3.11}$$

where U_f = fluid velocity

U_p = particle velocity

V = relative velocity ($= U_f - U_p$)

ρ_f = fluid density

ρ_p = particle density

d_p = particle diameter

μ = viscosity of fluid

It is assumed that the turbulence is homogeneous and time-invariant (ergodic hypothesis), the particles are smaller than the turbulence microscale, Stokes drag law is applicable (spherical particles), the particle is always surrounded by the same fluid molecules, and there is no interaction between the particles. Homogeneity of the small-scale turbulence is a reasonable assumption and the ergodic hypothesis is applicable here. For the smoke fluid used in these experiments ($\rho_p = 1117 kg/m^3$) the particle diameter ranged from $0.5 \mu m$ to $60 \mu m$, according to the manufacturer's specifications, although the majority of the particles should be closer to the lower bound due to evaporation of the smoke fluid. The turbulence Taylor microscale for isotropic turbulence may be estimated from (Hinze (1975)):

$$\lambda^2 = 15 \frac{L\nu}{u'} = 15 \frac{DL}{ReTu} \tag{3.12}$$

where D is the injection hole diameter, L is the turbulence macroscale ($L \approx D/2$), Re is the Reynolds number, and Tu is the turbulence intensity. For the present experiments the turbulence intensity at the jet exit reached a maximum of approximately 0.35. At a Reynolds number of 5000 and a jet diameter of $0.127m$, the calculated turbulence microscale is $\lambda = 0.0083m$, indicating that $d_p/\lambda \ll 1$. Stokes drag law will be applicable as long as the relative velocity V remains small. Equation (3.11) may be simplified

in this case since the particle density is much greater than that of the surrounding air ($\rho_p \gg \rho_f$) so the terms involving ρ_f may be dropped and only the first two terms in Equation (3.11) are necessary (Hinze (1975)), greatly simplifying the analysis. The frequency of the turbulent fluctuations may be estimated from $f_{turb} \approx U/\lambda = 691.6Hz$ for the conditions mentioned above. In order for the particles to follow the fluid velocity within 1%, the solution of the simplified Equation (3.11) indicates a particle diameter of $d_p = 9.5\mu m$. This estimate indicates that the particles followed the flow with reasonable accuracy.

3.2.3 Turbulence Measurements

While LDV is a very useful technique for evaluating details of various flowfields, care must be taken in interpreting data obtained from turbulent flows. Even with a good velocity bias correction scheme such as transit-time or inverse velocity weighting, errors may occur due to the turbulent nature of the flow (Fuchs *et al.* (1993)). In their simulations of a turbulent flowfield the percent error in the mean velocity and variance is defined as:

$$\beta_1 = \frac{\langle U \rangle - U}{U} \qquad \text{and} \qquad \beta_2 = \frac{\langle \overline{uu} \rangle - \overline{uu}}{\overline{uu}} \tag{3.13}$$

where $\langle\rangle$ indicates the estimate of the true value. When ensemble averaging was used, it was found that β_1 increased with the square of the turbulence intensity ($Tu^2 = \overline{uu}^2/U^2$) for turbulence intensities below 30%. This value represents the maximum likely error in the mean velocity. When transit-time weighting was applied the error β_1 was greatly reduced ($\beta_1 \approx 5\%$) but β_2 could still be relatively large ($\beta_2 \approx -20\%$).

In the present study, inverse velocity weighting was applied to correct for the velocity bias which is conceptually the same as transit-time weighting, provided that all three velocity components are measured. While differences exist between the parameters used

in the simulations of Fuchs *et al.* (1993) and those present in the current experiments, the results do provide a sense of the magnitude of the bias caused by turbulence and the level to which the bias may be corrected. Inverse velocity weighting is a reasonable method to use for dealing with velocity bias but errors will still remain, with the magnitude varying with the local flow conditions. However, additional corrections beyond the initial weighting scheme are difficult to justify and the errors induced by the turbulent flow are probably the primary cause of uncertainty in the experiments.

3.2.4 Probe Positions

3.2.4.1 LDV Measurement Volume

The position of the measurement volume in the tunnel coordinate system was determined after the probes were aligned so that the sampling volume from each probe intersected at a common location (see section 2.1.2.4). The standard deviation of the repeated measurements gives the positioning accuracy of the measurement volume relative to the tunnel coordinate system. The largest value obtained for the positioning error was $0.25mm$ which is 2% of the jet hole diameter.

3.2.4.2 FID Sampling Tubes

The positioning accuracy of the FID sampling tubes was $\pm 1mm$. There was a concern that due to the length of the thin tubes the flow might cause the tubes to deflect. However, observations indicated that even at high crossflow speeds the tubes remained steady.

3.3 Upstream Boundary Layer

The boundary layer five jet diameters upstream ($x/D = -5$) from the centre of the row of jets in each case was measured and the results are shown in Fig. 3.4. The data for each case represent the spanwise average upstream of the jet from which the data were taken. It can be seen that the boundary layer was approximately $2.0D$ thick for all cases. The normalized square root of the turbulence kinetic energy, $\sqrt{k}/V_\infty$, ranges from 1–3% and reaches a maximum of approximately 10% near the wall. It should be noted that the boundary layer thickness and hole size are of the same order of magnitude. It is this important aspect of the flow that makes analytical approaches difficult, as discussed in the literature review of section 1.2.1, and variations in the upstream boundary layer thickness result in significant differences in the downstream flow field (Sinha *et al.* 1991).

There are some differences in the profiles for each case, particularly for the turbulence kinetic energy. It is likely that the changes in freestream turbulence are due to dust accumulation on the flow conditioning screens. The variation in the boundary layer velocity profiles are a consequence of the differing turbulence levels. It is unlikely that the variation is due to the particular geometries' influence on the upstream boundary layer since there was little spanwise variation in the data for each jet and the differences exist into the freestream flow. The differences should not be a problem for comparisons with computational results as the individual profiles are input as boundary conditions for each case.

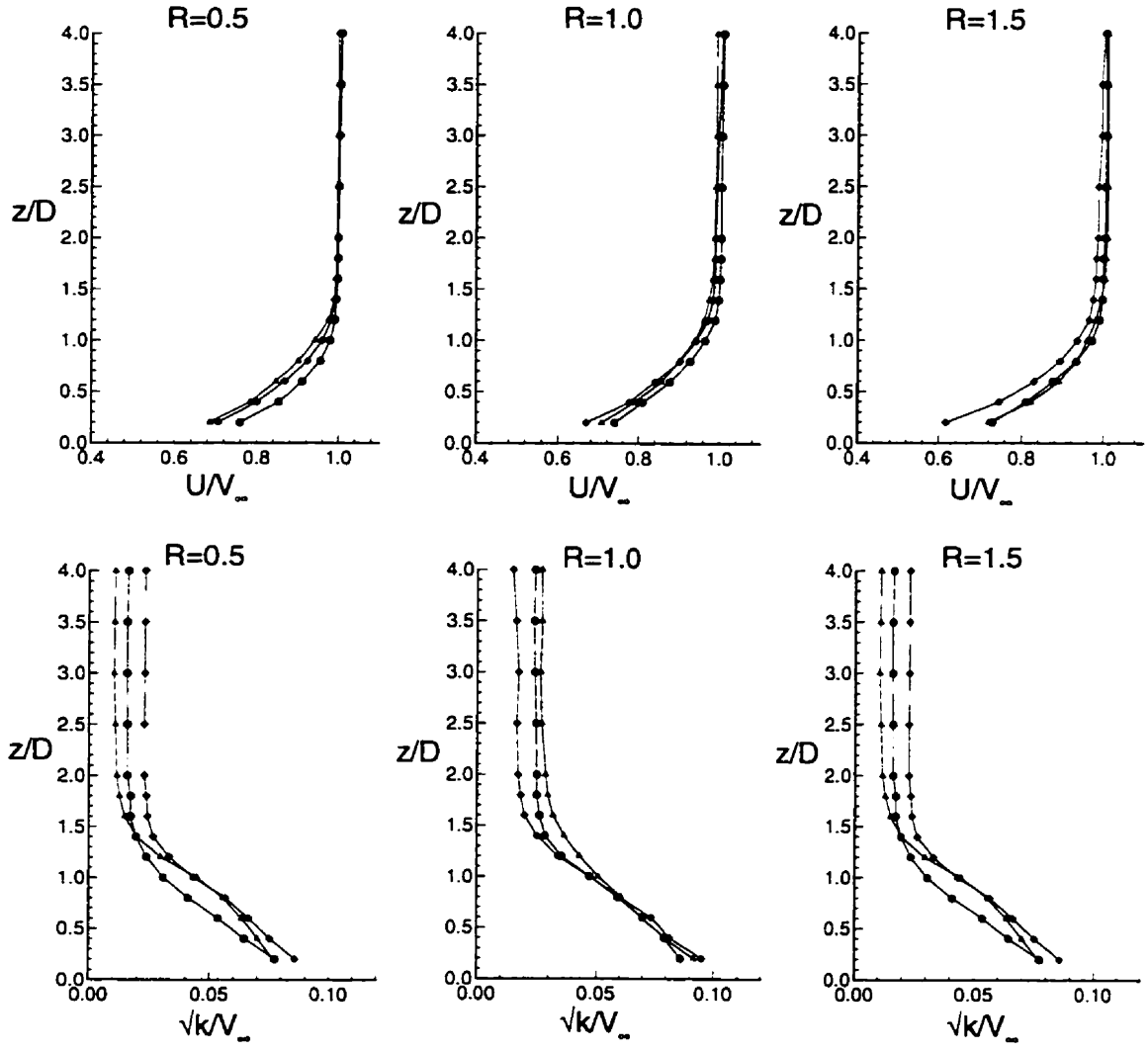

Figure 3.4: Upstream boundary layer: Streamwise ($L/D = 4$) ▲, Spanwise ♦, Compound-Angle •.

3.4 Periodicity

As seen in Fig. 2.2, planes of periodicity were assumed at the edges of the experimental domain for the spanwise and compound-angle jets. As the row of jets in either case was finite in extent the validity of this assumption is examined here. Plots of the streamwise velocity, U/V_j, and turbulence kinetic energy, $\sqrt{k}/V_j$, along the planes of periodicity $y/D = 1, -2$ are shown in Fig. 3.5, for the spanwise jets, and Fig. 3.6, for the compound-angle jets. In both cases the velocity ratio presented is $R = 1.5$, which corresponds to the most difficult test for the assumption. The results at lower R are better than those presented here.

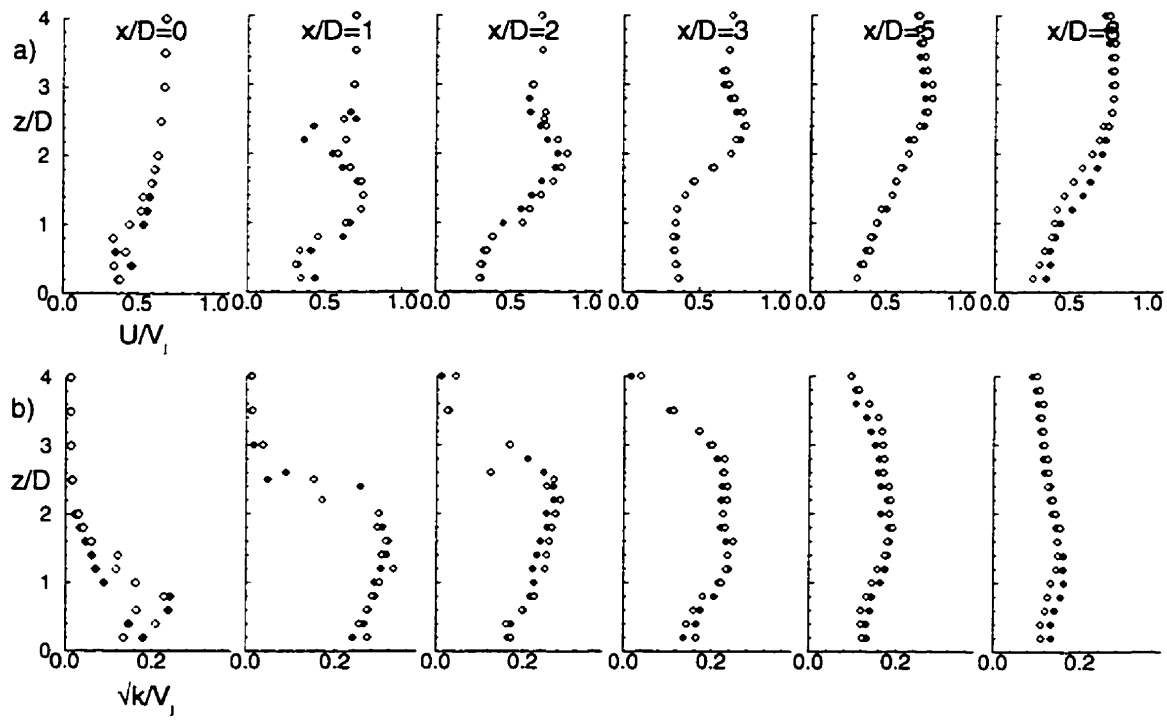

Figure 3.5: Comparison of flow along planes of periodicity for spanwise jets ($y/D = 1\bullet, -2\circ$): a) U/V_j, b) $\sqrt{k}/V_j$.

The agreement between the two planes is reasonable for the spanwise jets. In the

immediate vicinity of the jet, at $x/D = 0$ and 1, the most noticable deviations from periodicity occur. The differences are primarily in regions with large gradients in velocity or turbulence kinetic energy. As such, the effect of any error in the probe positioning would be more apparent. The differences may also arise from slight differences in the adjacent jet holes. Farther downstream the agreement is quite good. For the spanwise jets, shown in Fig. 3.6 the comparison between the profiles along the planes of periodicity is excellent. In many locations it appears that only one set of data points are present. The periodicity of the flow greatly simplifies the numerical simulation and experimental exploration of these jets as the entire row does not have to be included in the computational or experimental domain.

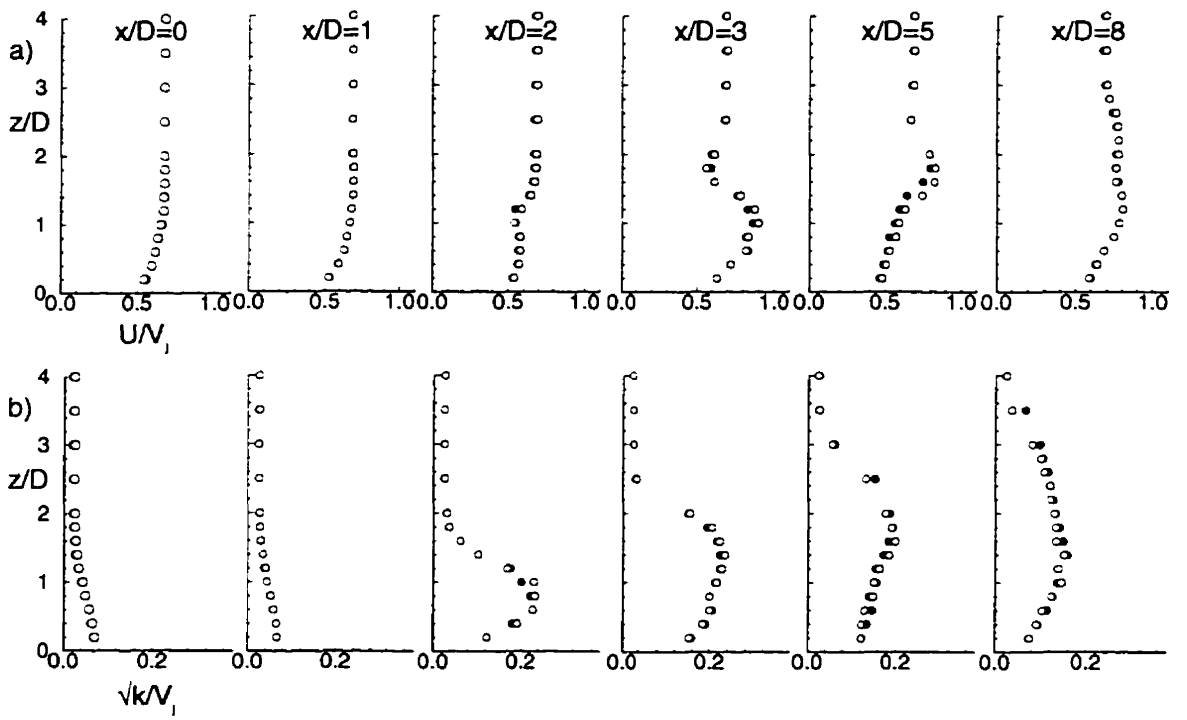

Figure 3.6: Comparison of flow along planes of periodicity for compound- angle jets ($y/D = 1\bullet, -2\circ$): a) U/V_j, b) $\sqrt{k}/V_j$.

3.5 Mean Velocity Field

In this section, the mean velocity fields for the various jet geometries and velocity ratios are presented. The data are normalized by the jet bulk velocity, V_j, and jet diameter, D. Note that for some of the plots, each axis and location are not labelled directly but rather given at the beginning and top of each row and column, respectively. Where possible, consistent symbols have been used for each geometry.

3.5.1 Jet Exit

In this section the normalized vertical component of velocity (W/V_j) at the jet exit ($z/D = 0$) for each case is presented. This variable was chosen since it gives the clearest representation of the effect the crossflow has on the jet exit flow. For the figures shown, the edges of each jet orifice are indicated by the bounding rectangle and the area containing the contours corresponds to the region where measurements were obtained. The view is down towards the wind tunnel floor with the crossflow in the positive x-direction from the bottom of the figures.

3.5.1.1 No Crossflow

A comparison between the two streamwise jet cases ($L/D = 8$ and $L/D = 4$) is shown in Fig. 3.7. In both cases the region of maximum vertical velocity occurs towards the upstream edge of the jet orifice. This is consistent with the presence of separated flow within the jet duct from the sharp-edged entrance producing a 'jetting effect' which was suggested by Pietrzyk *et al.* (1989) and later supported by Leylek and Zerkle (1994). The primary difference between the two cases is in the magnitude of the peak velocity. For the longer entry length, $L/D = 8$, case the peak velocity is approximately $0.7V_j$ which is 12% less than the peak of $0.8V_j$ for the $L/D = 4$ case. Again, this is consistent

with the suggested 'jetting effect' as the separated region is closer to the measurement plane in the $L/D = 4$ case.

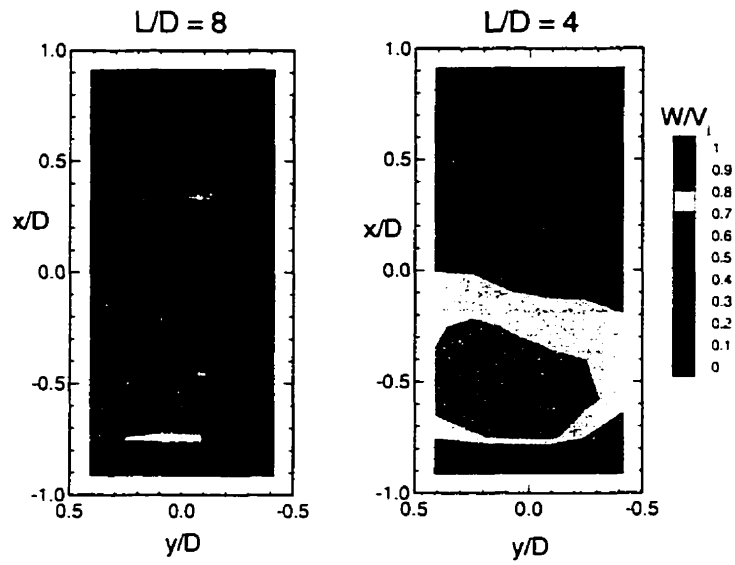

Figure 3.7: Jet exit plane ($z/D = 0$) contours of W/V_j with no crossflow.

Note that the 'jetting effect' is a consequence of the vertical velocity in the plenum. If a crossflow were present within the plenum the exit profiles would exhibit different characteristics (Thole *et al.* 1997).

3.5.1.2 Streamwise (L/D = 8)

The normalized vertical velocity contours for the three jet-to-crossflow velocity ratios are shown in Fig. 3.8. At the highest velocity ratio, $R = 1.5$, which corresponds to the lowest crossflow velocity, the region of peak velocity is still skewed towards the upstream edge of the jet. As the velocity ratio decreases, corresponding to increases in the crossflow velocity, the region of peak velocity shifts towards the downstream edge of the jet exit with the velocity profile becoming more uniform. This is in contrast to the situation

for perpendicular jets where the exit profile becomes more non-uniform as the crossflow velocity is increased (Ajersch *et al.* (1997)).

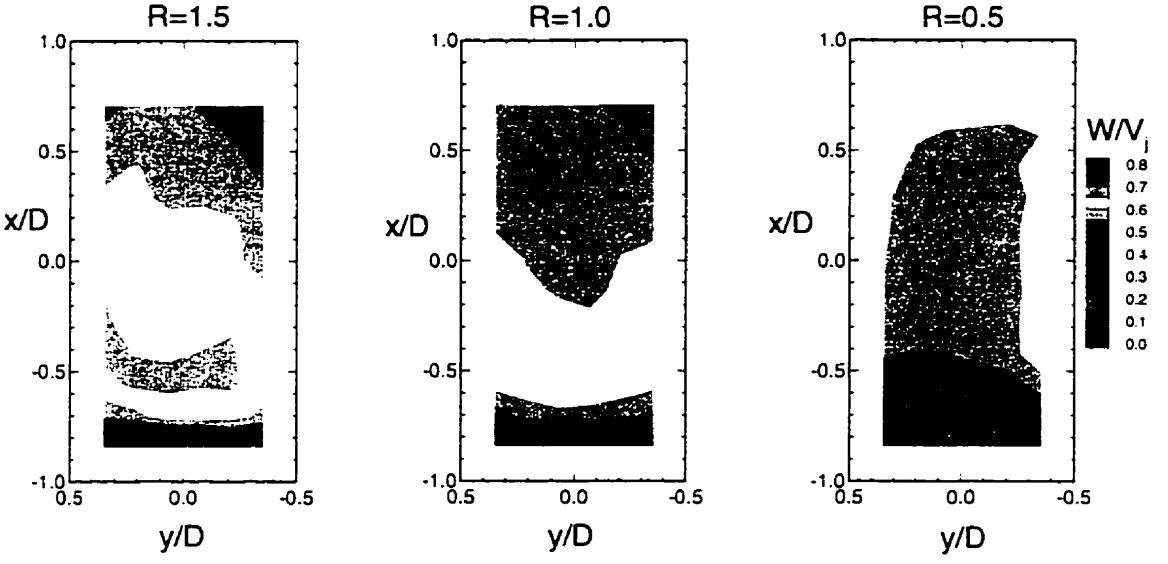

Figure 3.8: Streamwise ($L/D = 8$) jet exit W/V_j contours.

3.5.1.3 Streamwise (L/D = 4)

The jet exit velocity profiles for the short entry length jet are qualitatively similar to the $L/D = 8$ case discussed above. Vertical velocity contours for this case are shown in Fig. 3.9. Again, the region of peak velocity is skewed towards the upstream edge of the jet exit at $R = 1.5$. At $R = 1.0$ the magnitude of the peak velocity is reduced but still skewed towards the upstream edge of the jet. The contour area representing $W/V_j \geq 0.7$ is essentially unchanged between the $R = 1.5$ and $R = 1.0$ cases, indicating greater resistance to deflection by the crossflow. This behaviour is consistent with the stronger 'jetting effect' which is present in the shorter entry length case. Finally, at $R = 0.5$ where the crossflow is strongest the exit profile is fairly uniform, although a slightly higher velocity region skewed towards the upstream edge is still noticeable.

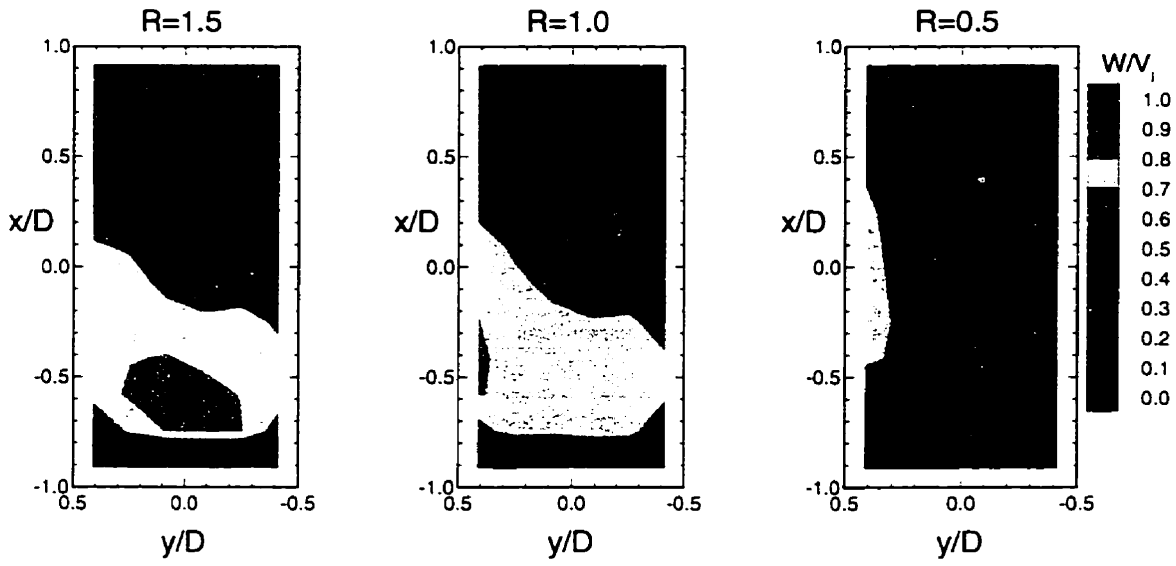

Figure 3.9: Streamwise ($L/D = 4$) jet exit W/V_j contours.

3.5.1.4 Spanwise

The behaviour of the spanwise jet is different than the previous two streamwise cases, as can be seen from examination of Fig. 3.10. The jet exits in the negative y-direction and, due to the inclination of the jet, a region of higher velocity is expected towards the positive y side of the jet exit. At $R = 1.5$ the higher-velocity region is still skewed towards the positive y-direction, although it has been deflected towards the downstream edge of the jet exit by the crossflow. As the crossflow increases (R decreases) the maximum vertical velocity increases which is in contrast to the trend shown for the two streamwise cases. In addition, the region of high vertical velocities is more strongly skewed in the positive y-direction. This result differs from velocity profiles at the jet exit which have been used as boundary conditions in earlier computational studies (Sathyamurthy and Patankar (1990), Zhou (1994)). The strong gradients in the velocity profile are indicative of the strong interaction between the jet and the crossflow for this geometry.

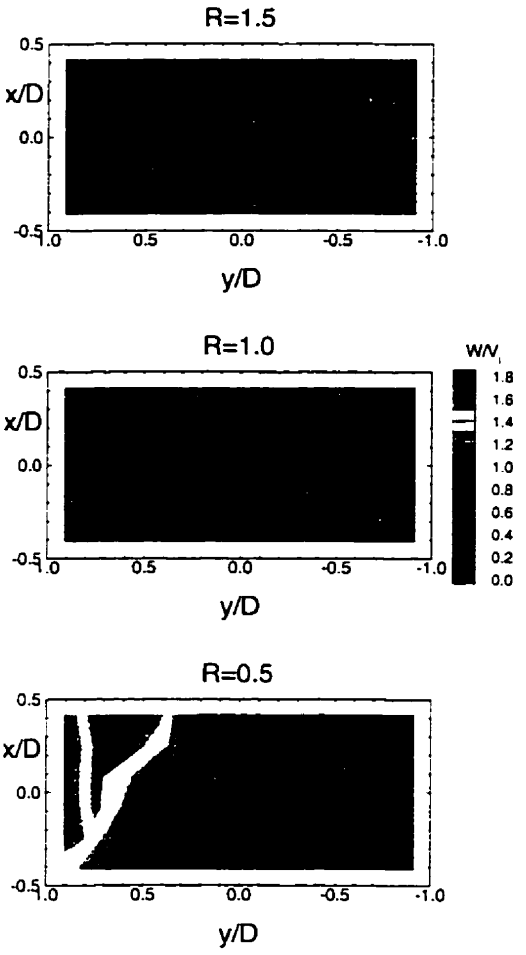

Figure 3.10: Spanwise jet exit W/V_j contours.

3.5.1.5 Compound-Angle

Contour plots of W/V_j for the compound-angle jet are shown in Fig. 3.11. As in the previous cases, the region of maximum velocity is skewed towards one side of the jet exit due to the 'jetting effect'. Although the jet has a component of velocity in the streamwise direction, the jet exit profiles resemble the spanwise injection case more closely than the streamwise cases. As R decreases the magnitude of the maximum velocity increases as the jet flow is deflected in the downstream direction. The location of the maximum velocity region remains almost constant as the velocity ratio is varied rather than shifting strongly to one side as the spanwise case does. The gradients in velocity at $R = 0.5$ also indicate a stronger interaction between the jet and the crossflow than in the two streamwise injection cases.

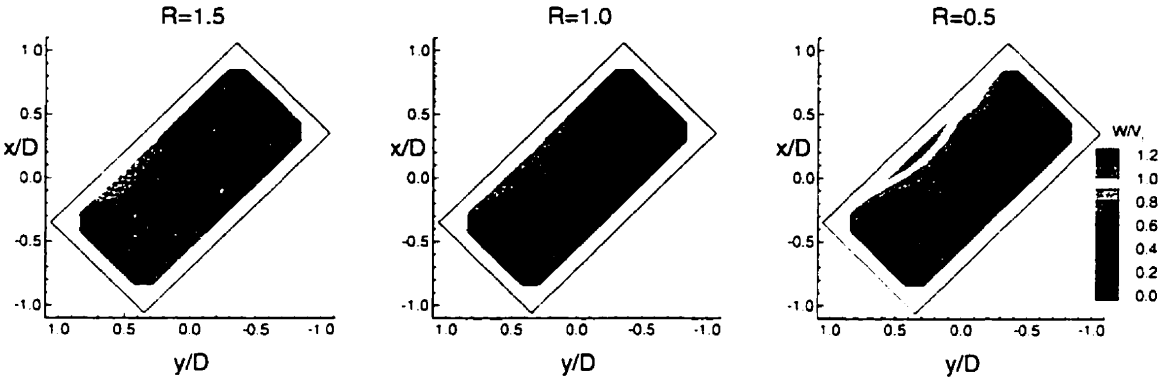

Figure 3.11: Compound-angle jet exit W/V_j contours.

3.5.2 Velocity Ratio R = 0.5

Comparisons of the normalized streamwise (U/V_j) component of velocity along the $y/D = 0$ plane are shown in Fig. 3.12. Few differences are noticed between the streamwise $L/D = 8$ and $L/D = 4$ cases. The velocity measured nearest to the wall $(z/D = 0.2)$

is slightly lower for the $L/D = 4$ case which may indicate that the jet is closer to separation from the downstream edge of the jet exit than the $L/D = 8$ case, but there is no indication in either case that separation has actually occurred. As the flow moves downstream to $x/D = 8$ the velocity profile begins to resemble a boundary layer again. It can be seen in the spanwise case that the flow at the jet exit is deflected in the streamwise direction by the strong crossflow. Immediately downstream of the jet at $x/D = 1$ the near-wall velocity drops to near zero indicating that the presence of the jet blocks the crossflow. As the flow progresses to $x/D = 2$ it can be seen that the near-wall velocity is actually higher than the velocities farther from the wall. This behaviour suggests that the high momentum crossflow fluid is being drawn towards the wall. The trend continues as the flow moves downstream until $x/D = 8$ where flow begins to return to a boundary-layer flow. The compound-angle jets exhibit similar behaviour to the spanwise jets with higher velocities measured adjacent to the wall, although this occurs farther downstream at $x/D = 3$. Again, the flow begins to resemble a boundary layer as it moves to $x/D = 8$. It should be noted that with all the cases presented here, the jets do not appear to penetrate beyond the boundary layer as the streamwise velocity for $z/D \geq 2$ remains constant at $U/V_j = 2$.

Plots of U/V_j along the $y/D = -1$ plane are shown in Fig. 3.13. The two streamwise cases do not change significantly from a typical boundary layer flow due to the strong deflection of the jet by the crossflow at this low blowing ratio. The $y/D = -1$ plane is $0.5D$ from the edge of the streamwise jets so no interaction is expected at $x/D = 0$. There is some indication that the jet has spread to $y/D = -1$ by $x/D = 2$ for both the $L/D = 8$ and $L/D = 4$ cases (the velocity profile is not as curved as it is farther upstream). The spanwise injection case is more interesting along this plane which passes along the edge of the jet orifice. There is a drop in U/V_j at $x/D = 0$ due to the blockage of the crossflow

by the jet. As the flow moves to $x/D = 1$ the near-wall streamwise velocity decreases further while the remaining flow is still essentially a boundary layer. At $x/D = 2, 3$ the near wall U/V_j is negative, indicating a region of backflow. Care should be taken not to interpret this region as separation and reattachment as would be the case for two-dimensional flow. Inspection of the jet exit flow in Fig. 3.10 indicates that the greatest blockage to the crossflow occurs at $y/D \approx 0.6$ which would create a low-pressure region immediately downstream of the jet exit. The low streamwise-momentum fluid from this region is likely transported laterally as the flow progresses downstream. This behaviour would be consistent with the presence of the low velocity region indicated in Fig. 3.12 at $x/D = 1$. More will be said of this later. Finally, in the case of the compound-angle jets, a higher velocity region is apparent near the wall immediately adjacent to the jet at $x/D = 0$ which again suggests that the crossflow fluid has been transported towards the wall. Inspection of Fig. 3.10 shows that this location is slightly upstream of the jet orifice along the $y/D = -1$ plane indicating the interaction between the jet and the crossflow at upstream locations. The flow farther downstream along this plane is relatively unremarkable as the velocity profile returns to resemble a boundary layer at $x/D = 8$.

Some insight into the behaviour of the velocity profiles described in the previous paragraphs may be found by considering the plots in Fig. 3.14. Here, V and W components of velocity are shown in spanwise y-z planes at $x/D = 1, 3, 8$ with the crossflow direction out of the page. The reference vector indicates the magnitude of the crossflow velocity where $V_\infty = 2.0V_j$ in this case. Again, the two streamwise cases ($L/D = 8$ and $L/D = 4$) exhibit quite similar behaviour. Only half of the flow field is shown in these two cases, due to the symmetry plane along $y/D = 0$. Immediately downstream of the jet exit the jet can be seen to expand as it is injected into the crossflow. As the flow moves

downstream to $x/D = 3$ there is some evidence of a vortex being formed near the floor of the tunnel which is characteristic of this flow field. There is still some evidence of the vortex at $x/D = 8$ although it is quite weak as the strong crossflow causes the jet to be deflected strongly towards the tunnel floor. As noted in the previous paragraphs, there is no indication that the jet flow has penetrated beyond the crossflow boundary layer for either of these cases. In the case of the spanwise jets there is a strong vortex which forms immediately downstream of the jet exit. The large vertical velocity that was noted at the jet exit plane in section 3.5.1.4 is apparent at $x/D = 1$, as is the strong flow to the downstream edge of the jet due to the suggested low pressure region described previously. As the flow moves downstream to $x/D = 3$ the vortex is still present and acts to draw the crossflow fluid down towards the tunnel floor which produces the high streamwise velocities noted in Fig. 3.12 near the wall. At $x/D = 8$ the vortex has not been lost and, even though the interaction between the jet and the crossflow is much stronger than in the streamwise injection cases, there is no evidence that the jet has penetrated beyond the crossflow boundary layer. The compound-angle jets show the beginning of the formation of a vortex at $x/D = 1$ and $y/D = 0.4$, although the downflow to the lee side of the jet is not as strong as for the spanwise case. As the flow progresses to $x/D = 3$ the vortex is still present but is much smaller than the vortex formed in the spanwise case. The downflow is still present at this location, resulting in the higher streamwise velocity near the wall found in Fig. 3.12. As was the case for the other injection geometries, even by $x/D = 8$ there is still no evidence that the jet has penetrated beyond the crossflow boundary layer.

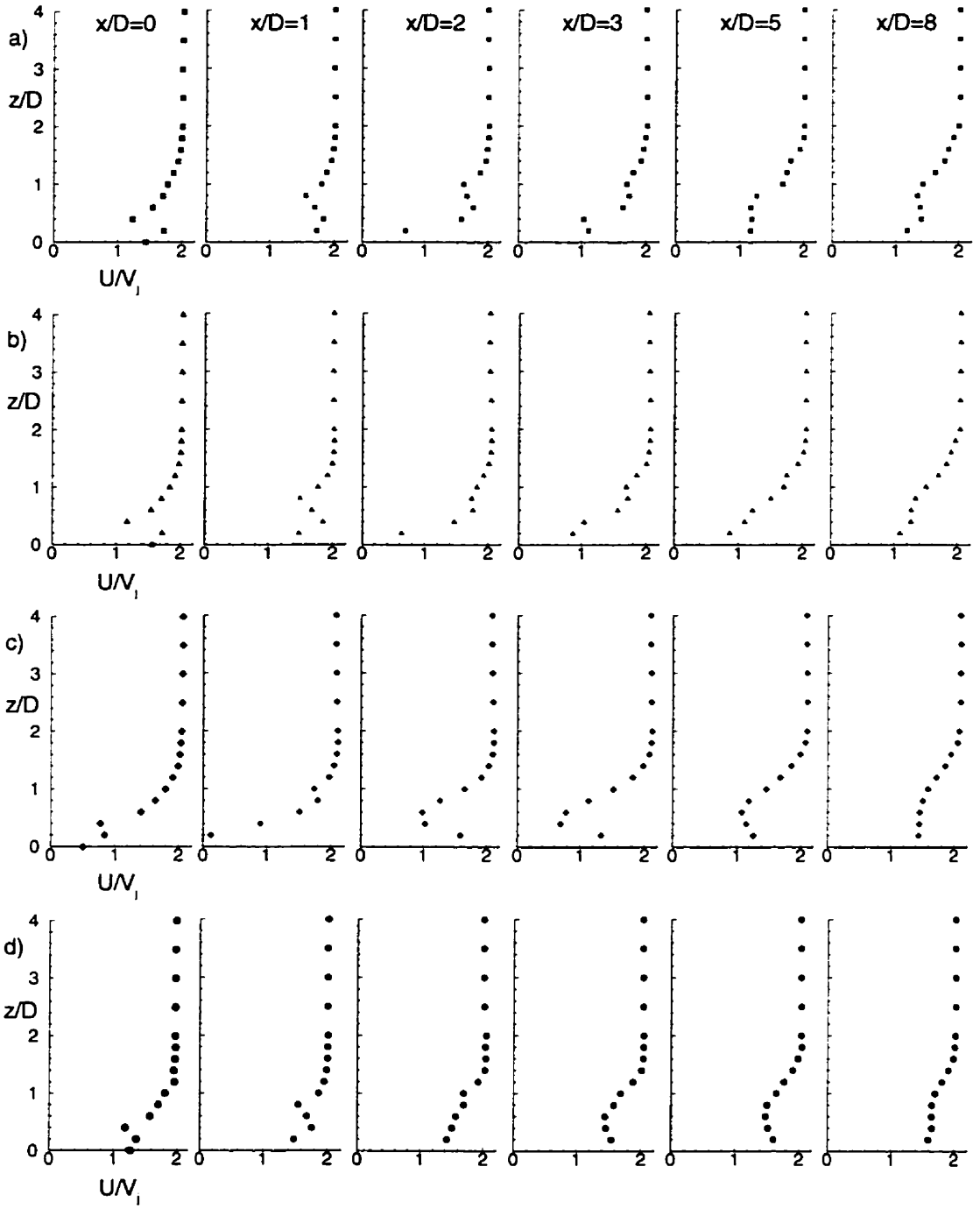

Figure 3.12: Streamwise (U/V_j) velocity along $y/D = 0$, $R = 0.5$ for: a) streamwise $L/D = 8$, b) streamwise $L/D = 4$, c) spanwise, and d) compound-angle jets.

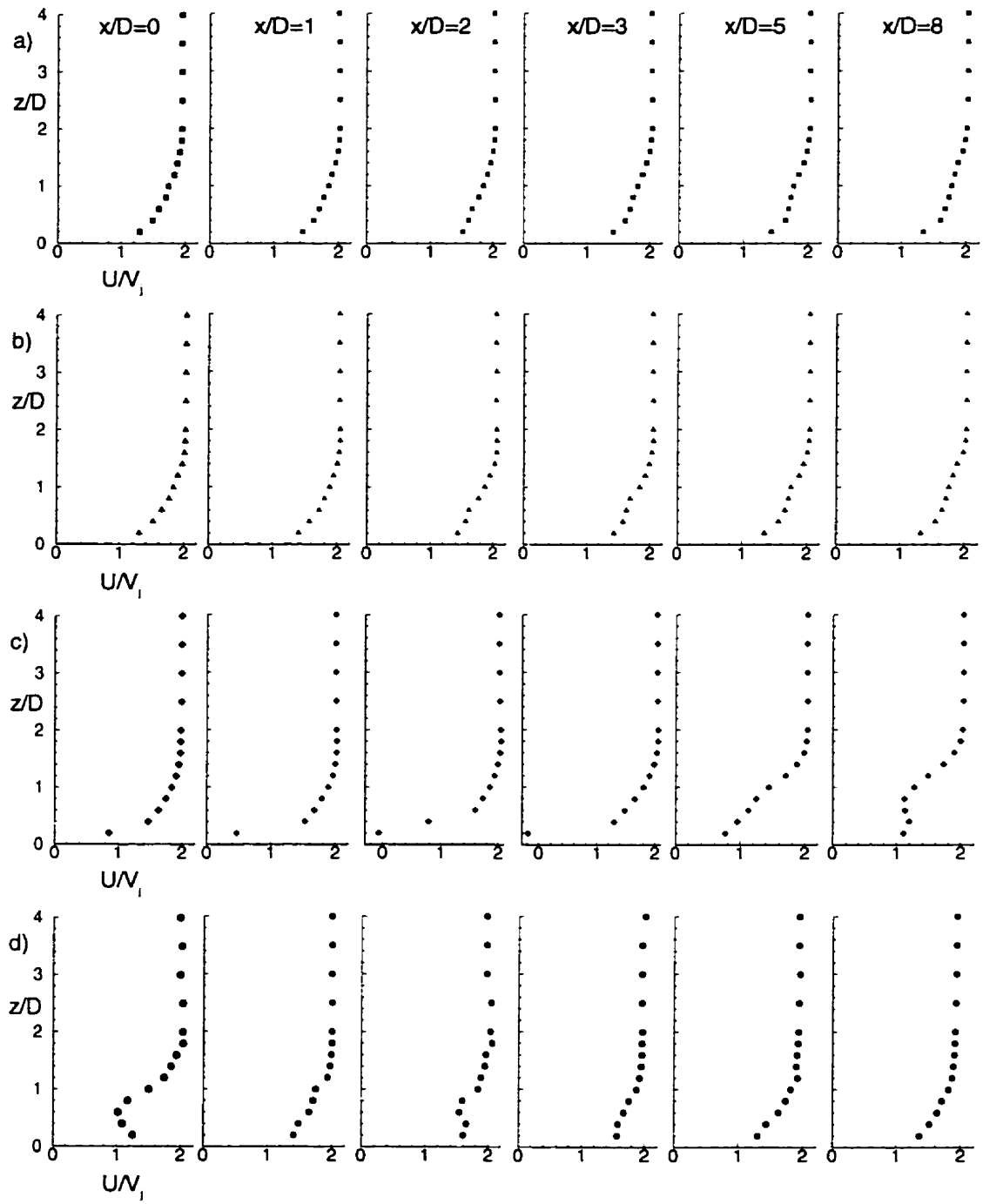

Figure 3.13: Streamwise (U/V_j) velocity along $y/D = -1$, $R = 0.5$ for: a) streamwise $L/D = 8$, b) streamwise $L/D = 4$, c) spanwise, and d) compound-angle jets.

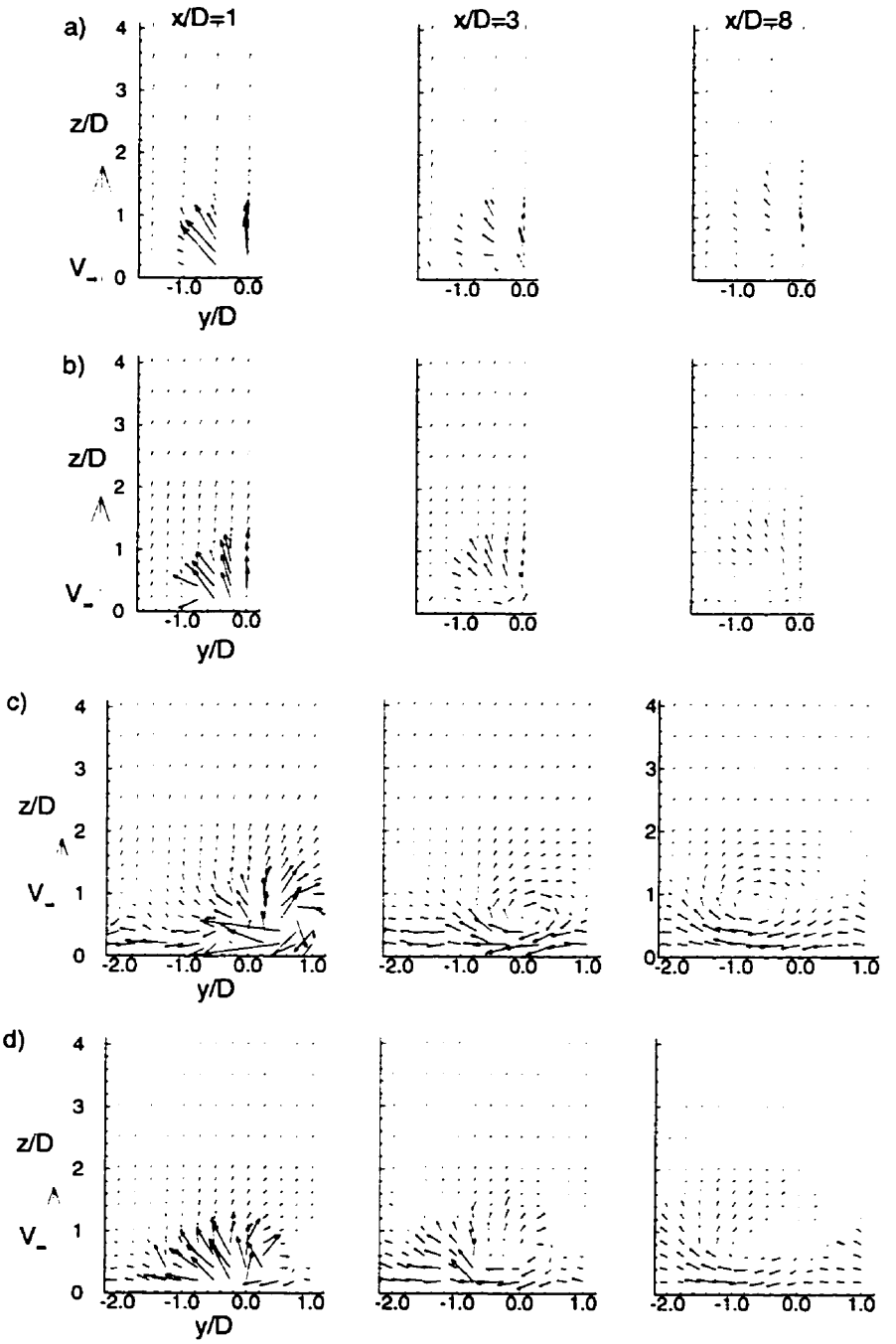

Figure 3.14: Velocity vectors in spanwise y-z planes at $R = 0.5$ (V and W components) for a) Streamwise ($L/D = 8$), b) Streamwise ($L/D = 4$), c) Spanwise, and d) Compound-angle jets.

3.5.3 Velocity Ratio R = 1.0

As noted at the beginning of this chapter, the characteristics of the flowfield at $R = 1.0$ are typically intermediate between the characteristics observed at $R = 0.5$ and $R = 1.5$. As such, data along only one streamwise plane will be presented here. Comparisons of the normalized streamwise component of velocity (U/V_j) for the various geometries at $R = 1.0$ along the $y/D = 0$ plane are shown in Fig. 3.15. As observed in the $R = 0.5$ case, the differences between the streamwise jets with $L/D = 8$ and $L/D = 4$ are small. At the downstream edge of the jet exit hole at $x/D = 1$ the near-wall velocity is slightly lower for the $L/D = 4$ case which suggests that the jet may be closer to separation than the $L/D = 8$ case. Recall from the jet exit velocity profiles discussed in 3.5.1.3 that the 'jetting effect' from the shorter entry length appeared stronger, producing a higher vertical velocity at the exit plane. However, at $x/D = 2$ the trend is reversed with the near-wall velocity in the $L/D = 8$ case dropping considerably, again suggesting that the jet is close to separation from the tunnel floor. In the $L/D = 4$ case the near-wall velocity is actually higher than it was at $x/D = 1$ and much higher than is observed for $L/D = 8$. As can be seen from the graphs, the streamwise component of velocity in the crossflow is lower than the near-wall velocity here. The most likely explanation is that the flow from the higher streamwise velocity portion of the jet has been drawn towards the floor due to the counter-rotating vortex pair. As the flow progresses downstream the differences between the two streamwise cases are minimal with the $L/D = 4$ case perhaps spreading more rapidly. At $x/D = 8$ it appears that the jet flow is beginning to penetrate beyond the boundary layer thickness of $z/D = 2$. For the spanwise jets it can be seen that the jet flow penetrates farther into the crossflow at $x/D = 0$ than was the case for $R = 0.5$, as expected. As the flow progresses downstream the higher near-wall velocities which occurred at $R = 0.5$ are not present which suggests that the crossflow is

not being drawn towards the floor as strongly. At $x/D = 8$ it is not clear whether the flow has penetrated beyond the boundary layer. Finally, the compound-angle jets are shown which behave in a similar manner to the spanwise jets, although the streamwise component of velocity at $x/D = 1$ is closer to that observed for the streamwise-inclined jets. Again, the near-wall velocity does not suggest that the crossflow fluid has been drawn towards the floor. The velocity profile appears to return to a boundary-layer flow by $x/D = 3$ and jet penetration beyond the crossflow boundary layer is not apparent.

Vector plots in the spanwise y-z planes are shown in Fig. 3.16 along with reference vectors indicating the magnitude of the crossflow velocity. Vortex formation appears at $x/D = 1$ for the streamwise jets which is earlier than observed for $R = 0.5$. As the flow progresses downstream the vortices become clearer and the jet flow appears to spread laterally to a greater extent than at $R = 0.5$. The spanwise jets show a marked departure from the flow at $R = 0.5$ as a vortex begins to form in a competely different location. From the jet exit velocity profiles in Fig. 3.10 the peak vertical velocity is at $y/D \approx 0.2$ rather than 0.6 as was the case at $R = 0.5$. Correspondingly, the vortex formation occurs at $y/D \approx -0.1$ rather than at $y/D \approx 0.6$. The vortex forms farther from the wall as the jet is able to penetrate farther into the flow at $R = 1.0$. As the flow moves downstream to $x/D = 3$ the vortex appears to have weakened and has almost disappeared by $x/D = 8$. The vortex observed at $x/D = 8$ is actually from the next jet in the row as the jets move in the $-y$ direction as they are deflected downstream by the crossflow. In the case of the compound-angle jets a small vortex is observed at $x/D = 1$, $y/D \approx 0.2$, likely due to the interaction of the jet and crossflow at the upstream corner of the jet exit hole. A clearer, stronger vortex forms at $R = 1.0$ than was observed at $R = 0.5$ as the flow moves downstream. The weaker crossflow in this case does not dissipate the jet flow as quickly.

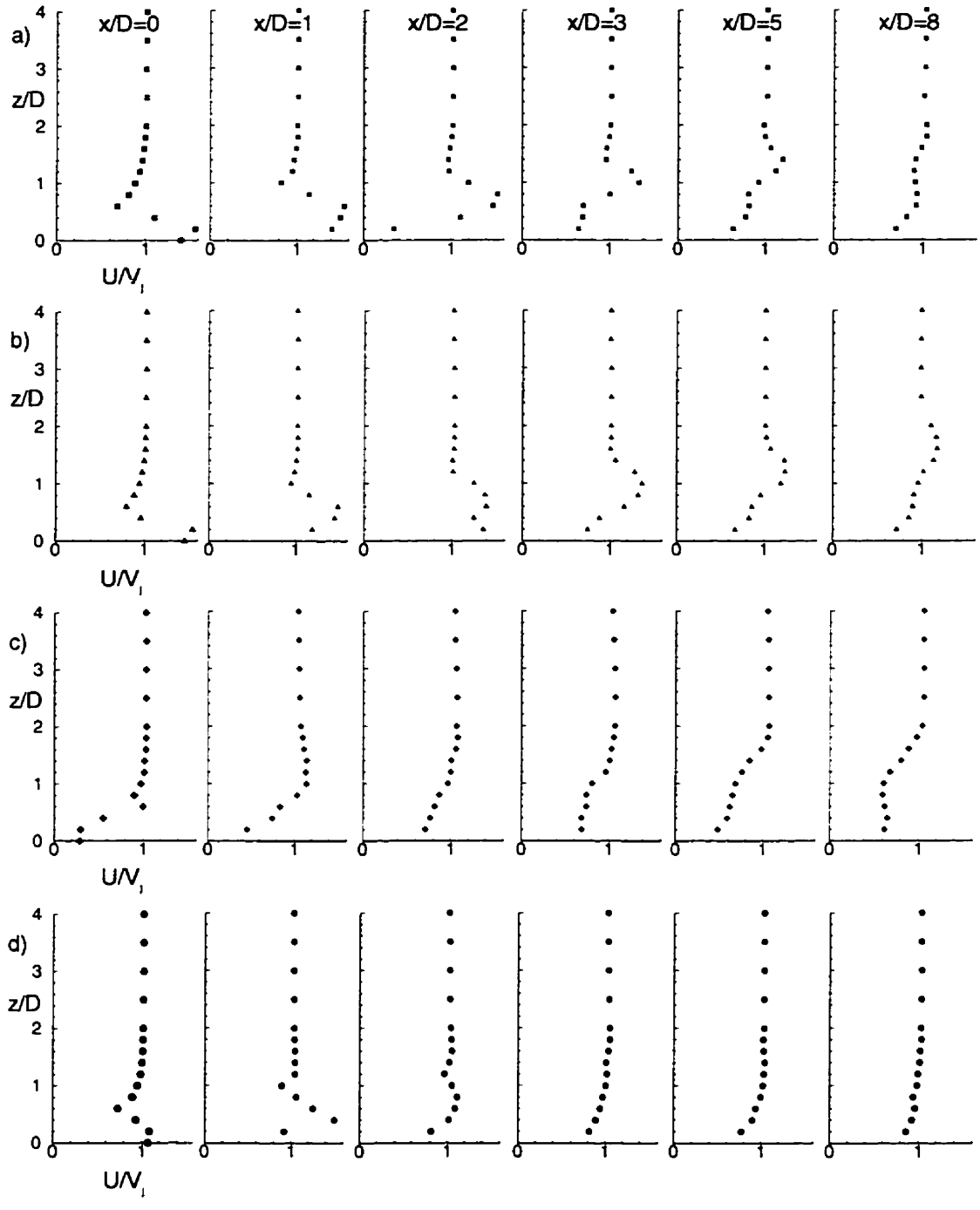

Figure 3.15: Streamwise (U/V_j) velocity along $y/D = 0$, $R = 1.0$ for: a) streamwise $L/D = 8$, b) streamwise $L/D = 4$, c) spanwise, and d) compound-angle jets.

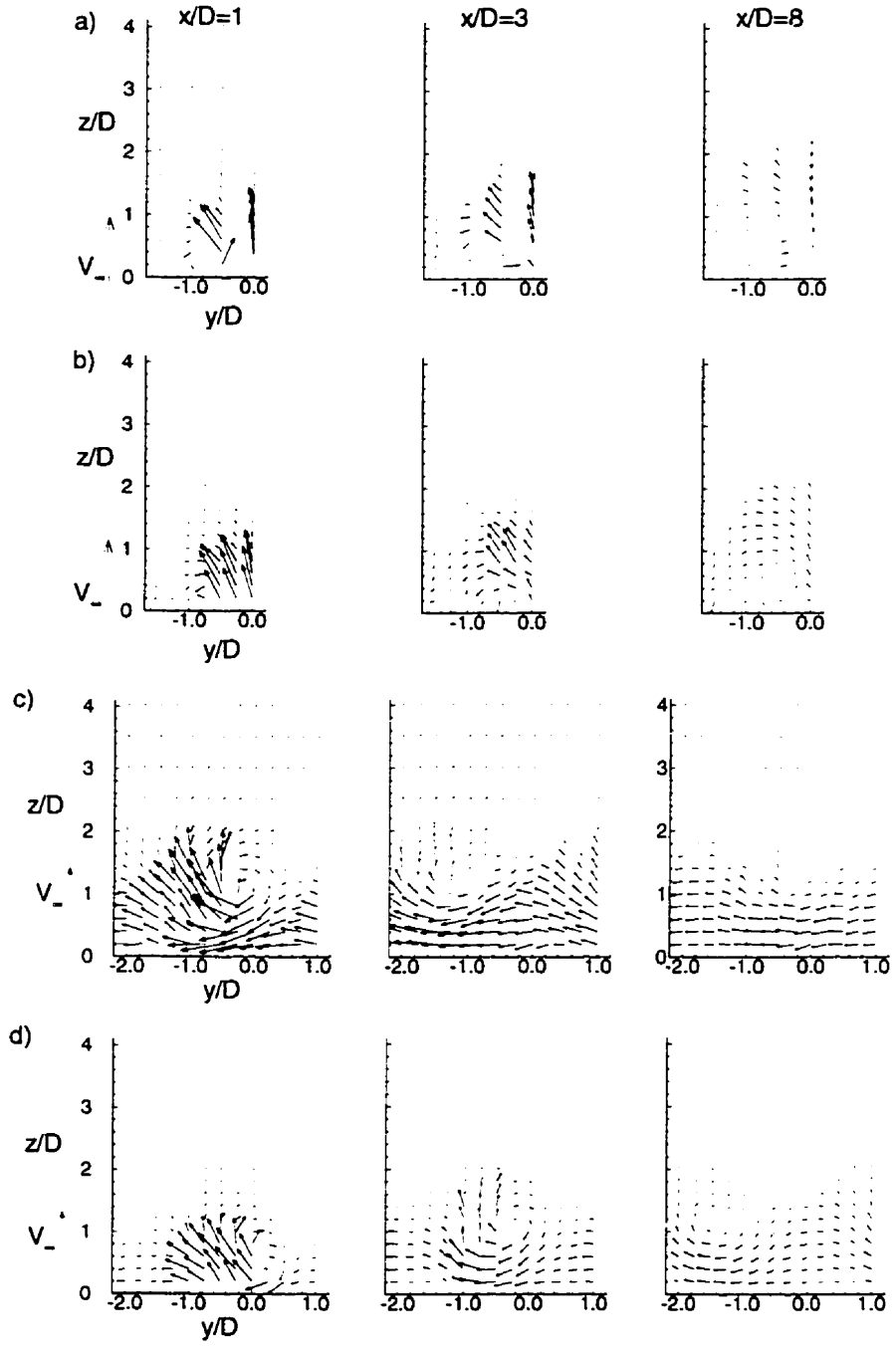

Figure 3.16: Velocity vectors in spanwise y-z planes at $R = 1.0$ (V and W components) for a) Streamwise ($L/D = 8$), b) Streamwise ($L/D = 4$), c) Spanwise, and d) Compound-angle jets.

3.5.4 Velocity Ratio R = 1.5

At $R = 1.5$ the injection of the jet into the crossflow in the two streamwise-inclined jet cases is quite strong, as shown in the U/V_j plots of Fig. 3.17 along the $y/D = 0$ plane. Again, there are few differences between the $L/D = 8$ and $L/D = 4$ cases. The lower near-wall velocity at $x/D = 1$ for the $L/D = 4$ case is again indicative of the stronger 'jetting effect' in this case but the differences disappear soon afterwards. As the flow progresses to $x/D = 8$ it is clear that the jets in both cases penetrate beyond the boundary layer into the crossflow. The peak streamwise velocity is slightly higher at the downstream locations for the short entry length which, again, is likely due to the stronger 'jetting effect'. Closer to the jet hole, the streamwise velocity from the $L/D = 8$ streamwise jets is slightly higher than for the $L/D = 4$ case as the weaker 'jetting effect' results in a stronger streamwise component of velocity as the flow leaves the jet hole. There is no evidence of flow separation for either jet at this velocity ratio. The velocity profiles for the spanwise-inclined jets indicate that the jet has penetrated beyond the boundary layer by $x/D = 2$. The velocity profiles farther downstream are fairly smooth which indicates that the interaction between the jet and the crossflow is not as strong as it was at the previous velocity ratios. The flow for the compound-angle jets does not appear to penetrate farther into the crossflow at $x/D = 1$ than it did for the lower velocity ratios which is likely the result of the lower peak vertical velocity at the jet exit for $R = 1.5$. The flow at $x/D = 2, 3$ is essentially a boundary layer and the jet does not appear to penetrate beyond the boundary layer until $x/D = 8$.

The streamwise velocity profiles along the $y/D = -1$ plane are shown in Fig. 3.18. The presence of the streamwise jets may be observed along this plane by $x/D = 1$, particularly for the $L/D = 8$ jet. The peak streamwise velocity is consistently higher for the longer entry length jet along this plane as the $L/D = 8$ jet appears to spread

laterally more quickly than the $L/D = 4$ jet. This spreading would explain the lower peak streamwise velocity along the $y/D = 0$ plane noted previously. The injection of the jet in the spanwise case at $x/D = 1$ is more noticeable along this plane as the jet flow is in the $-y$ direction. Again, the jet appears to penetrate beyond the boundary layer very quickly; by $x/D = 1$ along this plane. The flow profiles downstream at $x/D = 5$, 8 are quite similar to those along the $y/D = 0$ plane, indicating more uniformity of the flow in the spanwise direction than at the lower blowing ratios. In the compound-angle case, the high near-wall velocity which was observed at $R = 0.5$ along this plane at $x/D = 0$ is no longer present which is likely due to the ability of the jet to penetrate more easily into the crossflow in this case. The jet exit velocity profile is not as skewed in this case and the jet flow is the dominant feature of the flow field. Downstream from the exit hole the presence of the jet is clear and appears to penetrate beyond the boundary layer by $x/D = 5$.

The velocity vectors in the spanwise $y - z$ planes at $R = 1.5$ are shown in Fig. 3.19. The magnitude of the crossflow velocity is indicated by the reference vectors. In the two streamwise jet cases, clear vortices form and grow as the flow moves downstream. A mirror image of the vector field along the $y/D = 0$ symmetry plane would reveal the counter-rotating vortex pair which has been observed many times for this class of flows. The flow in the spanwise jet case indicates the beginning of a vortex at $x/D = 1$. The presence of the adjacent jet is apparent at $y/D = 1.0$ as the weak crossflow allows the jets to penetrate strongly in the spanwise direction. Downstream at $x/D = 3$ the vortex appears to have weakened due to the interaction between the adjacent jets which prevents the vortex flow from completing its circuit. The flow at $x/D = 8$ is fairly uniform in the spanwise direction, as noted in the previous paragraphs. The lateral injection of the jet in the compound-angle case is apparent at $x/D = 1$ and a vortex begins to form. The

presence of the adjacent jet is not apparent until farther downstream at $x/D = 3$. The jet vortex is still clear at this location. At $x/D = 8$ two weaker vortices are visible on the graph. The spanwise flow is not as uniform as it was for the spanwise-inclined jets, indicating the weaker jet-to-jet interaction for this case.

3.5.5 Summary

Overall there are few differences between the mean velocity fields for the two streamwise-inclined jet cases ($L/D = 8, 4$) as the velocity ratio changes. As R is increased the jets penetrate farther into the crossflow and the vortices which are formed become clearer. In the spanwise jet case the strong vortices which are present at $R = 0.5$ grow weaker and disappear downstream as R is increased. This is in contrast to the results found by Honami *et al.* (1994), as mentioned in the literature review, where the large vortex which was formed grew as R was increased. This difference is due to the difference in the jet-to-jet spacing, s/D. In the present experiments the jets were $s/D = 3$ apart while the experiments of Honami *et al.* (1994) were at $s/D = 5$. Consequently the jet-to-jet interaction which becomes important in the present experiments does not occur and the large vortices may form. The compound-angle jets behave in a similar manner to the spanwise-inclined jets with a single vortex formed downstream of the jet exit, although the jet-to-jet interaction is not as significant at higher velocity ratios for this case.

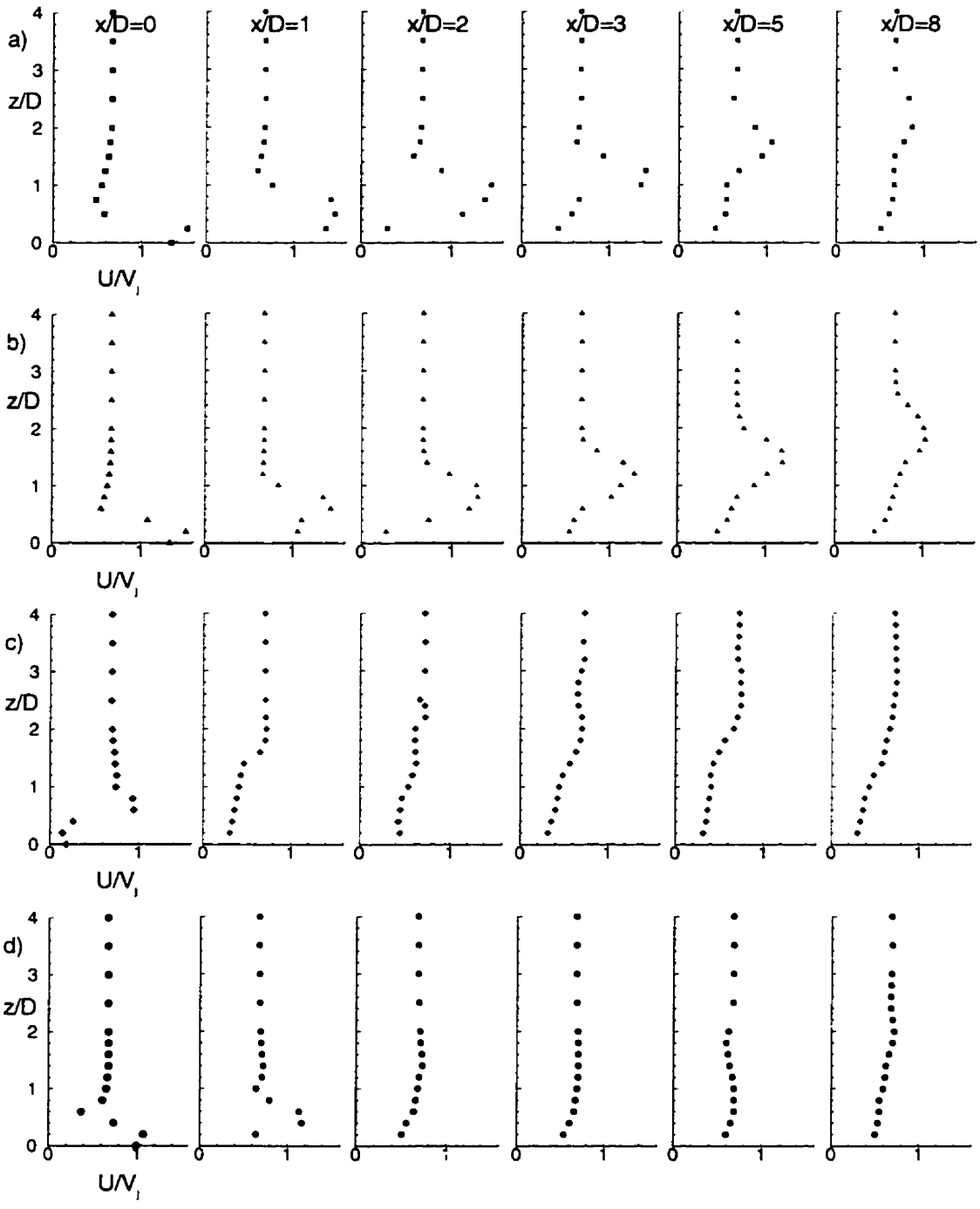

Figure 3.17: Streamwise (U/V_j) velocity along $y/D = 0$, $R = 1.5$ for: a) streamwise $L/D = 8$, b) streamwise $L/D = 4$, c) spanwise, and d) compound-angle jets.

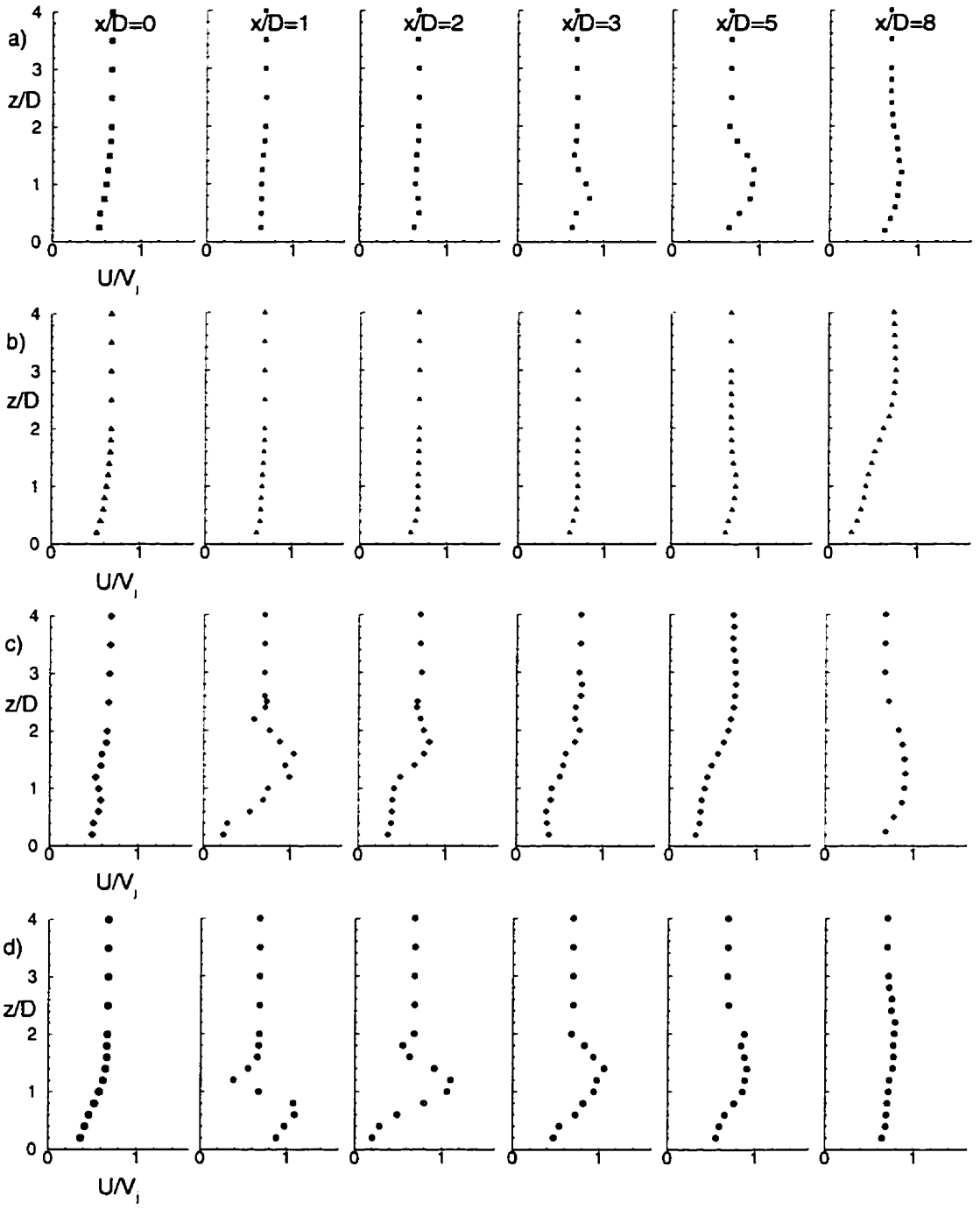

Figure 3.18: Streamwise (U/V_j) velocity along $y/D = -1$, $R = 1.5$ for: a) streamwise $L/D = 8$, b) streamwise $L/D = 4$, c) spanwise, and d) compound-angle jets.

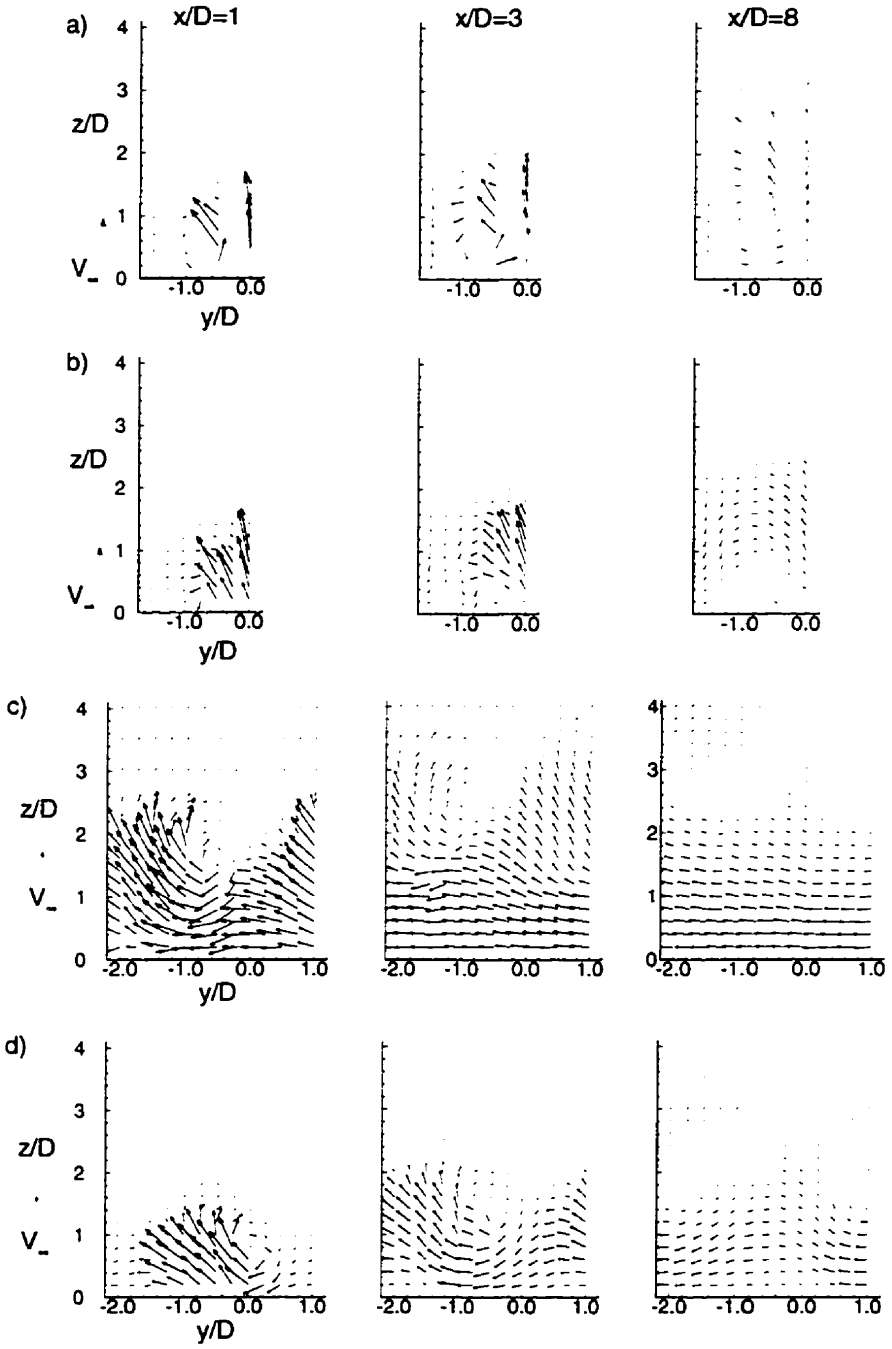

Figure 3.19: Velocity vectors in spanwise y-z planes at $R = 1.5$ (V and W components) for a) Streamwise ($L/D = 8$), b) Streamwise ($L/D = 4$), c) Spanwise, and d) Compound-angle jets.

3.6 Turbulence Data

In this section, the turbulence fields for the various jet geometries and velocity ratios are presented. As was the case for the mean velocity data, for some of the plots, each axis and location are not labelled directly but rather given at the beginning and top of each row and column, respectively. Where possible, consistent symbols have been used for each geometry. The data presented include the turbulence kinetic energy, the turbulent Reynolds stresses, and an examination of the anisotropy of the turbulent normal stresses. Data obtained at $R = 1.0$ is not presented here since bounds of the jet behaviour are well represented by the data at $R = 0.5$ and $R = 1.5$.

3.6.1 Jet Exit

In this section the normalized square root of the turbulence kinetic energy ($\sqrt{k}/V_j$) at the jet exit ($z/D = 0$) for each case is presented. For the figures shown, the edges of each jet orifice are indicated by the bounding rectangle and the area containing the contours corresponds to the region where measurements were obtained. The view is down towards the wind tunnel floor with the crossflow in the positive x-direction from the bottom of the figures.

3.6.1.1 No Crossflow

The turbulence kinetic energy ($\sqrt{k}/V_j$) at the jet exit plane ($z/D = 0$) for the two streamwise-inclined jet cases with no crossflow present is shown in Fig. 3.20. The overall turbulence levels are lower for the longer entry-length jet ($L/D = 8$) with $\sqrt{k}/V_j \approx 0.15$ over most of the exit plane. In the case of the $L/D = 4$ jet the turbulence level reaches a maximum of $\sqrt{k}/V_j \approx 0.25$ towards the downstream side of the jet hole. The increased turbulence level in this region is due to the closer proximity of the shear layer formed due

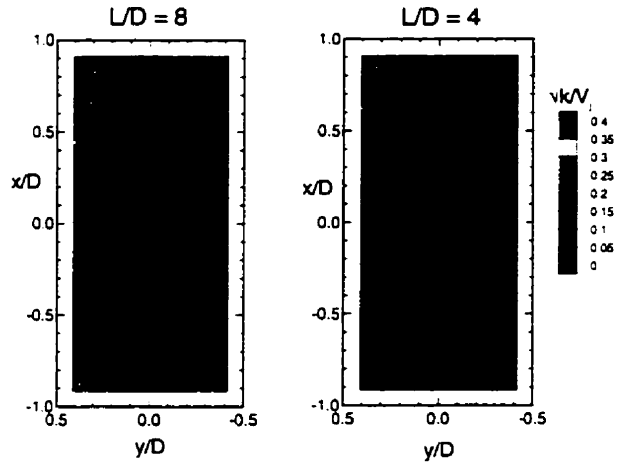

Figure 3.20: Jet exit plane ($z/D = 0$) contours of $\sqrt{k}/V_j$, no crossflow.

to the 'jetting effect' mentioned previously. If the separated flow anticipated from the sharp-edged inlet to the jet hole had a moving reattachment point near the exit plane there would be a resulting increase in the measured, time-averaged turbulence level.

3.6.1.2 Streamwise (L/D = 8)

Figure 3.21 shows the contours of $\sqrt{k}/V_j$ at the jet exit plane for all three jet-to-crossflow velocity ratios (R). It is apparent that the turbulence levels are fairly constant over the jet exit plane at $\sqrt{k}/V_j \approx 0.10$ for $R = 1.5, 1.0$ and increasing to 0.15 for $R = 0.5$. The increase in the turbulence level at $R = 0.5$ is due to the stronger deflection of the jet due to the crossflow.

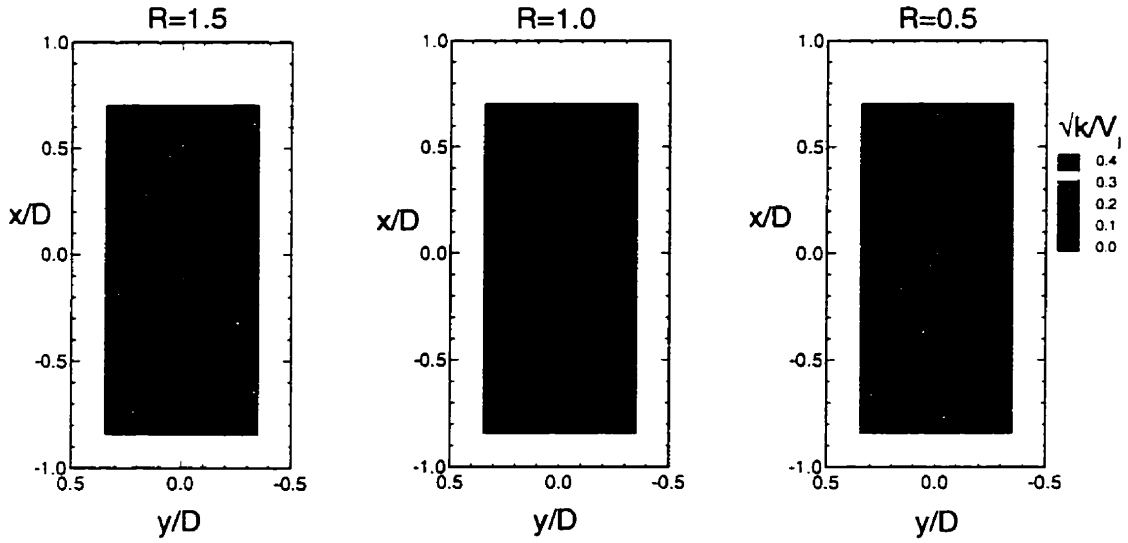

Figure 3.21: Streamwise ($L/D = 8$) jet exit $\sqrt{k}/V_j$ contours.

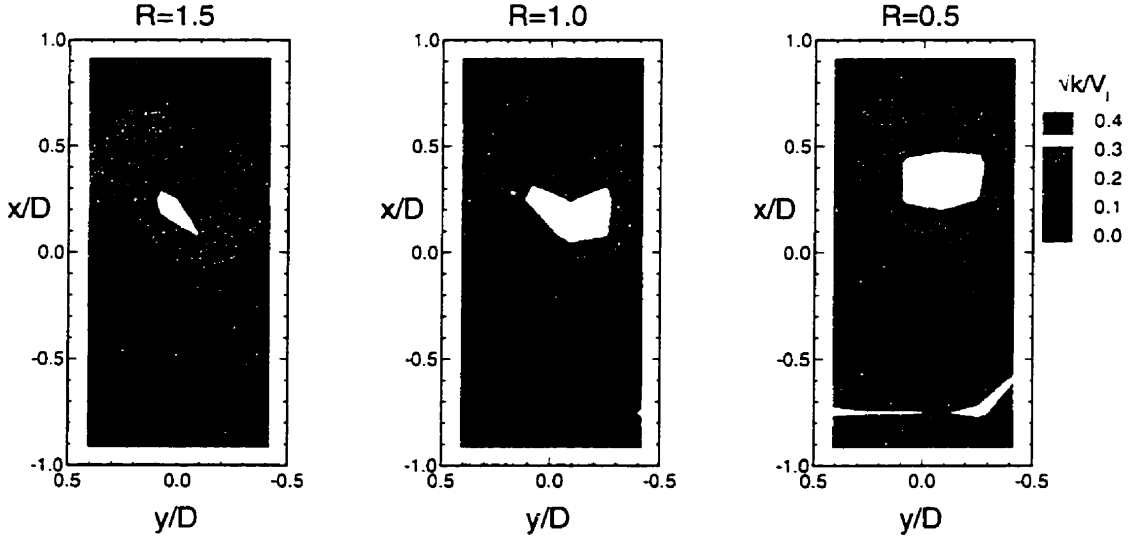

Figure 3.22: Streamwise ($L/D = 4$) jet exit $\sqrt{k}/V_j$ contours.

3.6.1.3 Streamwise (L/D = 4)

Contours of $\sqrt{k}/V_j$ at the jet exit plane for all three velocity ratios for the short entry-length streamwise jet are shown in Fig. 3.22. In contrast to the contours for the $L/D = 8$ geometry, there is a significant variation in the turbulence kinetic energy over the $z/D = 0$ exit plane. The gradients in k tend to appear at the locations where the gradients in W/V_j occur, as discussed previously in section 3.5.1.3 and shown in Fig. 3.9. The rise in $\sqrt{k}/V_j$ occurs near $x/D = 0$ which increases from $\sqrt{k}/V_j \approx 0.15$ towards the upstream $(-x)$ side of the jet to $\sqrt{k}/V_j \approx 0.3$ at all velocity ratios. The increased turbulence levels are likely caused by the shear layer which is formed due to the 'jetting effect' from the sharp-edged entrance to the jet orifice. At $R = 0.5$ there is an increase in $\sqrt{k}/V_j$ towards the upstream edge of the jet exit which would be caused by the resulting shear layer from the strong deflection of the jet by the crossflow.

3.6.1.4 Spanwise

The $\sqrt{k}/V_j$ contours for this case are found in Fig. 3.23 at all three velocity ratios. There is some resemblance between the contours for this case and those for the streamwise $(L/D = 4)$ case. The gradients in k occur mid-way across the jet exit near $y/D = 0$ and rise from $\sqrt{k}/V_j \approx 0.1$ to $\sqrt{k}/V_j \approx 0.3$. Again, the shear layer produced at the sharp-edged entrance to the jet hole is likely responsible for this change. At $R = 0.5$ the gradient in $\sqrt{k}/V_j$ at $y/D = 0.5$ corresponds to the strong gradient in W/V_j shown in Fig. 3.10 indicating turbulence generation due to shear. The peak turbulence level reaches $\sqrt{k}/V_j \approx 0.35$ at $R = 0.5$ as the crossflow deflects the jet strongly in this region.

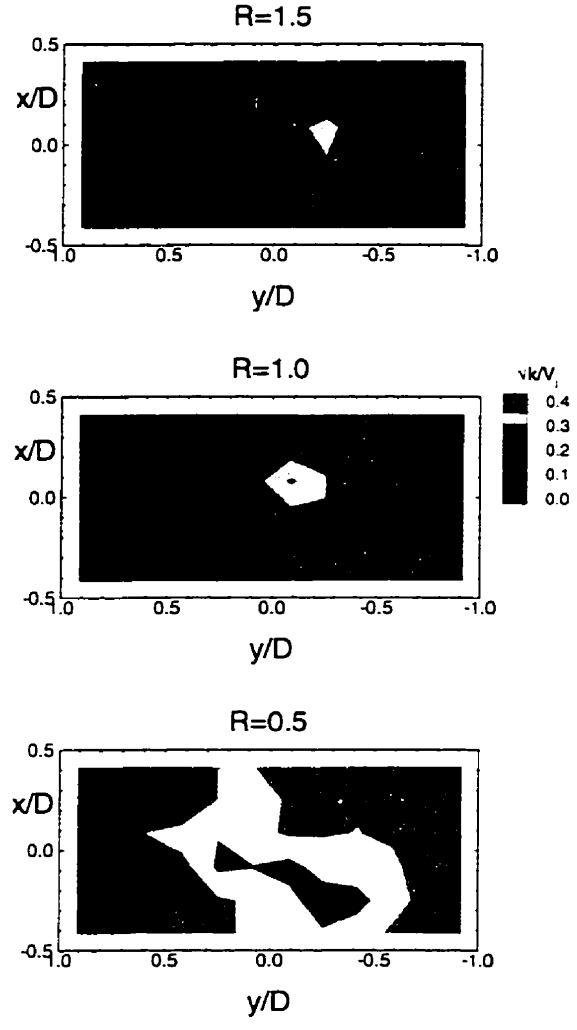

Figure 3.23: Spanwise jet exit $\sqrt{k}/V_j$ contours.

3.6.1.5 Compound-Angle

In the case of the compound angle jets, shown in Fig. 3.24, the peak turbulence kinetic energy is slightly lower than that obtained for the other jet geometries with an entry length of $L/D = 4$. In this case, the turbulence kinetic energy ranges from $\sqrt{k}/V_j \approx 0.1$ to $\sqrt{k}/V_j \approx 0.25$. As R decreases to 0.5 the peak value of $\sqrt{k}/V_j$ does not change appreciably, nor does its location. The overall turbulence level towards the upstream side of the jet exit increases slightly due to the interaction between the jet and the crossflow. Note that there are some odd contours at one edge of the jet, particularly noticeable at $R = 1.0$. These are due to the plotting software and should not be interpreted as the actual experimental data.

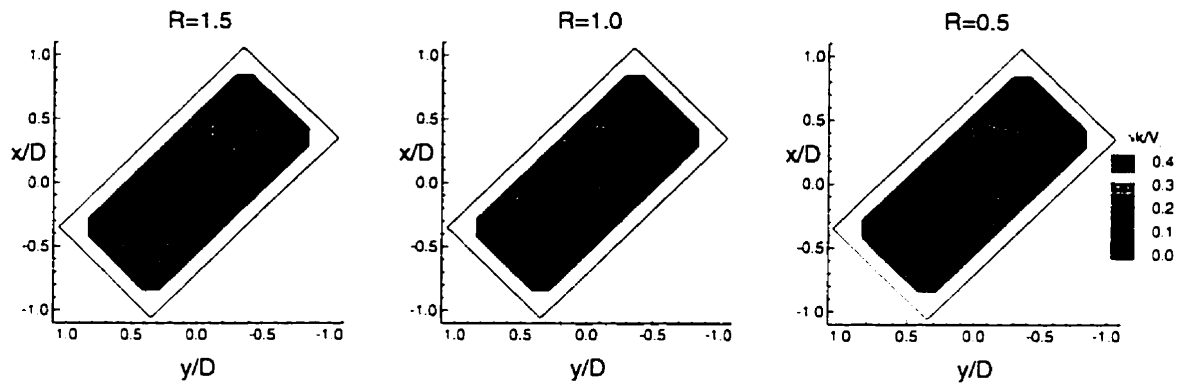

Figure 3.24: Compound-angle jet exit $\sqrt{k}/V_j$ contours.

3.6.2 Turbulence Kinetic Energy

Plots of the turbulence kinetic energy along the same x-z planes used for the presentation of the streamwise velocity are discussed in this section. Note that the jet bulk velocity , V_j, has been used to normalize $\sqrt{k}$ rather than the crossflow velocity, V_∞. Consequently, the turbulence levels shown appear to differ from those shown for the upstream boundary layers discussed in section 3.3. The values presented in the following sections may be converted for comparison by multiplying the V_j-normalized value by R. The individual turbulent normal stresses, u', v', and w' are not presented here as the profiles exhibit the same trends as the turbulence kinetic energy.

3.6.2.1 Velocity Ratio R = 0.5

A comparison of the normalized turbulence kinetic energy $(\sqrt{k}/V_j)$ along the $y/D = 0$ plane for the various geometries is shown in Fig. 3.25. There are few differences between the $(\sqrt{k}/V_j)$ profiles for the $L/D = 8$ and $L/D = 4$ streamwise jet cases. In the near-jet region at $x/D = 1, 2$ the near-wall turbulence levels are higher for the $L/D = 4$ case due to the increased turubulence level in the jet. Farther downstream the profiles become more similar as the strong crossflow dominates the flowfield. At $x/D = 8$ the turbulence level at $z/D = 2$ is essentially unchanged from the freestream value indicating that the jets have not penetrated beyond the boundary layer. The turbulence levels for the spanwise jets are significantly higher than for the other jet geometries due to the much stronger interaction between the jet and the crossflow. The higher turbulence levels at the jet exit are apparent in the near-hole region with a maximum of $(\sqrt{k}/V_j) \approx 0.44$ reached at $x/D = 1$. Farther downstream the turbulence decays rather slowly, fuelled by the strong velocity gradients noted in Fig. 3.12. The lower turbulence level near

the wall at $x/D = 3,5$ is likely due to the proximity of the tunnel floor and the lower-turbulence level fluid from the freestream being drawn towards the floor. Even with the highly turbulent nature of this flow, the turbulence level at $x/D = 8$, $z/D = 2$ is only slightly above the freestream value indicating that the jet flow is only beginning to penetrate beyond the boundary layer. The $(\sqrt{k}/V_j)$ profiles for the compound-angle case are remarkably similar to those for the streamwise-inclined $L/D = 4$ case. A slightly lower near-wall value for the compound-angle case at $x/D = 3$ is apparent, again due to the entrainment of lower-k fluid from the freestream which is drawn towards the wall, as suggested by the velocity profile in Fig. 3.12. The similarity is likely a consequence of the strong deflection of the compound-angle jet in the streamwise direction by the crossflow. Again, jet penetration beyond $z/D = 2$ at $x/D = 8$ is not apparent.

The turbulence kinetic energy along $y/D = -1$ is plotted in Fig. 3.26. For the two streamwise cases the profiles are again quite similar. Evidence of the lateral spreading of the jet may be seen at $x/D = 2$. The high turbulence levels noted for the spanwise jet along $y/D = 0$ are again present, reaching a peak of $(\sqrt{k}/V_j) \approx 0.55$ at $x/D = 1$. The magnitude of the turbulence level in this region tends to suggest some larger-scale unsteadiness in the flow. As the flow moves downstream the profiles begin to resemble those along $y/D = 0$ as the jet flow moves laterally across the tunnel. The influence of the compound-angle jet at $x/D = 0$ is apparent at $z/D = 1$. The increased turbulence levels at $x/D = 1$ are due to the transport of the turbulence from the jet exit into the crossflow. As the flow moves downstream it begins to resemble a boundary layer again, as observed from the velocity profiles of Fig. 3.13. In all these cases the flow does not appear to have penetrated beyond the boundary layer at $x/D = 8$.

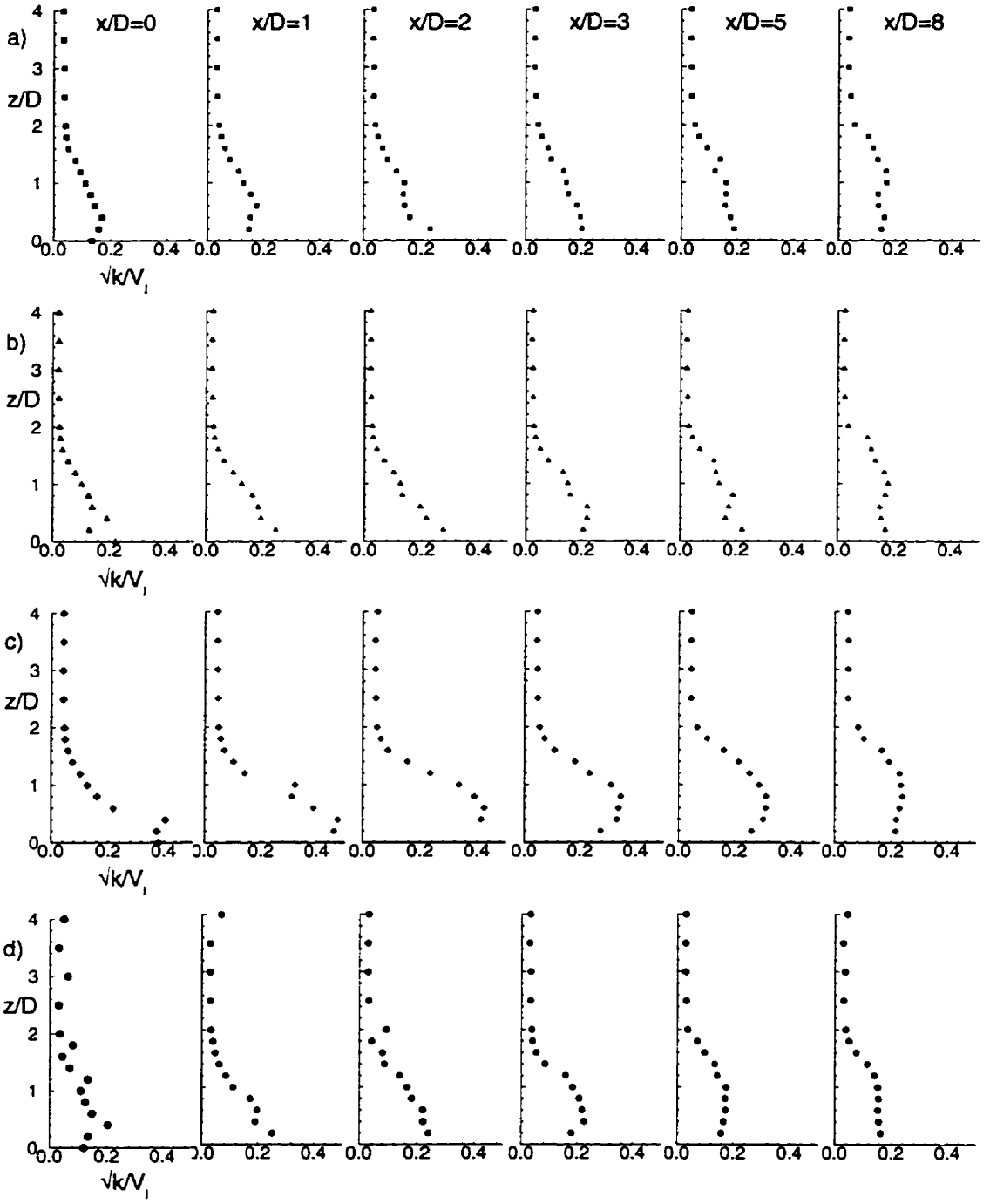

Figure 3.25: Turbulence kinetic energy ($\sqrt{k}/V_j$) along $y/D = 0$, $R = 0.5$ for: a) streamwise $L/D = 8$, b) streamwise $L/D = 4$, c) spanwise, and d) compound-angle jets.

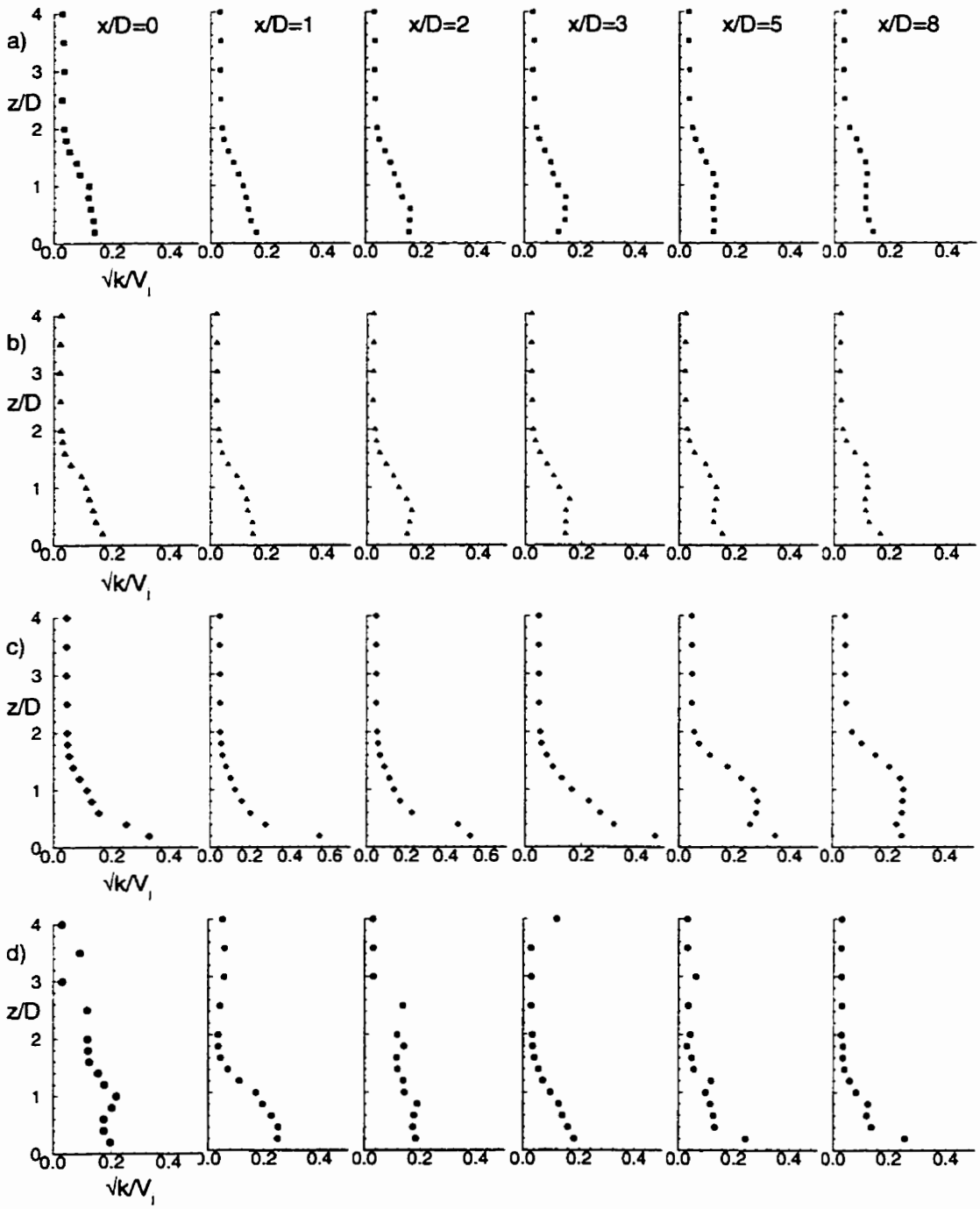

Figure 3.26: Turbulence kinetic energy ($\sqrt{k}/V_j$) along $y/D = -1$, $R = 0.5$ for: a) streamwise $L/D = 8$, b) streamwise $L/D = 4$, c) spanwise, and d) compound-angle jets.

3.6.2.2 Velocity Ratio R = 1.5

Profiles of $(\sqrt{k}/V_j)$ along the $y/D = 0$ plane for each geometry are shown in Fig. 3.27. As was the case for the two streamwise jet cases at $R = 0.5$, there are few differences between the turbulence profiles for the long and short entry lengths. Slightly higher turbulence levels are apparent for the $L/D = 4$ case at $x/D = 1$ due to the transport of the higher turbulence levels at the jet exit for this geometry. In both cases there is a strong jump in $(\sqrt{k}/V_j)$ at $z/D = 1$ for this location indicating the shear layer between the jet and the weaker crossflow. At this velocity ratio the streamwise jets appear to have penetrated beyond the boundary layer by $x/D = 5$. The spanwise jet case is again characterized by the high turbulence levels in the near-hole region with $(\sqrt{k}/V_j) \approx 0.4$ at $x/D = 0$. The jump in the turbulence levels in this region correspond to the increase in streamwise velocity indicated in Fig. 3.17 and is due to the transport of the higher turbulence levels at the jet exit as well as the strong interaction between the jet and the crossflow. The jet appears to have penetrated to the edge of the boundary layer by $x/D = 1$ and is clearly into the crossflow farther downstream. At $x/D = 2$ there is a jump in $(\sqrt{k}/V_j)$ at $z/D = 2.5$ which appears contrary to the trend established by the surrounding data. The reason for this discrepancy is unclear but the value cannot be discarded as an error as the same observation is made at $x/D = 3$, $z/D = 3.5$. It is possible that it is a consequence of the presence of the adjacent jet which is seen in the vector plot in Fig. 3.19. Since the jets are not perfectly stationary, the increase in $(\sqrt{k}/V_j)$ could be due to the motion of the edge of the jet through the measurement volume. In the case of the compound-angle jet the increase in $(\sqrt{k}/V_j)$ due to the jet fluid is clear. The jet appears to have penetrated beyond the boundary layer by $x/D = 5$. There appears to be a drop in the overall turbulence level within the jet at $x/D = 3$ which increases again by $x/D = 5$. This change is due to the lateral motion of the jet in

the $-y$-direction as it is not deflected as strongly by the crossflow at this velocity ratio. The increase at $x/D = 5$ is simply due to the presence of the adjacent jet.

Along the $y/D = -1$ plane, shown in Fig. 3.28, the lateral spreading of the streamwise $L/D = 8$ jet noted in section 3.5.4 is apparent. The $L/D = 8$ jet also appears to have penetrated farther into the crossflow in the vertical (z) direction than the $L/D = 4$ jet as well. In the spanwise jet case, the jumps in $(\sqrt{k}/V_j)$ noted at $x/D = 2$ and $x/D = 3$ along $y/D = 0$ in the previous paragraph also appear to be present at $x/D = 3$ and $x/D = 5$ along $y/D = -1$. This observation would be consistent with the lateral movement of the jet as the flow progresses downstream. The penetration of the jet beyond the boundary layer is clear at $x/D = 1$. The behaviour of the compound-angle jet along this plane is similar to that described in the previous paragraph, without the drop in $(\sqrt{k}/V_j)$.

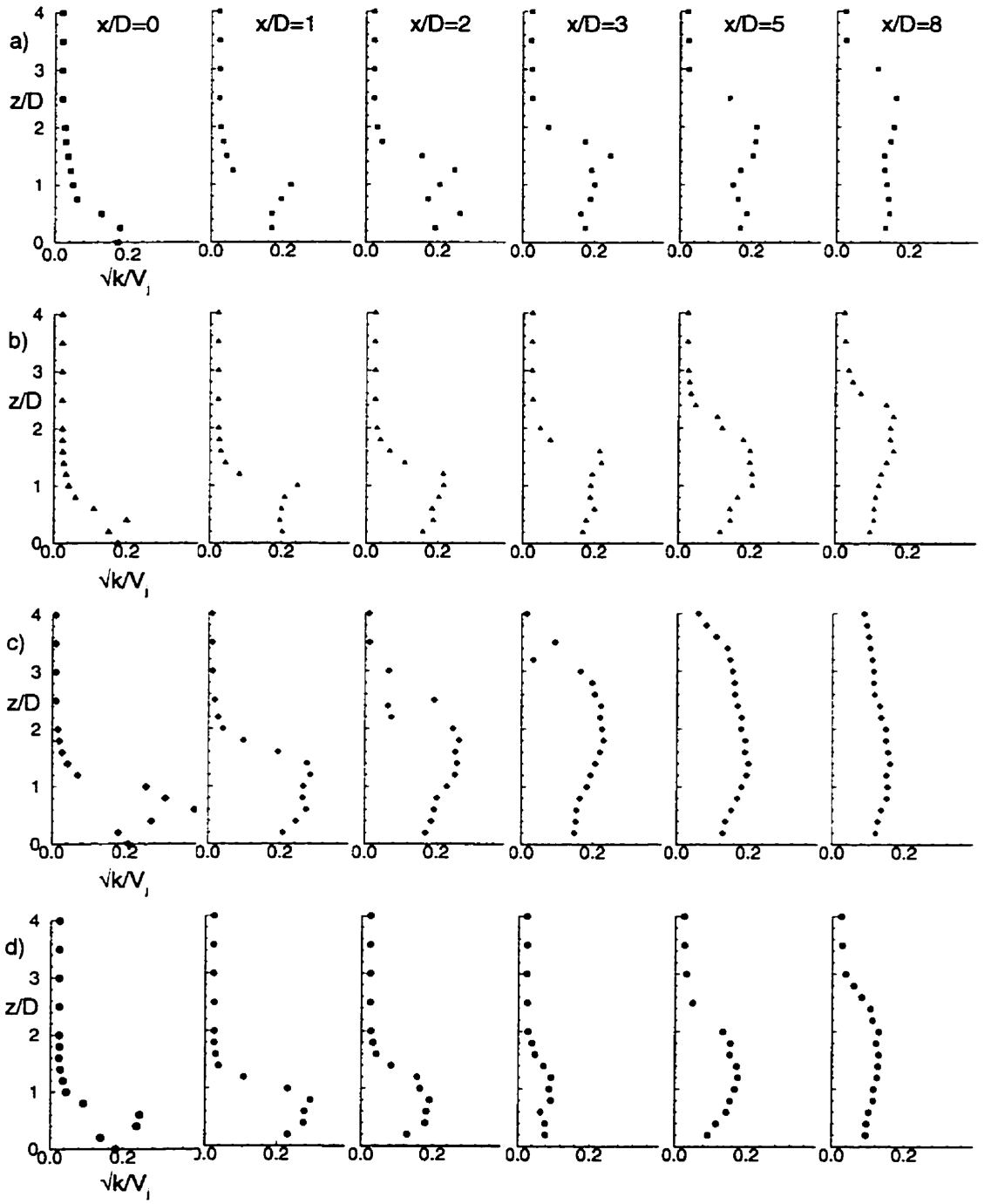

Figure 3.27: Turbulence kinetic energy ($\sqrt{k}/V_j$) along $y/D = 0$, $R = 1.5$ for: a) streamwise $L/D = 8$, b) streamwise $L/D = 4$, c) spanwise, and d) compound-angle jets.

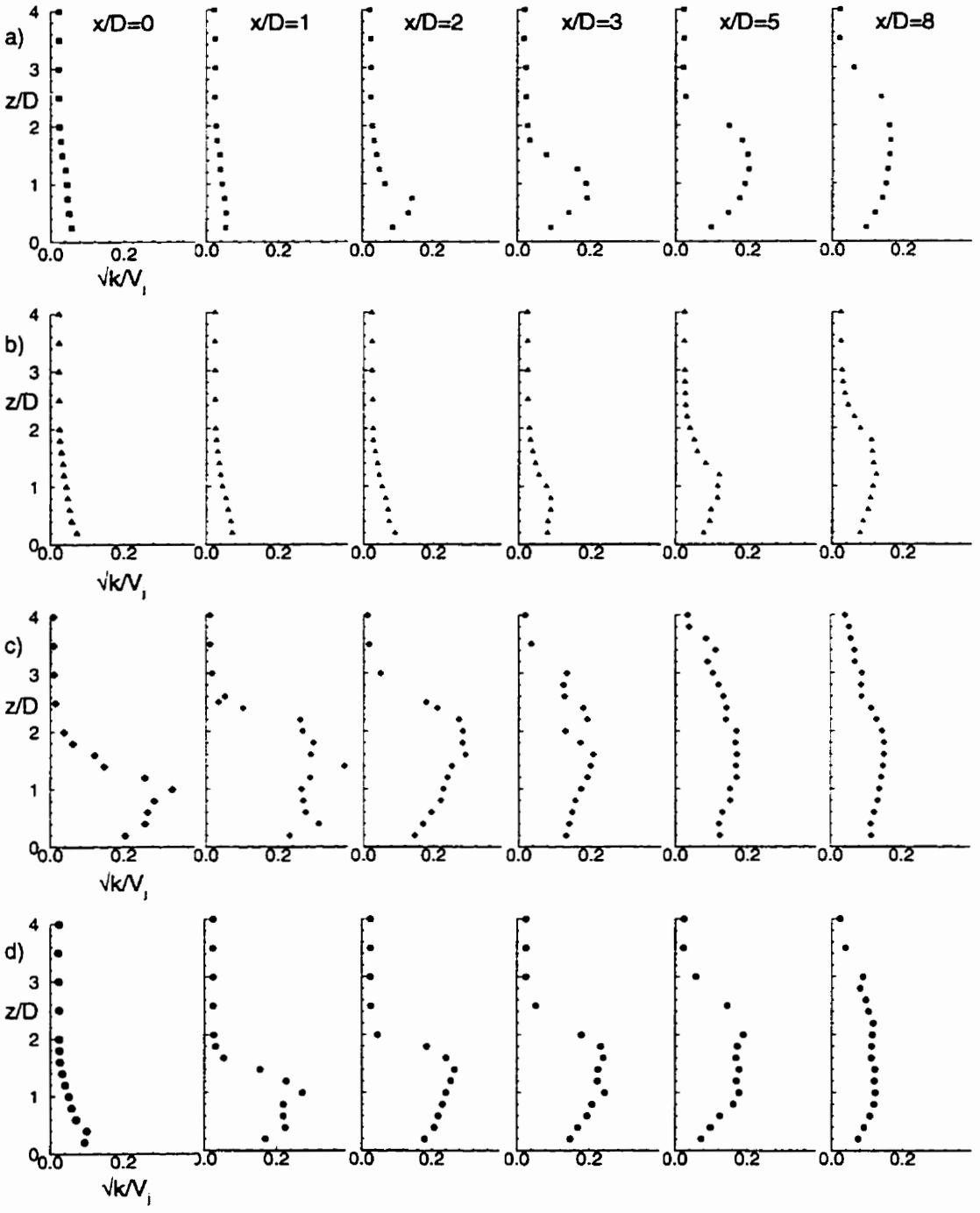

Figure 3.28: Turbulence kinetic energy ($\sqrt{k}/V_j$) along $y/D = -1$, $R = 1.5$ for: a) streamwise $L/D = 8$, b) streamwise $L/D = 4$, c) spanwise, and d) compound-angle jets.

3.6.3 Anisotropy

As mentioned in section 3.6.2 the profiles of the individual normal stresses are similar to the profiles for the turbulence kinetic energy at the same locations. However, more information about the turbulent nature of the flow may be obtained by considering the relative magnitudes of the normal stresses. Many of the more common turbulence models used in computational modelling make use of the assumption of isotropic turbulence. The discussion in this section examines the deviation of this flow from isotropy.

In order to compare the turbulent normal stress, two ratios of the r.m.s. normal stresses are defined. The first, called the v'-ratio, is defined as:

$$\frac{v' - u'}{u'} \tag{3.14}$$

and the second, called the w'-ratio, is defined as:

$$\frac{w' - u'}{u'} \tag{3.15}$$

A value of zero for both ratios indicates that the turbulence is isotropic. A value of, say 0.5, for the v'-ratio indicates that v' is 50% greater than u'. Only the results from the $R = 1.5$ case are presented as the deviation from isotropy is more evident.

Contours of the v'-ratio for the various geometries at $R = 1.5$ are shown in Fig. 3.29. For both of the streamwise injection cases a region of anisotropy occurs at the upper edge of the jet along the centreline ($y/D = 0$) where the v'-ratio reaches approximately -0.4. Recall from the velocity profiles in Fig. 3.17 that there is a considerable streamwise velocity gradient ($\partial U/\partial z$) in this region. This velocity gradient contributes to the production of u' resulting in the relative deficit in v'. This observation is typical of a normal boundary layer flow where the $\partial U/\partial z$ gradient is the only significant velocity gradient

in the flow. Closer to the floor at $x/D = 8$ along the jet centreline the v'-ratio is close to zero corresponding to the small gradient in $\partial U/\partial z$ at this location. A similar trend is clear for the spanwise jets at $x/D = 3$ where the v'-ratio again drops to approximately -0.3 at $y/D = 1, -2$. Again, this corresponds to the velocity gradient $\partial U/\partial z$ which can be seen in the periodicity check of Fig. 3.5. A large $\partial U/\partial z$ gradient may also be found at $x/D = 1$ along the $y/D = 0$ plane for the compound-angle jets near $z/D = 1$. However, the v'-ratio is fairly high (≈ 0.4) in this region corresponding to the large $\partial V/\partial z$ gradient which contributes to the production of v'.

The w'-ratio contours for the $R = 1.5$ case are shown in Fig. 3.30 for the different geometries. Peak values of the w'-ratio are typically larger than those for the v'-ratio, unlike the usual boundary layer case where the reverse would be expected. This trend is likely due to the fact that contributions to the w' normal stress are from the gradients $\partial W/\partial x$ and $\partial W/\partial y$. As the jets enter the crossflow they are turned in the crossflow direction as they move downstream or, conversely, the crossflow is deflected by the jet. This results in a $\partial W/\partial x$ gradient along the upper edge of the jets producing higher values of the w'-ratio in these regions. There is some discrepancy between the streamwise $L/D = 8$ and $L/D = 4$ cases at the downstream $x/D = 8$ plane. In the $L/D = 8$ case the w'-ratio drops to below -0.2 near $z/D = 2$ while the w'-ratio is around 0.6 for the $L/D = 4$ case at the same location. It is unclear what the source of this discrepancy is. The primary difference between the two geometries is the stronger vertical velocity at the jet exit for the $L/D = 4$ case which would result in a stronger $\partial W/\partial x$ gradient for this case. However, it would be reasonable to expect higher values of w' in the near-hole region if this was the case. Regions where the w'-ratio reaches 1.0 are apparent at $x/D = 1$ for both the spanwise and compound-angle jets. These areas correspond to locations where strong vortices are present. The swirling flow of the vortices results in a relatively large $\partial W/\partial y$ gradient which contributes to w' in these regions.

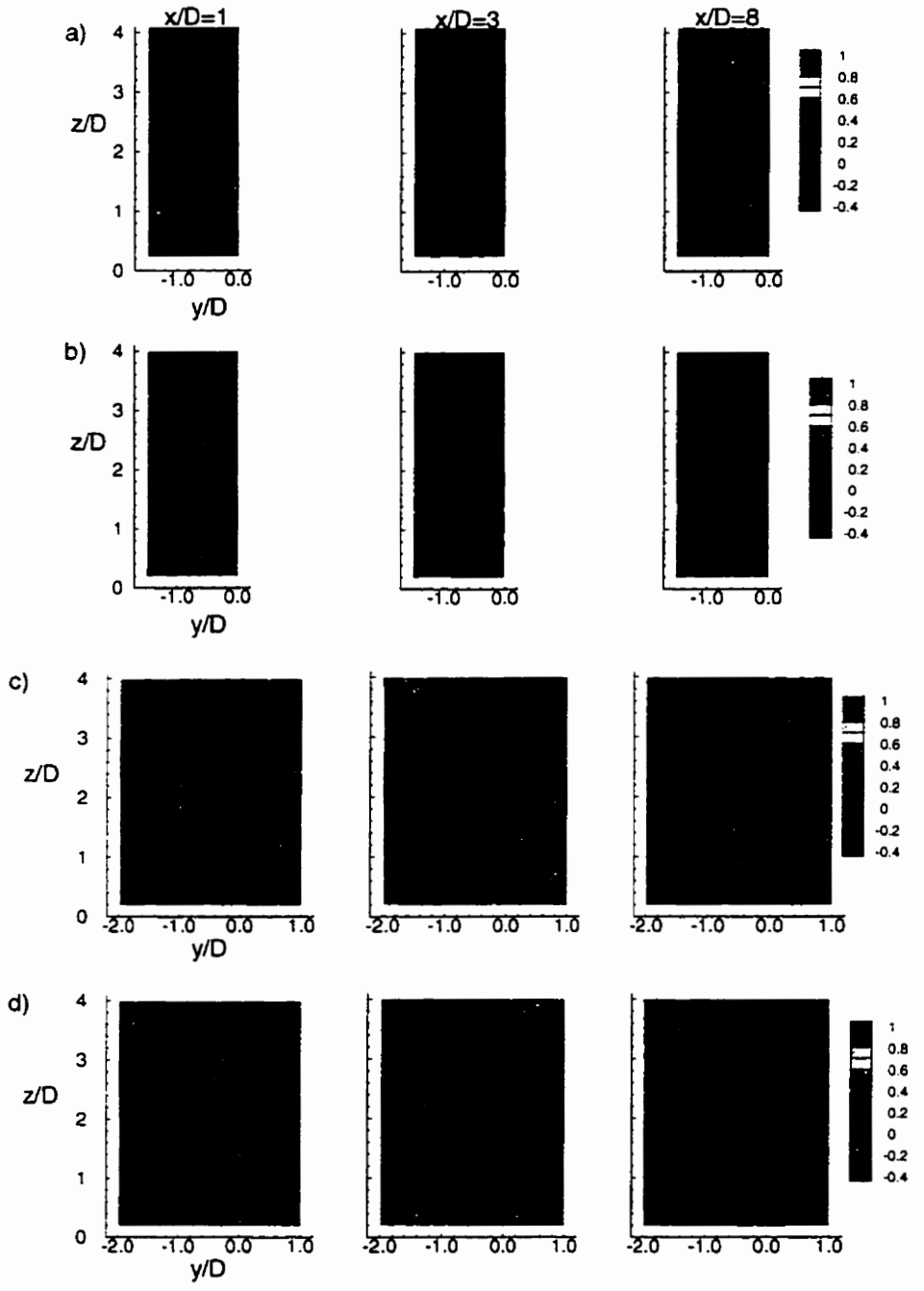

Figure 3.29: Contours of the v'-ratio at $R = 1.5$ for: a) streamwise $L/D = 8$, b) streamwise $L/D = 4$, c) spanwise, and d) compound-angle jets.

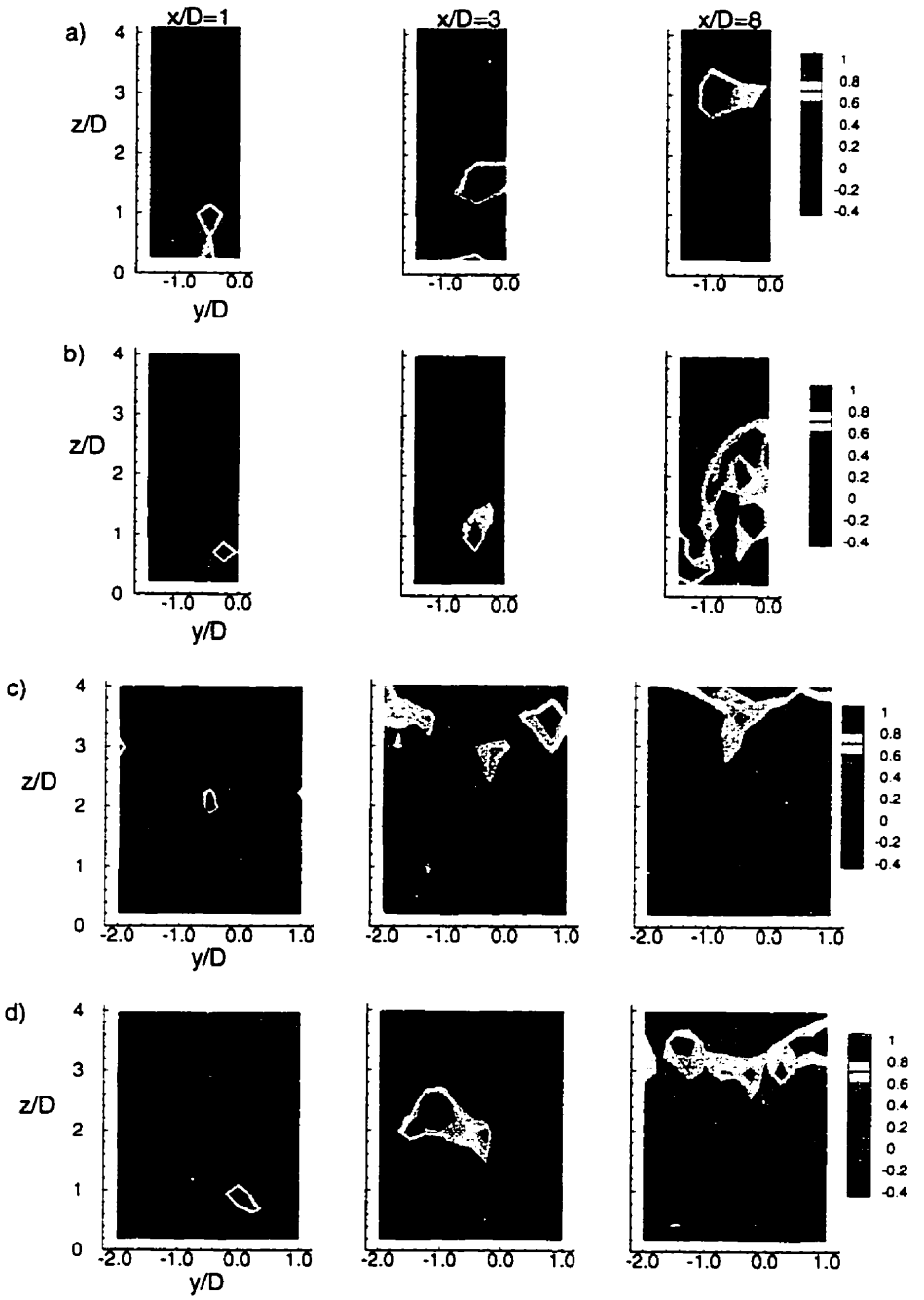

Figure 3.30: Contours of the w'-ratio at $R = 1.5$ for: a) streamwise $L/D = 8$, b) streamwise $L/D = 4$, c) spanwise, and d) compound-angle jets.

3.6.4 Turbulent Shear Stresses

The turbulent shear stresses are often unmeasured and not reported due to the lack of available tools. However, with the three-component LDV system operating in coincidence mode used here it was possible to measure these quantities. The three turbulent shear stresses are presented as contour plots in spanwise $y - z$ planes for the $R = 0.5$ and $R = 1.5$ velocity ratios.

In the following discussion, reference is made to the production of the turbulent shear stresses from the velocity gradients in the flow field. For reference, the production terms from the Reynolds stress equations are provided as follows (White (1991)):

$$P_{\overline{uv}} = -\overline{uv}\frac{\partial U}{\partial x} - \overline{v^2}\frac{\partial U}{\partial y} - \overline{vw}\frac{\partial U}{\partial z} - \overline{u^2}\frac{\partial V}{\partial x} - \overline{uv}\frac{\partial V}{\partial y} - \overline{uw}\frac{\partial V}{\partial z} \tag{3.16}$$

$$P_{\overline{uw}} = -\overline{uw}\frac{\partial U}{\partial x} - \overline{vw}\frac{\partial U}{\partial y} - \overline{w^2}\frac{\partial U}{\partial z} - \overline{u^2}\frac{\partial W}{\partial x} - \overline{uv}\frac{\partial W}{\partial y} - \overline{uw}\frac{\partial W}{\partial z} \tag{3.17}$$

$$P_{\overline{vw}} = -\overline{uw}\frac{\partial V}{\partial x} - \overline{vw}\frac{\partial V}{\partial y} - \overline{w^2}\frac{\partial V}{\partial z} - \overline{uv}\frac{\partial W}{\partial x} - \overline{v^2}\frac{\partial W}{\partial y} - \overline{vw}\frac{\partial W}{\partial z} \tag{3.18}$$

3.6.4.1 Velocity Ratio R = 0.5

Contours of $\overline{uw}/V_j^2$ are shown in Fig. 3.31 for $R = 0.5$. The $\overline{uw}$ stress appears to correspond fairly closely with the gradients in $\partial U/\partial z$, suggesting that the $\overline{uw}$ stress is produced primarily by the $\overline{w^2}\partial U/\partial z$ term in the production equation 3.17. For the streamwise jets at $x/D = 1$, a region of positive $\overline{uw}$ is observed near the top of the jet which corresponds to the negative $\partial U/\partial z$ gradient in this region. Towards the sides of

the plots ($y/D < -1$) regions of negative $\overline{uw}$ are clear which are due to the boundary-layer flow where the positive $\partial U/\partial z$ gradient results in a negative $\overline{uw}$ stress. Farther downstream at $x/D = 8$ the top of the jet flow is characterized by a negative $\overline{uw}$ as the streamwise velocity profile returns to a more typical boundary layer flow. For the spanwise jet, the change in the sign of $\overline{uw}$ at $x/D = 3$, $y/D = 0$ as z/D increases corresponds closely to the change in the sign of $\partial U/\partial z$. A region of negative $\overline{uw}$ is apparent over the top of the jet as the flow moves downstream, again corresponding to the boundary layer-type velocity profile produced as the higher-velocity crossflow moves over the jet. Note that the magnitude of the $\overline{uw}$ stress is much higher for the spanwise jets than it was for the streamwise jets due to the stronger interaction between the jet and the crossflow. The corresponding -$\overline{uw}$ region over the top of the jet is clear for the compound-angle jet at $x/D = 8$ as well, although the magnitude is closer to that for the streamwise jets.

Contour plots of $\overline{uv}/V_j^2$ at $R = 0.5$ are shown in Fig. 3.32. Along the plane of symmetry $y/D = 0$ for the streamwise inclined jets $\overline{uv}$ should be zero. While this is the case for most of the domain, there appear to be locations where $\overline{uv}$ does not equal zero along the symmetry plane, such as at $x/D = 3$, $z/D = 0.2$ for both streamwise jet cases. The source of this discrepancy is unclear although it is possible that more data points are needed in this region to provide a better average due to the high turbulence levels. The $\overline{uv}$ shear stress is an indicator of the lateral turbulent mixing of the jet with the crossflow and some correlation should be expected along the edges of the jets. No clear trend is evident for the streamwise jets as the flow is dominated by the crossflow turbulence. Near the floor at $y/D = -1$ a small region where $\overline{uv}$ is negative can be seen at most of the x/D locations. These are regions where $\partial V/\partial z$ is typically large which contributes to the production of $\overline{uv}$. At $x/D = 8$ larger, crescent-shaped region of positive $\overline{uv}$ is

apparent. In this region, the lower streamwise velocity of the jet flow relative to the crossflow results in a negative $\partial U/\partial y$ gradient (for $y/D < 0$), adding to the production of positive $\overline{uv}$. For the spanwise jets, two regions of negative $\overline{uv}$ are apparent in the $x/D = 1$ plane. These locations correspond to large $\partial U/\partial z$ and $\partial U/\partial y$ gradients which result in contributions to $-\overline{uv}$. Farther downstream at $x/D = 3$ regions of positive $\overline{uv}$ may be observed. Near $y/D = -0.2$ the sign of $\overline{uv}$ changes from negative to positive as z/D increases away from the wall. Near the wall there is a large positive $\partial V/\partial z$ gradient while $\overline{uw}$ is positive, resulting in a contribution to $-\overline{uv}$. Farther from the wall $\partial V/\partial z$ is still positive but $\overline{uw}$ has changed sign so there is a contribution to $+\overline{uv}$. Note that over the same region the contribution to the production of $\overline{uv}$ from the $\partial U/\partial z$ term is opposite in sign to that from the $\partial V/\partial z$ term indicating the importance of $\partial V/\partial z$ to the production of $\overline{uv}$ in this region. For the compound-angle jets at $x/D = 1$ the sign of $\partial V/\partial z$ is positive over most of the plane and the sign of $\overline{uv}$ tends to correspond to the sign of $\overline{uw}$. For both the spanwise and compound-angle jets at $x/D = 8$ the values of $\overline{uv}$ are smaller than at the upstream locations as the gradients become much smaller.

Contour plots of $\overline{vw}/V_j^2$ at $R = 0.5$ are shown in Fig. 3.33. According to Andreopoulos and Rodi (1984), the $\overline{vw}$ stress acts to damp out the secondary vortex motion in the flow. In a region with a clearly-developed vortex flow the velocity gradients $\partial V/\partial z$ and $\partial W/\partial y$ are the primary contributors to the production of $\overline{vw}$ in Equation 3.18. However, for the streamwise jets at $R = 0.5$ no clear vortex motion develops. At $x/D = 1$ a region of $-\overline{vw}$ is apparent for both cases. For the $L/D = 8$ case the $\partial W/\partial y$ gradient is small in this region so it is the positive $\partial V/\partial z$ term which generates the shear stress. For the $L/D = 4$ case the region of $-\overline{vw}$ is at a location where both gradients are present. The $\overline{w^2}$ normal stress is larger in this location, suggesting that the $\partial V/\partial z$ gradient is primarily responsible for the generation of $\overline{vw}$. Farther downstream the magnitude of the $\overline{vw}$ stress

drops as no strong vortices develop and the gradients in $\partial V/\partial z$ and $\partial W/\partial y$ are small. The magnitude of $\overline{vw}$ is much larger for the spanwise jet case which corresponds to the strong vortex formation at $R = 0.5$. At $x/D = 1$ the region of negative $\overline{vw}$ near $y/D = 0$ corresponds to strong positive $\partial V/\partial z$ and $\partial W/\partial y$ gradients. The region of positive $\overline{vw}$ near $y/D = 0.8$ corresponds to strong negative $\partial V/\partial z$ and $\partial W/\partial y$ gradients. As the flow progresses downstream and the vortex weakens there is a corresponding drop in the magnitude of $\overline{vw}$. The same trends may be observed for the compound-angle case. Regions of positive $\overline{vw}$ may be observed downstream for the compound-angle case corresponding to the negative $\partial W/\partial y$ velocity gradient.

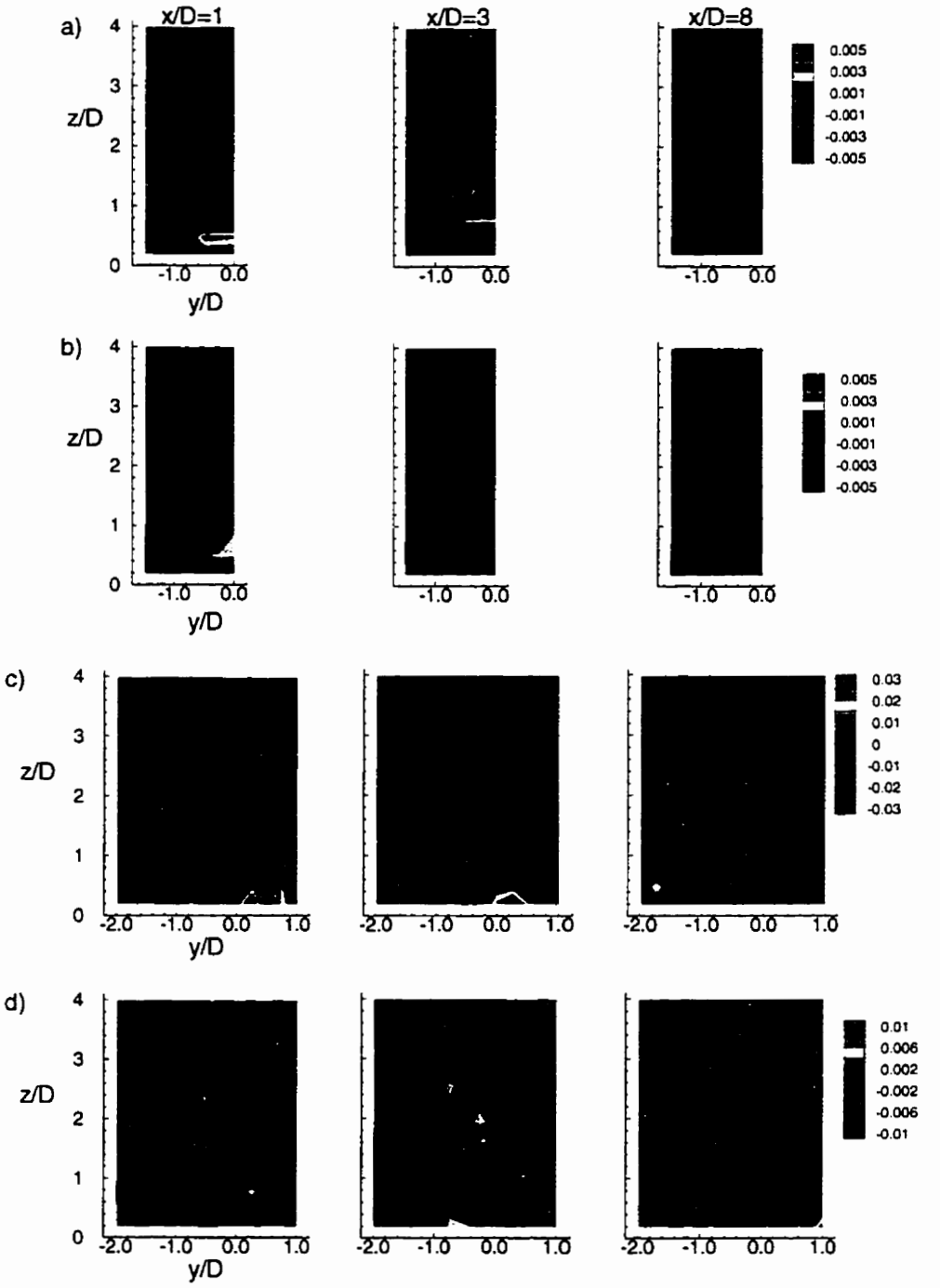

Figure 3.31: Turbulent Shear Stress $\overline{uw}/V_j^2$ at $R = 0.5$ for: a) streamwise $L/D = 8$, b) streamwise $L/D = 4$, c) spanwise, and d) compound-angle jets.

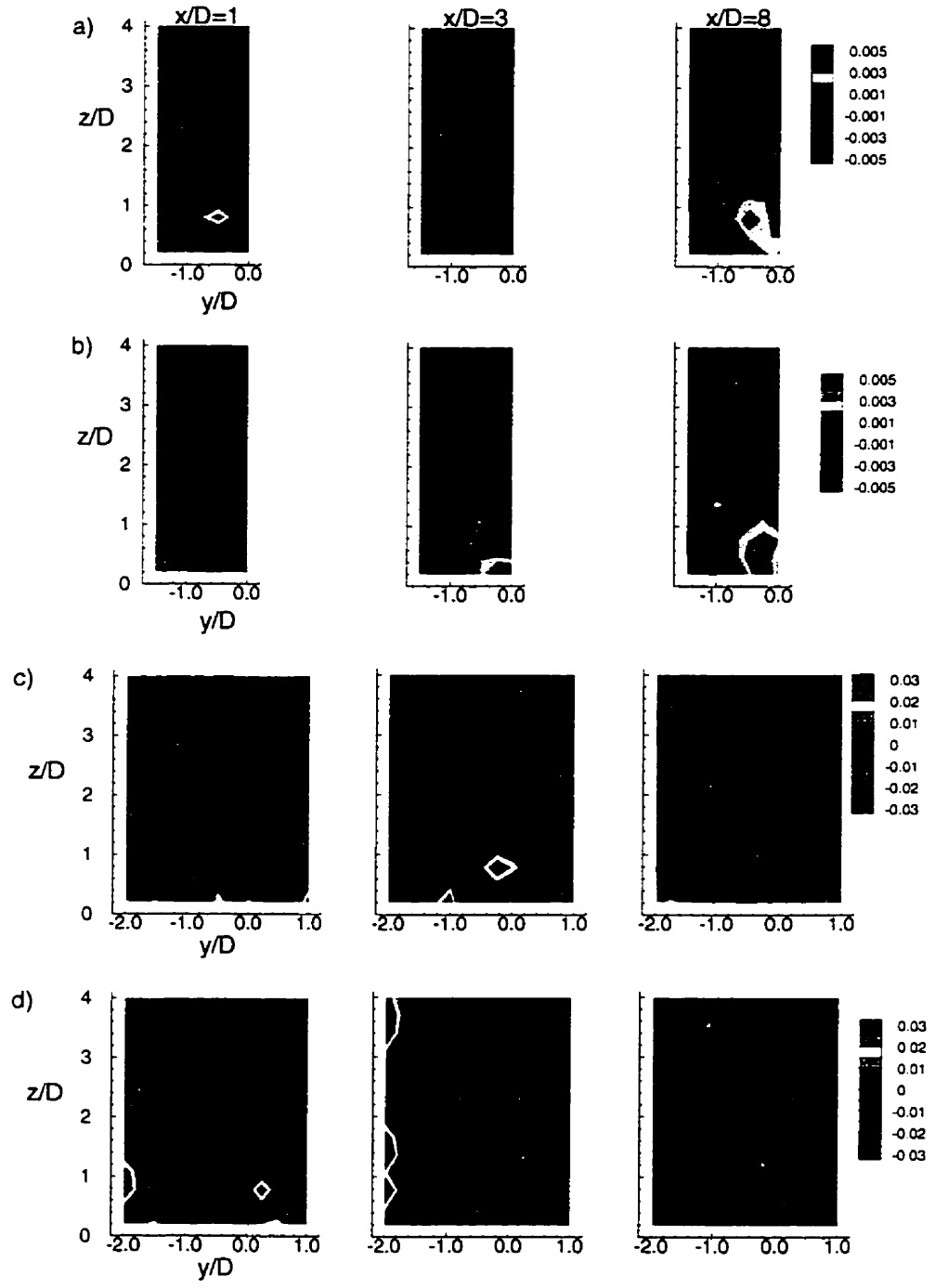

Figure 3.32: Turbulent Shear Stress $\overline{uv}/V_j^2$ at $R = 0.5$ for: a) streamwise $L/D = 8$, b) streamwise $L/D = 4$, c) spanwise, and d) compound-angle jets.

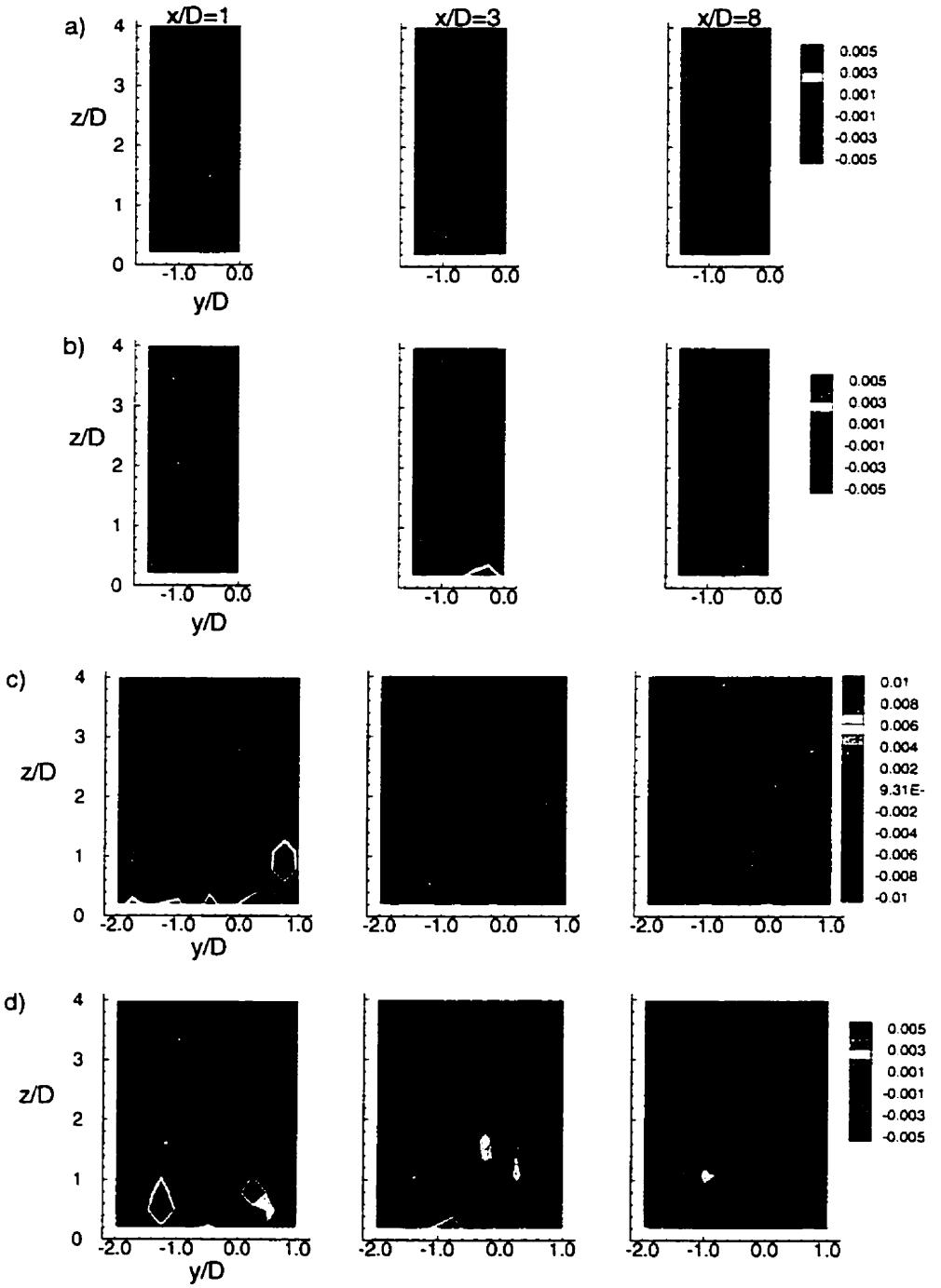

Figure 3.33: Turbulent Shear Stress $\overline{vw}/V_j^2$ at $R = 0.5$ for: a) streamwise $L/D = 8$, b) streamwise $L/D = 4$, c) spanwise, and d) compound-angle jets.

3.6.4.2 Velocity Ratio R = 1.5

Contour plots of $\overline{uw}/V_j^2$ are shown in Fig. 3.34 for $R = 1.5$. As for the $R = 0.5$ velocity ratio, the $\overline{uw}$ stress corresponds closely with the gradients of $\partial U/\partial z$. A large region of positive $\overline{uw}$ over the top of the streamwise jets is clear at all downstream locations. Unlike the $R = 0.5$ case where the sign of the shear stress changes from positive to negative, the strong jet results in a negative $\partial U/\partial z$ velocity gradient along the upper edge of the jet. The greater lateral spread of the streamwise $L/D = 8$ jet case is apparent from the plots. Along the underside of the streamwise jets a region of negative $\overline{uw}$ exists due to the positive $\partial U/\partial z$ gradient as the jet penetrates beyond the boundary layer into the crossflow. The large regions of negative $\overline{uw}$ near the tunnel floor at the edges of the jet at $R = 0.5$ are not present here due to the weaker velocity gradient in the boundary layer at the lower crossflow velocity. A large region of positive $\overline{uw}$ is clear at $x/D = 1$ for the spanwise jets and the effect of the adjacent jet may be observed for $y/D > 0$. At $y/D = -1$ the region of $+\overline{uw}$ extends from near the floor to $z/D \approx 1.8$ even though this is a region with a positive $\partial U/\partial z$ gradient which should result in a negative shear stress. It appears that the negative $\partial W/\partial y$ gradient due to the vortex forming in this region is the principle source of $\overline{uw}$. Immediately above the region of positive $\overline{uw}$ is a region of $-\overline{uw}$. The $\partial U/\partial z$ gradient is small in this region so it appears that the $-\overline{uw}$ stress is the result of the positive $\partial W/\partial y$ gradient contribution. Note that $\overline{uv}$ is positive in this region as well so the sign of the contribution in Equation 3.17 does not change. The region of positive $\overline{uw}$ over the upper edge of the jet is clear for the compound-angle jet case. At $x/D = 1$ a small region of $-\overline{uw}$ is apparent immediately above the positive region for the same reasons explained in the spanwise jet case. At $x/D = 3$ a region of $-\overline{uw}$ due to the positive $\partial U/\partial z$ gradient is seen, similar to that observed for the streamwise jet cases. For both the spanwise and compound-angle jet cases the $\overline{uw}$ values drop by $x/D = 8$ as

there are no strong velocity gradients present in the flow at this downstream location.

Contours of $\overline{uv}/V_j^2$ are shown in Fig. 3.35 for $R = 1.5$. The stronger lateral mixing of the streamwise jets as compared to the $R = 0.5$ case is clear, particularly in the near-hole region. As was the case for the $\overline{uw}$ stress, the sign of the $\overline{uv}$ stress does not change sign as the flow moves downstream due to the strong jet flow relative to the crossflow. This strong jet flow produces a positive $\partial U/\partial y$ gradient at the edge of the jet resulting in a $-\overline{uv}$ contribution. Towards the inside of the jet at $x/D = 8$ for both streamwise cases a region of positive $\overline{uv}$ may be seen. This appears to be due to the negative $\partial V/\partial z$ gradient present in the flow due to the vortex. The drop in $\overline{uv}$ towards the symmetry plane $y/D = 0$ is more clear at this higher velocity ratio. For the spanwise jets regions of negative $\overline{uv}$ shear stress are clear over the upper edge of the jet at $x/D = 1$. It appears that the positive $\partial V/\partial z$ gradient is the primary source of $\overline{uv}$ in this region as the gradient $\partial U/\partial z$ is small. The region of positive $\overline{uv}$ visible near $y/D = 0$, $z/D = 1$ is again due to the positive $\partial V/\partial z$ contribution but the sign of $\overline{uw}$ is negative in this region. As was the case with the $\overline{uw}$ stress, the magnitude decreases quickly as the flow progresses downstream. Finally, in the case of the compound-angle jets the effect of the strong jet flow producing a positive $\partial U/\partial y$ gradient at $y/D = -1.2$ may be observed at $x/D = 1$. At $y/D = 0.2$ a region of positive $\overline{uv}$ is found near the floor, corresponding to the negative $\partial U/\partial y$ gradient on the opposite side of the jet. Again, as the flow moves downstream the $\overline{uv}$ stress dissipates quickly.

Contour plots of $\overline{vw}/V_j^2$ at $R = 1.5$ are shown in Fig. 3.36. Due to the stronger vortex motion at this velocity ratio the magnitude of $\overline{vw}$ is larger for the streamwise jets than at $R = 0.5$. Farther downstream, towards the floor the sign of $\overline{vw}$ is positive due to the negative $\partial V/\partial z$ gradient. For the spanwise jet case, the regions of negative $\overline{vw}$ near the upper edge of the jet are due to the positive $\partial V/\partial z$ gradient at the top of the vortex

which is forming. Towards the floor, $\partial W/\partial y$ is negative, resulting in the positive $\overline{vw}$ observed in this region. The magnitude of the $\overline{vw}$ stress drops quickly as the flow moves downstream due to the interaction between the adjacent jets which prevents the vortices from forming as they did in the $R = 0.5$ case. The contours for the compound-angle case are also characterized by the $-\overline{vw}$ values along the upper edges of the jet. The region of positive $\overline{vw}$ at $y/D = 0$ is due to the strong negative $\partial W/\partial y$ gradient as the vortex begins to form at $x/D = 1$. Again, the magnitude of $\overline{vw}$ decreases as the vortex dissipates.

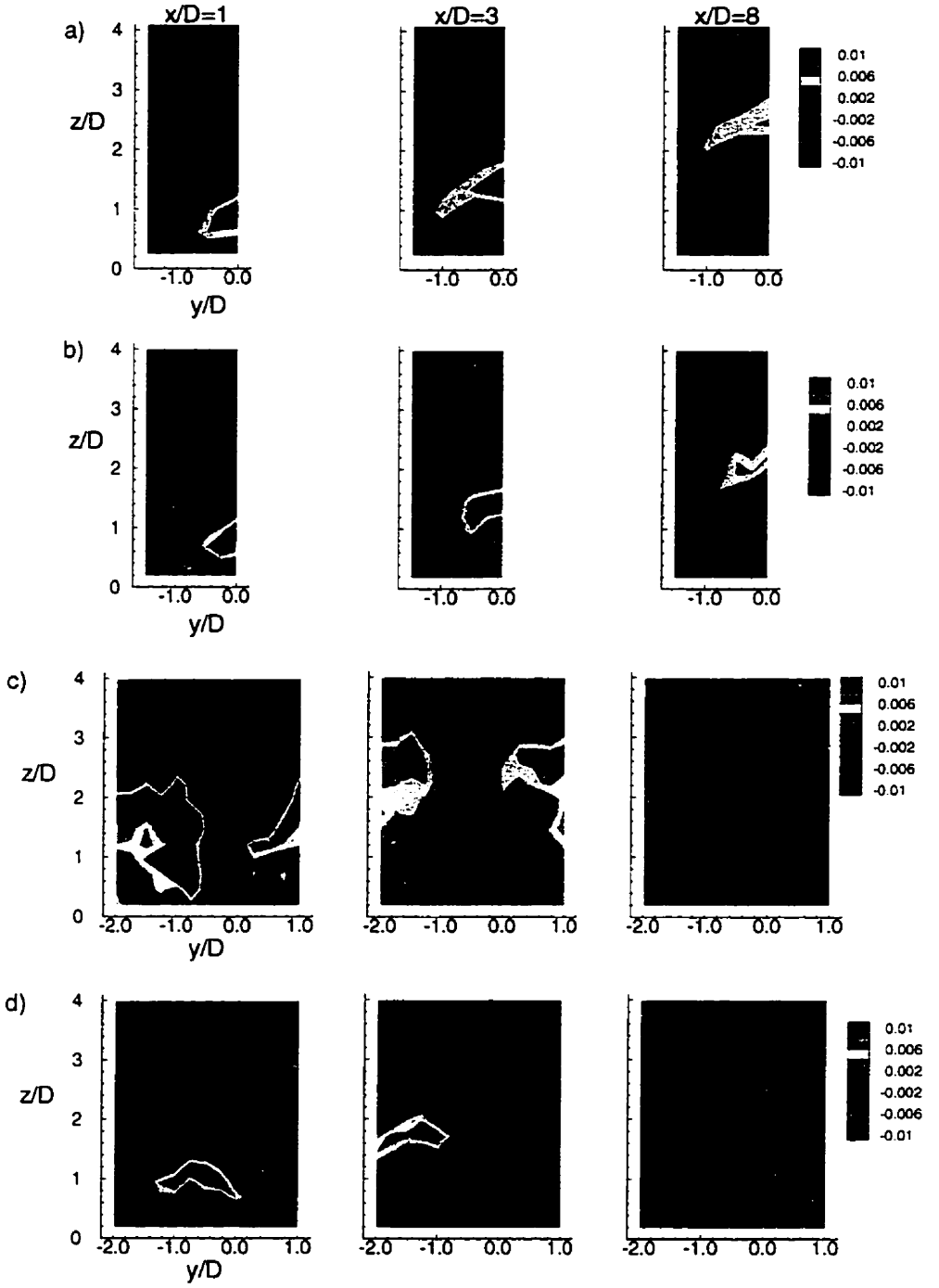

Figure 3.34: Turbulent Shear Stress $\overline{uw}/V_j^2$ at $R = 1.5$ for: a) streamwise $L/D = 8$, b) streamwise $L/D = 4$, c) spanwise, and d) compound-angle jets.

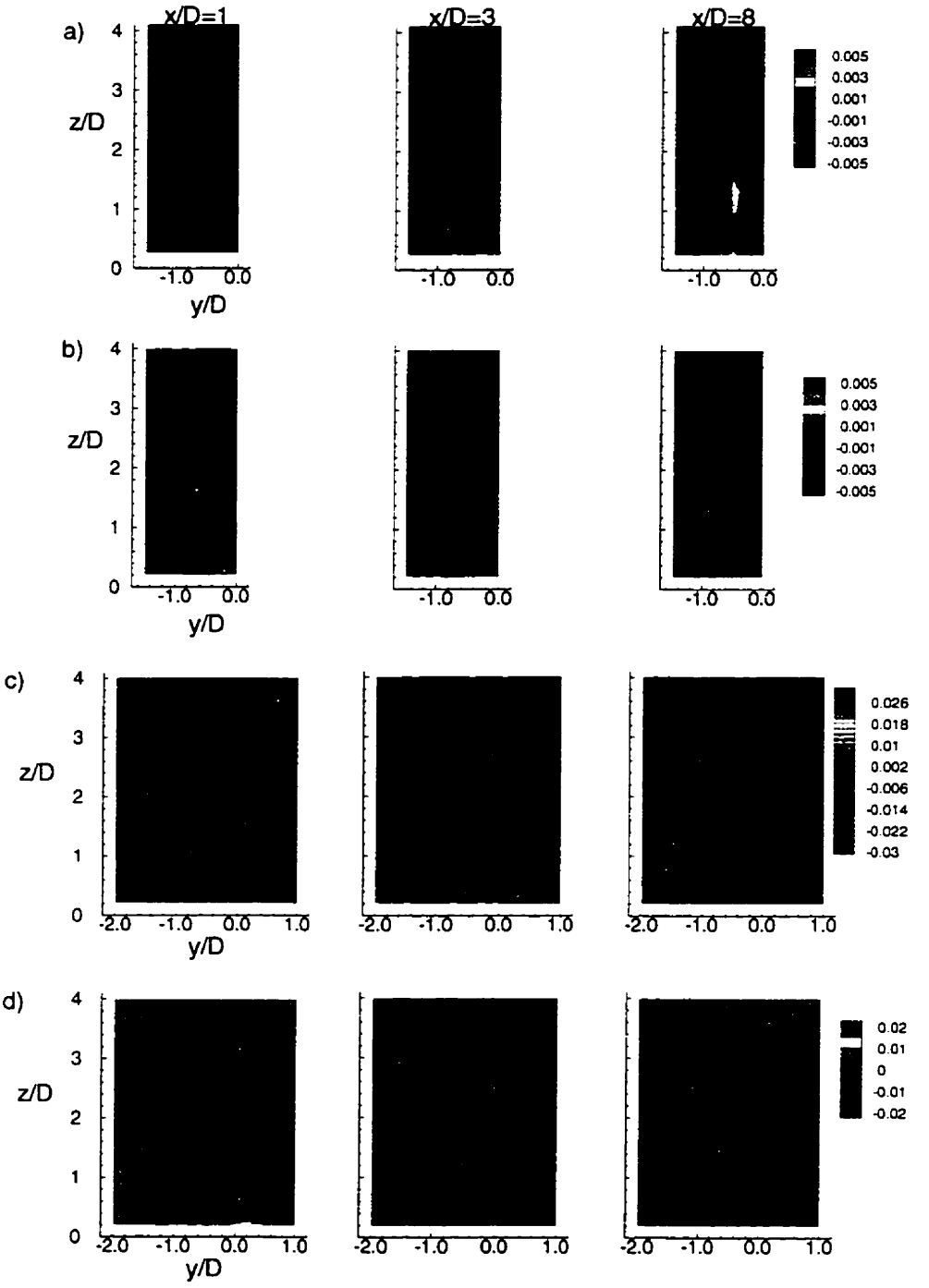

Figure 3.35: Turbulent Shear Stress $\overline{uv}/V_j^2$ at $R = 1.5$ for: a) streamwise $L/D = 8$, b) streamwise $L/D = 4$, c) spanwise, and d) compound-angle jets.

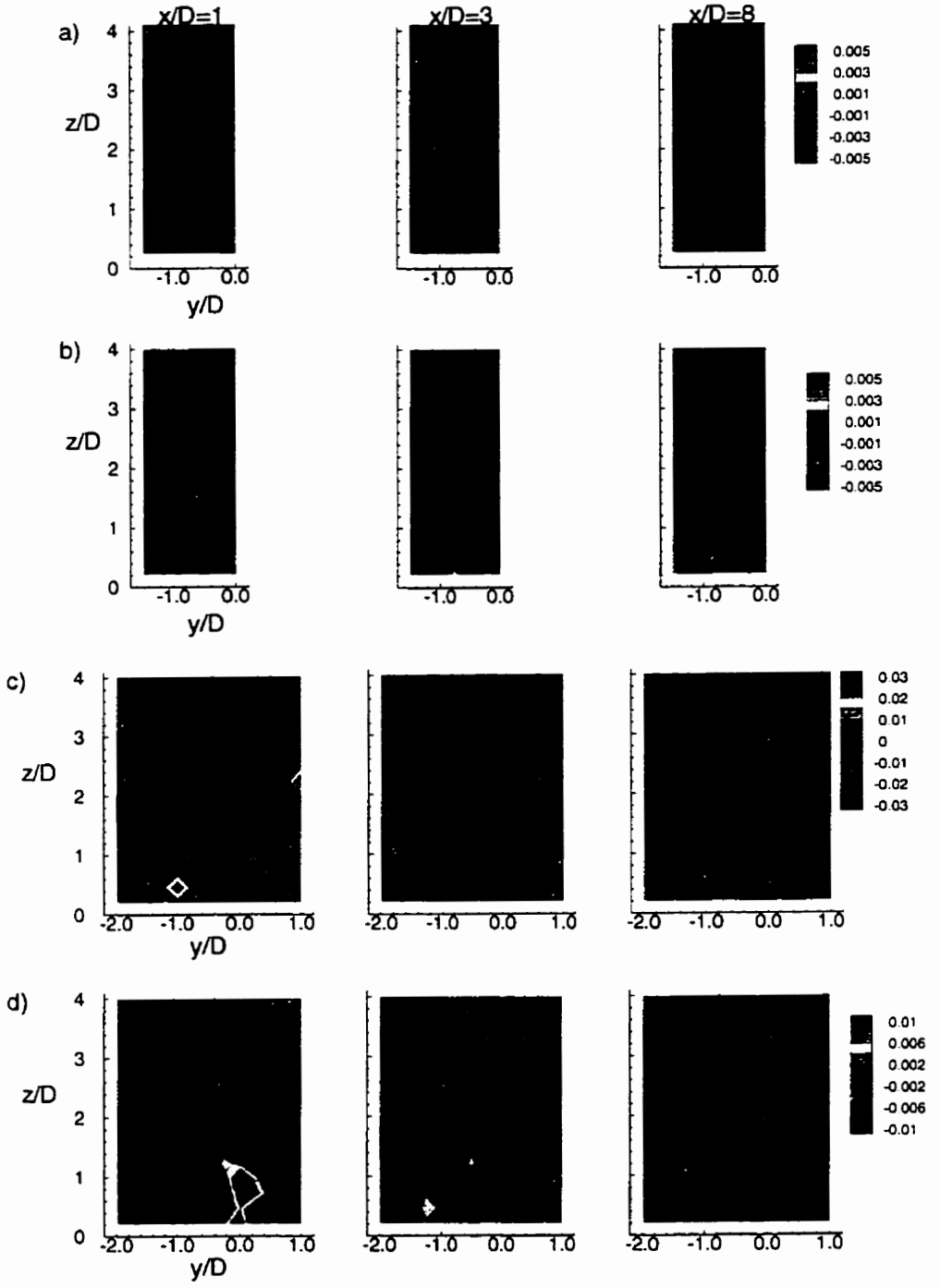

Figure 3.36: Turbulent Shear Stress $\overline{vw}/V_j^2$ at $R = 1.5$ for: a) streamwise $L/D = 8$, b) streamwise $L/D = 4$, c) spanwise, and d) compound-angle jets.

3.6.5 Summary

As was the case for the mean velocities, there are few differences between the turbulence kinetic energy profiles for the two streamwise-inclined jet cases. In the near-hole region the short entry length jets ($L/D = 4$) tend to have higher values of $\sqrt{k}/V_j$ due to the nearer proximity of the shear layer within the jet hole from the 'jetting effect'. Overall, the spanwise jets exhibit the largest turbulence kinetic energy values due to the much stronger interaction with the crossflow, as compared to the other geometries.

The anisotropy of the turbulent normal stresses for all four geometries at $R = 1.5$ is clear. The presence of strong local velocity gradients in all three coordinate directions at various locations within the flow field tend to promote the production of a particular shear stress at a given location. For example, the higher values of the w' stress relative to the u' stress along the sides of the streamwise inclined jets due to the $\partial W/\partial y$ velocity gradient in these locations.

The turbulent shear stresses exhibit similar behaviour to the normal stresses in that the mean velocity gradients tend to promote the production of a particular stress at a given location in the flow field. Typically, the magnitude of the shear stresses are larger at the higher velocity ratio of $R = 1.5$, but due to the complexity of the flow it is not possible to make a general conclusion about the relationship between velocity ratio and shear stresses. In the case of the spanwise and compound-angle jets the magnitude of the turbulent shear stresses decreases as the flow moves downstream due to the weaker mean velocity gradients which are present.

3.7 Scalar Transport

The use of the FID system allowed for the measurement of the transport of the jet fluid mixed with a trace amount of propane. From this data, the film cooling effectiveness

(FCE or η_f) may be inferred along the tunnel floor and the penetration and spreading of the jet into the crossflow may be determined. As noted in the Introduction, most experimental studies which focus on the hydrodynamic flow field infer the jet penetration and spreading from differences between the local and free stream velocities or turbulence kinetic energies. The validity of this approach is examined here. In their study of a single jet normal to the crossflow, Crabb *et al.* (1981) found large differences between the distributions of velocity and scalar concentration. Scalar transport measurements were not made for the streamwise $L/D = 8$ case and the results presented here are for the remaining geometries.

3.7.1 Jet Penetration and Spreading

Contours of the jet fluid concentration at three spanwise $y - z$ planes downstream of the jet exit are shown in the following sections. A value of one indicates that the flow consists of purely jet fluid at that point, while a value of zero indicates crossflow fluid. The velocity vectors in these spanwise planes, also shown in Fig. 3.14, 3.16, and 3.19, are superimposed on the contours in order to better describe the flow behaviour. The region covered by the contours indicates the region where data were obtained with the upper z/D edge at the height where concentration readings of less than 0.02 were obtained from all the probes. In other words, the domain was not extended to include the zero values of concentration farther away from the wall.

3.7.1.1 Velocity Ratio R = 0.5

The jet concentration contours for this velocity ratio are shown in Fig. 3.37. The streamwise ($L/D = 4$) jets do not penetrate very far into the crossflow, reaching a maximum of $z/D = 1.4$ at $x/D = 8$. Even though the velocity vectors indicate lateral

(V-component) velocities, the spreading indicated by the contours is fairly small. This is due to the high crossflow velocity (indicated by the reference vector) which transports the flow downstream rapidly. A clear jet core is visible at $x/D = 8$ centred at $z/D = 0.4$ from the floor. In the case of the spanwise jets, the jet flow spans almost the entire width of the field, as expected from the orientation of the jet which injects jet fluid in the negative y-direction. The jet has penetrated to $z/D = 1$ at $x/D = 1$ due to the high vertical velocities at the jet exit which are seen at $y/D = 0.25$ in the figure. At $x/D = 3$ a jet core is clearly present slightly above the floor level. The peak jet concentration is much lower in this case than it was for the streamwise jets indicating much faster mixing with the crossflow in the near-hole region. This behaviour would be expected from the strong vortex which is apparent for the spanwise case. Along the floor there is a noticable variation in jet concentration. The region of higher concentration between $y/D = -1$ and -2 is from the jet flow farther upstream. The region of lower concentration at $y/D = 0$ is from the crossflow between adjacent jets which has been trapped at the wall. Farther downstream at $x/D = 8$ it is apparent that the jet has not penetrated beyond $z/D = 2$. The vortex which is present appears to draw the lower concentration fluid from the crossflow down towards the wall. The compound-angle case appears to be intermediate between the two other geometries. The penetration of the jet into the crossflow by $x/D = 1$ is relatively high due to the strong vertical component of velocity at the jet exit. Farther downstream however, the jet penetration is more comparable to that for the streamwise case. The mixing between the jet and the crossflow is not as strong as in the spanwise case. The vortex which is formed in this case is clearly drawing the crossflow fluid down towards the wall, reducing the floor area covered by the jet flow. The presence of the adjacent jet is apparent at $x/D = 8$.

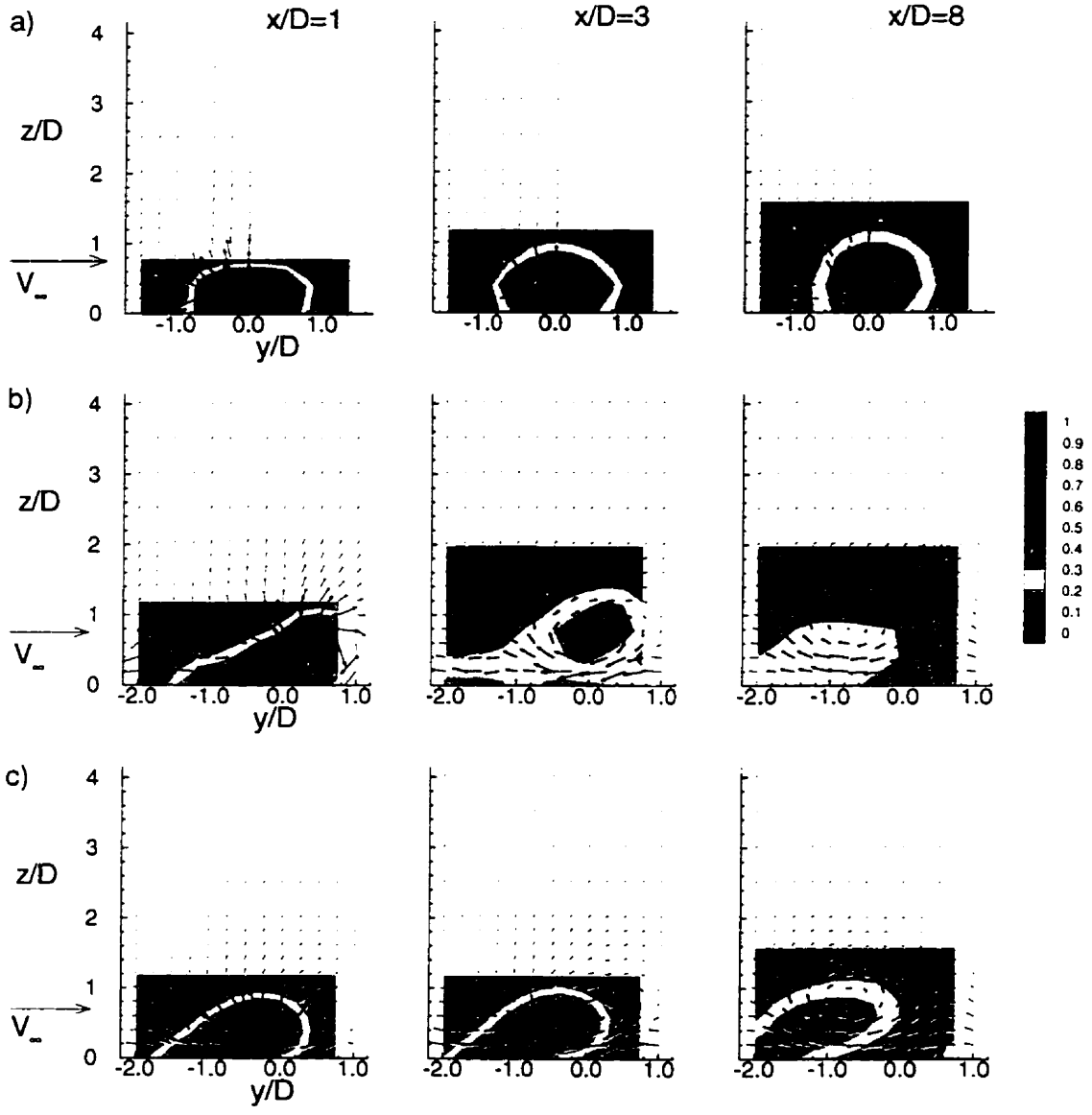

Figure 3.37: Concentration contours and velocity vectors in spanwise $y - z$ planes for $R = 0.5$: a) streamwise $L/D = 4$, b) spanwise, c) compound-angle jets.

3.7.1.2 Velocity Ratio R = 1.5

Plots of jet concentration and velocity vectors in spanwise planes for the various geometries are shown in Fig. 3.38. Clearly the jet flow penetrates farther into the crossflow and spreads laterally to a greater extent for all the geometries than was evident at $R = 0.5$. In the case of the streamwise $L/D = 4$ jets it appears that the jet almost lifts off from the floor at $x/D = 3$. The vortices which form draw the crossflow fluid towards the floor and towards $y/D = 0$ leaving only a narrow region of the floor surface covered by the jet flow. This effect becomes more pronounced farther downstream at $x/D = 8$ where the vortices have lifted farther off the floor and are stronger. A clear core region is still present although it is clear that more mixing between the jet and crossflow has occurred at $R = 1.5$ than was the case at $R = 0.5$. The flows from adjacent jets are just beginning to merge by this downstream location. The spanwise jet fluid almost penetrates beyond the $2D$-thick boundary layer as early as $x/D = 1$. The location of peak penetration has shifted from $y/D \approx 0.4$ at $R = 0.5$ to $y/D \approx -1.2$ due to the weaker crossflow in this case. A clear jet core is evident at $x/D = 3$ and the presence of the adjacent jet is seen. Along the floor at $z/D = 0$ a region of higher jet concentration is observed which is likely jet fluid from the adjacent jet that was moved towards the floor by the start of a vortex similar to that seen at $x/D = 1$. Similarly, the regions of lower concentration are due to the crossflow fluid which was drawn towards the floor by the downward flow farther upstream. Farther downstream at $x/D = 8$ the jet flow appears to have mixed fairly well with the crossflow and spread laterally to merge with the adjacent jet. Interestingly, the concentration immediately adjacent to the floor is lower than that observed in the rest of the flow below $z/D = 2$. It appears that the crossflow fluid noted at $x/D = 3$ has become trapped at the floor. The concentration along the floor farther downstream would likely increase as the flow mixed with the fluid farther from the wall. In the compound-angle

jet case the vortex drawing crossflow fluid towards the floor at $x/D = 1$ is clear. As the flow moves downstream a large region of the floor surface is exposed to the crossflow fluid. As in the streamwise case a clear jet core is still evident at $x/D = 8$ and the jet has almost lifted off from the floor.

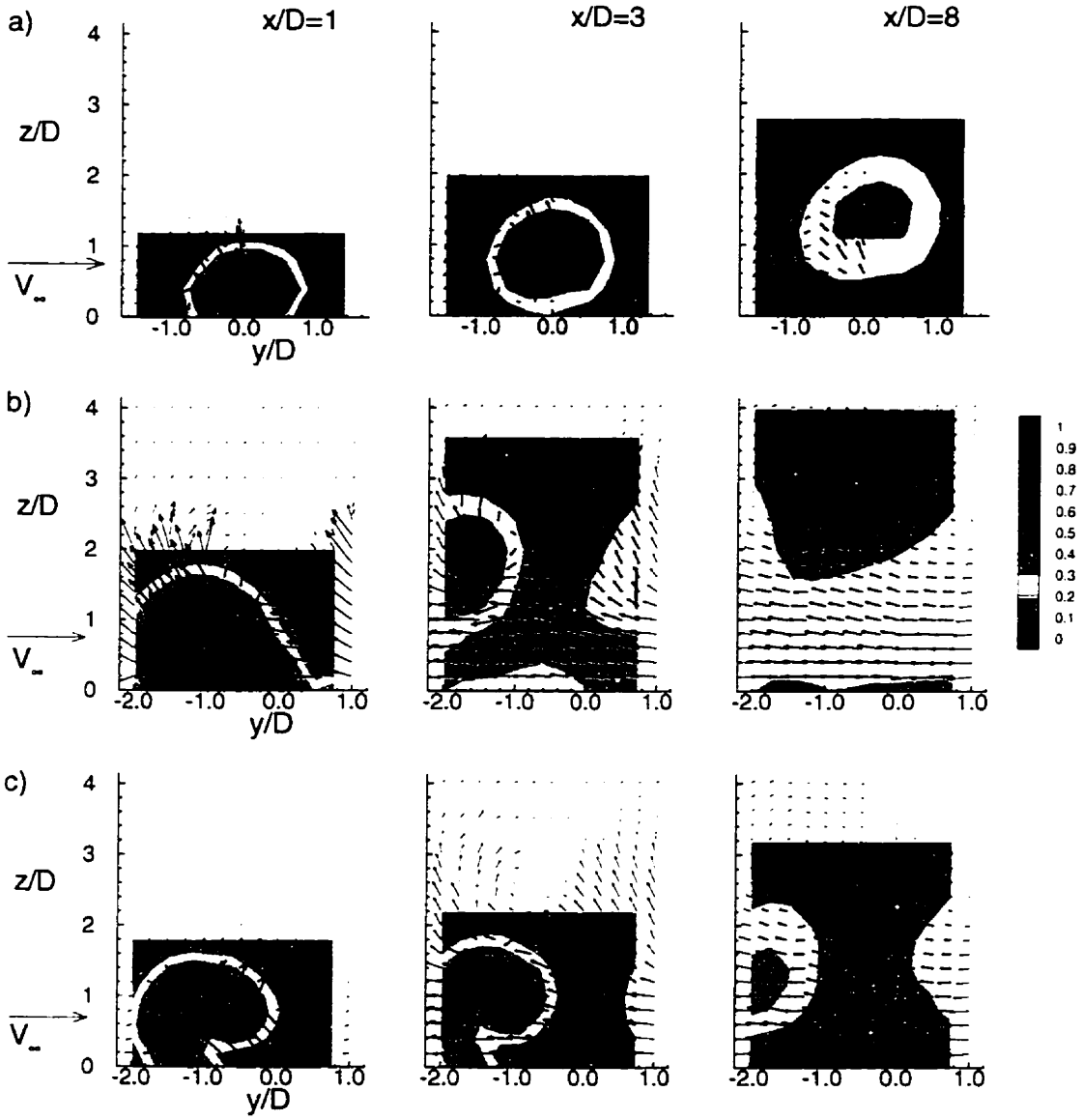

Figure 3.38: Concentration contours and velocity vectors in spanwise $y - z$ planes for $R = 1.5$: a) streamwise $L/D = 4$, b) spanwise, c) compound-angle jets.

3.7.2 Film Cooling Effectiveness

The definition of the adiabatic film cooling effectiveness, η_f, from Equation (1.2) requires that the adiabatic wall temperature be measured which may be difficult to realize in practice. Alternatively, a heat/mass transfer analogy may be used, as discussed by Goldstein (1971). With this analogy it can be seen that the impermeable wall along the tunnel floor is quite accurately 'adiabatic'. The film cooling effectiveness is then expressed as:

$$\eta_f = \frac{C_w - C_\infty}{C_2 - C_\infty} \tag{3.19}$$

where C is the mass concentration of the contaminant and the subscripts w, ∞, and 2 refer to the wall, free stream, and jet conditions respectively. In the present experiments, only the jet flow was contaminated making $C_\infty = 0$ and $\eta_f = C_w/C_2$.

Contours of η_f along the tunnel floor ($z/D = 0$) for the streamwise $L/D = 4$ case are shown in Fig. 3.39. At all three velocity ratios a region of $\eta_f = 1$ is observed at $x/D = 1$ corresponding to the downstream edge of the jet exit hole. At $R = 0.5$ the jet spreads laterally to $y/D = \pm 1$ which remains roughly constant as the flow moves downstream. The concentration remains high along the jet centreline ($y/D = 0$) due to the strong deflection of the jet towards the floor by the crossflow. At $R = 1.0$ the downstream spreading of the jet along the floor is much less than at $R = 0.5$ corresponding to the greater penetration of the jet into the crossflow. A small region of higher η_f is seen at $x/D = 5$ along the jet centreline indicating possible reattachment of the jet flow with the floor. Finally, at $R = 1.5$ where the jet penetrates strongly into the crossflow, the region covered by the jet flow is narrow, approximately $1D$ wide, leaving much of the floor exposed to the crossflow fluid.

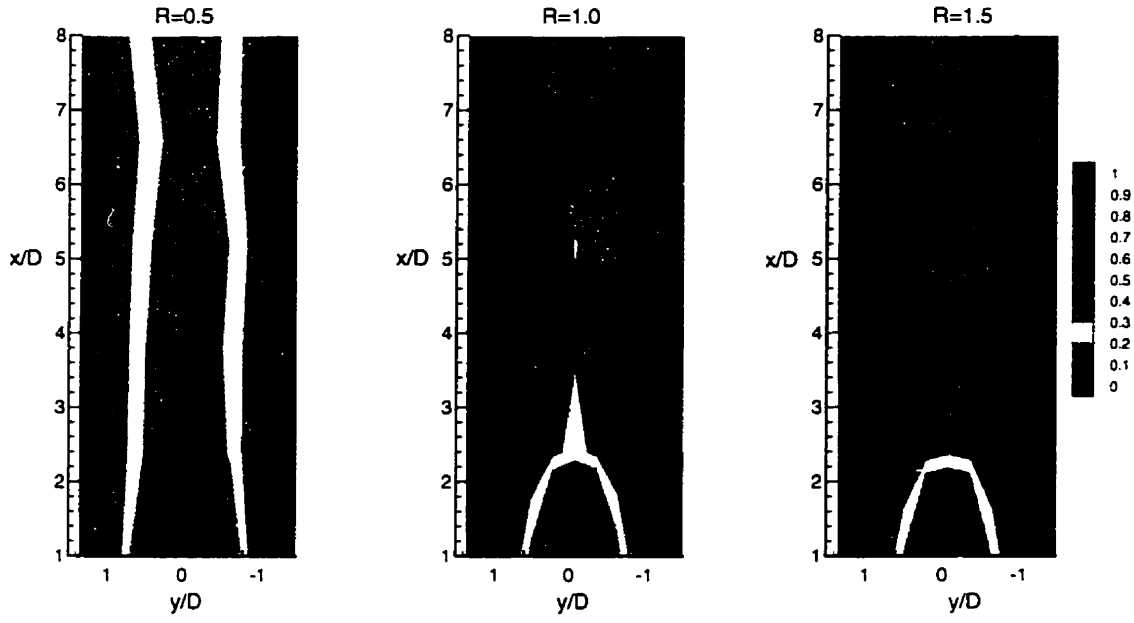

Figure 3.39: Contours of η_f along $z/D = 0$ for the streamwise $L/D = 4$ jet case.

The contours of η_f for the spanwise injection case are shown in Fig. 3.40. The deflection of the jet in the streamwise direction is apparent at $R = 0.5$ with a small region of low film coverage at $x/D = 0.5$, $y/D = -1.8$ due to the presence of the strong crossflow in the space between adjacent jets. Farther downstream at $x/D = 2$ another region of low η_f is apparent where the crossflow between adjacent jets has penetrated along the floor. The entire floor is covered by the jet flow although the typical η_f values are fairly low, around 0.2. At $R = 1.0$ the region where $\eta_f > 0.3$ is smaller as the jet penetrates farther into the crossflow. The presence of the adjacent jet is apparent at $x/D = 2$. A small region of lower η_f is also clear at $y/D = -1$. The stronger lateral movement of the jet is clear. The region where $\eta_f > 0.3$ spreads across the entire width of the measurement plane at $R = 1.5$. The region of lower η_f noticed at $R = 1.0$ is also present at $x/D = 2$. As noted in section 3.7.1.2, this is due to the crossflow fluid

which is drawn towards the floor by the beginning of vortex formation farther upstream. Farther downstream the overall η_f is lower than at the other velocity ratios as the jet has penetrated into the crossflow to a greater extent. However, the lower concentration along the floor at $x/D = 8$ is contained in the thin layer shown in Fig. 3.38.

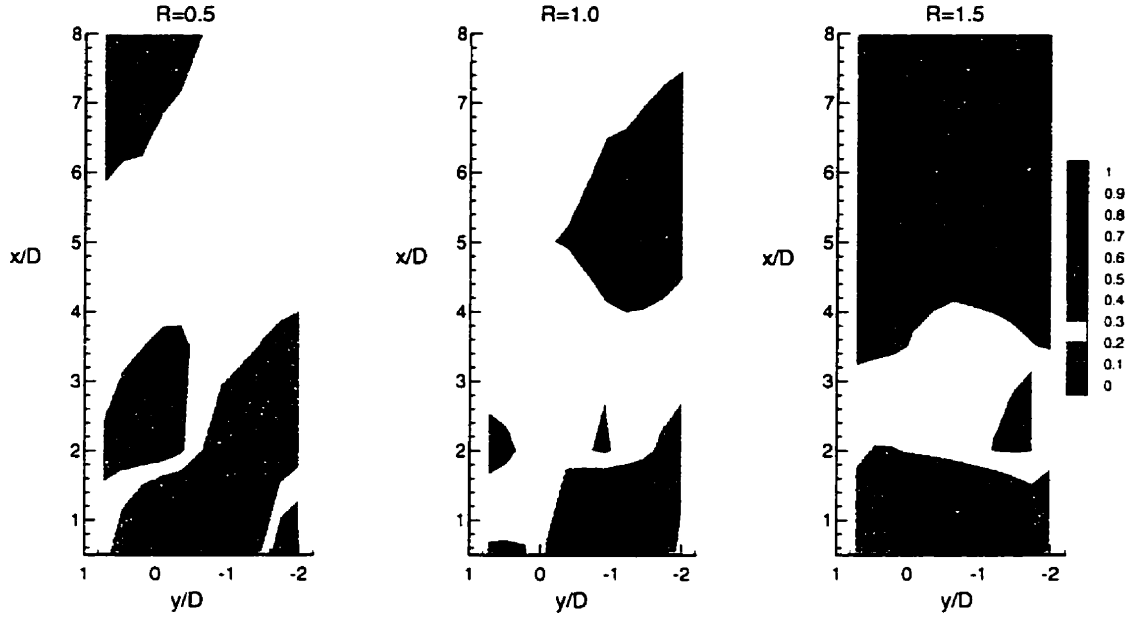

Figure 3.40: Contours of η_f along $z/D = 0$ for the spanwise jet case.

For the compound-angle geometry the contours of η_f are shown in Fig. 3.41. The deflection of the jet in the downstream direction is apparent at all three velocity ratios. At $R = 0.5$ the region of $\eta_f > 0.5$ extends downstream to $x/D = 5$, comparable to the streamwise $L/D = 4$ jets. The region between adjacent jets where no film coverage is present is clear as the jets do not appear to merge along the floor by $x/D = 8$. As the velocity ratio is increased the region between adjacent jets becomes wider as the jets penetrate farther into the crossflow. At $R = 1.0$, as was the case for the streamwise jets, a small region of higher η_f is present at $x/D = 5$.

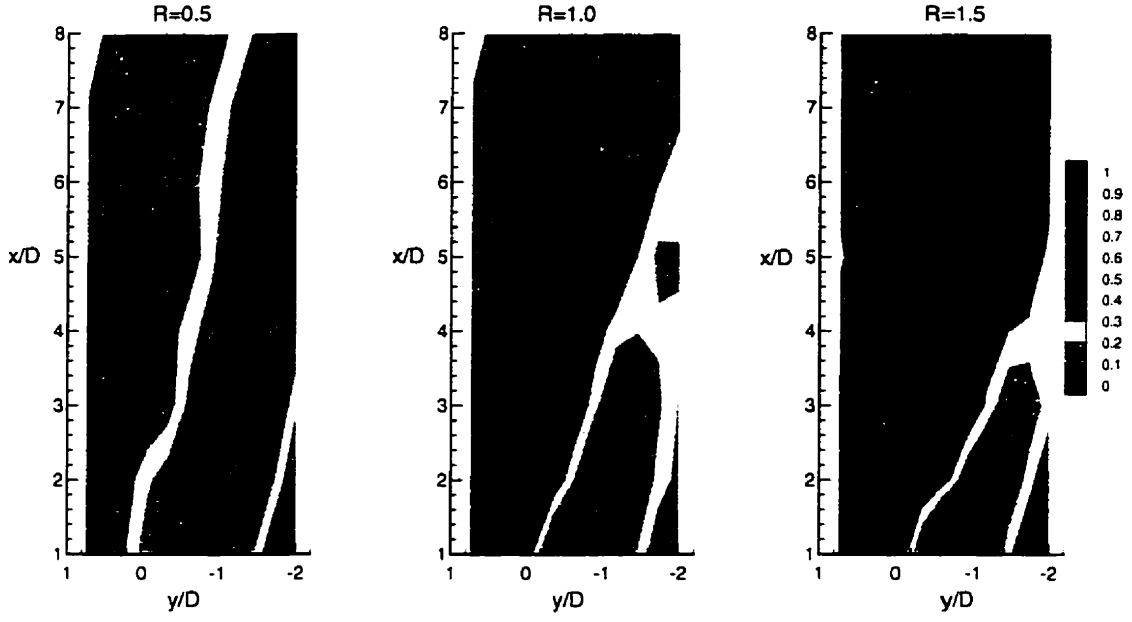

Figure 3.41: Contours of η_f along $z/D = 0$ for the compound-angle jet case.

Often the film cooling effectiveness is reported as a spanwise average along the floor. Plots of $\overline{\eta_f}$ at the various velocity ratios are shown in Fig. 3.42 as a function of downstream position. At $R = 0.5$, $\overline{\eta_f}$ is comparable for all three geometries with the compound-angle case decaying less quickly than the other two cases. Recall that at this low blowing ratio none of the jet cases appeared to penetrate beyond the boundary layer. As the velocity ratio increases the value of $\overline{\eta_f}$ for the streamwise jets drops rapidly as the flow moves downstream due to the large area of the floor which is exposed to the crossflow, as seen in Fig. 3.39. For the compound-angle jets the overall shape of the curve doesn't change as R increases but there is a downward shift in the values of $\overline{\eta_f}$ at most downstream locations. This trend seems reasonable considering the contour plots in Fig. 3.41 which exhibit the same behaviour at each velocity ratio. The trend in the $\overline{\eta_f}$ curves for the spanwise-inclined jets differs from that observed for the other jets in that

there is no significant decrease in $\overline{\eta_f}$ as R increases.

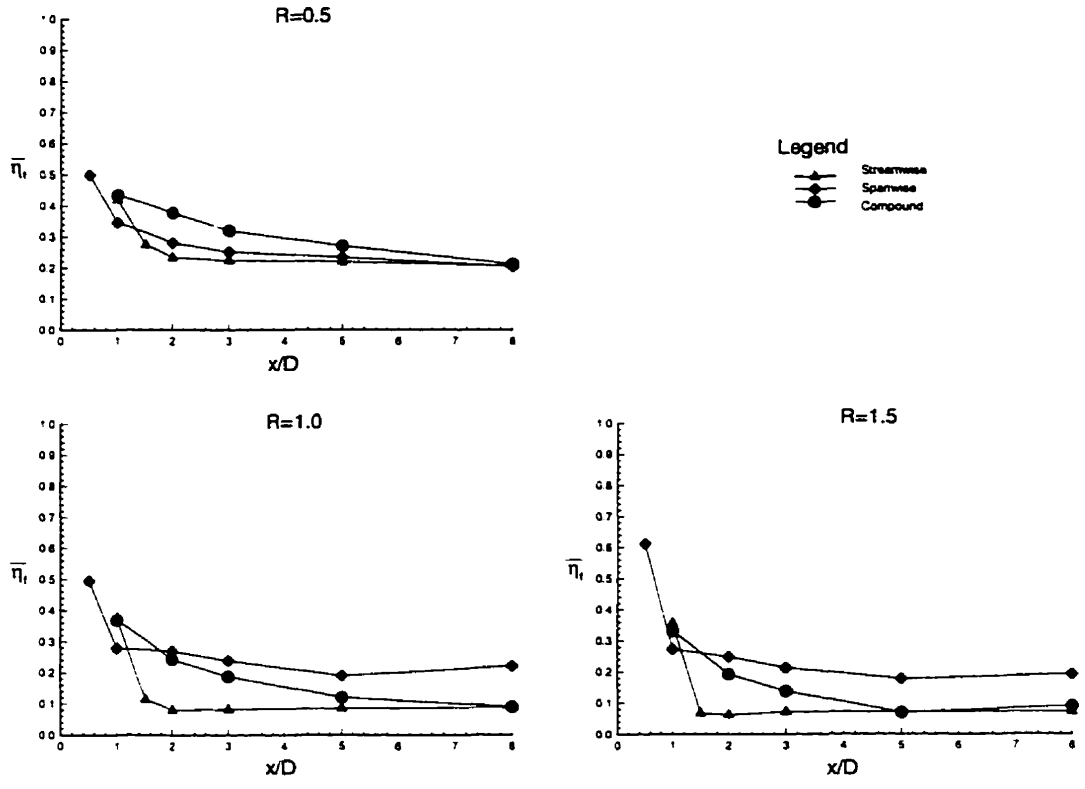

Figure 3.42: Spanwise-averaged FCE ($\overline{\eta_f}$) vs. downstream distance

Although η_f measurements were not made for the streamwise $L/D = 8$ jets the behaviour observed in sections 3.5 and 3.6 may be used to comment on this geometry. Recall that the longer entry length jets appeared to spread laterally more quickly than the $L/D = 4$ streamwise jets at higher R-values. This would suggest that the $\overline{\eta_f}$ values would be higher for the $L/D = 8$ case. However, particularly in gas turbine film cooling applications, long entry lengths are not possible. In addition, the quicker spreading rate may be indicative of more rapid mixing between the jet and crossflow, reducing the cooling effectiveness.

3.7.3 Other Measures of Jet Penetration

Comparisons between the jet penetration measured with the FID system and that inferred from the mean velocity and turbulence profiles are shown in Fig. 3.43 to 3.46 along the $y/D = 0$ plane for the various velocity ratios and geometries. The velocity or turbulence axis scale is indicated along the bottom of each graph and the jet concentration, C/C_j, is indicated along the top. The FID data are indicated with hollow symbols.

The comparisons between streamwise velocity, U/V_j, and jet concentration, C/C_j for $R = 1.5$ are shown in Fig. 3.43. For this velocity ratio, where the streamwise component of the jet velocity is greater than the free stream velocity, the streamwise $L/D = 4$ jet penetration is reasonably well predicted by the profile of U/V_j. The strong streamwise component of velocity is not present in the case of the spanwise jet and the analogy between U/V_j and C/C_j is not as clear. Since the jet flow obtains its streamwise momentum from the crossflow it makes sense that the velocity profile would approach the free stream values relatively quickly. Finally, for the compound-angle jet case the jet penetration is well predicted at $x/D = 1$ but by $x/D = 2$ the velocity profile looks like a boundary layer while there is a distinct variation in jet concentration at the same location. Farther downstream at $x/D = 5, 8$ the agreement improves again. At $x/D = 3$ it can be seen that the jet concentration is essentially zero. Comparison with Fig. 3.38 indicates that this location is between the adjacent jets.

The turbulence kinetic energy, $\sqrt{k}/V_j$, is compared with the jet concentration for $R = 1.5$ in Fig. 3.44. The agreement is reasonable for all three jet geometries, with the possible exception of the compound-angle case at $x/D = 3$. In all of these cases the jets penetrate beyond the boundary layer with a resulting increase in the turbulence level above the free stream value.

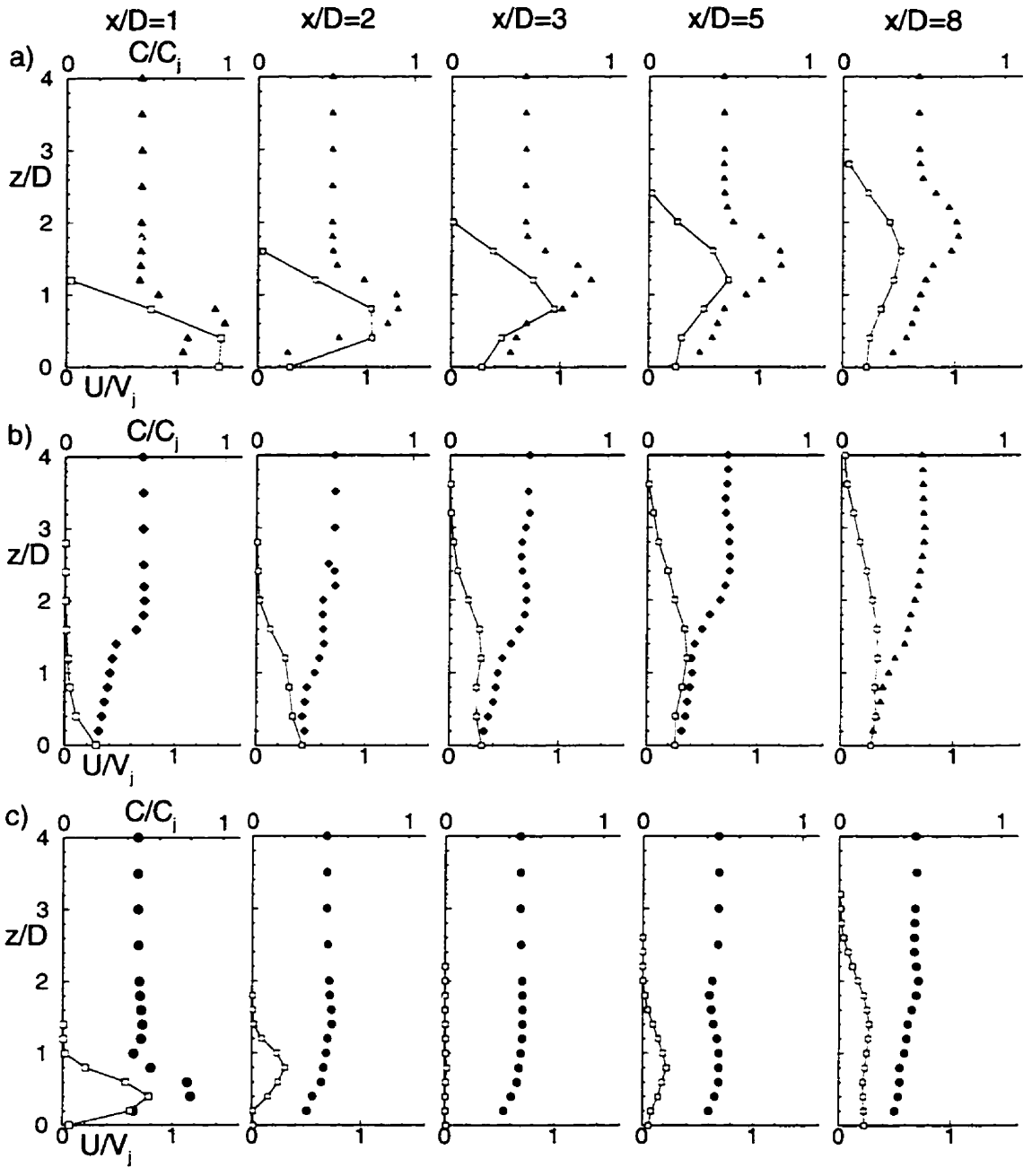

Figure 3.43: Jet penetration comparison with U/V_j for $R = 1.5$ along $y/D = 0$: a) streamwise ($L/D = 4$), b) spanwise, and c) compound-angle jets. (Solid = LDV, Hollow = FID)

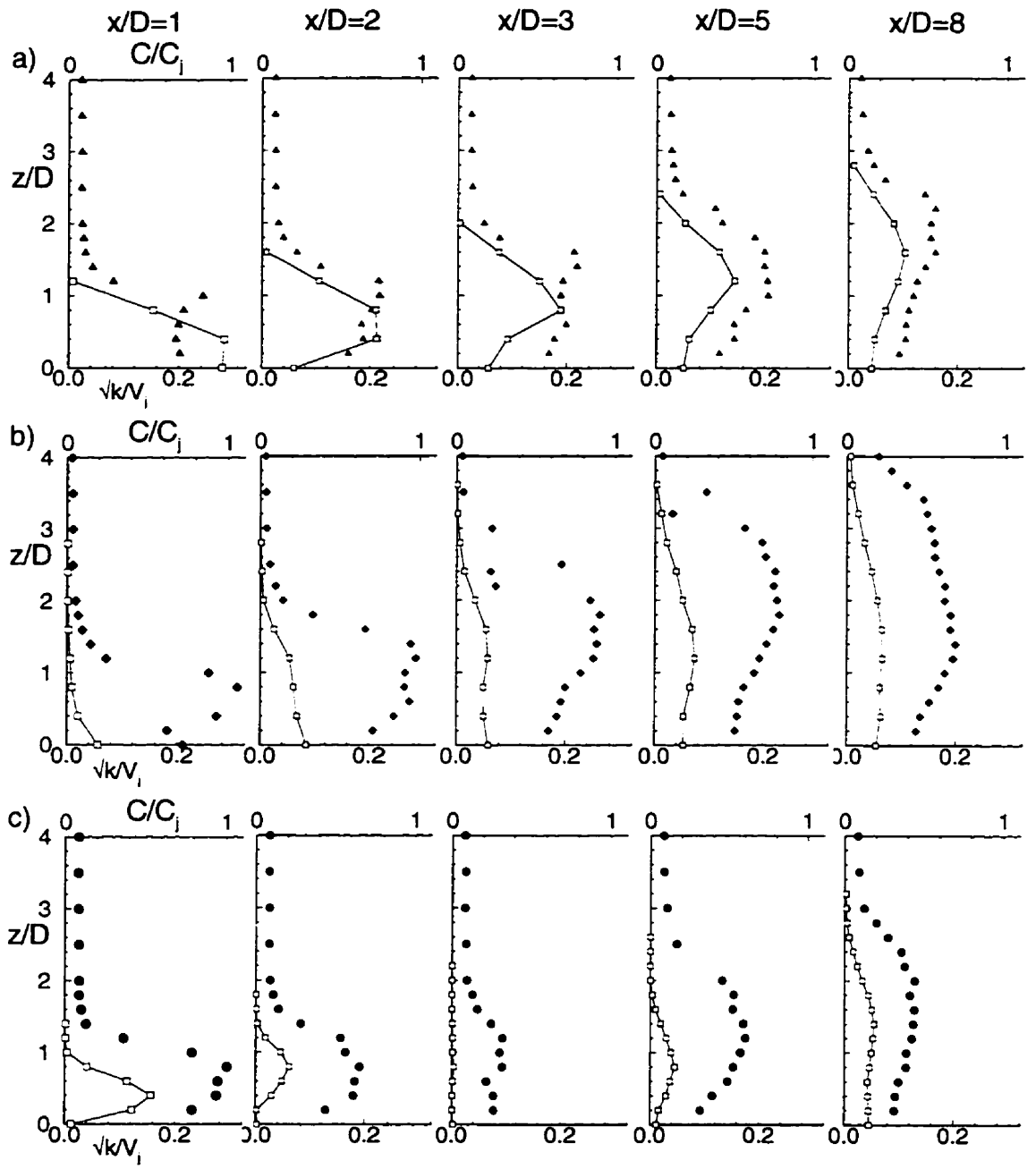

Figure 3.44: Jet penetration comparison with $\sqrt{k}/V_j$ for $R = 1.5$ along $y/D = 0$: a) streamwise ($L/D = 4$), b) spanwise, and c) compound-angle jets. (Solid = LDV, Hollow = FID)

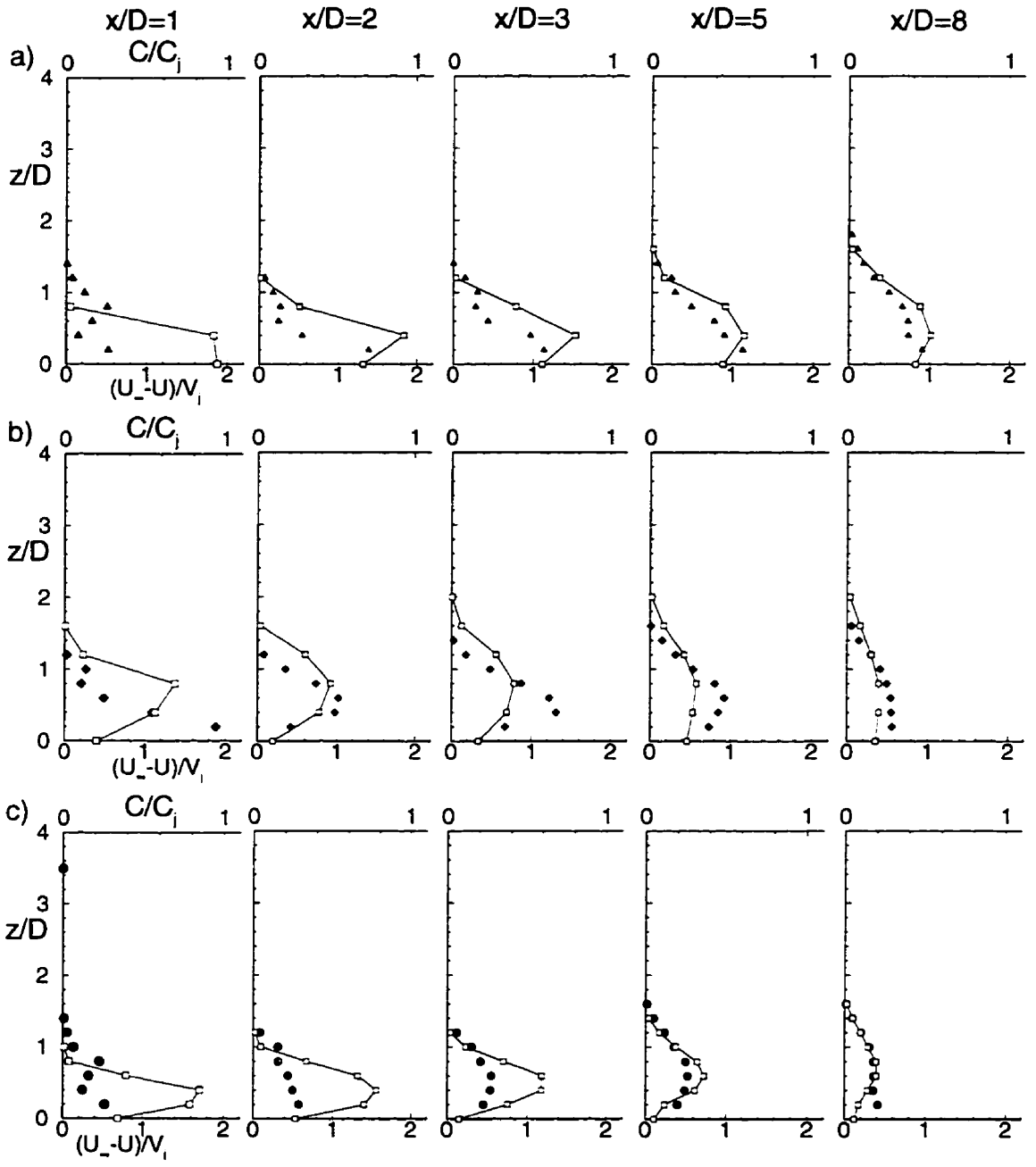

Figure 3.45: Jet penetration comparison with U/V_j for $R = 0.5$ along $y/D = 0$: a) streamwise ($L/D = 4$), b) spanwise, and c) compound-angle jets. (Solid = LDV, Hollow = FID)

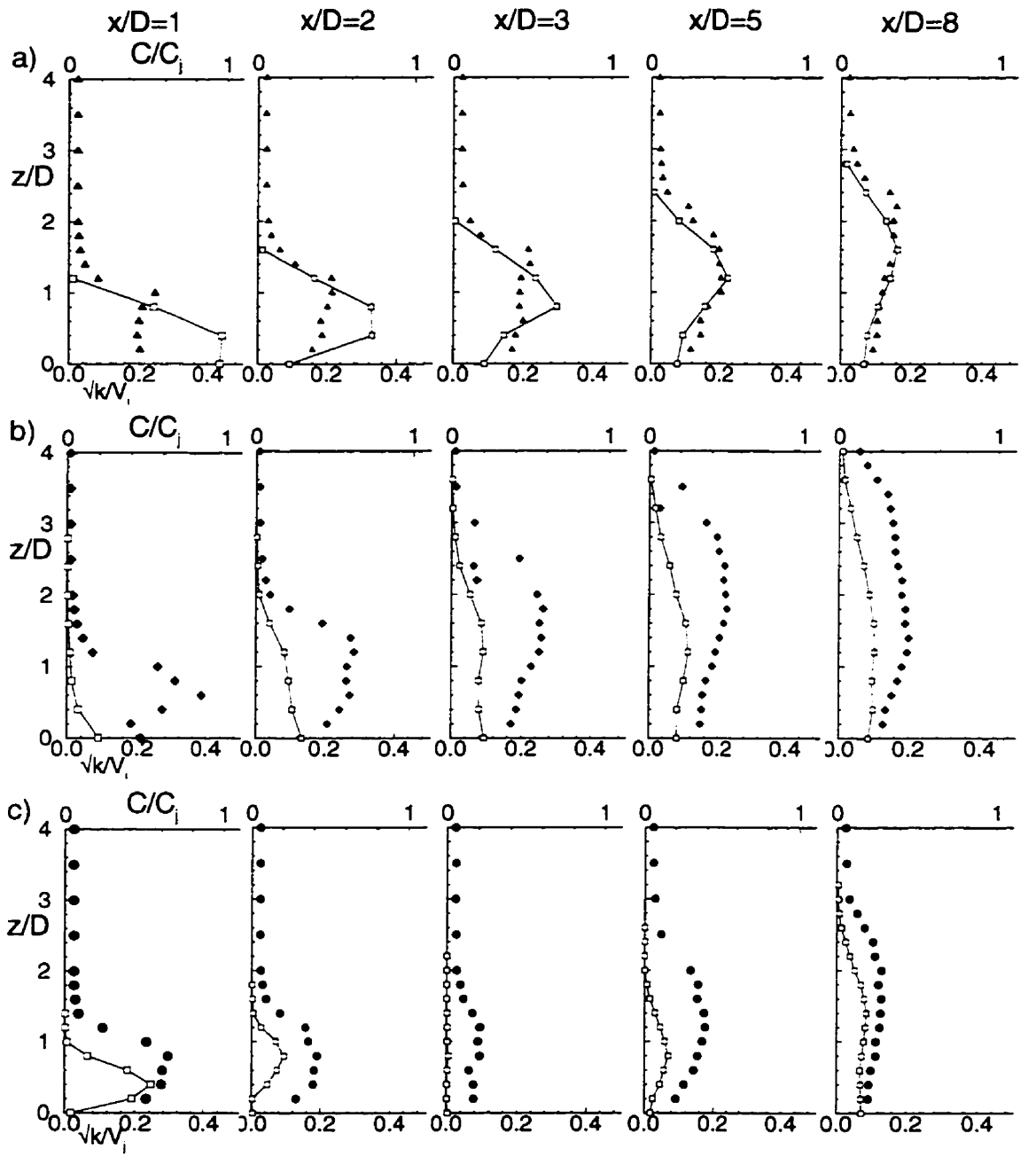

Figure 3.46: Jet penetration comparison with $\sqrt{k}/V_j$ for $R = 0.5$ along $y/D = 0$: a) streamwise ($L/D = 4$), b) spanwise, and c) compound-angle jets. (Solid = LDV, Hollow = FID)

At $R = 0.5$ the velocity deficit, $(U_\infty - U)/V_j$, is compared with C/C_j along $y/D = 0$ in Fig. 3.45. The extent of jet penetration is predicted fairly well in most cases for all three geometries. However, recall that at $R = 0.5$ none of the jets appeared to penetrate beyond the thickness of the upstream boundary layer. Consequently, much of the velocity deficit which is observed could be attributed the boundary layer, rather than the jet flow.

Finally, the comparison of $\sqrt{k}/V_j$ with C/C_j at $R = 0.5$ is shown in Fig. 3.46. The difficulty associated with interpreting the difference between $\sqrt{k}/V_j$ in the freestream and the turbulence within the boundary layer as being caused by the jet flow is clear. In the spanwise case, which penetrates to almost the entire boundary layer thickness by $x/D = 1$, the agreement is good. For the streamwise $L/D = 4$ and compound-angle cases the agreement only improves as the jets actually penetrate farther into the boundary layer. It is difficult, as was the case for the velocity deficit discussed previously, to attribute a particular turbulence level to either the boundary layer or to the jet flow.

From the preceeding discussion it can be seen that the use of the mean velocity or turbulence field as an estimator of jet penetration works best for situations where the jet is stronger than the crossflow. Perhaps at low velocity ratios a comparison between the local velocity or turbulence field with the upstream profiles would be more suitable. In either case, a disturbance from free stream conditions does not imply the presence of fluid from the jet. The compound-angle jet case shown in Fig. 3.38 at $x/D = 3$ is a good case in point. There is clearly a weak vortex centred near $z/D = 2.5$, $y/D = -0.8$ which is above the extent of jet penetration at this location.

3.7.4 Summary

Measurements of jet penetration and spreading indicate that none of the jets penetrate beyond the boundary layer at $R = 0.5$. Spanwise-averaged film cooling effectiveness is

typically better at the lower blowing ratios due to better lateral spreading of the jet fluid along the floor. In the spanwise case the improvement in $\overline{\eta_f}$ as R decreases is less apparent than in the streamwise case due to the increased mixing between the jet and the crossflow produced by the vortex which is formed. Evidence that fluid from the crossflow is trapped between the floor and the jet flow in the spanwise case is found at $R = 1.5$ resulting in a lower η.

While $\overline{\eta_f}$ is typically better for the spanwise and compound-angle jets, as compared with the streamwise jets, the blockage to the crossflow is more significant, which has implications for turbine performance. The choice of an optimum geometry for a particular film cooling situation would have to consider both the aerodynamic losses and the blowing ratio in the region of interest. Near the leading edge of a turbine blade the local R values would be lower than at locations farther downstream. As can be seen from the flat plate data presented here, the compound-angle geometry performs better than the other geometries at $R = 0.5$ in the near-hole region. Farther downstream where R increases, better film coverage may be obtained with spanwise jets.

The comparison of different measures of jet penetration indicates that there is no general way to infer the jet fluid distribution from mean streamwise velocity or turbulence kinetic energy profiles. The streamwise jets show the best agreement between the jet concentration and the other measures of jet penetration and spreading since the jets are injected in the same direction as the crossflow and the comparisons were made along the centre plane of the jet. For the spanwise and compound-angle cases it may make more sense to use the velocities in the plane of the jet centreline which curves as the flow is deflected downstream. However, locating the jet centreline is difficult without measurements of the jet concentration. At best, a sense of the degree to which the crossflow is disturbed by the jets may be obtained with these alternate methods.

Chapter 4

Computational Methods

One of the objectives of this study is the numerical prediction of the flow field and scalar transport from a row of inclined jets in a crossflow. It is intended that the flat-plate experimental data will be used to validate numerical simulations of this class of flows.

In this chapter the governing equations used in the computations are indicated, the turbulence models are discussed, and the near-wall treatment, along with the other boundary conditions, is reviewed. The discretization of these equations in curvilinear coordinates is shown. More details on the computational approach used here for general, curvilinear coordinate systems may be found in He and Salcudean (1994), and He (1995).

4.1 Introduction

Most fluid flow and heat transfer phenomena in engineering can be adequately described by a few, fundamental, physical laws describing the conservation of mass, momentum, and energy. For incompressible flow of a Newtonian fluid with constant properties and neglecting body forces, the equations are as follows:

$$\nabla \cdot \mathbf{U} = 0 \tag{4.1}$$

$$\rho \frac{D\mathbf{U}}{Dt} = -\nabla P + \nabla \cdot (\mu \nabla \mathbf{U}) \tag{4.2}$$

$$\rho c_p \frac{DT}{Dt} = \nabla \cdot (\kappa \nabla T) + \Phi \tag{4.3}$$

where Φ is called the dissipation function as it indicates the energy which is dissipated into heat. For low speed flows, Φ is usually negligible. Details of the derivation of these equations may be found in White (1991). Equations (4.1), (4.2), and (4.3) are assumed to be valid for both laminar and turbulent flows since the smallest scales of turbulence are still large enough so that the fluid can be treated as a continuum.

In theory, turbulent fluid flows can be predicted by numerically solving the governing equations. However, direct numerical simulation of turbulent flows requires that the smallest scales of the turbulence are resolved. This requirement means that the grid size must be on the order of the Kolmogorov scale, $\eta = (\frac{\nu^3}{\epsilon})^{\frac{1}{4}}$ for numerical simulation. As a consequence, only the larger supercomputers available today are capable of performing these computations for simple turbulent flows at low Reynolds numbers. Since most flows of engineering interest exceed the existing computational power, an alternative approach must be used.

Following the approach proposed by Osborne Reynolds, we assume that the instantaneous value of any variable in a turbulent flow can be decomposed into two parts: a mean and a fluctuating component. Then, for a general variable Θ:

$$\Theta = \overline{\Theta} + \theta \tag{4.4}$$

and the time-averaged value, $\overline{\Theta}$, is defined as:

$$\overline{\Theta} = \frac{1}{\Delta t} \int_t^{t+\Delta t} \Theta dt \tag{4.5}$$

where Δt is the averaging time which is larger than the largest time scale of the turbulence. The Reynolds-averaged equations, as they are known, in Cartesian tensor notation are:

$$\frac{\partial U_i}{\partial x_i} = 0 \tag{4.6}$$

$$U_j \frac{\partial U_i}{\partial x_j} = -\frac{1}{\rho}\frac{\partial P}{\partial x_i} + \frac{\partial}{\partial x_j}\left[\nu\left(\frac{\partial U_i}{\partial x_j} + \frac{\partial U_j}{\partial x_i}\right) - \overline{u_i u_j}\right] \tag{4.7}$$

$$\rho U_i \frac{\partial \Phi}{\partial x_i} = \frac{\partial}{\partial x_i}\left(\Gamma \frac{\partial \Phi}{\partial x_i} - \overline{u_i \phi}\right) + S \tag{4.8}$$

where the Einstein summation convention is assumed for the subscripts i and j. Note that the transport equation for a general scalar, Φ, is given in (4.8) rather than the temperature, T, for generality and should not be confused with the dissipation function in Eq. (4.3). In these equations U_i and u_i are the mean and fluctuating velocities respectively, P is the mean static pressure, ν is the kinematic viscosity, Γ is the scalar molecular diffusivity, and S is a source term. This system of equations contains unknown variables: the Reynolds stresses, $\overline{u_i u_j}$, and the turbulent scalar flux, $\overline{u_i \phi}$. In order to obtain a closed set of equations some assumptions must be made to relate the Reynolds stresses and the turbulent scalar flux to other existing variables through the process of turbulence modelling.

4.2 Turbulence Modelling

In basic terms the principle in turbulence modelling is to represent the unknown Reynolds stresses and turbulent scalar flux in terms of known parameters. There are two main

categories of modelling approaches. The first, known as turbulent-viscosity modelling, is based on the suggestion of Boussinesq (1877) that the Reynolds stresses are proportional to the mean strain rates. The approach is based on an analogy to the viscous stresses in laminar flows. The turbulent eddies were thought of as lumps of fluid which, like molecules, collide and exchange momentum. The second category, known as turbulent stress modelling, is based on the development of differential equations describing the transport of individual stresses (Launder and Spalding (1972)). Only the first class of models will be discussed here.

4.2.1 Eddy Viscosity and Diffusivity

The turbulent, or eddy viscosity is defined by the following equation:

$$\overline{u_i u_j} = \frac{2}{3} k \delta_{ij} - \nu_t \left(\frac{\partial U_i}{\partial x_j} + \frac{\partial U_j}{\partial x_i} \right) \tag{4.9}$$

where ν_t is the turbulent eddy viscosity, $k(= \frac{1}{2}\overline{u_i u_i})$ is the turbulent kinetic energy, and δ_{ij} is the Kronecker delta. In contrast to the molecular viscosity ν, the eddy viscosity is not a fluid property but depends strongly on the state of the turbulence and may vary significantly from point to point within a flow. Equation (4.9) only provides the framework for building a turbulence model and is not a model in itself. The distribution of ν_t must be determined for the flow.

By analogy to the turbulent momentum transport, the turbulent scalar transport is often assumed to be related to the gradients of the transported quantity:

$$\overline{u_i \phi} = -\Gamma_t \frac{\partial \Phi}{\partial x_i} \tag{4.10}$$

where Γ_t is the turbulent diffusivity of the scalar quantity. Again, Γ_t is not a property of

the fluid but rather a property of the flow. The Reynolds analogy between heat or mass transport and momentum transport suggests that Γ_t is closely related to ν_t as follows:

$$\Gamma_t = \frac{\nu_t}{\sigma_t} \tag{4.11}$$

The new term, σ_t is the turbulent Prandtl or Schmidt number (for heat or mass transport respectively). Experiments have shown that σ_t does not vary significantly across most flows, as well as from flow to flow (Rodi (1984)). As such, many models make use of Eq. (4.11) with σ_t as a constant.

The analogy between molecular motion and turbulent motion gives the general form of the eddy viscosity relationship. Since the molecular viscosity is proportional to the average velocity and mean free path of the molecules, the eddy viscosity is assumed proportional to a velocity characterizing the fluctuating turbulent motion and a typical length scale of this motion. If the turbulent velocity fluctuations are to be characterized by only one velocity scale, the most natural scale is $\sqrt{k}$ where k is the turbulence kinetic energy. Since most of the energy is contained in the large scales, $\sqrt{k}$ is a velocity scale for the large-scale turbulent motion. Noting the proportionality between the eddy viscosity and turbulent velocity and length scales mentioned above, the eddy viscosity relation becomes:

$$\nu_t = c'_\mu \sqrt{k} L \tag{4.12}$$

where c'_μ is an empirical constant and L is the turbulence length scale. Equation (4.12) is known as the Kolmogorov-Prandtl expression. Kolmogorov and Prandtl suggested that the distribution of k could be determined by solving a transport equation for k which can be derived from the Navier-Stokes equations. The result for high Reynolds numbers

is (neglecting buoyancy):

$$\frac{Dk}{Dt} = -\frac{\partial}{\partial x_i}\left[\overline{u_i\left(\frac{u_j u_j}{2} + \frac{p}{\rho}\right)}\right] - \overline{u_i u_j}\frac{\partial U_i}{\partial x_j} - \nu\overline{\frac{\partial u_i}{\partial x_j}\frac{\partial u_j}{\partial x_i}} \tag{4.13}$$

The exact equation is not used because new, unknown correlations are present in the formulation. The first term on the right-hand side is the diffusion of k. By analogy to the scalar diffusion of Φ in Eq. (4.11), the diffusion flux of k is modelled as follows:

$$-\overline{u_i\left(\frac{u_j u_j}{2} + \frac{p}{\rho}\right)} = \frac{\nu_t}{\sigma_k}\frac{\partial k}{\partial x_i} \tag{4.14}$$

where σ_k is an empirical diffusion constant. The second term on the right-hand side of Eq. (4.13) is the production of k by shear and is modelled using the eddy viscosity expression in Eq. (4.9). The final term is the viscous dissipation of k and is modelled by the expression:

$$\epsilon = c_D\frac{k^{3/2}}{L} \tag{4.15}$$

from dimensional analysis, where c_D is another empirical constant. The modelled k-equation then becomes:

$$\frac{Dk}{Dt} = \frac{\partial}{\partial x_i}\left[\left(\nu + \frac{\nu_t}{\sigma_k}\right)\frac{\partial k}{\partial x_i}\right] + \nu_t\left(\frac{\partial U_i}{\partial x_j} + \frac{\partial U_j}{\partial x_i}\right)\frac{\partial U_i}{\partial x_j} - c_D\frac{k^{3/2}}{L} \tag{4.16}$$

For high turbulence Reynolds number flows ($Re_t = k^2/\nu\epsilon > 100$), $\nu_t \gg \nu$, so ν is often dropped from the expression.

Although there are shortcomings in the underlying assumptions of the eddy viscosity concept the approach has been widely used since the velocity and length scales of the turbulent motion may be approximated reasonably well in many flows (typically

two-dimensional, thin shear layers). As can be seen from the preceeding discussion, the velocity scale is determined from the turbulence kinetic energy. The length scale L which characterizes the size of the large, energy-containing eddies is subject to transport processes in a similar manner to the energy k. Difficulties in finding widely-valid formulations for calculating or prescribing L stimulated the use of a transport equation for L. A length scale equation does not necessarily require the length scale itself as the dependent variable. Any combination of the form $Z = k^m L^n$ will work since k is known from solving the k-equation (Rodi (1984)). In the following sections, two different forms of the length scale equation are shown which are used in the numerical simulations.

4.2.2 The k-ϵ Model

The length scale equation used for this well-known turbulence model is based on the dissipation rate of turbulence kinetic energy, $\epsilon(\propto k^{3/2}/L)$. Combining Eq. (4.12) and (4.15) the eddy viscosity is expressed as:

$$\nu_t = C_\mu \frac{k^2}{\epsilon} \tag{4.17}$$

where $C_\mu(= c'_\mu c_D)$ is an empirical constant. An exact transport equation for ϵ may be derived but, as with the exact transport equation for k, there are terms which must be modelled. At high Reynolds numbers, where local isotropy of the turbulence is present, the two equations which form the $k-\epsilon$ turbulence model are:

$$\frac{Dk}{Dt} = \frac{\partial}{\partial x_i}\left[\left(\nu + \frac{\nu_t}{\sigma_k}\right)\frac{\partial k}{\partial x_i}\right] + G - \epsilon \tag{4.18}$$

for k, and:

$$\frac{D\epsilon}{Dt} = \frac{\partial}{\partial x_i}\left[\left(\nu + \frac{\nu_t}{\sigma_\epsilon}\right)\frac{\partial k}{\partial x_i}\right] + C_1\frac{\epsilon}{k}G - C_2\frac{\epsilon^2}{k} \tag{4.19}$$

for ϵ, where G is the generation rate of k given by:

$$G = -\overline{u_i u_j}\frac{\partial U_i}{\partial x_j} = \nu_t\left(\frac{\partial U_i}{\partial x_j} + \frac{\partial U_j}{\partial x_i}\right)\frac{\partial U_i}{\partial x_j} \tag{4.20}$$

and σ_k, σ_ϵ, C_1, and C_2 are constants. The usual values of the constants are given in Table 4.3 and were determined based on the experimental observations of grid-generated turbulence and near-wall turbulent flows. (Launder and Spalding (1974)).

C_μ	C_1	C_2	σ_k	σ_ϵ
0.09	1.44	1.92	1.0	1.3

Table 4.3: The $k-\epsilon$ turbulence model constants.

Solutions of the two transport equations for k and ϵ completely define the turbulence parameters which can subsequently be used to close the Reynolds-averaged Navier-Stokes equations. Note that in the derivation of the $k-\epsilon$ equations it was assumed that the turbulence Reynolds number was high ($Re_t = k^2/\nu\epsilon > 100$). In regions near solid walls where viscous effects are important this high Reynolds number assumption is no longer valid and other methods must be used. These methods are discussed in section 4.2.5.

4.2.3 The Baseline (BSL) Model

As noted previously, the turbulence length scale equation can take many different forms. The use of the turbulence frequency or specific dissipation rate ω ($\propto k^{1/2}/L$) proposed

by Kolmogorov and later advocated by Wilcox (1988) provides essentially the same information for the eddy viscosity as the $k-\epsilon$ model. In this case, the eddy viscosity is determined from:

$$\nu_t = \frac{\mu_t}{\rho} = \frac{k}{\omega} \tag{4.21}$$

The original $k-\omega$ model proposed by Wilcox (1988) is as follows for incompressible flow:

$$\frac{D\rho k}{Dt} = \tau_{ij}\frac{\partial U_i}{\partial x_j} - \beta^*\rho\omega k + \frac{\partial}{\partial x_j}\left[(\mu + \sigma_{k1}\mu_t)\frac{\partial k}{\partial x_j}\right] \tag{4.22}$$

for k where β^* and σ_{k1} are empirical constants. The transport equation for ω is given by:

$$\frac{D\rho\omega}{Dt} = \frac{\gamma_1}{\nu_t}\tau_{ij}\frac{\partial U_i}{\partial x_j} - \beta_1\rho\omega^2 + \frac{\partial}{\partial x_j}\left[(\mu + \sigma_{\omega 1}\mu_t)\frac{\partial \omega}{\partial x_j}\right] \tag{4.23}$$

where γ_1, β_1, and $\sigma_{\omega 1}$ are empirical constants. The Reynolds stresses are modelled using the eddy viscosity concept with a slightly modified form:

$$\tau_{ij} = -\rho\overline{u_i u_j} = \mu_t\left(\frac{\partial U_i}{\partial x_j} + \frac{\partial U_j}{\partial x_i} - \frac{2}{3}\frac{\partial U_k}{\partial x_k}\delta_{ij}\right) - \frac{2}{3}k\delta_{ij} \tag{4.24}$$

The advantage of the Wilcox $k-\omega$ model is that no special treatment is required in the near-wall region as is the case for the standard $k-\epsilon$ model. However, it has been found that the $k-\omega$ model has a very strong sensitivity to the freestream values, ω_∞, specified for ω outside the boundary layer (Menter (1992)). The idea behind Menter's baseline (BSL) model (Menter (1994)) is to retain the good performance of the Wilcox $k-\omega$ model in the near-wall region and take advantage of the freestream independence of the $k-\epsilon$ model in the outer part of the boundary layer. Towards this end, the $k-\epsilon$

model is transformed into a $k-\omega$ formulation as follows:

$$\frac{D\rho k}{Dt} = \tau_{ij}\frac{\partial U_i}{\partial x_j} - \beta^*\rho\omega k + \frac{\partial}{\partial x_j}\left[(\mu + \sigma_{k2}\mu_t)\frac{\partial k}{\partial x_j}\right] \tag{4.25}$$

for k where β^* and σ_{k2} are empirical constants. The transformed ϵ equation is given by:

$$\frac{D\rho\omega}{Dt} = \frac{\gamma_2}{\nu_t}\tau ij\frac{\partial U_i}{\partial x_j} - \beta_2\rho\omega^2 + \frac{\partial}{\partial x_j}\left[(\mu + \sigma_{\omega 2}\mu_t)\frac{\partial \omega}{\partial x_j}\right] + 2\rho\sigma_{\omega 2}\frac{1}{\omega}\frac{\partial k}{\partial x_j}\frac{\partial \omega}{\partial x_j} \tag{4.26}$$

where γ_2, β_2, and $\sigma_{\omega 2}$ are empirical constants. It can be seen that an additional cross-diffusion term appears in the ω equation and that the modelling constants are different. A small additional diffusion term was also neglected in the transformation as it was found to have virtually no effect on the solutions (Menter (1992)). The original model is then multiplied by a function F_1 and the transformed model by a function $(1-F_1)$ and both are added together. The result is as follows:

$$\frac{Dk}{Dt} = \overline{u_i u_j}\frac{\partial U_i}{\partial x_j} - \beta^*\omega k + \frac{\partial}{\partial x_j}\left[(\nu + \sigma_k\nu_t)\frac{\partial k}{\partial x_j}\right] \tag{4.27}$$

$$\frac{D\rho\omega}{Dt} = \frac{\gamma}{\nu_t}\tau_{ij}\frac{\partial U_i}{\partial x_j} - \beta\rho\omega^2 + \frac{\partial}{\partial x_j}\left[(\mu + \sigma_\omega\mu_t)\frac{\partial \omega}{\partial x_j}\right] + 2\rho(1-F_1)\sigma_{\omega 2}\frac{1}{\omega}\frac{\partial k}{\partial x_j}\frac{\partial \omega}{\partial x_j} \tag{4.28}$$

The constants in the BSL model are determined in the same manner as the equations. If ϕ_1 is a constant in the original model ($\sigma_{k1},\dots$), ϕ_2 is a constant in the transformed $k-\epsilon$ model ($\sigma_{k2},\dots$), and ϕ is the corresponding constant in the BSL model ($\sigma_k,\dots$),

then the relation between them is:

$$\phi = F_1\phi_1 + (1 - F_1)\phi_2 \tag{4.29}$$

The values of the constants are given in Table 4.4. The blending function is given by:

$$F_1 = \tanh(\arg_1^4) \tag{4.30}$$

$$\arg_1 = \min\left[\max\left(\frac{\sqrt{k}}{0.09\omega y}; \frac{500\nu}{y^2\omega}\right); \frac{4\rho\sigma_{\omega 2}k}{CD_{k\omega}y^2}\right] \tag{4.31}$$

where y is the distance to the nearest surface and $CD_{k\omega}$ is the positive portion of the cross-diffusion term of Eq. (4.28):

$$CD_{k\omega} = \max\left(2\rho\sigma_{\omega 2}\frac{1}{\omega}\frac{\partial k}{\partial x_j}\frac{\partial \omega}{\partial x_j}, 10^{-20}\right) \tag{4.32}$$

In the present code, the BSL model was implemented as a two-layer $k-\epsilon$ model (Rodi (1991)) with the original $k-\omega$ model in the sublayer and the $k-\epsilon$ model in the high Reynolds number region. This is achieved by changing the argument of F_1 for the BSL model from Eq. (4.31) to:

$$\arg_1 = \min\left(\frac{500\nu}{y^2\omega}; \frac{4\rho\sigma_{\omega 2}k}{CD_{k\omega}y^2}\right) \tag{4.33}$$

This modification ensures that F_1 is zero for $y^+ > 70$.

	σ_k	σ_ω	β	β^*	κ	γ
ϕ_1 $(k-\omega)$	0.5	0.5	0.0750	0.09	0.41	$\frac{\beta_1}{\beta^*} - \frac{\sigma_{\omega 1}\kappa^2}{\sqrt{\beta^*}}$
ϕ_2 $(k-\epsilon)$	1.0	0.586	0.0828	0.09	0.41	$\frac{\beta_2}{\beta^*} - \frac{\sigma_{\omega 2}\kappa^2}{\sqrt{\beta^*}}$

Table 4.4: The BSL turbulence model constants.

4.2.4 The Shear Stress Transport (SST) Model

The SST model of Menter (1994) is also based on blending the $k-\omega$ model near walls with the standard $k-\epsilon$ model away from the surface. However, rather than just using the $k-\omega$ model in the sublayer, the SST model takes advantage of the superior performance of the $k-\omega$ model in the logarithmic layer (Menter (1996)). The blending to the $k-\epsilon$ model takes place in the wake portion of the boundary layer. In addition, the definition of the eddy viscosity is modified in order to account for the effect of the transport of the principal turbulent shear stress in adverse pressure gradient boundary layers. Equations (4.27) and (4.28) are used for the SST model with the blending function F_1 defined as in Eq. (4.30) and (4.31).The ϕ_1 constants are changed to those shown in Table 4.5. The eddy viscosity is redefined in the following way:

$$\nu_t = \frac{a_1 k}{\max(a_1\omega; \Omega F_2)} \tag{4.34}$$

where a_1 is Bradshaw's constant ($= 0.31$), Ω is the absolute value of the vorticity, and F_2 is a blending function that is equal to one for boundary layer flows and zero for free shear layers:

$$F_2 = \tanh(\arg_2^2) \tag{4.35}$$

$$\arg_2 = \max\left(2\frac{\sqrt{k}}{0.09\omega y}; \frac{500\nu}{y^2\omega}\right) \tag{4.36}$$

	σ_k	σ_ω	β	β^*	κ	γ	a_1
ϕ_1 $(k-\omega)$	0.85	0.5	0.0750	0.09	0.41	$\frac{\beta_1}{\beta^*} - \frac{\sigma_{\omega 1}\kappa^2}{\sqrt{\beta^*}}$	0.31

Table 4.5: The SST turbulence model constants.

4.2.5 Near-Wall Treatment

The standard $k-\epsilon$ turbulence model described in section 4.2.2 cannot model the viscous effects which are important in the vicinity of solid boundaries. Close to a solid wall the local turbulence Reynolds number becomes small and the viscous effects dominate over the turbulent effects. Two methods may be used in these near-wall regions in order to model the effect the wall has on the main flow: the wall function method and low-Reynolds-number modelling. In the present work, only wall functions were used with the $k-\epsilon$ model and will be discussed in the following paragraphs.

The standard wall function (Launder and Spalding (1974)) provides the boundary conditions for a solid wall, such as the wall shear stress, τ_w, the turbulence kinetic energy, and the dissipation rate, by placing the first computational grid point at a location sufficiently remote from the wall (say, $y^+ = 30 \rightarrow 300$ (y^+ is defined below in Eq. (4.37))) where the flow is fully turbulent. It is assumed that the flow in the vicinity of the wall behaves locally as a one-dimensional Couette flow and similar conditions to those of an equilibrium turbulent boundary layer flow prevail. The distance from the wall is non-dimensionalized as:

$$y^+ \equiv \frac{u_\tau y_p}{\nu} \tag{4.37}$$

where y_p is the normal distance from the wall to the point 'p' and u_τ is known as the friction velocity which is defined as:

$$u_\tau \equiv \sqrt{\frac{\tau_w}{\rho}} \tag{4.38}$$

The velocity tangential to the wall at this point, U_p, is expressed as:

$$\frac{U_p}{u_\tau} = \frac{1}{\kappa}\ln(Ey^+) \qquad \text{for} \quad y^+ > 11.36 \tag{4.39}$$

where κ is the von Karman constant ($\kappa = 0.41$) and E is another empirical constant which is taken as 9.97 for a smooth wall. The wall shear stress may found iteratively from:

$$\tau_w = \rho\kappa C_\mu^{1/4} k^{1/2} \frac{U_p}{\ln(Ey^+)} \tag{4.40}$$

The boundary conditions used for the kinetic energy and dissipation equations are:

$$k_p = \frac{u_\tau^2}{\sqrt{C_\mu}} \tag{4.41}$$

$$\epsilon_p = \frac{u_\tau^2}{\sqrt{\kappa y_p}} \tag{4.42}$$

Detailed descriptions may be found in Launder and Spalding (1974) and He *et al.* (1997).

It is recognized that the use of wall functions as the near-wall treatment may be inadequate in some regions of the flow investigated here. Previous work on perpendicular square jets (Zhou (1994)) has indicated that better predictions of the complicated, three-dimensional flow field are obtained with more refined near-wall treatments. However,

the computations for inclined jets on curvilinear grids presented here are a preliminary study to identify the aspects of the flow which are of primary importance for numerical simulation. As such, the additional complexity of other near-wall treatments was avoided at this stage. The BSL model allows for the use of the $k-\epsilon$ model away from the wall with a more refined treatment of the near-wall flow from the $k-\omega$ model.

In the case of the blended two-equation turbulence models the approach is similar but the wall shear stress is calculated from:

$$\tau_w = \mu \frac{U_p}{y_p} \tag{4.43}$$

provided that $y^+ \leq 3$ for the nearest node to the wall. The boundary conditions for ω and k at a solid surface are (Menter (1994)):

$$\omega = 10\frac{6\nu}{\beta_1 y_p^2} \qquad \text{and} \qquad k = 0 \tag{4.44}$$

4.3 Solution in Curvilinear Coordinates

In order to obtain a numerical solution to the governing equations presented in the previous sections, the equations are discretized using the finite volume method. The resulting system of algebraic equations is then solved iteratively. In the following sections the solution method on curvilinear grids is presented. More details on the computational approach used here for general, curvilinear coordinate systems may be found in He and Salcudean (1994), and He (1995). These methods have been implemented in a curvilinear, multigrid, finite volume code called CMGFD.

4.3.1 Geometric Quantities for Curvilinear Finite Volumes

In the CMGFD code, the physical geometric quantities for each control volume are used to formulate the numerical scheme, and are shown in Fig. 4.1. A uniform grid with mesh size $\Delta\xi_i = 1$ is assumed in the transformed computational domain. The unit tangent vectors, $\mathbf{e}_i(i = 1, 2, 3)$, are calculated at the centre of the corresponding control volume surface and are locally parallel to the coordinate lines ξ_i. The surface area vectors, $\mathbf{S}^i(i = 1, 2, 3)$, are defined at the same point as $\mathbf{e}_i$ and are normal to the surface of the control volume. The magnitude of $\mathbf{S}^i(|\ \mathbf{S}^i\ |)$ is equal to the corresponding surface area. The volume of the cell is denoted as V.

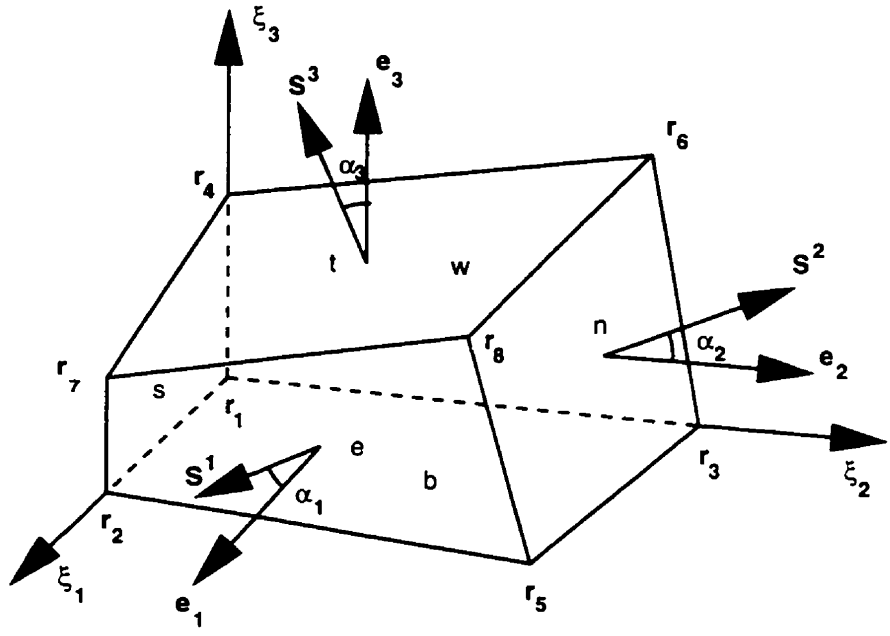

Figure 4.1: Physical geometric quantities for a control cell.

The basic grid quantities $\mathbf{e}_i$, $\mathbf{S}^i$, and V are calculated directly using the discrete grid points. For convenience, two additional quantities are defined. The first is the angle

between the surface area vector $\mathbf{S^i}$ and the tangential vector $\mathbf{e}_i$, which is denoted α_i. This angle is a measure of the non-orthogonality of the grid and is zero for orthogonal grids. The second quantity is a rescaled surface area vector defined as $\mathbf{e^i} = \frac{\mathbf{S^i}}{|\mathbf{S^i}|\cos\alpha_i}$. More details on the calculation of these quantities may be found in He and Salcudean (1994).

4.3.2 Discretization

The transport of a general quantity ϕ is broken into orthogonal and non-orthogonal components. The orthogonal component of the flux has the same form as for a Cartesian co-ordinate system and methods such as the hybrid scheme or the power-law scheme (Patankar (1980)) for regular geometries can be applied to these terms. A second-order-accurate scheme was developed for the non-orthogonal terms. Again, more details may be found in He and Salcudean (1994).

4.3.3 Calculation of the Flow Field

Different sets of velocity unknowns may be chosen for the solution in curvilinear co-ordinates and a review of the various possibilites is given by Rodi *et al.* (1989). In the CMGFD code the physical tangential velocity components are used as the dependent variables and are denoted as U^{ξ_i}. These variables are the coefficients resulting from the velocity expansion in the unit tangent basis vectors, $\mathbf{e}_i$:

$$\mathbf{U} = U^{\xi_1}\mathbf{e_1} + U^{\xi_2}\mathbf{e_2} + U^{\xi_3}\mathbf{e_3} \tag{4.45}$$

The tangential velocity components are uniquely determined by Eq. (4.45) and have the following expressions:

$$U^{\xi_i} = \frac{\mathbf{S^i}\cdot\mathbf{U}}{|\,\mathbf{S^i}\,|\cos\alpha_i} = \mathbf{e^i}\cdot\mathbf{U} \tag{4.46}$$

It can be seen that the physical tangential velocity components are the volume flow rates normalized by the appropriate geometric quantities.

A staggered grid arrangement is adopted in which the pressure is located at the geometric centre of the control volume and the tangential velocity components U^{ξ_i} lie at the midpoints of the respective control volume surfaces. The use of the tangential velocity components as dependent variables gives rise to additional curvature terms in the momentum equations. These curvature terms are not discretized directly since they involve second-order derivatives of the grid co-ordinates which are difficult to discretize accurately when the grids are not smooth. An algebraic manipulation of the discretizations for the Cartesian velocity components is used which avoids the direct disctretization of the curvature terms. A coupled equation solver is used in place of the complicated pressure correction equation associated with the grid non-orthogonality.

4.4 Computational Domain

The computational domain consists of two main blocks or segments. The first block is the jet hole and the second is the main flow region. The extent of the domain and the grids used for each numerical simulation are described in the following paragraphs.

Due to the symmetry condition along the planes down the centreline of the jet and between adjacent jets, the computational domain for the streamwise inclined jet case included only half of the jet. The half-jet block consisted of $16 \times 4 \times 16$ nodes in the x-, y-, and z-directions respectively. The main flow region was composed of $60 \times 12 \times 40$ nodes and extended from $x/D = -5$ upstream to $x/D = 45$ in the streamwise direction and from $z/D = 0$ to $z/D = 30$ from the floor. The main flow block was $1.5D$ wide in the y-direction due to the symmetry condition. The grid is shown in Fig. 4.2. Note that the close-up view of the jet only shows the $x - z$ plane. The view of the jet in the

$y - z$ plane is the same as that shown for the spanwise case in Fig. 4.3 (although only half as wide) since the same grid was used for both cases and rotated for the particular geometry.

For the spanwise and compound-angle jets there were no symmetry planes which could be used to reduce the computational domain so the entire $3D$ span in the y-direction was used. The main flow region was otherwise the same in extent as the streamwise jets. For the spanwise jet case, the jet block consisted of $8 \times 16 \times 16$ nodes and the main flow block consisted of $60 \times 24 \times 40$ nodes in the x-, y-, and z-directions respectively. For the compound-angle jet case, the jet block consisted of $10 \times 10 \times 12$ nodes and the main flow block consisted of $33 \times 30 \times 26$ nodes in the x-, y-, and z-directions respectively. The grids for the spanwise and compound-angle cases are shown in Fig. 4.3 and 4.4 respectively. Note that in Fig. 4.4 for the compound-angle jets that the grid along the floor of the wind tunnel in the $x - y$ plane is shown, rather than the end view of the $y - z$ plane shown in the previous figures. Due to the complicated geometry for the compound-angle case it was difficult to obtain a more uniform grid and still maintain the ordered node arrangement required for a structured grid. The use of unstructured grids for this case would clearly be an advantage.

4.4.1 Boundary Conditions

The boundary conditions for the computations were the same for all three geometries with the exception of the sides of the domain in the streamwise case. As mentioned previously, the size of the computational domain was reduced due to the symmetry planes for the streamwise jet. The symmetry condition was enforced by setting $\partial/\partial y = 0$ and zero flux conditions along the sides of the main flow region and along the centreline of the jet hole. For the spanwise and compound-angle cases a periodic condition was set along the sides

of the domain. At the entrance to the jet hole a uniform, vertical velocity was specified which gave a bulk jet velocity corresponding to the appropriate experimental case.

At the upstream edge of the main flow region the experimental data were used to provide the boundary conditions. Polynomial curves were fit to the profiles of streamwise velocity (U) and turbulence kinetic energy (k) which were measured at $x/D = -5$. Since the flow was essentially a boundary layer at this upstream location a mixing-length approach was used to determine the turbulence dissipation rate (ϵ). The damping function of van Driest was used to determine the mixing length (van Driest (1956)):

$$L_m = \kappa z \left[1 - \exp\left(-\frac{z^+}{A} \right) \right] \tag{4.47}$$

where $A \approx 26$ for flat-plate flow, $\kappa = 0.41$, z is the (dimensional) distance from the wall, and z^+ is the non-dimensional distance from the wall indicated in Eq. (4.37).

The walls in the domain along the tunnel floor and edges of the jet were treated with a no-slip condition while the upper boundary of the domain was treated with a free-slip, zero flux condition. Finally, the downstream edge of the domain was treated with a zero-gradient ($\partial/\partial x = 0$) condition. The boundary conditions are indicated on the figures showing the grids for the different geometries (4.2, 4.3, and 4.4).

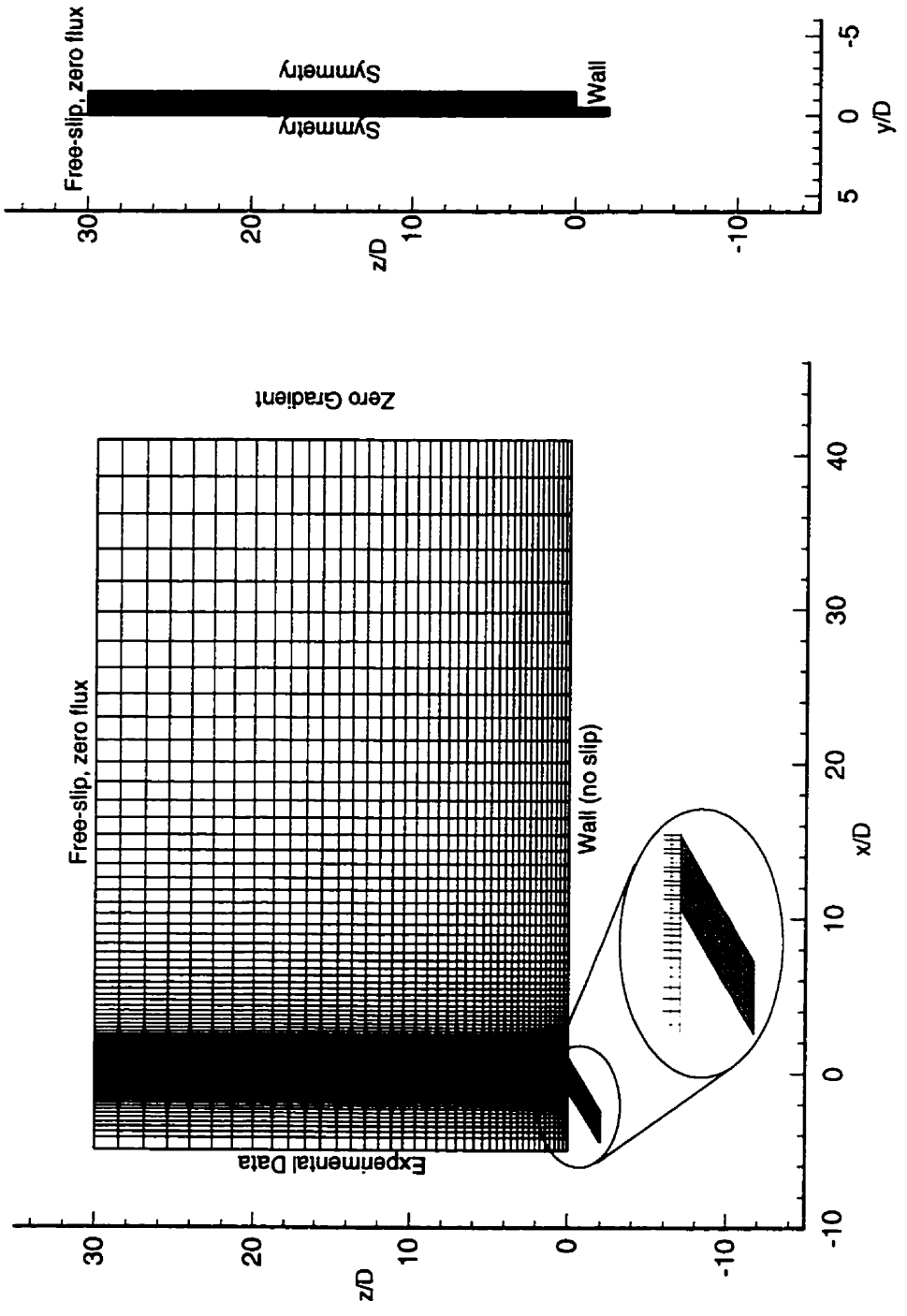

Figure 4.2: Computational grid for streamwise jet.

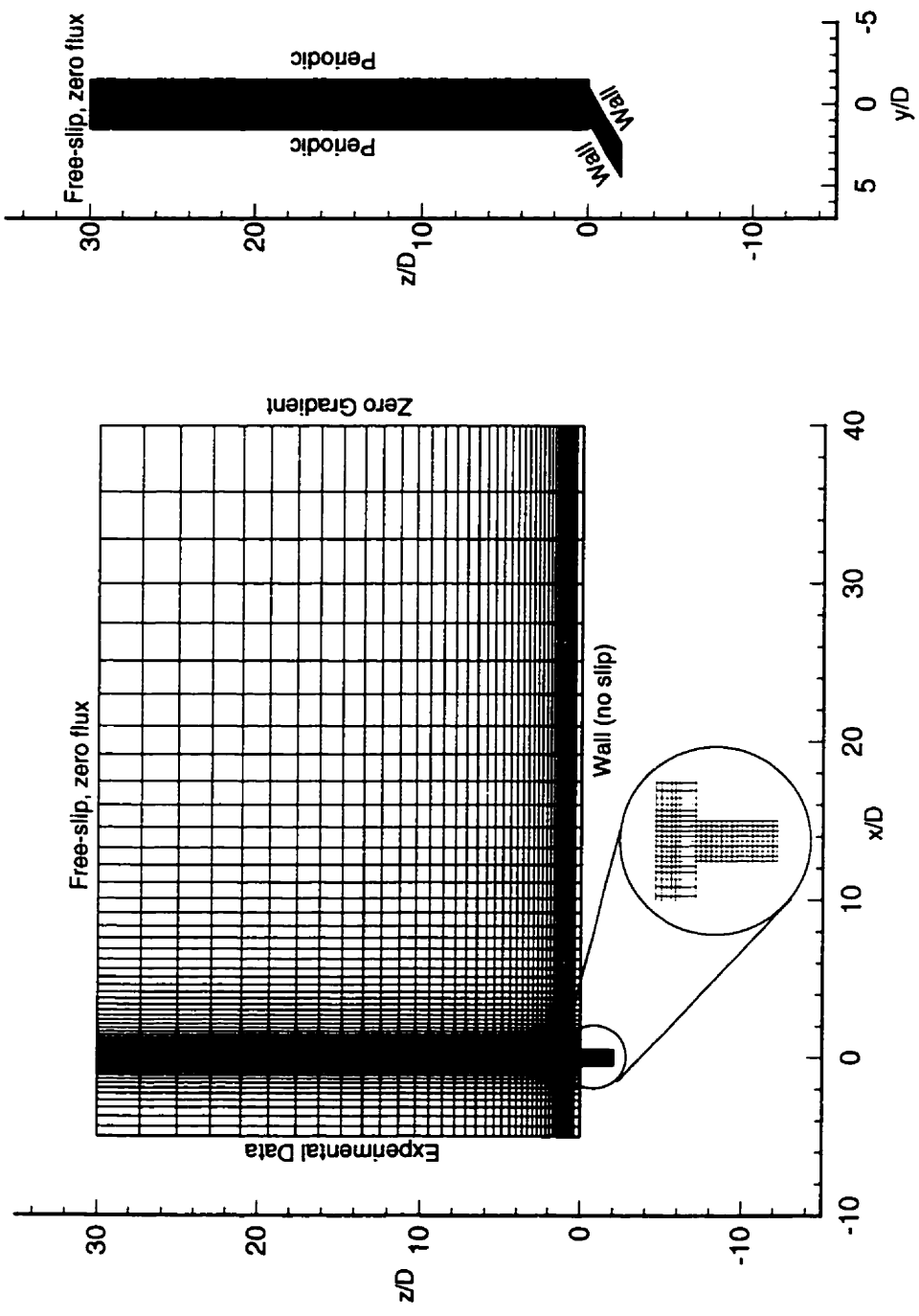

Figure 4.3: Computational grid for spanwise jet.

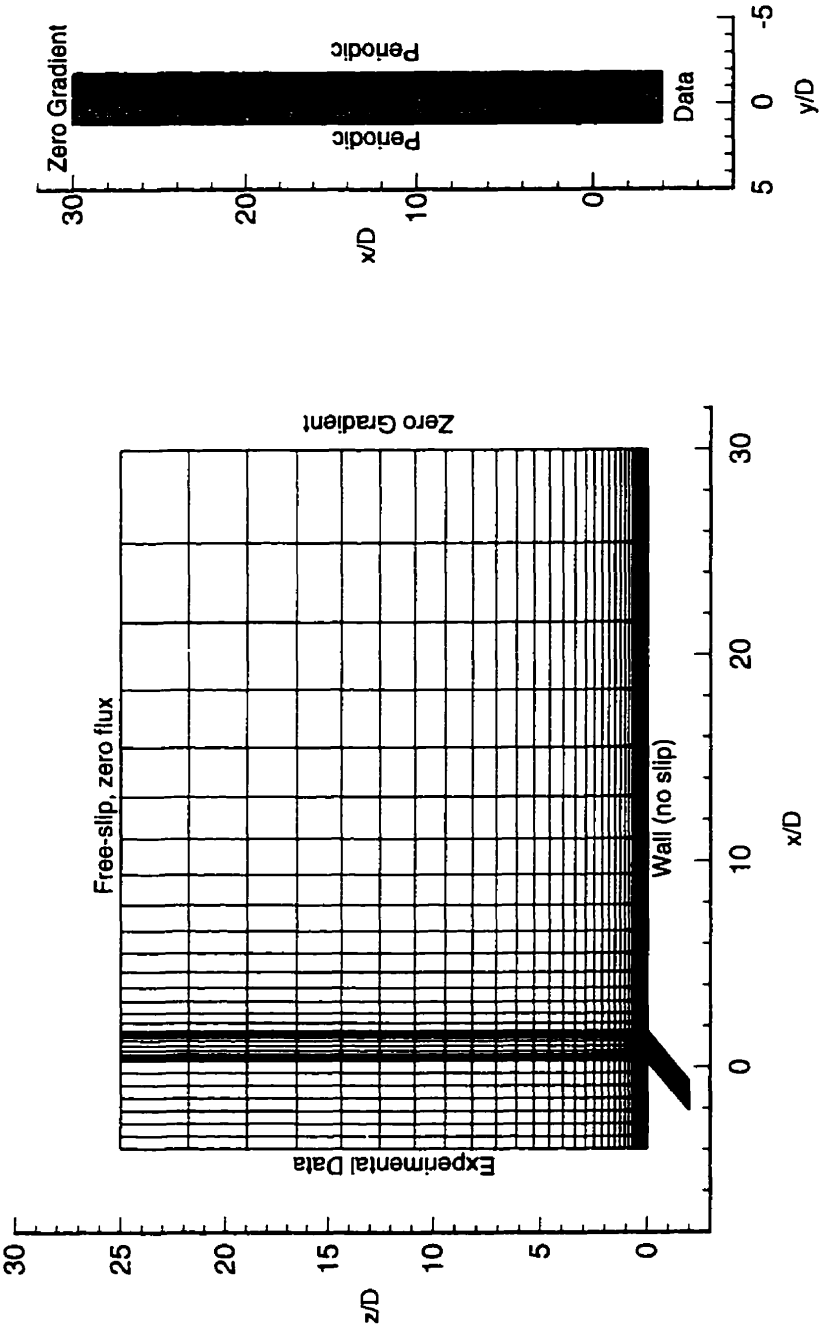

Figure 4.4: Computational grid for compound-angle jet.

Chapter 5

Computational Results

In this chapter the comparisons between the experimental data and the computational results are presented. Comparisons between the numerical results using the standard $k-\epsilon$ (SKE), Menter's baseline (BSL), and Menter's shear stress transport (SST) models are made. The computational data are exploratory in nature and suggestions are made regarding modifications to aspects of the numerical modelling which would likely result in the most significant improvements in the results. The computational data for the compound-angle geometry were provided by Dr. Ibrahim Hassan, a Postdoctoral Fellow currently working with the research group at UBC.

5.1 Mean Velocity Field

In this section, comparisons are made between the velocity fields obtained from the experiments and from the computations using the standard $k-\epsilon$ (SKE) model. The experimental data are provided on the same graphs where possible. The jet exit velocity data from the experiments for the spanwise jet case are shown in Fig. 3.10 on page 62. For the velocity vectors in the spanwise $y-z$ planes at $R=0.5$, the comparisons are made with the graphs of Fig. 3.14 on page 69. For the velocity vectors in the spanwise $y-z$ planes at $R=1.5$, the comparisons are made with the graphs of Fig. 3.19 on page 79.

5.1.1 Jet Exit

Only the spanwise case is presented here since the trend observed here differs from the experimental observations. In the case of the streamwise and spanwise cases the computed velocity profiles are in reasonable agreement with the experiments, although the magnitudes differ slightly.

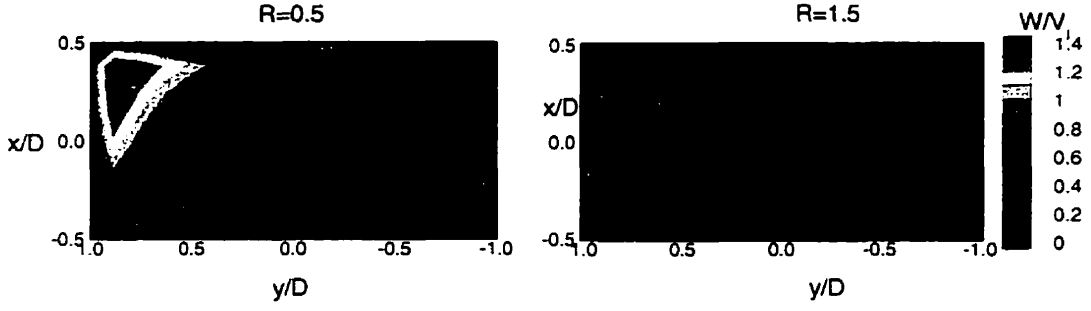

Figure 5.1: Computed spanwise jet exit W/V_j contours

The vertical velocity (W/V_j) contours at the jet exit plane are shown for the spanwise jet case at $R = 0.5$ and $R = 1.5$ in Fig. 5.1. For both velocity ratios the region of peak vertical velocity is skewed towards the $+y$ side of the jet exit. However, the experimental data indicate the location of peak W/V_j at $R = 1.5$ to be centred near $y/D = 0$ and pushed farther towards the downstream edge of the jet than shown in the computations. In addition, as the velocity ratio decreased the region of peak velocity became more strongly skewed in the positive y-direction. Here, the region of peak W/V_j is pushed towards the downstream edge of the jet, as expected, but the peak vertical velocity is much closer to the $y/D = 1$ edge of the jet exit. Since the other two jet cases tend to be in better overall agreement with the experimental trends it appears that the plenum region below the jet entrance has a more significant effect on the jet flow for the spanwise jet case, or that the interaction between the jet and crossflow at the jet exit is more

significant for the spanwise case.

5.1.2 Velocity Ratio R = 0.5

Comparisons between the streamwise (U) component of velocity from the experiments and from the computations at $R = 0.5$ using the standard $k - \epsilon$ (SKE) model are shown along the $y/D = 0$ plane in Fig. 5.2. At $x/D = 1$ it can be seen that the streamwise component of velocity in the jet flow near the wall is not well predicted by the computations. As the flow progresses downstream the agreement improves due to the strong crossflow which returns the flow to a boundary layer profile relatively quickly. The higher velocity region near the floor in the spanwise jet case is not picked up until $x/D = 3$. The velocity gradient in this region is not as strong as found in the experiments, as observed for the streamwise case. The compound-angle jet computations show some of the correct trends, particularly as the flow moves farther downstream, although the higher velocity near the floor is again underpredicted. As was the case for the streamwise jet, the injection of the jet is missed at $x/D = 1$.

The vector plots in Fig. 5.3 show the spanwise and vertical components of velocity at various x/D planes, calculated from the SKE model. Clear vortices are apparent in the streamwise case as the flow moves downstream. Recall from the discussion in section 3.5.2 that only very weak vortices formed in the experimental measurements as the jet flow was deflected strongly towards the floor by the crossflow. It appears that the jets are penetrating farther into the crossflow in the computations and explains the poor prediction of the streamwise component of velocity along the jet centreline. In the case of the spanwise jets, the initial vortex formation at $x/D = 1$ begins at $y/D \approx 1.0$, rather than at $y/D \approx 0.5$ (see Fig. 3.14 for comparison) and progresses laterally more slowly than indicated by the experiments. The vortices tend to be farther from the floor in the

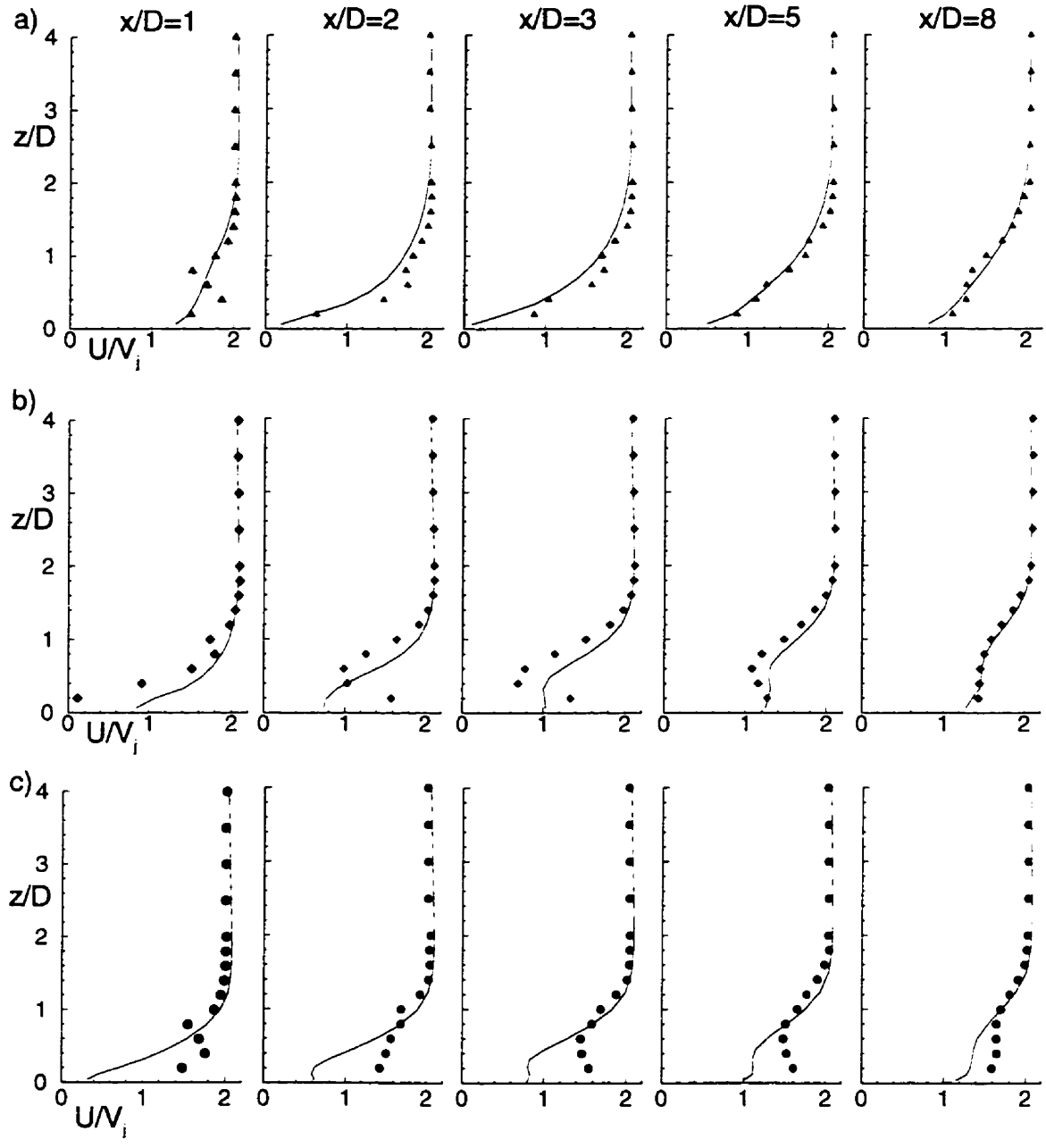

Figure 5.2: Streamwise velocity along $y/D = 0$ at $R = 0.5$ from experiments (symbols) and the SKE model: a) streamwise ($L/D = 4$), b) spanwise, c) compound-angle jets.

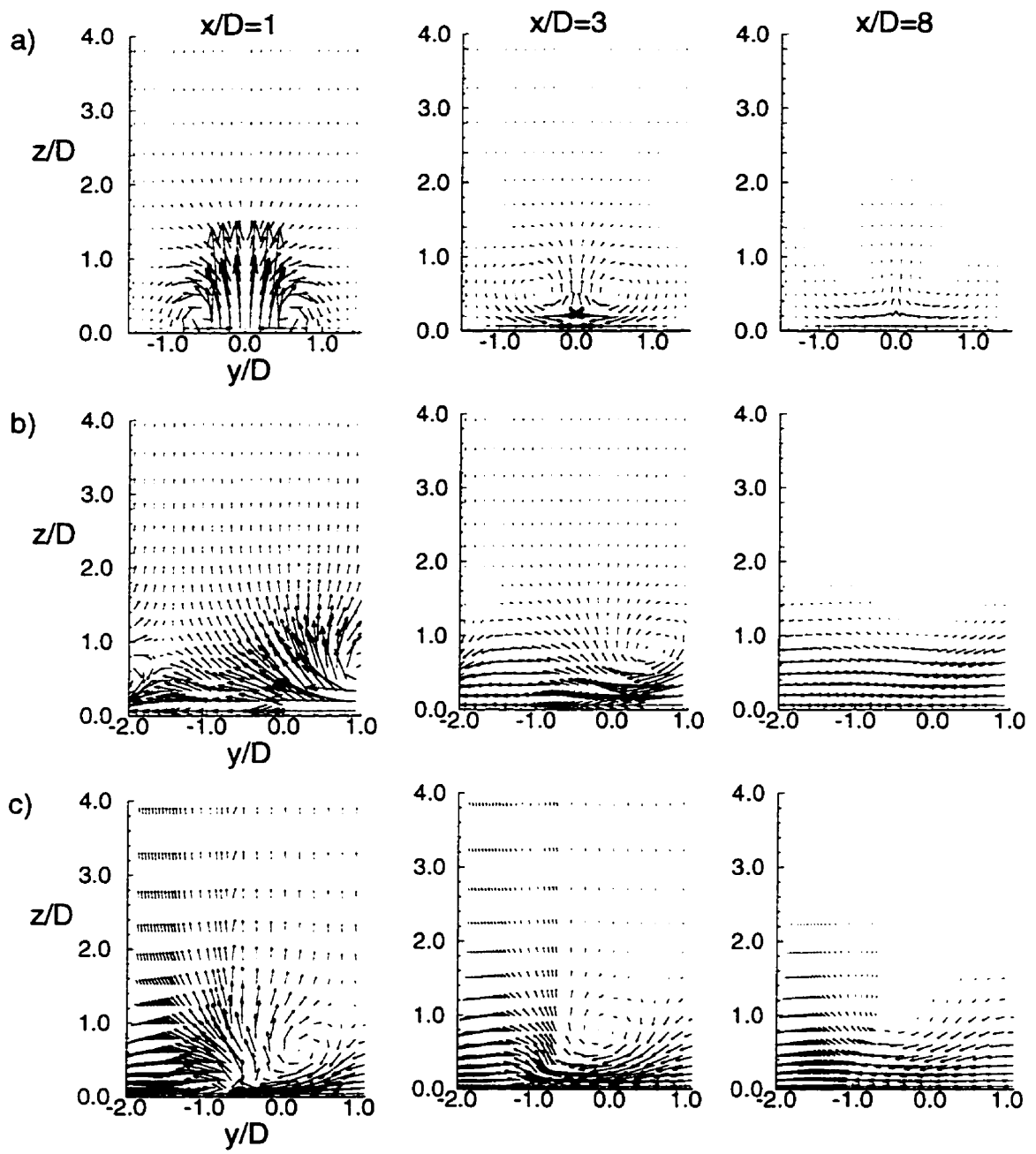

Figure 5.3: Velocity vectors in spanwise y-z planes at $R = 0.5$ computed using the SKE model (V and W components): a) streamwise ($L/D = 4$), b) spanwise, c) compound-angle jets.

computed results as compared with the experiments. The initial vortex formation in the case of the compound-angle jets is near the correct location at $x/D = 1$. As the flow progresses downstream the location of the vortex in the computations remains close to the location indicated by the experiments, although the computed results predict a slightly greater lateral movement. The explanation for the higher streamwise velocities near the wall along $y/D = 0$ was that the vortex caused the higher-velocity crossflow fluid to be drawn towards the floor. Since the vortex locations are different in the computed results, the disagreement between the streamwise velocity profiles along a particular streamwise plane are not unexpected.

5.1.3 Velocity Ratio R = 1.5

The experiments and computational results for the streamwise velocity at $R = 1.5$ using the SKE model are shown along the $y/D = 0$ plane in Fig. 5.4. The presence of the strong streamwise injection is apparent for the computed results in the streamwise jet case although the magnitudes are underpredicted. Again, as the flow begins to return to a boundary layer flow the agreement between the experiments and computations improves. The agreement in the case of the spanwise jets is reasonable, although the peak streamwise velocities in the near-hole region are overpredicted. The computations in the compound-angle case again indicate the presence of the streamwise component of jet velocity at $x/D = 1$ although underpredicting the experimental values. The agreement at $x/D = 2, 3$ is good as the region is between the adjacent jets and appears to be a boundary-layer flow. Farther downstream the influence of the adjacent jet is observed and the computations and experiments show some discrepancies.

The vector plots in Fig. 5.5 show the spanwise and vertical components of velocity at various x/D planes, calculated from the SKE model at $R = 1.5$. Again, the clear vortices

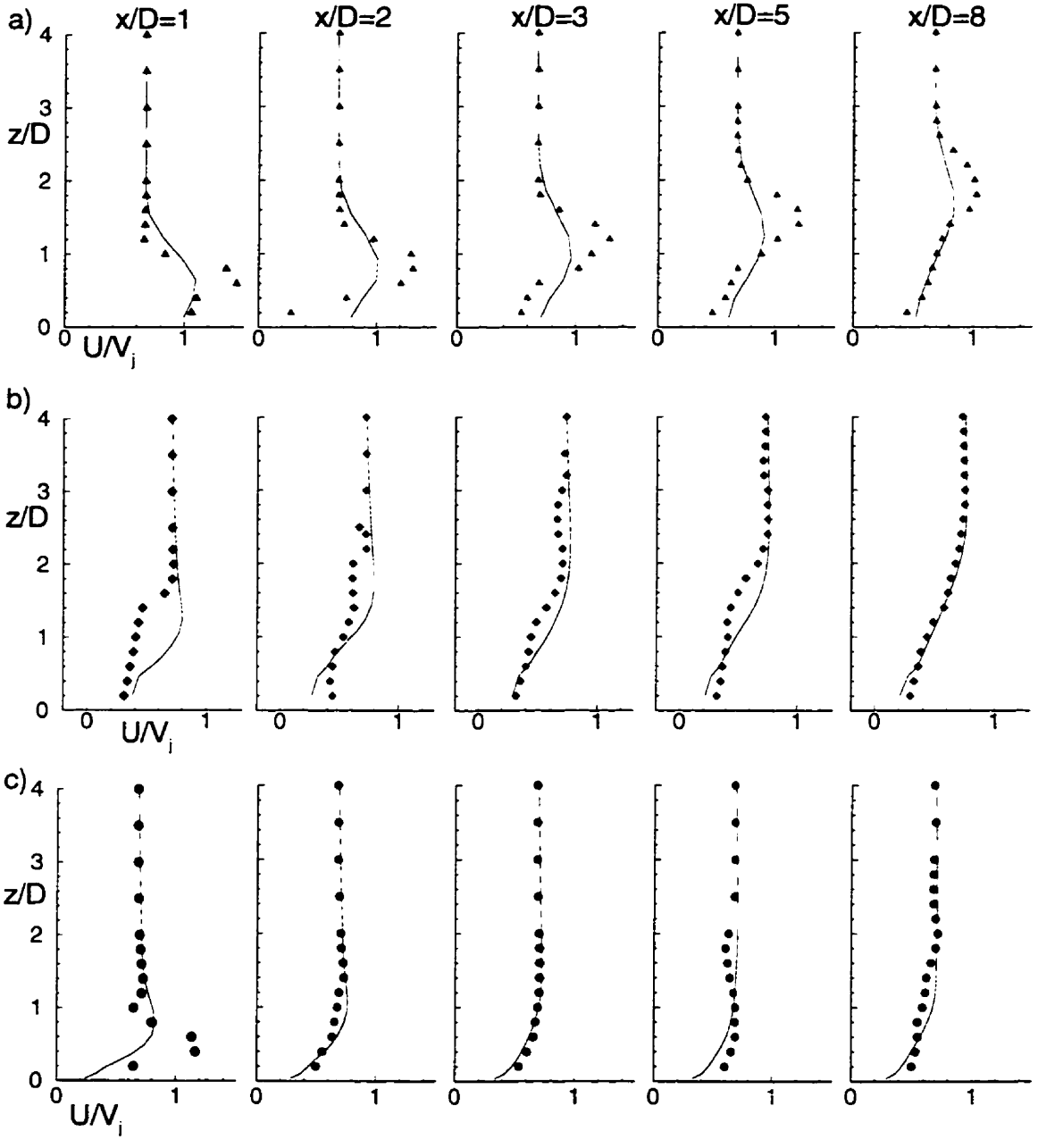

Figure 5.4: Streamwise velocity along $y/D = 0$ at $R = 1.5$ from experiments (symbols) and the SKE model: a) streamwise ($L/D = 4$), b) spanwise, c) compound-angle jets.

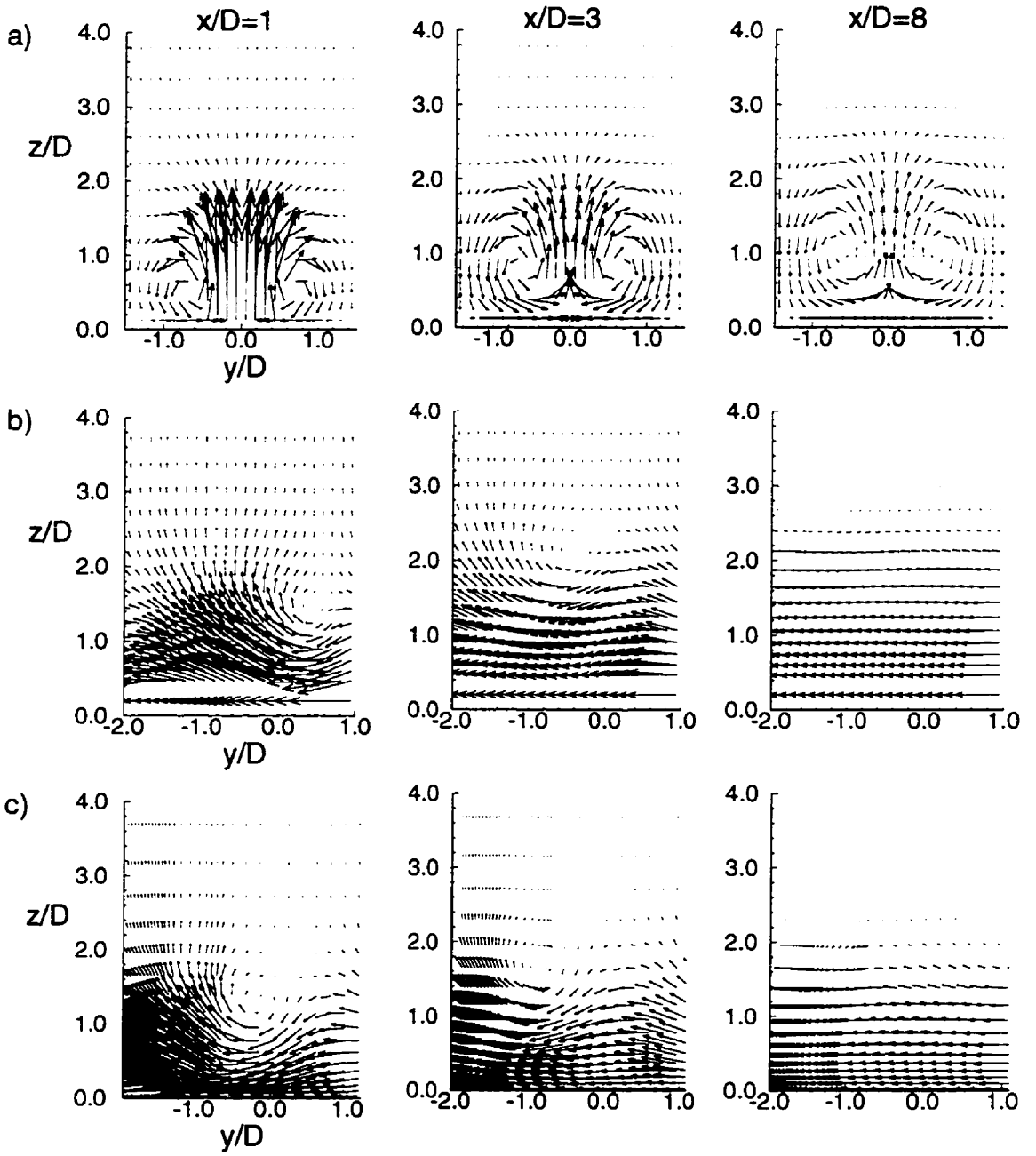

Figure 5.5: Velocity vectors in spanwise y-z planes at $R = 1.5$ computed using the SKE model (V and W components): a) streamwise ($L/D = 4$), b) spanwise, c) compound-angle jets.

are apparent at $x/D = 1$ in the streamwise case which are more completely formed than indicated by the experimental data at this location. The jets are penetrating farther into the crossflow which allows for the early formation of the vortices. Downstream at $x/D = 8$ the vortex location is comparable to that found in the experiments. As was the case at $R = 0.5$, the spanwise jet computations show the vortex formation occurring in a different location than indicated by the experiments. The differences in the jet exit velocity profiles between the experiments and computations are likely the cause of this discrepancy. In the compound-angle jet case the vortex formation occurs farther from the tunnel floor than indicated by the experimental data. In both the spanwise and compound-angle jet cases the early vortex formation may dictate the mixing between the jet and the crossflow at the downstream locations. More details may be found in section 5.3.2.

5.2 Turbulence Kinetic Energy

5.2.1 Velocity Ratio R = 0.5

Comparisons between the normalized turbulence kinetic energy ($\sqrt{k}/V_j$) from the experiments and from the computations at $R = 0.5$ using the standard $k - \epsilon$ (SKE) model are shown along the $y/D = 0$ plane in Fig. 5.6. The trend in the turbulence kinetic energy is reasonably well predicted in the case of the streamwise jets although the magnitude is typically higher for the computed values. It appears that the turbulence generation within the upstream boundary layer is over-predicted by the turbulence model since the boundary layer profile at $x/D = -5$ for the computations was matched to the experiments at this location. The greater jet penetration which is predicted by the computations also contributes to the higher k-values as compared to the experiments. Towards the floor at $x/D = 5, 8$ the increase in k is not picked up by the computations, likely due to the

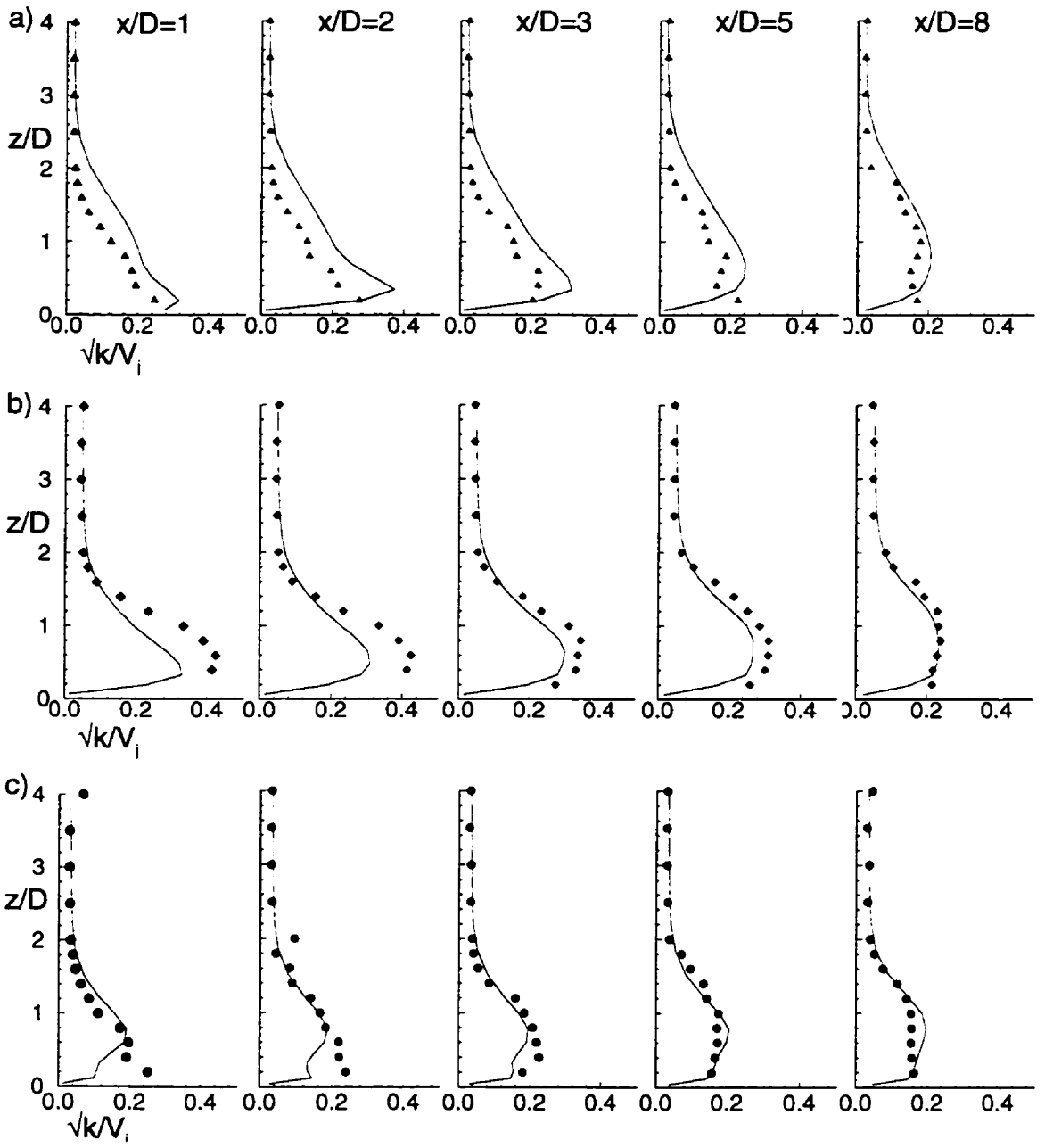

Figure 5.6: Turbulence kinetic energy along $y/D = 0$ at $R = 0.5$ from experiments (symbols) and the SKE model: a) streamwise ($L/D = 4$), b) spanwise, c) compound-angle jets.

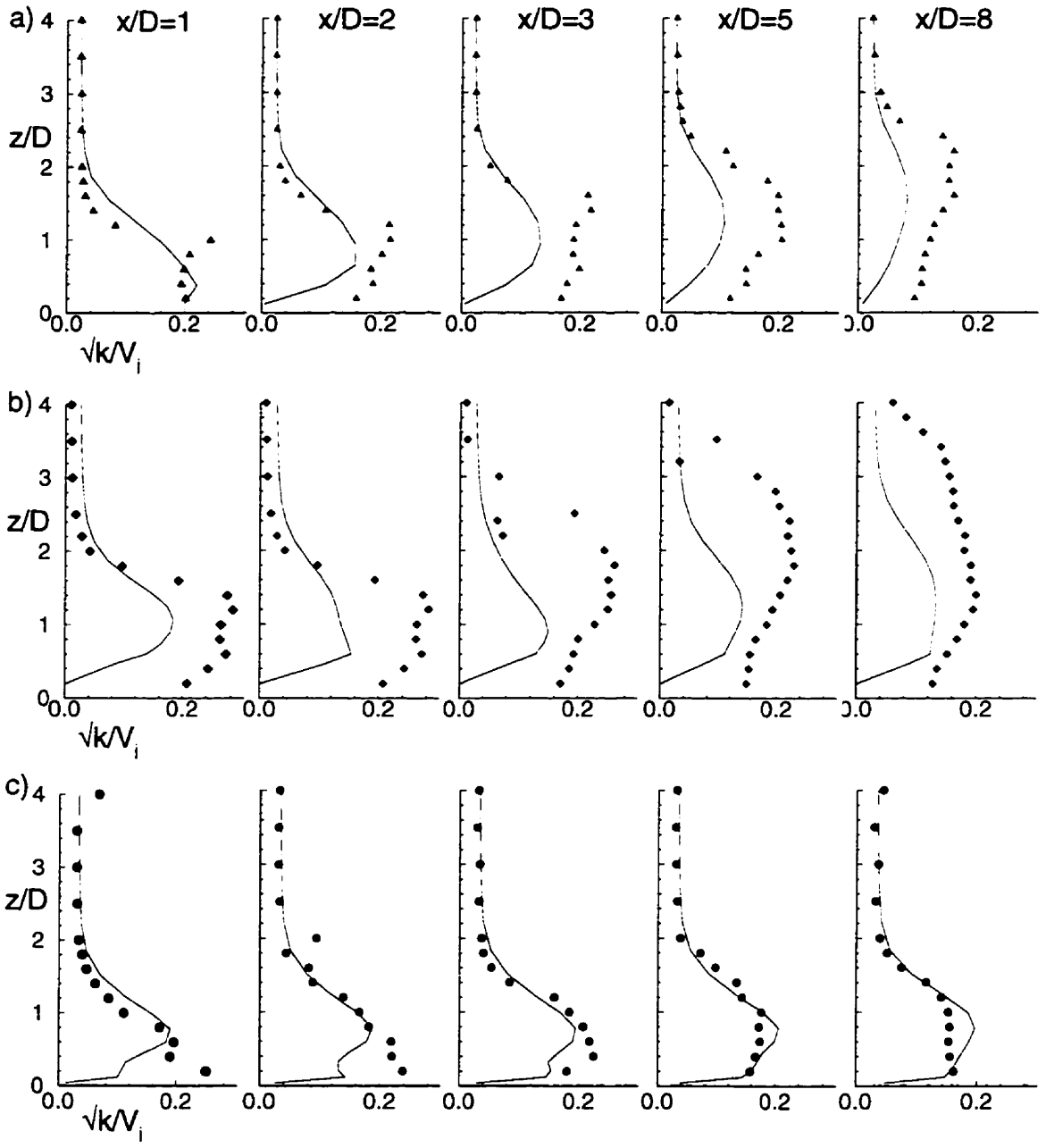

Figure 5.7: Turbulence kinetic energy along $y/D = 0$ at $R = 1.5$ from experiments (symbols) and the SKE model: a) streamwise ($L/D = 4$), b) spanwise, c) compound-angle jets.

use of wall functions in this region. For the spanwise jets, the turbulence kinetic energy is underpredicted at most locations. Again, as the flow moves downstream, the agreement between the computations and experiments improves. The agreement between the computations and experiments for the compound-angle jets appears to be slightly better than was the case for the two previous geometries close to the jet exit. However, the near-wall values of $\sqrt{k}/V_j$ show a decrease for the computations rather than the increase found with the experiments at $x/D = 1, 2$, similar to the streamwise jets.

5.2.2 Velocity Ratio R = 1.5

At the high velocity ratio the turbulence kinetic energy is typically underpredicted by the computations, as seen in Fig. 5.7. In the case of the streamwise jets the initial injection of the jet at $x/D = 1$ is predicted fairly well, but the computed results drop below the experimental values quickly. Recall from the profiles of the streamwise velocity profiles for this case that the gradients in U were smaller for the computed results than for the experimental data which may partially account for the discrepancy. A similar trend exists for the spanwise jets where the high levels of $\sqrt{k}/V_j$ are not well predicted. The agreement in the compound-angle case is reasonable, although the near-wall $\sqrt{k}/V_j$ values are underpredicted at $x/D = 1, 2$.

5.3 Scalar Transport

Comparisons between the experimental data and computational results using the SKE model are made in this section. Experimental data is presented with the computations where possible. For the concentration contours in the spanwise $y - z$ planes at $R = 0.5$, the comparisons are made with the graphs of Fig. 3.37 on page 114. For the concentration contours in the spanwise $y - z$ planes at $R = 1.5$, the comparisons are made with the

graphs of Fig. 3.38 on page 117.

5.3.1 Velocity Ratio R = 0.5

Contours of the jet concentration in spanwise $y - z$ planes are shown in Fig. 5.8. In the case of the streamwise jets at $x/D = 1$ the computations predict jet penetration to $z/D = 1.2$ which is greater than the penetration to $z/D = 0.8$ from the experiments at this location. Farther downstream the agreement between the experiments and computations improves with the computations and experiments indicating penetration to $z/D = 1.5$ and $z/D = 1.4$ respectively. It appears that the computations under-predict the rate at which the jets continue to penetrate into the crossflow. The lateral spread of the jet fluid is reasonably well predicted by the computations, although consistently lower than the experiments indicate for this geometry. For the spanwise jets the extent of the penetration into the crossflow is underpredicted in the computational results at the downstream locations indicated in Fig. 5.8. The distribution of the jet fluid within the jet is in reasonable agreement however, with a peak concentration at $x/D = 3$ of between 0.3 and 0.4 for the experiments and between 0.5 and 0.6 for the computations. At $x/D = 8$ the jet fluid concentration along the floor is higher in the computed results as compared with the experiments. As noted in the discussion on the mean velocity field, the location of the jet in the compound-angle computations is in reasonable agreement with the experimental data. In addition, the distribution within the jet is comparable to the experimental results.

A comparison of the experimental and computational data for the spanwise distribution of jet fluid at $R = 0.5$ along the tunnel floor is shown in Fig. 5.9. The agreement for the streamwise jets is reasonable with the computations slightly underpredicting the lateral spread of the jet along the floor. The spanwise jet computations are in reasonable

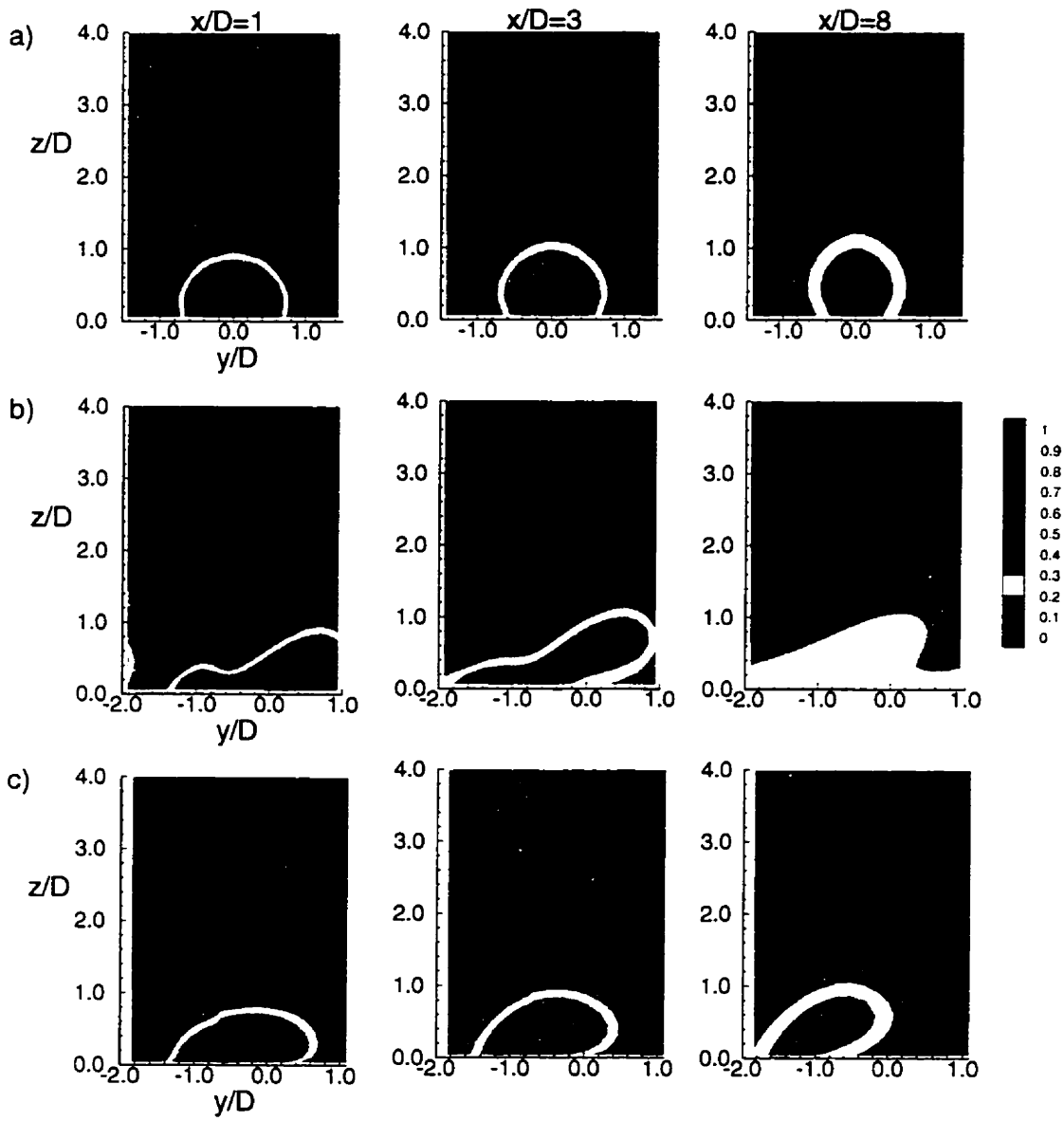

Figure 5.8: Concentration contours in spanwise y-z planes at $R = 0.5$ computed using the SKE model: a) streamwise ($L/D = 4$), b) spanwise, c) compound-angle jets.

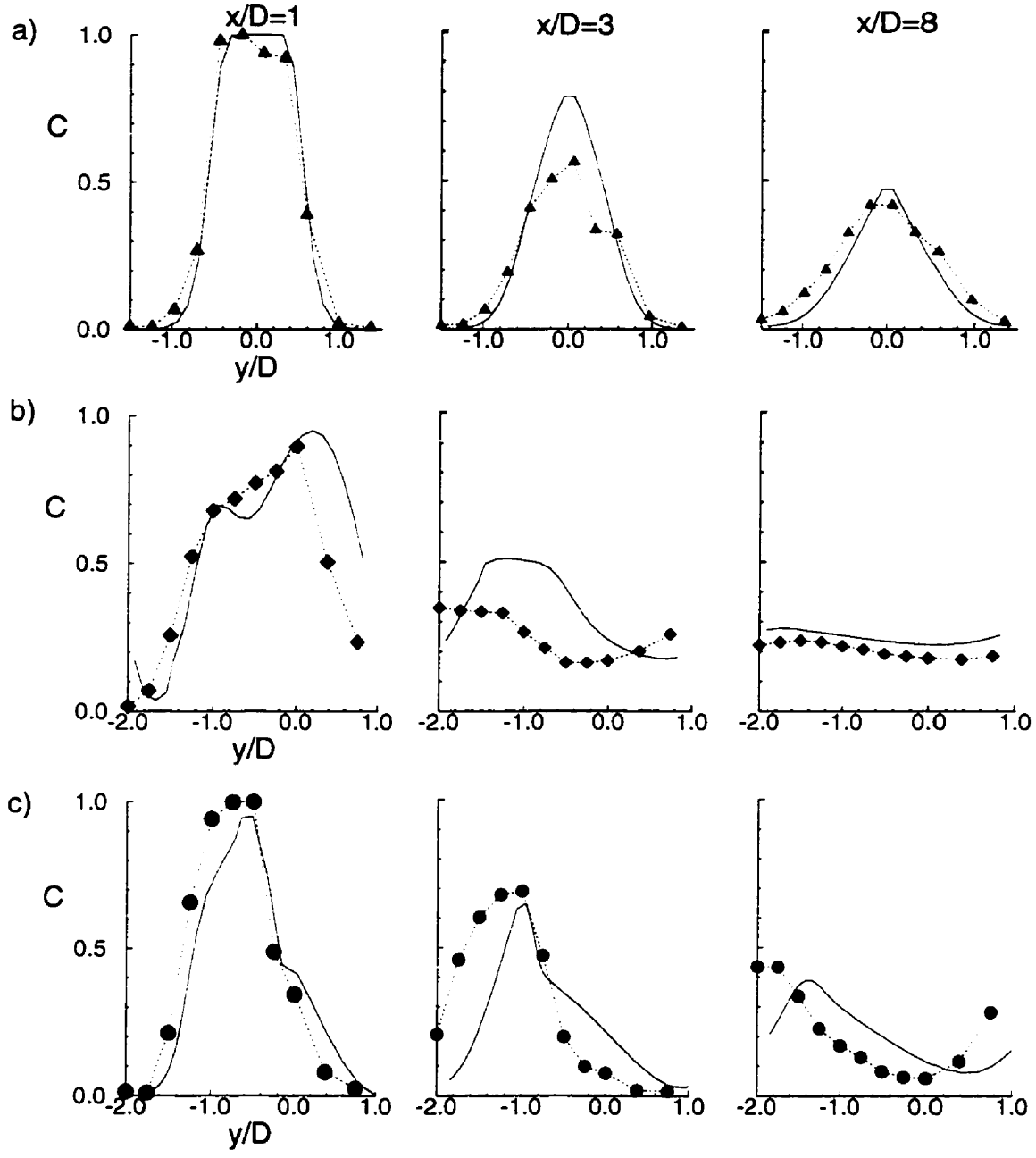

Figure 5.9: Comparison of spanwise distribution of jet fluid at $R = 0.5$, $z/D = 0$ from experiments (symbols) and the SKE model: a) streamwise ($L/D = 4$), b) spanwise, c) compound-angle jets.

agreement with the experimental data although there is a significant difference between the peak concentration at $x/D = 3$. The concentration along the floor is typically over-predicted by the computations for the spanwise jets. For the compound-angle jets, as the flow progresses downstream the trend in the distribution of jet fluid is captured reasonably well, but difference in the lateral location of the jet along the floor is apparent.

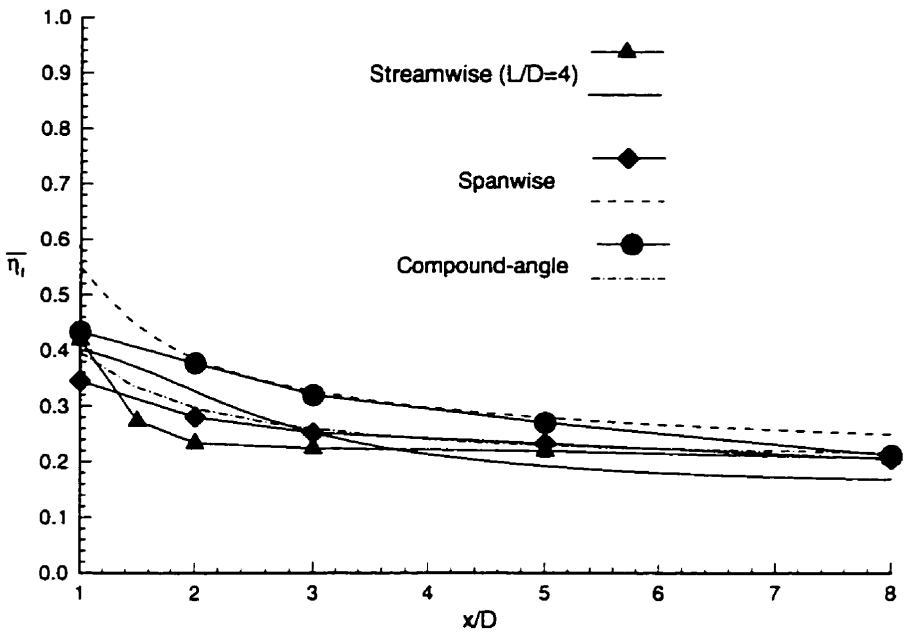

Figure 5.10: Comparison of spanwise-averaged film cooling effectiveness at $R = 0.5$, $z/D = 0$ from experiments (symbols) and the SKE model.

The spanwise-averaged film cooling effectiveness ($\overline{\eta_f}$) at $R = 0.5$ is shown in Fig. 5.10. The agreement at $x/D = 1$ for the streamwise case is good, as would be expected from the spanwise distribution from Fig. 5.9. However, the rapid drop in $\overline{\eta_f}$ observed in the experiments is not picked up by the computations. As the flow progresses downstream the predicted $\overline{\eta_f}$ drops below the experimental values as the lateral spreading of the jet

is underpredicted by the computational results. The spanwise jet case is overpredicted by the computations as the spanwise-averaged cooling effectiveness is always higher than the experimental data indicate which is consistent with the spanwise distribution of jet fluid noted in Fig. 5.9. Although the extent of jet penetration into the crossflow is comparable for the experiments and computations the average concentration is higher for the computations. It appears that the extent to which the crossflow fluid is drawn towards the floor by the strong vortex which is formed at $R = 0.5$ is underpredicted in the computations. Conversely, $\overline{\eta_f}$ is consistently underpredicted by the computations in the compound-angle jet case over most of the domain, although the agreement downstream at $x/D = 8$ is good.

5.3.2 Velocity Ratio R = 1.5

Contours of the jet concentration in spanwise $y - z$ planes are shown in Fig. 5.11. The computed results show the same trend found at $R = 0.5$ as the initial penetration of the jets in the near-hole region is greater for the computations but the agreement improves as the flow moves downstream. Again, it appears that the computations under-predict the rate at which the jets continue to penetrate into the crossflow. The overall shape of the concentration contours for the spanwise jet computations is in reasonable agreement with the experimental data. The distribution of the jet fluid differs significantly, however, with much higher concentrations in the near-wall region. Recall from the experimental data that a region of lower jet concentration was present near the wall at $x/D = 8$ while the computations predict the highest concentration in the near-wall region. The agreement at $x/D = 1$ for the compound-angle jets is quite good as the penetration and general shape of the jet fluid region matches the experimental data. Farther downstream the lateral spreading of the jet is overpredicted by the computations and the space between

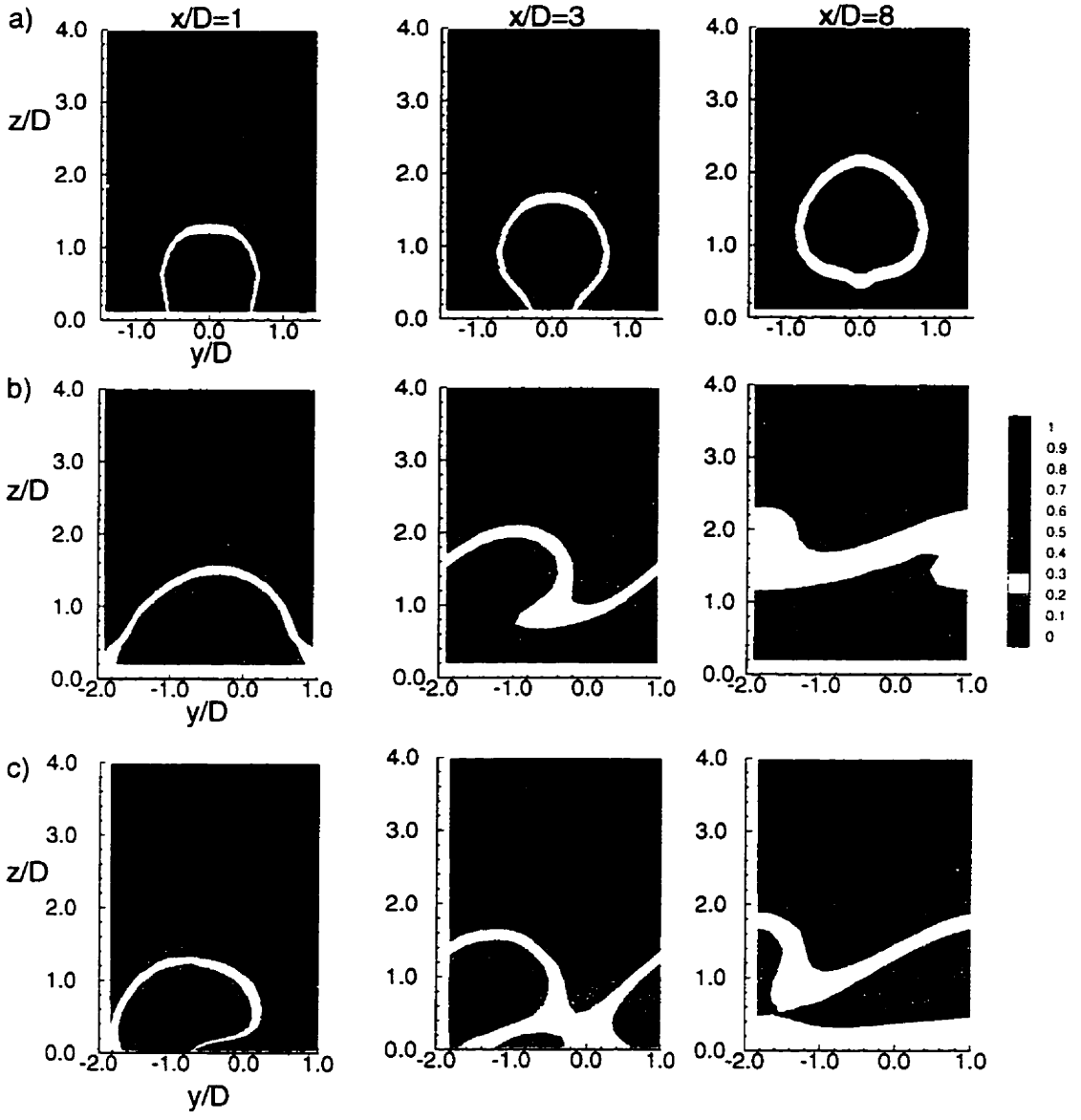

Figure 5.11: Concentration contours in spanwise y-z planes at $R = 1.5$ computed using the SKE model: a) streamwise ($L/D = 4$), b) spanwise, c) compound-angle jets.

the fluid from adjacent jets disappears. As noted in the discussion on the mean velocity fields in the spanwise and compound-angle cases the formation and location of the vortices for these cases differs from the experimental data. For the spanwise jets the computations predict vortex formation farther from the wall than found in the experiments. These differences may result in the more even distribution of jet fluid as a vortex does not draw the crossflow fluid down towards the floor for better mixing with the jet fluid. A similar trend is observed for the compound-angle jet computations, as the vortex forms farther from the floor than the experiments indicate which again contributes to the more even spread of the jets and higher jet concentration closer to the wall.

The spanwise distribution of jet fluid along the floor at $R = 1.5$, comparing the experimental and computational results, is shown in Fig. 5.12. Again, the agreement for the streamwise jets is good, with the lateral spreading of the jet underpredicted by the computations. The differences in the jet fluid distribution for the spanwise jet case are clear as the concentration of jet fluid is much higher along the floor as the mixing with the crossflow is underpredicted. As noted in the discussion of the jet fluid distribution shown in Fig. 5.11 the computed initial distribution of jet fluid along the floor at $x/D = 1$ is in reasonable agreement with the experimental data for the compound-angle jets, although the location of the peak concentration is offset. The greater lateral spread of the jet fluid along the floor is clear at $x/D = 3$ where the experiments indicate a clear jet region between $y/D = -1$ and $y/D = -2$. The computational results show a more even distribution of jet fluid in this region and, as in the spanwise case, the concentration of jet fluid is higher at the downstream locations.

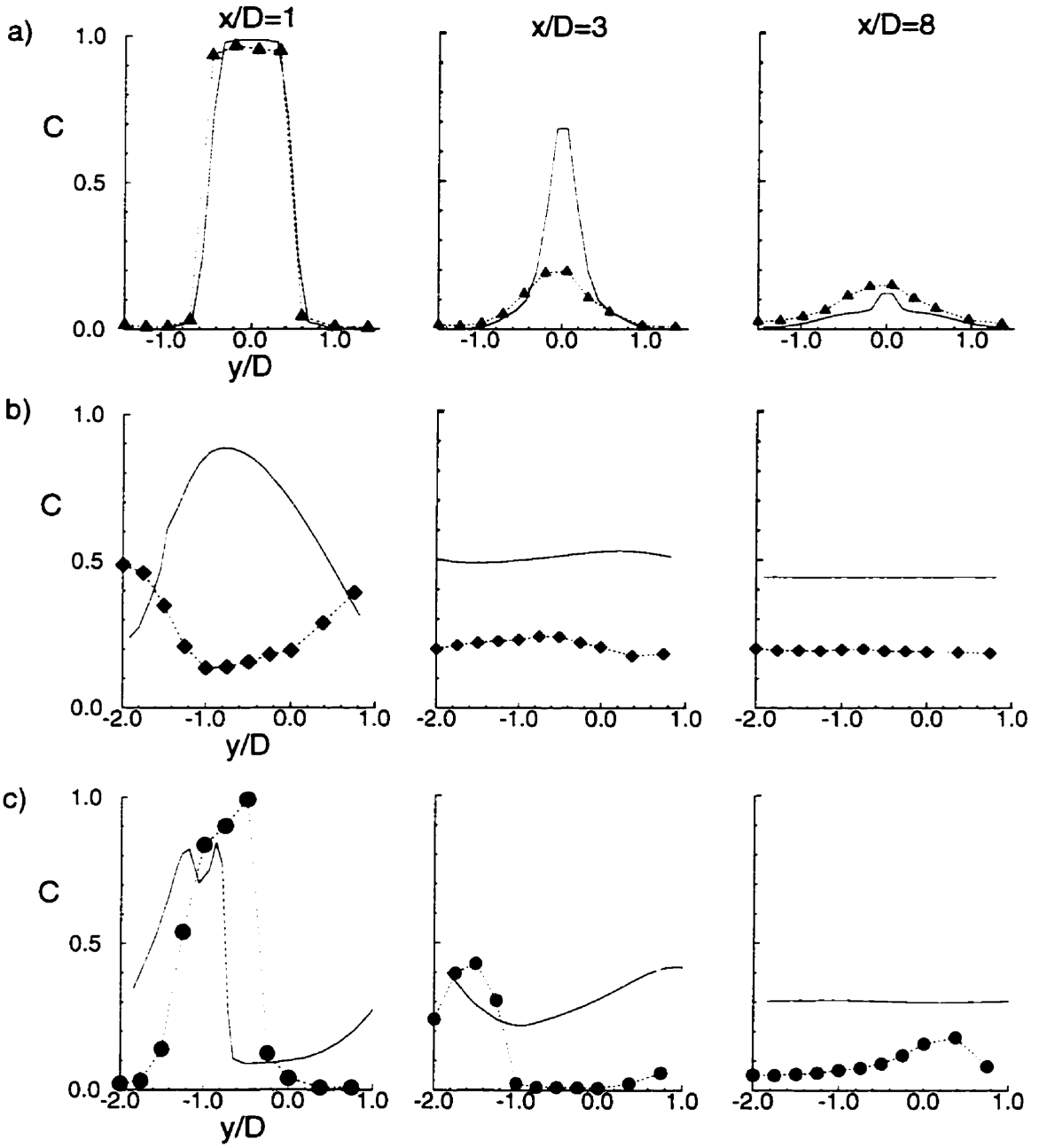

Figure 5.12: Comparison of spanwise distribution of jet fluid at $R = 1.5$, $z/D = 0$ from experiments (symbols) and the SKE model: a) streamwise ($L/D = 4$), b) spanwise, c) compound-angle jets.

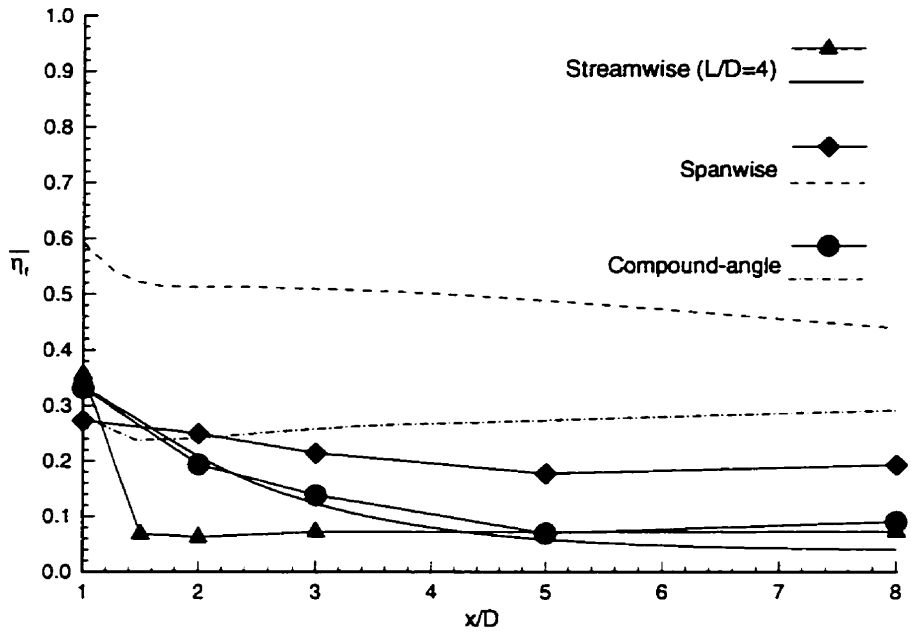

Figure 5.13: Comparison of spanwise-averaged film cooling effectiveness at $R = 1.5$, $z/D = 0$ from experiments (symbols) and the SKE model.

The spanwise-averaged film cooling effectiveness ($\overline{\eta_f}$) at $R = 1.5$ is shown in Fig. 5.13. The same trend observed for the streamwise jets at $R = 0.5$ is also apparent here, although more pronounced. The initial agreement at $x/D = 1$ is good but the sudden drop in $\overline{\eta_f}$ which is found in the experiments is missed by the computations. Farther downstream the predicted $\overline{\eta_f}$ again drops below the experimental values as the lateral spreading of the jet is underpredicted by the computations. The overpredicted $\overline{\eta_f}$ for the spanwise jet case is again much more pronounced at $R = 1.5$ than at $R = 0.5$. However, in light of the differences in the distribution of the jet fluid between the experiments and computations noted in the previous paragraphs at this velocity ratio the differences are not unexpected. The compound-angle jet computations indicate a gradual increase in $\overline{\eta_f}$

as the flow progresses downstream and the jet fluid spreads across the floor. The increase in $\overline{\eta_f}$ is not unreasonable as the same trend is observed in the experimental data for both the spanwise and compound-angle jets between $x/D = 5$ and $x/D = 8$.

5.4 Comparison of Turbulence Models

For the purposes of this comparison, only the compound-angle geometry will be presented. The computational results using the SKE, BSL, and SST turbulence models are compared with the experimental data.

5.4.1 Velocity Ratio R=0.5

In Fig. 5.14 the streamwise (U/V_j) velocity and turbulence kinetic energy $(\sqrt{k}/V_j)$ along the $y/D = 0$ plane at $R = 0.5$ are shown. None of the models pick up the streamwise component of velocity from the jet at $x/D = 1$. Farther downstream the blended models (BSL and SST) are slightly closer to the experimental data but all three models show the same trend and underpredict the streamwise velocity in the jet-affected region. For the normalized turbulence kinetic energy $(\sqrt{k}/V_j)$ the trends are similar for all three models away from the wall. Closer to the wall the BSL and SST models appear to give a better representation of the kinetic energy profiles near the jet exit where k is higher near the wall. Farther downstream, however, the SKE model appears to be in better agreement with the experimental data in the near-wall region.

A comparison of the predicted spanwise distribution of jet fluid along the floor is shown in Fig. 5.15. In the near-hole region the BSL and SST models predict a slightly wider region of jet coverage than the SKE model. Farther downstream at $x/D = 8$ the SKE model typically predicts lower values of concentration than the other models. The location of the peak concentration is captured best by the SST model in this case.

Finally, the spanwise-averaged film cooling effectiveness is compared in Fig. 5.16. In the near-hole region the SST model appears to have the best agreement with the experiments. However, the rate of decay of $\overline{\eta_f}$ is underpredicted as the flow progresses downstream.

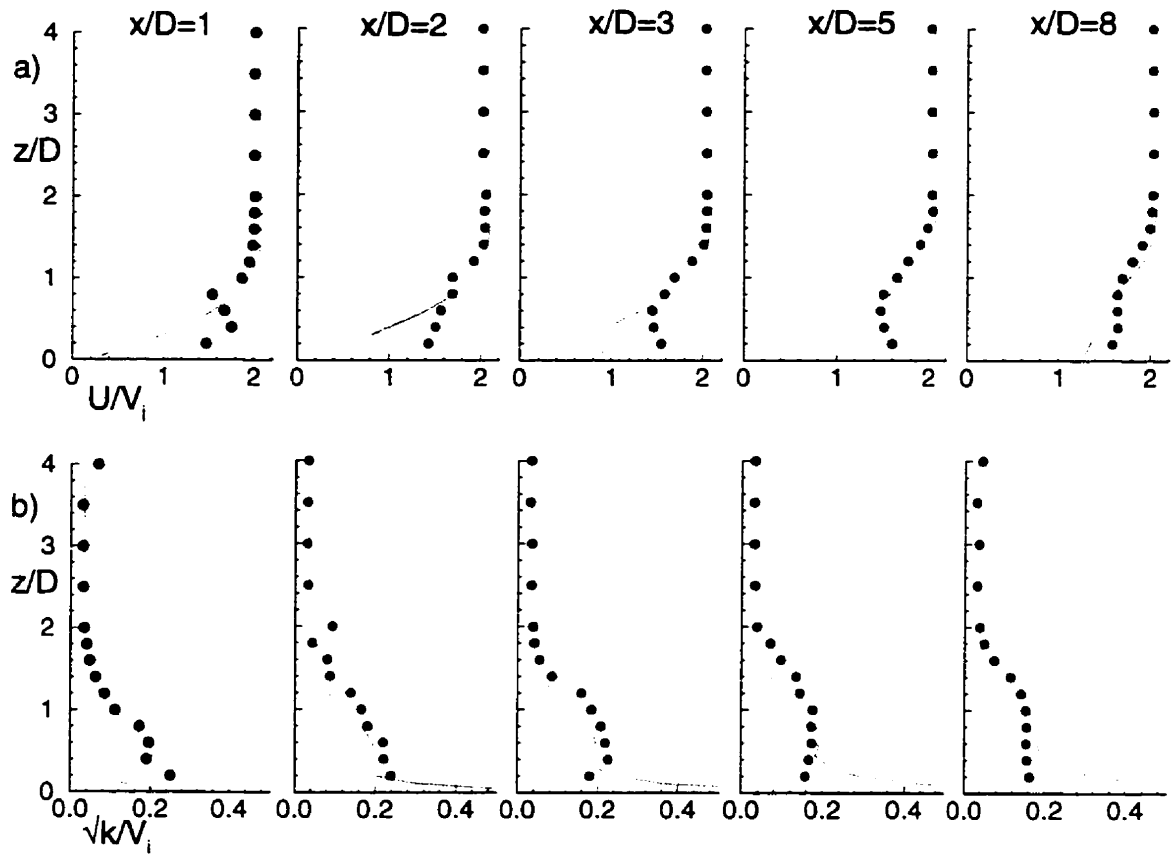

Figure 5.14: Comparison of SKE (blue), BSL (red), and SST (green) turbulence models with experiments (•) along $y/D = 0$ at $R = 0.5$ for the compound-angle jets: a) streamwise velocity (U/V_j), b) turbulence kinetic energy ($\sqrt{k}/V_j$).

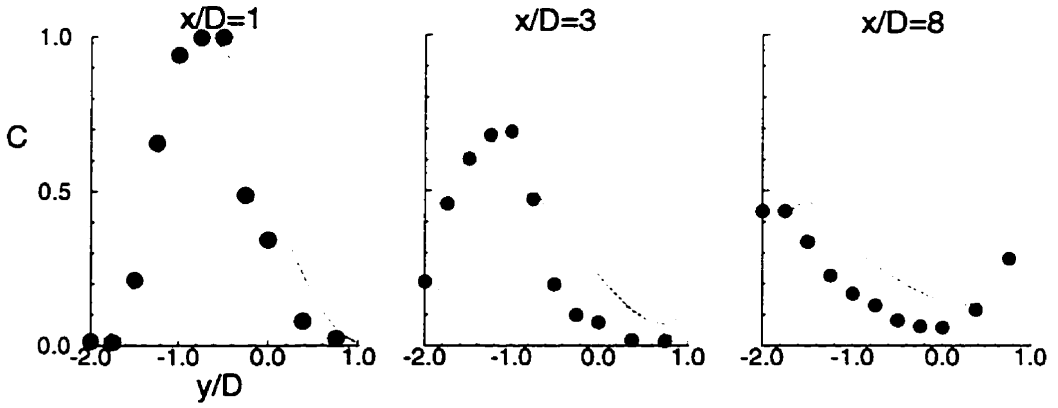

Figure 5.15: Comparison of spanwise jet distribution along $z/D = 0$ from SKE (blue), BSL(red), and SST (green) turbulence models with experiments (•) at $R = 0.5$ for the compound-angle jets.

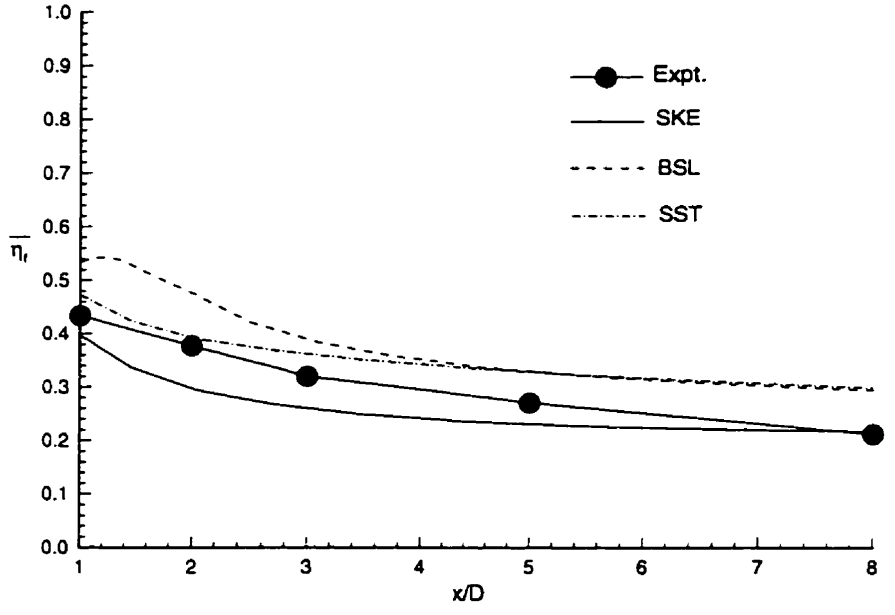

Figure 5.16: Comparison of spanwise-averaged film cooling effectiveness at $R = 0.5$, $z/D = 0$ from SKE, BSL, and SST turbulence models and experiments for the compound-angle jets.

5.4.2 Velocity Ratio R=1.5

In Fig. 5.17 the streamwise (U/V_j) velocity and turbulence kinetic energy ($\sqrt{k}/V_j$) along the $y/D = 0$ plane at $R = 1.5$ are shown. The predicted velocity profiles are almost identical for the three turbulence models as the flow behaves essentially as a boundary layer. The predicted $\sqrt{k}/V_j$ profiles are typically better for the BSL and SST models, particularly in the near-hole region. Overall, the BSL model is closest to the experimental data but, other than at $x/D = 3$, the turbulence levels are underpredicted.

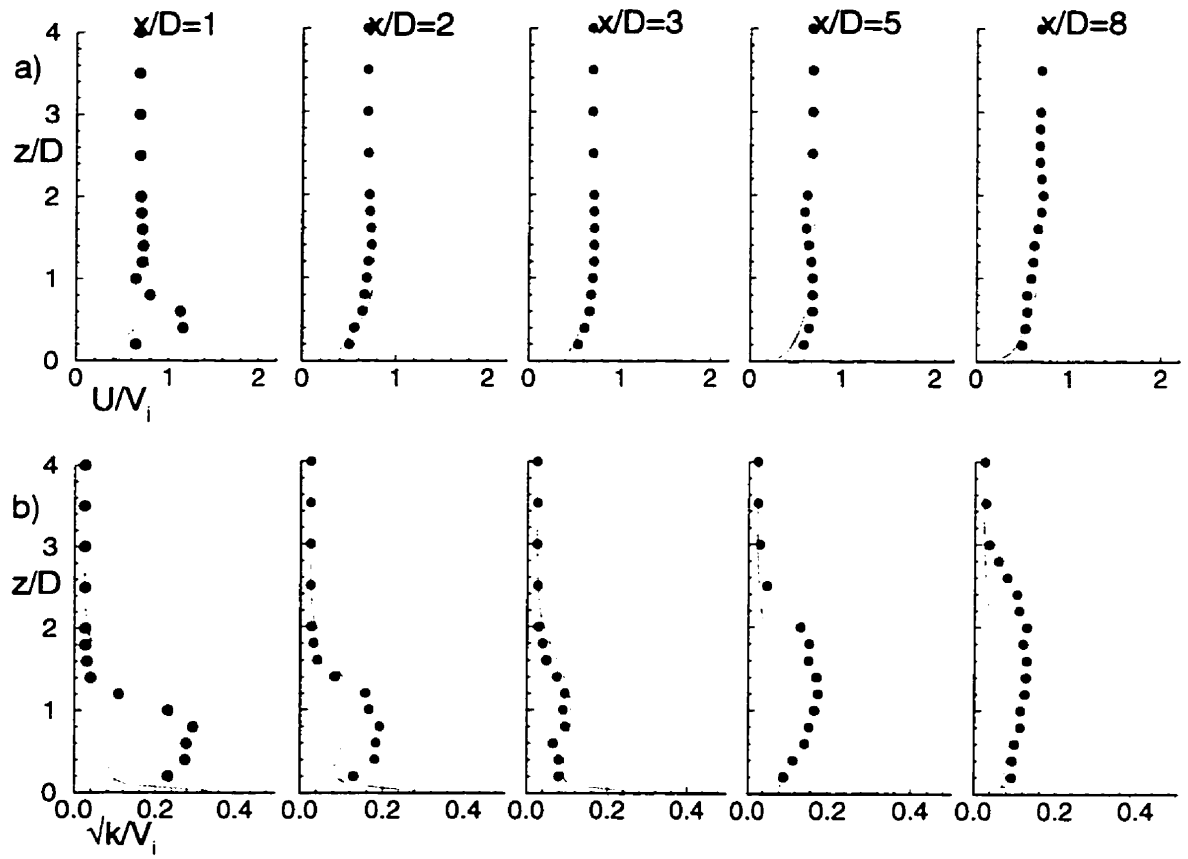

Figure 5.17: Comparison of SKE (blue), BSL (red), and SST (green) turbulence models with experiments (•) along $y/D = 0$ at $R = 1.5$ for the compound-angle jets: a) streamwise velocity (U/V_j), b) turbulence kinetic energy ($\sqrt{k}/V_j$).

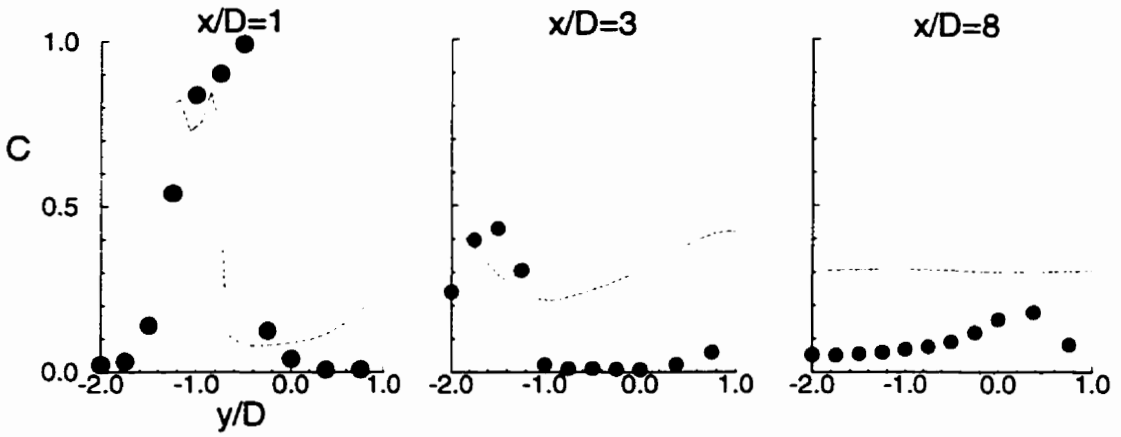

Figure 5.18: Comparison of spanwise jet distribution along $z/D = 0$ from SKE (blue), BSL (red), and SST (green) turbulence models with experiments (•) at $R = 1.5$ for the compound-angle jets.

A comparison of the predicted spanwise distribution of jet fluid along the floor is shown in Fig. 5.18. As was the case at $R = 0.5$, the BSL and SST models predict a slightly greater spread of the jet in the near hole region than the SKE model. Overall, the BSL and SST models are nearly identical for the prediction of jet fluid along the floor. The predicted values are typically higher than those indicated by the SKE model but the same trends are observed for all three models.

Finally, the spanwise-averaged film cooling effectiveness is compared in Fig. 5.19. As expected from the similarity of the spanwise distribtions in Fig. 5.18, the predicted $\overline{\eta_f}$ is nearly the same for the BSL and SST models. Again, all the models overpredict $\overline{\eta_f}$ as the flow moves downstream due to the greater lateral spread of jet fluid predicted by the models.

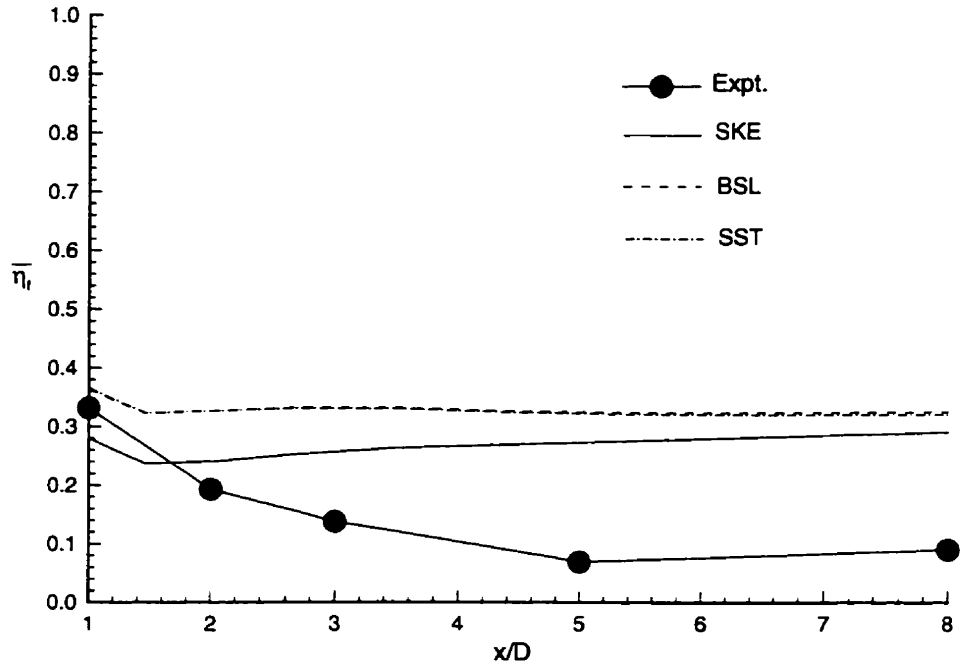

Figure 5.19: Comparison of spanwise-averaged film cooling effectiveness at $R = 1.5$, $z/D = 0$ from SKE, BSL, and SST turbulence models and experiments for the compound-angle jets.

5.5 Summary

The comparisons between the experimental and computational results have shown some common trends among the various cases examined. At the high, $R = 1.5$, velocity ratio the turbulence levels are consistently underpredicted in the computations. This is due to the assumption of local equilibrium of the production and dissipation of turbulence kinetic energy. For jets in a crossflow at high R the turbulence production and dissipation can vary widely in space. This non-equilibrium turbulence cannot be resolved by the equilibrium eddy viscosity concept assumed in the models here, which use a single time

scale to describe both the turbulent transport and dissipation of the turbulence kinetic energy. Zhou (1994) found considerable improvement in the predictions of turbulence kinetic energy for a $2D$ slot at $R = 0.4$ by using a multiple-time-scale turbulence model (Kim and Chen (1989)) rather than the SKE model, indicating the importance of the non-equilibrium turbulence assumption.

Another assumption in the eddy viscosity formulation used here is that of turbulence isotropy. Recall from the discussion in section 3.6.3 that the turbulent normal stresses can be quite anisotropic along the edges of the jets. In addition, the contribution of certain velocity gradients to the production of the turbulent shear stresses is ignored by the usual eddy viscosity relationship. For example, the $\overline{uv}$ shear stress is expressed as:

$$\overline{uv} = -\nu_t \left(\frac{\partial U}{\partial y} + \frac{\partial V}{\partial x} \right) \tag{5.1}$$

in the eddy viscosity relationship from Eq. (4.9). However, from the discussion in section 3.6.4 it is apparent that the $\partial V/\partial z$ gradient makes a significant contribution to the production of $\overline{uv}$, particularly in the case of the spanwise jets. Since the $\overline{uv}$ stress is an indicator of the lateral turbulent mixing, the omission of the contribution to $\overline{uv}$ by the $\partial V/\partial z$ gradient may result in the underprediction of the lateral spreading of the jets. In the case of the spanwise and compound-angle jets at $R = 1.5$ it was noted that the lateral spreading of the jet was overpredicted by the numerical models. In these cases it was noted that the location of vortex formation differed from the experiments and was likely the source of the discrepancy between the two results in the near-hole region. A test case with a different jet hole entry velocity direction produced the same flat distribution of jet fluid concentration along the floor at $R = 1.5$ for the far downstream locations which indicates that not all of the discrepancies may be attributed to disagreement between the experiments and computations at the jet exit.

The comparisons between the SKE, BSL, and SST turbulence models indicates that none of the methods clearly perform better than the others. The turbulence kinetic energy profiles near the wall are typically better for the blended (BSL and SST) models which do not use wall functions. However, the predicted concentration of jet fluid near the wall from the BSL and SST models is consistently higher than both the experiments and SKE data.

It should be noted that the turbulence models are not the only source of errors in the computational results. In the current version of the CMGFD code the numerical scheme is based on the power-law approach of Patankar (1980). When the computational grid is not aligned with the flow the phenomenon known as 'false diffusion' can result in less accurate solutions. This difficulty is particularly relevant for the spanwise jet computations where the jet flow is highly skewed to the grid, particularly in the near-hole region. Another, perhaps more difficult problem lies in the unsteady nature of the flow. As noted in the discussion of the experimental results, higher values of k were found near the edges of the jets since the jets are not perfectly stationary in space. The motion of the shear layer through the LDV measurement volume will result in a higher measured turbulence level. In addition, unsteady vorticity from the upstream edge of the jet is transported downstream along the upper edge of the jet (Haven and Kurosaka (1997)), further complicating the flow field. It is not clear that higher-order turbulence closures would be able to resolve this effect.

Chapter 6

Conclusions and Recommendations

An investigation into the characteristics of the complex flow from a row of inclined square jets on a flat plate in a crossflow has been conducted. Four different geometries were studied: 1) streamwise inclined jets with a long ($L/D = 8$) entry length, 2) streamwise inclined jets with a short ($L/D = 4$) entry length, 3) spanwise inclined jets ($L/D = 4$), and 4) compound-angle inclined jets ($L/D = 4$). In all cases the jets were inclined at a 30° angle to the wind tunnel floor. Velocity ratios of $R = 0.5$, 1.0, and 1.5, which are of interest for gas turbine film cooling applications, were examined. Mean velocity and turbulence measurements were made using a three-component LDV system operating in coincidence mode to allow the turbulent Reynolds stresses to be determined. Jet penetration, spreading, and film cooling effectiveness were measured using a flame ionization detector after the jet flow was seeded by trace amounts of propane. The jet Reynolds number was fixed at approximately 5000 for all cases. Numerical simulations were performed for the short entry length cases using three different turbulence models: the standard $k - \epsilon$ model, Menter's baseline blended $k - \epsilon/k - \omega$ model, and Menter's shear stress transport model.

6.1 Conclusions

The detailed measurements of the mean flow and turbulence fields, as well as the scalar transport data, has provided additional insight into the complex flow produced by inclined jets in a crossflow. At $R = 0.5$ none of the jets penetrate beyond the boundary layer

as the strong crossflow deflects the jets strongly towards the floor. As the velocity ratio is increased to $R = 1.5$ the jets eventually penetrate beyond the boundary layer and the blockage to the crossflow is increased. The strong deflection of the jets at $R = 0.5$ results in higher spanwise-averaged film cooling effectiveness ($\overline{\eta_f}$) than at $R = 1.5$ as the jet fluid remains attached to the floor. The formation of strong vortices at $R = 0.5$ for the spanwise jets results in a less significant change in $\overline{\eta_f}$ as compared with the other geometries. The compound-angle jets appear to provide the best $\overline{\eta_f}$ in the near-hole region at $R = 0.5$ while the spanwise jets provide the best coverage at higher R. Considerations of aerodynamic performance and local variations in R over the surface of an actual turbine blade must be taken into account in determining the optimal geometry.

The flow at the jet exit is strongly influenced by the crossflow, as well as by the inlet conditions at the entrance to the jet orifice. Differences in the entry length for the streamwise inclined jets result in different exit profiles of vertical velocity components and turbulence kinetic energy. The differences are attributed to the proximity of the shear layer produced by the 'jetting effect' within the hole due to the inclination of the jet orifice. In contrast to the velocity profiles for the streamwise jets which become more uniform as R decreases (crossflow speed increases), the velocity profiles at the jet exit for the spanwise geometry become more skewed at the lower velocity ratios and differ from the assumed profiles used in earlier numerical studies.

The turbulence field has been shown to be highly anisotropic, particularly at the high velocity ratio. The turbulent shear stresses exhibit similar behaviour to the normal stresses in that the mean velocity gradients tend to promote the production of a particular stress at a given location in the flow field. Typically, the magnitude of the shear stresses are larger at the higher velocity ratio of $R = 1.5$, but due to the complexity of the flow it is not possible to make a general conclusion about the relationship between velocity ratio

and shear stresses. In the case of the spanwise and compound-angle jets the magnitude of the turbulent shear stresses decreases as the flow moves downstream due to the weaker mean velocity gradients which are present.

The combination of mean velocity, turbulent Reynolds stress, and jet concentration measurements has provided a good data set for validation of turbulence models and numerical methods for this class of flows. The preliminary computational investigation has shown that the flow field produced by inclined jets in a crossflow is a challenging test for numerical modelling. Three eddy-viscosity models were used in the computations: the standard $k - \epsilon$ (SKE) model, Menter's blended baseline (BSL) model, and Menter's blended shear stress transport (SST) model.

Agreement between experimental and computational results tends to deteriorate as R increases due to the increased anisotropy and unsteadiness of the flow. The standard eddy-viscosity model used in these computations is unable to account for the turbulence anisotropy and generation of turbulent shear stresses by velocity gradients which are not found in the standard model. The assumption of equilibrium turbulence which is used tends to result in lower predicted turbulence kinetic energy and weaker velocity gradients than observed in the experiments. Of the three turbulence models tested, there is no consistent improvement in the accuracy of the predictions for any particular model. As noted earlier, the highly three-dimensional nature of the flow provides a challenging test for turbulence models which have largely been calibrated using two-dimensional data.

6.2 Recommendations

The recommendations for future work are primarily directed towards the numerical modelling of the flow field produced by inclined jets in a crossflow. However, some experiments in key areas would help complete the bridge between the particular configuration used

here and the conditions in an actual gas turbine engine. The experimental recommendations are as follows:

1. Experimental measurements of the heat transfer coefficents for the configurations studied here would complete the study of the 'three-temperature' problem described in the Introduction.

2. An investigation of the characteristics of round, spanwise inclined jets would be of interest. This study would help determine the near-hole differences in mixing and vortex formation between round and square jets in a crossflow.

3. The introduction of density differences between the jet and crossflow would assist in determining the extent to which the results presented here may be applied to flows with similar mass flux or momentum flux ratios but with differing density ratios. The use of a foreign gas, such as CO_2, would likely be impractical due to the length of time required to obtain the LDV data and the flow rate required from the jets. A low-temperature jet flow may provide the appropriate density ratios.

The computational recommendations are as follows:

1. The use of higher-order differencing schemes should be investigated. The power-law scheme used in the present computations is based on an assumption of quasi-one-dimensional flow. While the effects of false diffusion are minimized on a fine grid, the number of cells required for the computations could be reduced.

2. Improved near-wall models should be implemented. The use of wall functions in a highly three-dimensional flow field is clearly not adequate for detailed simulations. In particular, the use of low-Re or two-layer models which do not restrict the near-wall cell size and allow accurate capture of the near wall jet flow at the higher velocity ratios should be investigated.

3. Turbulence models which accurately represent anisotropic turbulence will likely be required to resolve the downstream characteristics of the jet flow. The assumption of equilibrium turbulence should also be investigated in the analysis of the turbulence models. A comparison between an anisotropic and a non-equilibrium turbulence model would lend some insight into the relative importance of these two effects in the behaviour of the flow. The use of the experimental jet exit data as a boundary condition for the main flow region may assist in determining the influence of the turbulence models on the prediction of the flowfield, separate from any discrepancies which may be introduced by the jet hole inlet conditions.

4. The computational domain should be extended into the plenum region for the spanwise jet computations, and possibly for the compound-angle jet case as well. It was noted that poor agreement between the experiments and the computations at the jet exit resulted in marked differences in the downstream flow field. The use of a higher-order differencing scheme noted above should allow for the use of more computational cells in the plenum region if memory limitations are a problem.

5. The use of unstructured grids should be investigated, particularly for the compound-angle jet case. Due to the geometric complexity of this case it is difficult to obtain a smoothly-varying grid with a standard structured grid.

6. A parametric study of the jet orientation should be undertaken to determine if there is a compound-angle geometry which could provide the good film coverage of the spanwise jets at high velocity ratios without the corresponding high crossflow blockage.

7. Once reasonable agreement between the experiments and computations for the flat plate has been obtained, the techniques should be extended to the simulation of

more realistic, curved turbine blade geometries.

Appendix A

Angular Alignment Measurements

In order to determine the angles of alignment of the probes with respect to the tunnel coordinate system (Fig. 2.1) 10 measurements of each angle at various locations in the tunnel were made. The angles about the x-, y-, and z-axes are referred to as α, β, and γ respectively, as shown in Fig. 2.4. The blue/green probe is referred to by a subscript "1" and the violet probe by a subscript "2". The measurement of the angle α_1 will be described. The measurement of the angles β_1 and α_2 is similar. A different method was needed to measure β_2, which will be presented, and a similar approach is used for γ_1. The angle γ_2 was not measured as it was not required.

To determine α_1 a machinist's square was placed on the floor of the wind tunnel. Using the unshifted component of the green beam pair initially, the y-traverse was adjusted until the beam intersected a mark on the arm of the square which was perpendicular to the floor. The position of the y-traverse at this location was recorded as y_1. The y-traverse was then adjusted which resulted in the point of beam intersection moving along the square until another reference mark was reached. The separation of the two marks, Δz, was known and the new position of the y-traverse was recorded as y_2. The value of α for the unshifted green beam was calculated from:

$$\alpha_{1,unshifted} = \arctan\left(\frac{y_2 - y_1}{\Delta z}\right) \tag{A.1}$$

The procedure was then repeated for the frequency-shifted component of the green beam

pair, which contacted the opposite side of the square, to determine $\alpha_{1,shifted}$. The final value of α_1 was calculated as an average of $\alpha_{1,unshifted}$ and $\alpha_{1,shifted}$.

To determine γ_1 the pinhole block was used. The shifted green (or blue) beam was positioned over the pinhole and the positions of the traverse mechanism were recorded (x_1, y_1). The traverse was then adjusted in the x- and y-directions until the unshifted green (or blue) component was centred over the pinhole where x_2 and y_2 were recorded. The angle was calculated from:

$$\gamma_{1,pinhole} = \arctan\left(-\frac{x_2 - x_1}{y_2 - y_1}\right) \tag{A.2}$$

The angle $\gamma_{1,pinhole}$ is not the true angle of alignment as there may be an error from the traverse itself if the traverse directions are not perfectly parallel to the corresponding tunnel directions. To measure this angle, the y-traverse (in the case of the green beam pair) was moved over a known distance (from the traverse), Δy, along a line parallel to the y-axis in the wind tunnel. The x-traverse was adjusted at the end of the traverse, if necessary, to bring the beam back in line with the y-axis. The locations at the beginning and end (x_1 and x_2) of the traverse were recorded and the traverse angle was calculated from:

$$\gamma_{1,traverse} = \arctan\left(-\frac{x_2 - x_1}{\Delta y}\right) \tag{A.3}$$

The angle of alignment was then:

$$\gamma_1 = \gamma_{1,pinhole} - \gamma_{1,traverse} \tag{A.4}$$

The measured angles of alignment are shown in Table A.6.

Geometry	Angle of Alignment [°] (Standard Deviation [°])				
	α_1	β_1	γ_1	α_2	β_2
Streamwise ($L/D = 8$)	6.001 (0.0599)	0.314 (0.3888)	-0.553 (0.1040)	5.580 (0.1066)	0.279 (0.3251)
Streamwise ($L/D = 4$)	6.828 (0.013)	0.134 (0.009)	-0.577 (0.094)	6.627 (0.010)	0.630 (0.106)
Spanwise	7.006 (0.008)	0.486 (0.010)	0.361 (0.104)	6.846 (0.020)	0.450 (0.175)
Compound-Angle	3.853 (0.029)	-3.667 (0.016)	0.029 (0.047)	6.746 (0.022)	0.830 (0.355)

Table A.6: Alignment Angles

Once the angles of alignment have been determined, the measured velocities can be transformed to velocity components parallel to the tunnel axes through a coordinate rotation. The inverted transformation matrices from Equation (2.4) for the various geometries and angles from Table A.6 are as follows:

$$\text{Streamwise } L/D = 8 \qquad \mathbf{C^{-1}} = \begin{bmatrix} 0.9999 & 0.0101 & 0.0044 \\ -0.0090 & 0.9952 & -0.1046 \\ -0.0058 & 0.0972 & 0.9945 \end{bmatrix} \tag{A.5}$$

$$\text{Streamwise } L/D = 4 \qquad \mathbf{C^{-1}} = \begin{bmatrix} 0.9999 & 0.0103 & 0.0011 \\ -0.0086 & 0.9933 & -0.1189 \\ -0.0120 & 0.1153 & 0.9930 \end{bmatrix} \tag{A.6}$$

$$\text{Spanwise} \qquad \mathbf{C^{-1}} = \begin{bmatrix} 1.0000 & -0.0052 & 0.0092 \\ 0.0072 & 0.9929 & -0.1219 \\ -0.0070 & 0.1192 & 0.9925 \end{bmatrix} \tag{A.7}$$

$$\text{Compound-angle} \qquad \mathbf{C}^{-1} = \begin{bmatrix} 1.0030 & -0.0080 & -0.0641 \\ 0.0015 & 0.9943 & -0.0674 \\ -0.0144 & 0.1177 & 1.0 \end{bmatrix} \tag{A.8}$$

While the matrix **C** can be inverted numerically in order to determine the transformed velocity components, the evaluation of the error requires the actual symbolic transformation (see section 3.2.1). The inverted transformation matrix is as follows:

$$\mathbf{C}^{-1} = \frac{\begin{bmatrix} c(\alpha_1 - \alpha_2)c\beta_2 c\gamma_1 & c\beta_2(s\alpha_2 s\beta_1 c\gamma_1 - c\alpha_2 c\beta_1 s\gamma_1) & c\gamma_1(s\alpha_1 c\beta_1 s\gamma_1 + c\alpha_1 s\beta_1 c\gamma_1) \\ c\alpha_2(c\alpha_1 c\beta_2 s\gamma_1 + s\alpha_1 s\beta_2 c\gamma_1) & c\alpha_2 c(\beta_1 - \beta_2)c\gamma_1 & c\gamma_1(c\alpha_1 s\beta_1 s\gamma_1 - s\alpha_1 c\beta_1 c\gamma_1) \\ c\alpha_1(s\alpha_2 c\beta_2 s\gamma_1 - c\alpha_2 s\beta_2 c\gamma_1) & c\beta_1(s\alpha_2 c\beta_2 c\gamma_1 + c\alpha_2 s\beta_2 s\gamma_1) & c\beta_1 c\alpha_1 \end{bmatrix}}{c\alpha_1 c\alpha_2 c\beta_1 c\beta_2 + c^2\gamma_1(s\alpha_1 s\alpha_2 c\beta_1 c\beta_2 + c\alpha_1 c\alpha_2 s\beta_1 s\beta_2) + \frac{1}{2}s(2\gamma_1)(s\alpha_1 c\alpha_2 c\beta_1 s\beta_2 - c\alpha_1 s\alpha_2 s\beta_1 c\beta_2)} \tag{A.9}$$

The notation $s\theta = \sin\theta$ and $c\theta = \cos\theta$ has been used for brevity.

Bibliography

Ajersch, P. (1993). "XFORMV20". Computer Program.

Ajersch, P. (1995). "Detailed Measurements of a Row of Jets in a Crossflow - With Applications". Master's thesis, University of British Columbia, Vancouver, Canada.

Ajersch, P., J.-M. Zhou, S. Ketler, M. Salcudean, and I. Gartshore (1997). "Multiple Jets in a Crossflow: Detailed Measurements and Numerical Simulations". *ASME Journal of Turbomachinery 119.*

Andreopoulos, J. and W. Rodi (1984). "Experimental Investigation of Jets in a Crossflow". *Journal of Fluid Mechanics 138*, 92–127.

Bergeles, G., A. Gosman, and B. Launder (1978). "The Turbulent Jet in a Cross Stream at Low Injection Rates: A Three-Dimensional Numerical Treatment". *Numerical Heat Transfer 1*, 217–242.

Boussinesq, J. (1877). "Theorie de l'ecoulement tourbillant". *Memoires Presentes par Divers Savants Sciences Mathematique et Physiques, Academie des Sciences, Paris 23*, 46.

Bury, K. (1995). "Statistical Models in Applied Science". Course Notes.

Crabb, D., D. Durão, and J. Whitelaw (1981). "A Round Jet Normal to a Crossflow". *ASME Journal of Fluids Engineering 103*, 142–153.

Demuren, A. (1993). "Characteristics of Three-Dimensional Turbulent Jets in Crossflow". *International Journal of Engineering Science 31*(6), 899–913.

Durst, F., A. Melling, and J. Whitelaw (1981). *Principles and Practice of Laser-Doppler Anemometry* (2 ed.). Academic Press.

Eckert, E. (1955). "Engineering Relations for Friction and Heat Transfer to Surfaces in High Velocity Flow". *Journal of the Aeronautical Sciences 22*, 585–587.

Eckert, E. (1984). "Analysis of Film Cooling and Full-Coverage Film Cooling of Gas Turbine Blades". *ASME Journal of Engineering for Gas Turbines and Power 106*, 206–213.

Edwards, R. (1987). "Report of the Special Panel on Statistical Particle Bias Probelms in Laser Anemometry". *ASME Journal of Fluids Engineering 109*, 89–93.

Fackrell, J. (1978). "A system for turbulent concentration measurements". *J. Phys. E: Sci. Instrum. 11*, 1015–1022.

Fackrell, J. (1980). "A flame ionization detector for measuring fluctuating concentration". *J. Phys. E: Sci. Instrum. 13*, 888–893.

Findlay, M., P. He, M. Salcudean, and I. Gartshore (1996). "A Row of Streamwise-Inclined Jets in Crossflow: Measurements and Calculations". *ASME Paper 96-GT-167*.

Findlay, M., M. Salcudean, and I. Gartshore (1997). "Jets in a Crossflow: Effects of Geometry and Blowing Ratio". *ASME Paper FEDSM97-3299*.

Forth, C. and T. Jones (1986). "Scaling Parameters in Film-Cooling". In *Heat Transfer 1986, Proceedings of the Eighth International Heat Transfer Conference*, pp. 1271–1276.

Fuchs, W., H. Nobach, and C. Tropea (1993). "The Simulation of LDA Data and its Use to Investigate the Accuracy of Statistical Estimators". *Technical Paper submitted to AIAA Journal*, 1–21.

Garg, V. and R. Gaugler (1997). "Effect of Velocity and Temperature Distribution at the Hole Exit on Film Cooling of Turbine Blades". *ASME Journal of Turbomachinery 119*(2), 343–351.

George, W. and J. Lumley (1973). "The Laser Doppler Velocimeter and Its Application to the Measurements of Turbulence". *Journal of Fluid Mechanics 60*, 321–362.

Goldstein, R. (1971). *Film Cooling*, Volume 7 of *Advances in Heat Transfer*, pp. 321–379. New York: Academic Press.

Goldstein, R., E. Eckert, and F. Burggraf (1974). "Effects of Hole Geometry and Density on Three-Dimensional Film Cooling". *International Journal of Heat and Mass Transfer 17*, 595–607.

Green, S. I. (Ed.) (1995). *Fluid Vortices*. The Netherlands: Kulwer Academic Publishers.

Haven, B. and M. Kurosaka (1996). "Improved Jet Coverage Through Vortex Cancellation". *AIAA Journal 34*(11), 2443–2444.

Haven, B. and M. Kurosaka (1997). "Kidney and anti-kidney vortices in crossflow jets". *Journal of Fluid Mechanics 352*, 27–64.

He, P. (1995). *Numerical Prediction of Film Cooling of Turbine Blades Using Multiblock Curvilinear Grids*. Ph. D. thesis, University of British Columbia, Vancouver, Canada.

He, P., Z. Nowak, I. Hassan, M. Salcudean, and I. Gartshore (1997, December). "A Complete Code for the Calculation of Laminar/Turbulent Flows and Heat Transfer in 3-D Complex Geometries using Multiblock Curvilinear Grids". Technical report, University of British Columbia.

He, P. and M. Salcudean (1994). "A Numerical Method for 3D Viscous Incompressible Flows Using Non-Orthogonal Grids". *Journal of Numerical Methods in Fluids 18*, 449–469.

Hill, P. and C. Peterson (1992). *Mechanics and Thermodynamics of Propulsion* (Second ed.). New York: Addison-Wesley.

Hinze, J. (1975). *Turbulence* (2 ed.). McGraw-Hill.

Holdeman, J. and R. Walker (1977). "Mixing of a Row of Jets with a Confined Crossflow". *AIAA Journal 15*(2), 243–249.

Honami, S., T. Shizawa, and A. Uchiyama (1994). "Behavior of the Laterally Injected Jet in Film Cooling: Measurements of Surface Temperature and Velocity/Temperature Field Within the Jet". *ASME Journal of Turbomachinery 116*, 106–112.

Kavsaoglu, M. and J. Schetz (1989). "Effects of Swirl and High Turbulence on a Jet in a Crossflow". *Journal of Aircraft 26*(6), 539–546.

Kavsaoglu, M., J. Schetz, and A. Jakubowski (1989). "Rectangular Jets in a Crossflow". *Journal of Aircraft 26*(9), 793–804.

Kim, S.-W. and C.-P. Chen (1989). "A Multiple-Time-Scale Turbulence Model Based on Variable Partitioning of the Turbulent Kinetic Energy Spectrum". *Numerical Heat Transfer, Part B 16*, 193–211.

Knuth, E. (1963a). "Use of Reference States and Constant-Property Solutions in Predicting Mass–, Momentum–, and Energy–Transfer Rates in High–Speed Laminar Flows". *International Journal of Heat and Mass Transfer 6*, 1–22.

Knuth, E. (1963b). "Use of Reference States in Predicting Transport Rates in High–Speed Turbulent Flows with Mass Transfers". *International Journal of Heat and Mass Transfer 6*, 999–1018.

Kohli, A. and D. Bogard (1995). "Adiabatic Effectiveness, Thermal Fields, and Velocity Fields for Film Cooling with Large Angle Injection". *ASME Paper 95-GT-219, to be published in the Transactions of the ASME.*

Launder, B. (1988). "On the Computation of Convective Heat Transfer in Complex Turbulent Flows". *ASME Journal of Heat Transfer 110*, 1112–1128.

Launder, B. and D. Spalding (1972). *Mathematical Models of Turbulence.* London: Academic Press.

Launder, B. and D. Spalding (1974). "The Numerical Computation of Turbulent Flows". *Computer Methods in Applied Mechanics and Engineering 3*, 269–289.

Lee, S., Y. Kim, and J. Lee (1995). "Flow Characteristics and Aerodynamic Losses of Film-Cooling Jets with Compound Angle Orientations". *ASME Paper 95-GT-38.*

Lee, S., J. Lee, and S. Ro (1994). "Experimental Study on the Flow Characteristics of Streamwise Inclined Jets in Crossflow on Flat Plate". *ASME Journal of Turbomachinery 116*, 97–105.

Leylek, J. and R. Zerkle (1994). "Discrete-Jet Film Cooling: A Comparison of Computational Results with Experiments". *ASME Journal of Turbomachinery 116*, 358–368.

Ligrani, P., S. Ciriello, and D. Bishop (1992). "Heat Transfer, Adiabatic Effectiveness, and Injectant Distributions Downstream of a Single Row and Two Staggered Rows of Compound Angle Film-Cooling Holes". *ASME Journal of Turbomachinery 114*, 687–700.

Ligrani, P. and A. Ramsey (1995). "Film Cooling From Spanwise Oriented Holes in Two Staggered Rows". *ASME Paper 95-GT-39, to be published in the Transactions of the ASME.*

Ligrani, P., J. Wigle, and S. Jackson (1994a). "Film-Cooling From Holes With Compound Angle Orientations: Part 1 – Results Downstream of Two Staggered Rows of Holes With 3d Spanwise Spacing". *Journal of Heat Transfer 116*, 341–352.

Ligrani, P., J. Wigle, and S. Jackson (1994b). "Film-Cooling From Holes With Compound Angle Orientations: Part 2 – Results Downstream of a Single Row of Holes With 6d Spanwise Spacing". *Journal of Heat Transfer 116*, 353–362.

MathSoft, I. (Ed.) (1994). *Mathcad 5.0 for Windows*, pp. 447. MathSoft, Inc.

McLaughlin, D. and W. Tiederman (1973). "Biasing Correction for Individual Realization of Laser Anemometer Measurements in Turbulent Flows". *Physics of Fluids 16*, 2082–2088.

Mehendale, A. and J. Han (1992). "Influence of High Mainstream Turbulence on Leading Edge Film Cooling Heat Transfer". *ASME Journal of Turbomachinery 114*, 707–715.

Menter, F. (1992). "Influence of Freestream Values on k-ω Turbulence Model Predictions". *AIAA Journal 30*(6), 1657–1659.

Menter, F. (1994). "Two-Equation Eddy-Viscosity Turbulence Models for Engineering Applications". *AIAA Journal 32*(8), 1598–1605.

Menter, F. (1996). "A Comparison of Some Recent Eddy-Viscosity Turbulence Models". *ASME Journal of Fluids Engineering 118*, 514–518.

Metzger, D., H. Carper, and L. Swank (1968). "Heat Transfer With Film Cooling Near Nontangential Injection Slots". *ASME Journal of Engineering for Power 90*, 157–163.

Nakao, S., Y. Terao, and K. Hirata (1987). "New Method for Eliminating the Statistical Bias in Highly Turbulent Flow Measurements". *AIAA Journal 25*(3), 443–447.

Needham, D., N. Riley, and C. Lytton (1990). "A Jet in a Crossflow. Part 2". *Journal of Fluid Mechanics 211.*

Needham, D., N. Riley, and J. Smith (1988). "A Jet in a Crossflow". *Journal of Fluid Mechanics 188.*

Orloff, K. and P. Snyder (1982). "Laser Doppler anemometer measurements using nonorthogonal velocity components: error estimates". *Applied Optics 21*(2), 339–344.

Ou, S. and J. Han (1994). "Leading Edge Film Cooling Heat Transfer Through One Row of Inclined Film Slots and Holes Including Mainstream Turbulence Effects". *ASME Journal of Heat Transfer 116*, 561–569.

Patankar, S. (1980). *Numerical Heat Transfer and Fluid Flow.* New York: McGraw-Hill.

Patankar, S., D. Basu, and S. Alpay (1977). "Prediction of the Three-Dimensional Velocity Field of a Deflected Turbulent Jet". *ASME Journal of Fluids Engineering 99*, 758–762.

Pietrzyk, J., D. Bogard, and M. Crawford (1989). "Hydrodynamic Measurements of Jets in Crossflow for Gas Turbine Film Cooling Applications". *ASME Journal of Turbomachinery 111*, 139–145.

Pratt & Whitney Canada (1993). "Private communication".

Quinn, W. (1992). "Streamwise Evolution of a Square Jet Cross Section". *AIAA Journal 30*(12), 2852–2857.

Quinn, W. and J. Militzer (1988). "Experimental and numerical study of a turbulent free square jet". *Physics of Fluids 31*(5), 1017–1025.

Rickards, J., C. Swales, C. Brake, and R. Barrett (1993). "An improved alignment technique enabling cross-coupled operation of a 3D LDA for small scale flow surveys". In J. Bessem et al. (Eds.), *Proceedings of the 5th International Conference on Laser Anemometry Advances and Applications*, pp. 711–718.

Rodi, W. (1984). *Turbulence Models and Their Application in Hydraulics* (2 ed.). Delft: IAHR.

Rodi, W. (1991). "Experience With Two-Layer Models Combining the k-epsilon Model With a One-Equation Model Near the Wall". *AIAA-91-0216*.

Rodi, W., S. Majumdar, and B. Schonung (1989). "Finite Volume Methods for Two-Dimensional Incompressible Flows with Complex Boundaries". *Computer Methods in Applied Mechanics and Engineering 75*, 369–392.

Salcudean, M., I. Gartshore, K. Zhang, and I. McLean (1994). "An Experimental Study of Film Cooling Effectiveness Near the Leading Edge of a Turbine Blade". *ASME Journal of Turbomachinery 116*, 71–79.

Sathyamurthy, P. and S. Patankar (1990). "Prediction of Film Cooling with Lateral Injection". In *Heat Transfer in Turbulent Flows*, Volume 138, pp. 61–70.

Schmidt, D. and D. Bogard (1995). "Pressure Gradient Effects on Film Cooling". *ASME Paper 95-GT-18*.

Sinha, A., D. Bogard, and M. Crawford (1991). "Gas Turbine Film Cooling: Flowfield Due to a Second Row of Holes". *ASME Journal of Turbomachinery 113*, 450–456.

Sterland, P. and M. Hollingsworth (1975). "An Experimental Study of Multiple Jets Directed Normally to a Cross-Flow". *Journal of Mechanical Engineering Science 17*(3), 117–124.

Stropky, D. (1993). *Inviscid Flow From a Slot Into a Cross Stream.* Ph. D. thesis, University of British Columbia, Vancouver, Canada.

Sun, Y. (1995). *An Experimental and Numerical Investigation of Heat Transfer Downstream of a Normal Film Cooling Injection Slot.* Ph. D. thesis, University of British Columbia, Vancouver, Canada.

Thole, K., M. Gritsch, A. Schultz, and S. Wittig (1997). "Effect of a Crossflow at the Entrance to a Film-Cooling Hole". *ASME Journal of Fluids Engineering 119*, 533–540.

van Driest, E. (1956). "On Turbulent Flow Near a Wall". *Journal of Aeronautical Science 23*, 1007.

Walters, D. and J. Leylek (1996). "A Systematic Computational Methodology Applied to a Three-Dimensional Film-Cooling Flowfield". *ASME Paper 96-GT-351*.

White, F. (1991). *Viscous Fluid Flow* (2 ed.). McGraw-Hill.

Wilcox, D. (1988). "Reassessment of the Scale-Determining Equation for Advanced Turbulence Models". *AIAA Journal 26*(11), 1299–1310.

Zhou, J.-M. (1994). *A Computational and Experimental Investigation of Gas Turbine Blade Film Cooling*. Ph. D. thesis, University of British Columbia, Vancouver, Canada.

IMAGE EVALUATION
TEST TARGET (QA-3)

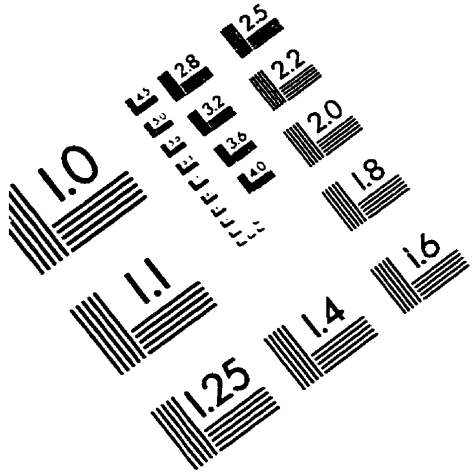

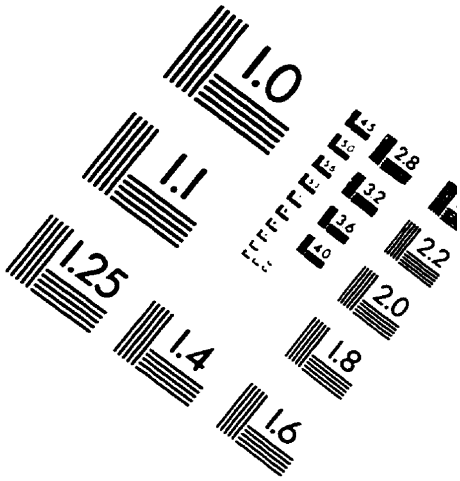

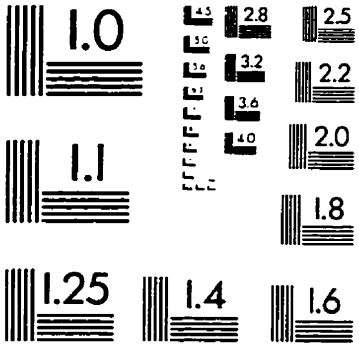

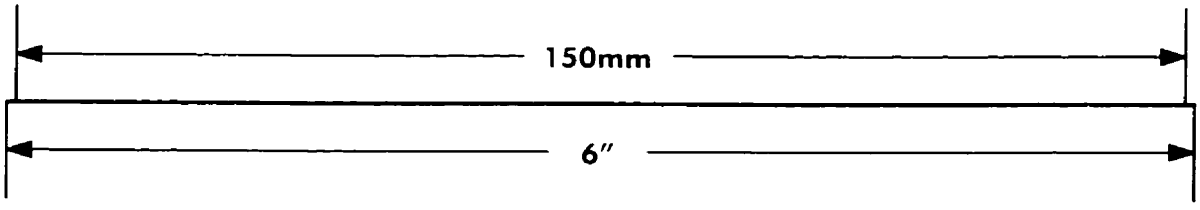

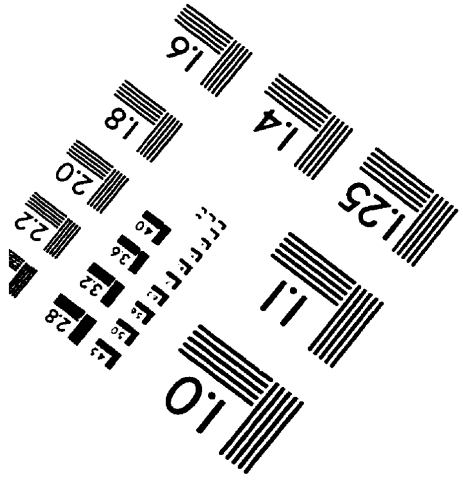

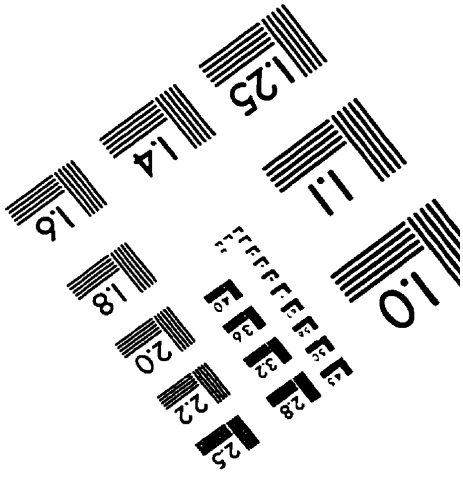

APPLIED IMAGE, Inc
1653 East Main Street
Rochester, NY 14609 USA
Phone: 716/482-0300
Fax: 716/288-5989